Assessment of electrical resistivity properties through development of three-dimensional numerical models

Thesis submitted for the degree of

Doctor of Philosophy

at the University of Leicester

by

Ceri Gwyn Williams BSc (Bristol, 1991)

Department of Geology

University of Leicester

February 1996

Assessment of electrical resistivity properties through development of three-dimensional numerical models

Ceri Gwyn Williams

Abstract

An understanding of the way in which electrical currents flow through geological materials enables pertinent problems to be addressed, for example: determination of oil saturation; prediction and monitoring of fluid flow; fracture characterisation; assessment of geological structure in a general sense. The objective of this work is to simulate current flow and electrical resistivity measurements made downhole and at the earth's surface in three dimensions. This enhances interpretation by enabling the geological controls on field measurements of resistivity properties to be assessed. In addition, a basis for a wide range of applications using quantitative analysis of electrical measurements is provided.

A finite difference numerical model based on the direct solution of a generalised form of Poisson's equation is developed. Both electric potential and current flow are readily simulated on a rectangular three-dimensional grid. Arbitrary resistivity distributions and electrical anisotropy can be accommodated. The model grid is advantageously analogous to (and therefore supersedes) resistor networks previously built to simulate resistivity logging tools.

The model is developed through three applications. The simulation of a novel multi-electrode focused surface array is used to assess and interpret field measurements. The Ocean Drilling Program High Temperature (ODPHT) tool, a new downhole focused resistivity device, is modelled on an adapted cylindrical grid in order to calculate its geometric factors. Finally, a generalised model of a downhole electrical imaging device based on Schlumberger's Formation MicroScanner is created. Current flow is simulated from an array of 5 mm diameter electric buttons that are passively focused into the formation. This is used to generate simulated electrical images. The numerical model is verified by comparison with field data in well-constrained situations.

Electrical measurements and current flow patterns have been investigated in three dimensions at a variety of scales. An enhanced understanding of the operation of surface and downhole electrical devices is gained through modelling selected geologically relevant scenarios. Specific benefits are: enhanced fault detection in the case of the surface array; quantitative characterisation of the ODPHT tool in idealised borehole environments; radial fracture characterisation using electrical images, and potential image artefacts due to localised off-hole anomalies.

To my family

for their love, friendship

and support

Contents

APPENDICES

Acknowledgements

Thanks go first and foremost to my supervisors: Peter Jackson at the British Geological Survey (BGS) for encouragement and support, and many discussions after 5-a-side football; Peter Harvey at Leicester University for reminding me of the geological aspects; both of them for their comments and suggestions throughout the writing of this thesis.

This PhD was instigated by Peter Jackson and Mike Lovell; without their help it would never have existed, and without Mike's whip-cracking I might still be writing it. Gordon Reece at Bristol was my external supervisor. I was funded by a Leicester University Open Research Scholarship; additional support was provided by Leicester University Borehole Research (LUBR), BGS, and awards from the SPWLA Foundation.

The Fieldwork in Saarland was organised by Roger Peart and Peter Jackson. Thanks to Phil Meldrum for many enjoyable hours in the back of a trailer, and to Peter Greenwood whose enthusiasm kept us all smiling. Thanks also to my other friends and colleagues at the BGS, especially Rob Flint for help with miscellaneous computer queries.

As a member of the LUBR group I was privileged to have use of facilities which eased many of the hassles of writing up. Thanks to everyone upstairs, especially Kate for a last-minute reference and Liane, Gail, Tim and Janette for their help and continual offers of assistance. I shared an office and held many discussions (in fluent PostScript) with George Zheng, and subsequently Carlos Gonçalves who set the pace by starting a family *and* effectively completing a PhD in a *foreign language* in two years. I follow in the footsteps of the 'old original' Borehole Boys, Jez Lofts and Jim Bristow, who have given me a lot to live up to, as well as much advice and encouragement.

Thanks to all my friends and colleagues in the Leicester Geology Department as a whole, especially anyone who asked me a question at one of my departmental seminars. Special thanks go to Vivi and Max Meju for lending me books and Chris Beckett for help and advice with occasional computer problems.

Not content with just working amongst geologists, I also lived amongst them, firstly with Jez, Giles and Stuart, then Duncan, and subsequently Tanya, Cayley, Laurence and Robin. Apart from being a bunch of great friends, they afforded a unique insight into the PhD process, preparing me for the stresses of writing up and provoking thoughts about what I was doing and where I was going. I wish those of them who haven't yet finished a speedy write-up and in particular hope that Duncan and Tanya will refrain from throttling each other in the process.

Special thanks to Anita for putting up with me all the time I've been studying, particularly when I was finishing, and in doing so demonstrating her faith in me.

At the beginning of my PhD I had the privilege of working with Jon Ball, who was a mathematician in a world of geoscientists, a diligent research scientist, a mentor, and an example for all of us. I can only speculate how much more my work would have benefited from his comments and advice were he still alive today.

CHAPTER 1

Introduction

1.1 Background

The electrical properties of rock formations and rock-forming minerals can be characterised by resistivity and the dielectric constant (magnetic permeability may also be considered as an additional, indirectly related parameter). Of these electrical resistivity has the most dominant influence on electrical conduction. In particular it is the fundamental physical property governing situations involving d.c. (direct current: time-invariant, or low frequency) as opposed to a.c. (alternating current) electricity.

The work described in this thesis is concerned only with d.c. electrical conduction. In terms of the characterisation of electrical properties attention is therefore directed towards resistivity (or its reciprocal, conductivity) (§A.1).

Resistivity can be thought of as a measure of how difficult it is to pass current through a material. Since electrical conduction generally takes place by ionic conduction via the fluid phase of a rock mass, the electrical resistivity is related (at least in a general sense) to the geometry of pore spaces and other void spaces such as fractures, which are important features of many rocks. This relationship between electrical and geological properties is utilised in a wide range of applications including:

ground measurements—characterisation of shallow subsurface geology—which has applications in civil engineering, engineering geology, hydrogeology and archaeology;

downhole logging—electrical logs give an indication of features such as bed boundaries, porosity and fluid property variations;

downhole imaging—allowing interpretation of geological features on the borehole wall, and enhancing core-log integration;

core analysis—porosity, saturation and permeability determination—enabling quantitative characterisation of reservoir fluids and fluid-flow properties.

The above discussion is expanded in Chapter 2.

The relationship between measured electrical parameters, the flow of electricity in the earth, and geological and petrophysical parameters is in general a complex one. The development of computer technology has provided considerable assistance for the interpretation of electrical resistivity; analysis of complex situations in three dimensions is now viable. Numerical simulations of the electrical response of the earth can be used in a number of ways to enhance resistivity data interpretation, for example:

- by providing a quantitative prediction of measurement responses in controlled situations;
- by assessing the response characteristics of resistivity measurement devices in three dimensions, to aid both the interpreter and the design engineer.

The importance of electrical measurements in terms of their wide range of applications and the requirement for numerical simulations to aid their interpretation is a primary motivation for this study.

1.2 Objectives of the research

The aims of this research work can be divided into *model development* objectives and *model application* objectives.

Model development objectives

The first task undertaken in this work was the development of a three-dimensional numerical simulation of the conduction of electricity in rocks. A variety of different approaches to this problem are described in the literature (§3.1). The aim of the present research work is to apply ideas for simulating focused electrical measurements using properties specific to the finite difference solution method (§3.2). The start point is a numerical model with a solution algorithm due to Reece (1986), which has been developed for resistivity modelling by Jackson (pers. comm., 1991).

Initial models are based on a rectangular grid, which is suited to modelling surface-based electrical measurements. An important division of electrical measurements concerns those made in boreholes, therefore a principal development goal is to make use of a grid involving radial symmetry.

Once basic models of electrical flow have been created, the next goal is to make modifications to allow specific measurement devices to be simulated. The research work has concentrated on three such devices, which form a natural progression in terms of model development:

1. a focused surface measurement array, which can be based on a rectangular grid;
2. a focused downhole logging device, which is simulated using a cylindrical grid; and
3. a downhole electrical imaging device, which is also based on a cylindrical grid, and requires the numerical simulation of a passive focusing mechanism.

Model application objectives

A primary goal is to demonstrate the validity of the numerical model. This can be done by comparing simulated data with field measurements taken from well-constrained situations.

The next step is to develop models to enhance understanding of tool characteristics and the nature of (selected) electrical measurements in specific situations corresponding to geologically relevant scenarios, by modelling current flow in three dimensions.

The eventual goal of modelling of this kind is to improve understanding of d.c. electrical flow through geological materials and thus to aid resistivity data interpretation, thereby expanding knowledge of the electrical properties (specifically, the resistivity distribution) of the survey region and enhancing applications which make use of such information.

1.3 Structure of this thesis

Each chapter in this thesis follows a progression. Chapter 2 and the first part of Chapter 3 are essentially reviews, outlining important principles and providing a basis from which a model of electrical current flow can be developed and adapted for investigating a range of problems. The second part of Chapter 3 outlines in detail the general principles of the basic model. Specific applications of the model, which again progress from the basic model, are described in Chapters 4 and 5.

Chapter 2 discusses the means by which electrical conduction takes place in rocks. With this in mind, the formulation of equations governing the electric potential in a conductive medium, which pose the mathematical problem to be solved by numerical modelling, are reviewed. Principles of electrical measurement methods are outlined. An overview of the

applications of electrical methods categorised as surface, conventional downhole, and downhole imaging is presented.

The first part of Chapter 3 reviews methods for modelling electrical flow by solving the governing equation (a generalised form of Poisson's equation) described in Chapter 2. The equation is classified in order to identify suitable solution methods. For simple cases direct solutions are available; in more general cases, a numerical solution method is required. A variety of alternative solution methods (of both kinds) are reviewed. The second part of Chapter 3 describes a numerical model, based on the finite difference method, which has been developed. This model forms a basis from which specific simulations (described in the two subsequent chapters) are developed and applied. Modifications to take account of borehole geometry are described with a view to enabling the model to cater for downhole measurements.

Chapter 4 describes extensions of the model to simulate ('actively') focused measurements. After a brief introduction to the nature and mechanisms of focused arrays (§4.0), two different applications of the technique are presented. Section 4.1 describes the application of the focused technique to measurements made by an array of electrodes at the earth's surface. The numerical algorithm used with the surface array measurements is applied both to synthetically focus field data and also to create a simulation of the measurement for use in the interpretation process. Selected case studies from fieldwork based in Germany are presented. Section 4.2 reports on a simulation of a novel focused downhole resistivity tool, which is used to derive geometric factors to aid in quantifying the tool measurements.

Chapter 5 describes the development and application of the numerical model to simulate downhole electrical imaging devices. Imaging tools are passively-focused devices; a resistor network analogy of the finite difference solution method is used in simulating the action of the focusing. The model is applied to a range of situations, demonstrating its viability and providing an insight into its response to selected, geologically relevant three-dimensional scenarios.

Chapter 6 brings the thesis to a conclusion by assessing the work described in this thesis with regards to the application and development objectives stated in Section 1.2. Recommendations for further work are made.

CHAPTER 2

Review: electrical conduction in rocks

In order to create a numerical model of the conduction of electricity in rocks, it is necessary to simulate both field observations and the flow of electrical current in the rock mass. An appreciation of these processes and their potential applications provides a motivation for this study in addition to a theoretical framework on which to base numerical simulations.

After reviewing the mechanisms of electrical conduction in rocks and rock-forming minerals and the way in which geological phenomena can influence electrical flow (§2.1) the theory of electromagnetism, as applied to d.c. (direct current) electricity in three dimensions (3D), is outlined (§2.2). This provides a foundation for a mathematical model of electrical conduction in rocks.

The practical means of determining electrical properties on the surface of and within the earth is by making electrical geophysical measurements. The principles of contemporary measurement methods are reviewed in Section 2.3. The same principles can be used in a numerical simulation in order to generate synthetic measurements.

Section 2.4 outlines some empirical relationships between electrical resistivity, porosity and other petrophysical parameters. The importance of electrical properties of rocks is subsequently demonstrated by describing applications in research and industry which utilise them. Applications are categorised according to whether they are based upon surface measurements, conventional downhole measurements, or downhole imaging. Numerical simulations have been developed in all three categories; these are described in chapters 3–5.

2.1 Background: electrical conduction processes in rocks

2.1.1 Direct current conduction

An electric current is a systematic drift of mobile charge-carriers. In the case of metallic conductors, the charge-carriers are free electrons associated with metallic bonds. Most rock-

forming minerals do not conduct in this way; for example quartz is a virtually perfect insulator: due to its crystal structure, there are no electrons available to carry a charge. Instead conduction takes place through the fluids which permeate the rock matrix by the flow of aqueous ions.

The rock matrix is generally permeated by voids of various descriptions: *pore spaces* are cavities between the mineral grains making up a rock, whereas *fissures* (often caused by chemical processes such as leaching) and *fractures* (mechanical discontinuities produced by stresses) are larger-scale, (often planar) discrete features. The voids are generally filled with fluids in subsurface rocks, and in such cases conduction can take place via the aqueous ions present in the saturating fluids. In general the process of electrical conduction is an electrolytic rather than an electronic one, and the electrical properties of most rocks are therefore directly related to the electrical properties of the saturating fluid and its distribution in the rock mass.

A simulation of electrical conduction does not need to account for the conduction process since these are irrelevant on a macroscopic scale. From a geological perspective, the fact that the fluid phase is providing the means for conduction may be used to make inferences about geological properties by using electrical properties (§2.4).

The approximate range of measured resistivity values for some common rock types is shown in Figure 2.1. It is apparent that resistivity can vary over eight orders of magnitude or more. In the case of sandstones, for example, lower values can be attributed to electrical conduction via pore waters in high-porosity rocks, while the higher values reflect conduction through the highly resistive rock matrix in a dry sample. Figure 2.1 does not give any indication of the distribution of values. More detailed information may be found in Carmichael (1989) who provides extensive tables of measured rock resistivities.

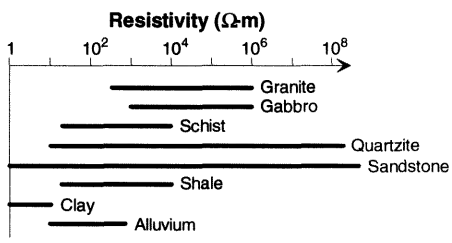

Figure 2.1 Approximate range of resistivity values of common rock types (after Kearey and Brooks, 1991).

The resistivity of a saturating fluid typically has a controlling effect on the bulk resistivity of the rock it saturates, since it is commonly several orders of magnitude less resistive than the rock matrix and therefore carries the majority of the electric current. The resistivity of saline water depends on salinity and temperature since these parameters affect the mobility and abundance of charge carriers. The variation of resistivity with these parameters is shown in Figure 2.2.

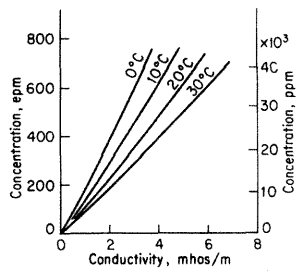

Figure 2.2 Conductivity of saline water with varying equivalent NaCl concentrations (from Grant and West, 1965).

Ellis (1987) demonstrates that the resistivity of an electrolyte may be expressed as $6\pi\eta a/nq^2$, where η is viscosity, a is the electrolytic particle diameter, and n is the number of charge carriers per unit volume each with a charge q. This relationship quantifies the relationship between resistivity of an electrolyte and its physical parameters, and provides a physical basis for resistivity.

Some typical resistivity values for waters of various origins are given in Table 2.1. It can be seen that there is a wide variation in values from the relatively pure (and therefore resistive) meteoric waters to saturating fluids which are much stronger electrolytes.

Determining the resistivity of saturating fluids is of particular importance in the downhole logging industry; this is reflected by a more comprehensive tables of resistivities of saline waters published by oil industry service companies.

The range of resistivity values in Figure 2.1 and Table 2.1 indicate that a model of electrical conduction in the earth needs to be able to cater for variations in resistivity of 4–5 orders of magnitude. This can be used as a guideline to guard against overflow or underflow problems in numerical calculations involving resistivity values.

Water type	Resistivity (Ω m) Range	Average
Meteoric waters	$30 - 10^3$	
Surface waters (igneous rocks)	$0.1 - 3 \times 10^3$	
Surface waters (sediments)	10 – 100	
Soil waters		100
Natural waters (igneous rocks)	0.5 – 150	9
Natural waters (sediments)	1 – 100	3
Sea water		0.2

Table 2.1 Resistivities of waters (from Telford et al., 1990).

Although the concentrations of electrolytes have a pronounced effect on the conductivity of a rock, there are other important parameters which have secondary effects. Electrical conduction in a rock is associated with its porosity and pore geometry and hence connected with its fluid flow properties. Note that *porosity* is simply the volume fraction of pore space in a rock; this definition does not take account of the geometry of the pore network (and the rock structure). The notion of *connected porosity* helps to emphasise the importance of pore channels being interconnected in order for electric current to pass easily: by considering connected pores only, isolated pore spaces which can occur in certain porosity styles are discounted. Isolated spaces are 'electrically redundant' in much the same way as branches of an electric circuit which do not form a complete loop. For a given formation, connected porosity may typically be related to (but is distinct from) hydraulic *permeability* which is a measure of how easily a fluid may pass through a porous material. The relationship is not in general an easily predictable one (see §2.4.1).

Pore geometry is related to the geological processes that created the rock. Porosity in sandstones is principally *primary*, consisting of voids between individual grains of rock, whereas carbonates often exhibit *secondary* porosity, which can be due to mechanical processes (which create discontinuities such as fractures, joints and bedding planes) or chemical processes (which cause, for example, fissures from solution of leachates). Such rocks are said to be *pervious*. So although limestones have low overall porosity, they have very good connected porosity (and permeability) due to the influence of discontinuities like fractures in the rock fabric.

2.1.2 Anisotropy

The electrical resistivity of rocks often exhibits a directional dependency, so that the measured resistivity depends upon the orientation in which the measurement is made. Materials for which this is the case are said to be *electrically anisotropic*.

In geological situations, electrical anisotropy can commonly be approximately characterised by two parameters: longitudinal resistivity, ρ_L, (generally measured parallel to mineral orientation or bedding), and transverse resistivity, ρ_T, measured normal to the direction of ρ_L (in reality ρ_L often exhibits a directional dependence since minerals and mineral orientations are rarely purely symmetrical. Variation in ρ_L is generally a number of orders of magnitude lower than the ρ_L:ρ_T variation, and can thus be discounted to a first approximation). The ratio of these two quantities is used to define a *coefficient of anisotropy*, λ (Kunz and Moran, 1958):

$$\lambda = \sqrt{\frac{\rho_T}{\rho_L}},$$

which may be used to quantify the degree of anisotropy possessed by a material. Values of λ for sedimentary rocks are typically in the range 1.1–2.5, whereas the figure can rise much higher in the case of metamorphosed sediments, gneisses and banded ores (Parkhomenko, 1967).

Geological situations which give rise to anisotropy are common, and may occur on a variety of scales. On the grain scale, platy minerals such as micas are often orientated parallel to each other so that conduction is better in the direction of orientation: the grain structure implies that pore connections are more direct in line with the minerals and more tortuous in the transverse direction. Preferential orientation is common in sedimentary rocks (especially shales) which are structured parallel to the plane of sedimentation (Kunz and Moran, 1958). Metamorphic processes can also cause re-orientation and alignment of mineral grains during deformation at high temperatures and pressures. In addition, banding in some metamorphic rocks provides preferential current flow directions (Parkhomenko, 1967).

Stress can also cause brittle deformation leading to the formation of joints and fractures which may be oriented in a preferential direction, reflecting the regional crustal stress direction. Such networks provide another potential source of electrical anisotropy.

Rocks which are microscopically isotropic often exhibit *structural anisotropy* due to the effects of sets of bedding planes and/or fractures. Macroscopic features such as bedding planes provide fluid and electrical flow barriers, causing preferential conduction parallel to them. In the case of sediments, bedding planes and grain orientation may lead to anisotropy at both scales complementing each other; similarly with fractures at different scales (Parkhomenko, 1967).

The mathematical representation of anisotropy (which can be more general than simply specifying λ) is discussed in Section 2.2.3; aspects of measuring anisotropy are outlined in Section 2.3.4.

2.1.3 Other conduction phenomena

In addition to electrolytic conduction, rock-forming minerals may conduct by a variety of other means. A concise summary of these phenomena is presented by Eskola (1992), whilst Parkhomenko (1967) and more recently Carmichael (1989) treat the subject of electrical conduction in rocks in much greater depth.

Although this study is concerned with the simulation of artificially induced electric currents, natural electric currents also exist which can be used in their own right to measure electrical properties (§2.3.1), but can also be a source of noise when making electrical measurements (§2.3.3). Natural electric currents are driven by electric potentials which may arise from a number of different causes (Telford et al., 1990): an *electrokinetic* (or *streaming*) potential is created when a solution is forced through a porous medium, whilst the *liquid-junction* (*diffusion*) potential, *shale* (*Nernst*) potential and *mineralization* potential arise from various electrochemical effects. In a general sense these are caused interactions between water and rock. Other electrical phenomena include large-scale *telluric* currents induced from sources such as the ionosphere and lightning strikes, and *bioelectric* currents associated with vegetation.

Frequency-dependent electrical conduction is observed in *dielectric* materials (which include the majority of rock-forming minerals) and is characterised by the dielectric constant (relative permittivity). The dielectric constant is unrelated to d.c. conduction, and is only of secondary importance to a.c. conduction (Keller and Frischknecht, 1966). It finds significance

in ground-penetrating radar surveys (Davis and Annan, 1989) since it has a controlling influence on the propagation of radar waves.

Semi-conducting minerals may have a noticeable effect on the conductivity of the rock matrix. Pyrite, chalcopyrite and pyrrhotite can form networks of conductive paths through the body of the rock, although other semi-conductors such as galena and magnetite tend to exist as isolated grains making their contribution much smaller.

When a steady direct current passing through a material which contains mineral particles is suddenly turned on or off, a finite delay is often observed before the current again reaches a steady value. This decay is a characteristic of electrolytic conduction and is caused by a build up of ions at the interface between the saturating solution (electrolyte) and the mineral particles. A *polarization potential*, which opposes the current flow, results; the effect is termed *induced polarization*. In rocks containing metalliferous minerals the induced polarization effect is termed *electrode polarization*, whereas in clays a similar effect is caused by *membrane polarization*.

Another conduction effect is *contact polarization* which is a consequence of the non-linearity of resistivity possessed by polarizable rocks: the measured resistance is observed to drop when the measurement current magnitude is increased, due to new electrochemical reactions being initiated.

The presence of clay minerals can have an important effect on the conductivity of a rock. Although dry clay is a relatively poor conductor, when even a small amount of moisture is present the clay's conduction improves dramatically. Clay platelets have an excess negative charge and attract hydrated cations from the saturating fluid resulting in an increased charge density in the vicinity of the clay. Since the clay is typically attached to the insulating rock matrix, this leads to a *surface conduction* effect (Winsauer and McCardell, 1953) where an extra conductive path exists in the thin layer of increased charge in addition to the conventional route through the pore fluid. Electrical double layer theory (Waxman and Smits, 1968) accounts for the resulting increased (excess) conductivity. Clays are often found in the pores of sedimentary rocks such as sandstones, and can also be associated with faults due to the action of preferential weathering.

In this work, only conventional conduction will be considered; the conduction effects described above fall outside the scope of the research work. This allows electrical properties

to be characterised by a frequency-independent resistivity function, and ensures that the linear dependence embodied in Ohm's law (equation 2.3) is a valid description of the relationship between current and potential. Despite these simplifications, a mathematical framework may be developed that approximates a wide variety of typical geological situations. This will be described in the following section.

2.2 The equations of electrical conduction

The fundamental relationships in current electricity are well known; they are used to develop vector equations for describing 3D electrical flow (Appendix A). A description of the generalised version of Ohm's law (which in its original form applied to electric circuits) which governs current flow in 3D is given in §A.2. These ideas are pertinent to this work since they serve as a reminder of the underlying physics involved in electrical conduction; they are also useful in developing and adapting the principal numerical model used in this work (which is described in Section 3.2).

2.2.1 Differential representation of electric potential

The governing equation for electrical flow and electric potential is derived from Ohm's law and Maxwell's equations of electromagnetism. From Maxwell's equations it can be shown (§A.2) that for d.c. situations the electric field $\mathbb{E}$ [V m^{-1}] may be expressed as the (vector) gradient of a scalar potential function V:

$$\mathbb{E} = -\nabla V . \tag{2.1}$$

In this context V is termed the electric potential and is measured in volts [V]. According to vector theory V may be expressed relative to an arbitrary datum; in practice it is nearly always *differences* in potential that are of interest [in this work, the term 'voltage' is taken to be synonymous with 'potential difference' (p.d.)]. In cases where *absolute* potential is of interest, the datum is usually defined so that the potential at infinity is zero. Numerical simulations typically deal with absolute potentials and so a suitable reference point must be found (usually this is on the boundary of the model).

Maxwell's equation expressing conservation of charge, and using continuity, is:

$$\nabla \cdot \mathbb{J} = -S , \tag{2.2}$$

where **J** is current density [A m^{-2}] (§A.2). The term S [A m^{-3}] represents any current sources in the region of interest. In the case of a single point source S is zero everywhere except the location of the source itself. If the source is of magnitude I and is located at (x_s, y_s, z_s) it may be expressed mathematically using Dirac delta functions as:

$$S = I\delta(x_s)\delta(y_s)\delta(z_s).$$

Where a source of magnitude I [A] is distributed through a volume $\Delta x \Delta y \Delta z$, S is given by:

$$S = \frac{I}{\Delta x \Delta y \Delta z}.$$

Ohm's law for a 3D, isotropic medium states (§A.2)

$$\mathbf{E} = \rho \mathbf{J}, \text{ or}$$

$$\mathbf{J} = \sigma \mathbf{E} \tag{2.3}$$

(ρ: resistivity [Ω m]). Equation (2.3) embodies the relationship between voltage and current in 3D space: the current density, **J**, is directly proportional to, and aligned with the vector gradient of the electric potential (i.e., the electric field, **E**).

By taking the scalar product of both sides of equation (2.3) with ∇, combining with equation (2.1), and substituting into equation (2.2), it can be shown that (Dey and Morrison, 1979):

$$\boxed{\nabla \cdot \frac{1}{\rho} \nabla V = -S}, \text{ or alternatively}$$

$$\boxed{\nabla \cdot \sigma \nabla V = -S}. \tag{2.4}$$

where σ is conductivity [S m^{-1}].

Equation (2.4) is the differential form of the governing equation of electric potential for direct-current (time invariant) situations. In 'mathematical' terms the parameters V, σ and S may be functions of space but not of time. To fully specify the conditions governing the electric potential in a given region ϑ, conditions must also be specified for the boundaries of ϑ (which may be at infinity). Usually this involves specifying the potential, V, or the potential gradient, $\partial V/\partial n$, (or a combination of both) on the boundary of ϑ (where n is the normal to the boundary).

Additional conditions can be specified for boundaries across which there is a discontinuity in ρ (or σ). In a geologically relevant situation this might correspond to the contact between two different geological units, or a sudden variation within an apparently homogeneous rock, e.g. a bedding contact or a fracture. Internal boundary conditions governing the variation in electric potential across such interfaces can be arrived at by using conservation laws. Consider such a boundary across which the resistivity changes from ρ_1 to ρ_2 (Figure 2.3). The current density either side of the interface is denoted by $\mathbf{J}_1$ and $\mathbf{J}_2$ and $\mathbf{n}$ is the unit vector normal to the interface.

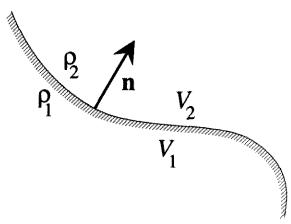

Figure 2.3 An internal boundary between different conducting zones.

To satisfy the requirements of conservation of energy, the amount of work needed to deposit a given charge on one side of the boundary must be the same as the work needed to deposit the same amount of charge on the other side. From the definition of electric potential (eq. A.1), the potential across the boundary must be continuous, i.e.

$$V_1 = V_2 . \tag{2.5}$$

In order to ensure conservation of charge, the component of current density, $\mathbf{J}$, normal to the boundary must be continuous (assuming there are no current sources at the interface itself):

$$\mathbf{J}_1 \cdot \mathbf{n} = \mathbf{J}_2 \cdot \mathbf{n} . \tag{2.6}$$

The above relations may alternatively be derived formally from Maxwell's equations (Grant and West, 1965).

Use of the del operator [∇ (§A.2)] enables expressions to be formulated which are not relative to any particular coordinate system; for example equation (2.4) is equivalent to

$$\frac{\partial}{\partial x}\left(\sigma \frac{\partial V}{\partial x}\right) + \frac{\partial}{\partial y}\left(\sigma \frac{\partial V}{\partial y}\right) + \frac{\partial}{\partial z}\left(\sigma \frac{\partial V}{\partial z}\right) = -S$$

in rectangular cartesian coordinates (x, y, z), or

$$\frac{1}{r}\frac{\partial}{\partial r}\left(\sigma r\frac{\partial V}{\partial r}\right)+\frac{1}{r^2}\frac{\partial}{\partial \theta}\left(\sigma\frac{\partial V}{\partial \theta}\right)+\frac{\partial}{\partial z}\left(\sigma\frac{\partial V}{\partial z}\right)=-S$$

in cylindrical polar coordinates (r, θ, z).

In the case of a region where the resistivity is constant (i.e. not a function of space) equation (2.4) becomes the Poisson equation:

$$\nabla^2 V = f \quad (\text{where } f = -\frac{1}{\sigma}S). \tag{2.7}$$

If in addition there is no source of charge (or current) in the region, equation (2.7) reduces to Laplace's equation:

$$\nabla^2 V = 0\,. \tag{2.8}$$

The mathematical aspects of solving equation (2.4) are discussed in detail in Chapter 3.

2.2.2 Integral representation of electric potential

Equation (2.4) is the *differential* form (i.e. involving derivative functions) of the governing equation for electrical potential. There is a corresponding *integral* form (i.e. involving *integral* functions) of this equation, which can be used as a starting point for alternative formulations to describe electrical flow in a 3D medium.

The integral form of equation (2.4), with boundary conditions as expressed by (2.5) and (2.6) is derived using Green's second identity (Kellogg, 1967). For a volume ϑ, the equation is of the form

$$V(\mathbf{r}) = \int_{\vartheta} G(\mathbf{r},\mathbf{r}_0)S(\mathbf{r}_0)\,\mathrm{d}\vartheta_0\,, \tag{2.9}$$

where $V(\mathbf{r})$ is electric potential, and S is the current source term. The vector $\mathbf{r}$ gives position (x, y, z) and $\mathbf{r}_0$ is the source location. The parameter G is the Green's function [termed the *kernel function* in the context of equation (2.9)] corresponding to the situation under investigation (Roach, 1982). The role of G in the integral equation (2.9) is closely related to the role of the electric potential, V, in the differential equation (2.4). Note that the definition of G incorporates any boundary conditions, so that equation (2.9) completely describes a specific problem.

Methods based on integral equations are generally the preferred approach to an electrical flow problem when only one or a few small anomalous bodies are to be modelled. For more complex situations, differential methods are favoured. More details of the application of the integral equation method are given in Section 3.1.3.3.

2.2.3 Anisotropy

The form of Ohm's law stated in equation (2.3) applies to isotropic materials, whose resistivity is independent of the direction in which measurement is made (i.e., independent of the direction of the applied electric field). In such cases, resistivity may be represented by a scalar value, and the electric field, **E**, and current density, **J**, are parallel. In the more general case, the resistivity (and therefore conductivity) may vary with direction, and in addition **E** and **J** are not necessarily parallel (Grant and West, 1965).

Denoting the component of electric current density in the x-direction by J_x, and considering this direction only, equation (2.3) becomes

$$E_x = \rho J_x . \tag{2.10}$$

If **E** and **J** are not parallel then there will be contributions to E_x from the other components of **J** and so (2.10) must be generalised to

$$E_x = \rho_{xx} J_x + \rho_{xy} J_y + \rho_{xz} J_z ,$$

where $\rho_{xy} J_y$ represents the contribution to E_x from the current density component J_y and so ρ_{xy} is a constant of proportionality relating E_x and J_y. Similar equations can be written down for E_y and E_z so the complete relationship between **E** and **J** may be written in matrix form (Parasnis, 1986) as

$$\begin{pmatrix} E_x \\ E_y \\ E_z \end{pmatrix} = \begin{pmatrix} \rho_{xx} & \rho_{xy} & \rho_{xz} \\ \rho_{yx} & \rho_{yy} & \rho_{yz} \\ \rho_{zx} & \rho_{zy} & \rho_{zz} \end{pmatrix} \begin{pmatrix} J_x \\ J_y \\ J_z \end{pmatrix} , \tag{2.11a}$$

or using by making use of suffices and the summation convention

$$E_i = \rho_{ij} J_j . \tag{2.11b}$$

The nine scalars represented by ρ_{ij} are the components of a second order resistivity tensor, $\underline{\rho}$. Equation (2.11) is a more general version of Ohm's law (equation 2.3). Equation (2.11) may be solved for $\mathbf{J}$, and will take the form

$$J_i = \sigma_{ij} E_j, \tag{2.12}$$

where the nine scalars σ_{ij} are the components of a conductivity tensor, $\underline{\sigma}$. The conductivity is now the matrix inverse (rather than simply the reciprocal) of the resistivity, i.e. $\underline{\sigma} = \underline{\rho}^{-1}$. Note that in general the corresponding elements of $\underline{\sigma}$ and $\underline{\rho}$ are not reciprocals of each other, i.e. $\sigma_{ij} \neq 1/\rho_{ij}$.

A simpler and more common form of anisotropy occurs when $\mathbf{E}$ and $\mathbf{J}$ are parallel. In equation (2.11) this corresponds to the off-diagonal elements of $\underline{\rho}$ being zero. In this case, the resistivity can be represented by three principal (diagonal) values which are often termed ρ_x, ρ_y, and ρ_z. The style of anisotropy described in Section 2.1.2, where the resistivity of a material can be characterised by longitudinal (ρ_L) and transverse (ρ_T) components, corresponds (with suitable orientation of coordinate axes) to $\rho_x = \rho_y = \rho_L$ and $\rho_z = \rho_T$.

Electrical anisotropy is commonly observed in rocks (§2.1.2). It is noted that any model of electrical conduction should be capable of catering for anisotropy in resistivity in order for it to be applicable to a substantial branch of typical geological situations.

2.3 Electrical measurement techniques

The numerical models that are developed and applied in this work simulate not only the electrical flow in the earth, but the response of electrical *measurements* made on and in the earth, since geophysical measurements are the practical means of determining electrical properties. It is therefore beneficial to review the principles employed in practical methods to determine the electrical properties of the earth described in Section 2.1. The mathematical framework described in Section 2.2 provides the basis for relationships necessary for conversion of raw measurement data (typically current magnitudes, voltages, and/or resistances) into resistivity values.

Particular attention is paid to measurement techniques that are closely related to the measurement devices modelled in this work.

2.3.1 Electrical methods

A variety of different geophysical electrical measurement methods have been developed both for application to specific problems and to make use of different electrical properties. For the purpose of this thesis attention will be directed only towards methods which involve the introduction of artificial d.c. electric currents into the earth, commonly termed **resistivity methods**. For specific surveys electrical resistivity methods may be combined with other electrical measurements in an integrated approach. The principal alternative methods are:

Self (spontaneous) potential—natural electric potentials are associated with certain minerals, especially sulphides; they are also generated in geothermal areas. In borehole geophysics, measurements of these potentials are used to differentiate between sandstones and shales;

Mise-à-la-masse—this is a specialised resistivity technique which involves injection of current directly into a conductive (typically ore) body which outcrops or is intersected by a borehole. Electric potentials are mapped in order to delineate the extent of the body underground;

Induced polarization—this method utilises the polarization effects described in Section 2.1.3. It is typically used in searches for base metals and groundwater. Downhole, it may be used in conjunction with conventional resistivity measurements to search for mineralization;

Electromagnetic (EM)—these methods make use of high frequency alternating currents to search for good conductors at generally shallow depths. A principal advantage is that such methods are non-contacting, allowing airborne surveys to be carried out. Downhole induction tools make use of EM principles in order to characterise resistivity properties close to the borehole;

Telluric methods are concerned with measurements of alternating telluric currents (Section 2.1) and aim to deduce information about electrical structure deep within the earth.

2.3.2 Measurement principles

Direct current resistivity measurements are generally made using four electrodes (if specialised electrical measurements such as those that make use of focusing mechanisms are

discounted). The four electrodes are a current source, C_1, which emits a current I, a current return, C_2, to complete the current circuit, and two potential electrodes P_1 and P_2 between which a measurement voltage is recorded (Figure 2.4).

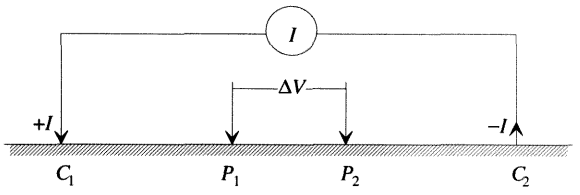

Figure 2.4 General electrode arrangement used in earth resistivity measurements.

The raw measurements are a p.d. (voltage), ΔV, and a current I. These are commonly used to calculate an *apparent resistivity*, ρ_a. The general form for an apparent resistivity expression may be written as

$$\rho_a = \mathrm{G}(\mathbf{r})\frac{\Delta V}{I} \tag{2.13}$$

where ρ_a is the apparent resistivity at some point of interest, ΔV is the measured voltage, and I is the measurement current magnitude. The parameter G is termed the *geometric factor*, and is in general a function of position, **r**. Any given electrode arrangement will have a characteristic function G, which is defined so that for a *homogeneous* medium of constant resistivity ρ_h, ρ_a equals ρ_h at all points. Substituting this condition into equation (2.13), for the homogeneous case,

$$\frac{I}{\Delta V_h}\rho_h = \mathrm{G}(\mathbf{r}), \tag{2.14}$$

where ΔV_h is a theoretical voltage calculated for a homogeneous half-space. Explicit expressions for apparent resistivity may therefore be found if an expression for the electric potential V_h is known since this allows calculation of p.d.'s between any two given points. (Suitable expressions are given in §3.1.2.)

The kind of spacing used depends upon what is to be measured. In general, resistivity measurements may be split into three groups (Keller and Frischknecht, 1966):

1. Those that measure a *voltage* between two widely-spaced potential electrodes;

2. Those that measure a *potential gradient* between two closely spaced potential electrodes;
3. Those that measure the *curvature of the potential function* by using closely-spaced current and potential electrodes.

In the context of the work described in this thesis it is pertinent to expand upon the first group of measurements: these may be divided into measurements where a *potential difference* is measured and measurements where the *electric potential* is measured, by placing one of the two potential electrodes effectively at infinity.

Surface electrode configurations

The most common electrode configurations are the Wenner (which has equal spacing between all four electrodes, and measures a p.d.) and the Schlumberger (with widely spaced, fixed current electrodes, and narrowly spaced potential electrodes, measuring the potential gradient). If both current and potential pairs are closely spaced, the array is termed 'dipole-dipole' (for measuring the curvature of the potential function).

If C_2 is placed a long way (effectively at infinity) from the other three electrodes (effectively at infinity), the spread is termed 'pole-dipole', also known as a half-Schlumberger array.

If both P_2 and C_2 are placed some distance away, the array is termed a 'pole-pole'. This is closely related to the focused surface measurement described in Section 4.1, and is intended to measure absolute potential rather than a voltage difference.

Downhole configurations

In the downhole situation the measurement electrodes are located in a full space rather than at the surface of a semi-infinite halfspace, but the principles involved are the same as those for surface measurements. The two basic electrode arrangements are the *normal* log and the *lateral* log. The normal log is analogous to the pole-pole surface measurement, with remote potential reference and current return electrodes. The lateral log corresponds to the pole-dipole surface array, with a remote current return and closely-spaced potential electrodes. Remote electrodes are usually placed many metres from the measurement electrodes, at the top of the tool sonde, or by making use of the logging cable armature.

The focused log described in Section 4.2 is similar to the Laterolog (Doll, 1951; 1953) and essentially makes the same measurement as a normal log while simultaneously emitting additional focusing currents.

Electrical imaging tools (Chapter 5) are based on button-type electrical measurements. Such tools have evolved from the dipmeter (Allaud and Ringot, 1969; Chauvel et al., 1984) which measures current intensity rather than electric potential and uses only two electrodes: a current source electrode from which the current intensity measurement is made, and a remote current return electrode. In terms of the current flow generated these tools are similar to the normal log, but the measurement made is completely different emphasising the fact that numerical models need to simulate the measurement process over and above the current flow in a region of interest if they are to be compared with actual field data.

2.3.3 Measurement distortions

A variety of practical problems are commonly encountered when making resistivity measurements, notably: electrolytic polarisation, which causes a build-up of ions at the current electrodes; telluric currents, which add a background signature to the measured current; and contact resistance between electrodes and the earth.

The first two phenomena are countered by using low-frequency a.c. currents which prevent the build up of ions and cancel out the effect of background currents (by averaging the measurement data). At low frequencies a.c. effects are considered negligible. Contact resistance is countered by making four-terminal resistance measurements.

During the field measurement process the above effects are removed by instrumentation and thus may be neglected for the purposes of numerical modelling (although there is in principle no reason why a simulation could not be developed to include the above effects). When comparing simulation results with field data is also important to bear in mind that the theoretical models can be several orders of magnitude more accurate than the field measurements.

In the case of pole-pole and pole-dipole measurements, distortions may be caused by the location of the current return electrode. A well documented effect on downhole lateral log measurements is the *Groningen effect* (Woodhouse, 1978; Lacour-Gayet, 1981), which is observed below extensive, highly resistive beds. In its original form it was known as the

Delaware effect (Suau et al., 1972). It is caused by bunching of current as it flows through the conductive borehole which provides a low resistance path through the resistive layer to the current return (Figure 2.5). A drop in electric potential at the remote reference electrode, *N*, results, causing the tool to produce anomalously high measurements up to 20 m (the distance to the reference electrode) below the base of the resistive layer. As indicated in part **b** of the figure, the Delaware effect can be overcome by locating the current return at the earth's surface. However, the effect of low, but finite, frequency a.c. measurement current means that the resistive bed can still cause a phantom increase in measured resistivity, due to mutual inductance phenomena (the effect of a finite *skin depth*); this phenomenon is the Groningen effect.

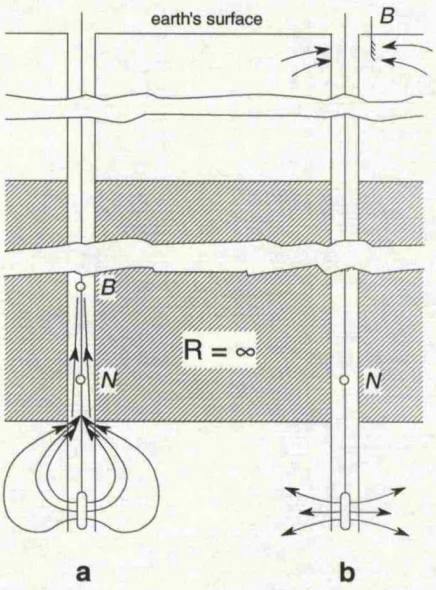

Figure 2.5 The Delaware effect (schematic) (after Suau et al., 1972).

Measurement distortions may also be caused in surface electrode spreads where the choice of location of the remote return electrode (e.g. in a conductive or resistive medium, or near to a low resistance return path such as a river) can distort the apparent location and magnitude of anomalies; this is discussed further in Section 4.1.

These effects serve to illustrate the effects of non-ideal measurements, and the importance of location of the return electrodes. In numerical simulations, similar care must be taken with regards to choosing a reference from which electric potential is measured.

2.3.4 Anisotropy

The effect and detection of anisotropy in *surface* measurements has been addressed by Asten (1974), Matias and Habberjam (1986), and Sinha and Bhattacharya (1967) amongst others. Edwards et al. (1984) address effects on a survey technique made on the sea floor.

The consequence of making *downhole* measurements in the presence of electrical anisotropy is analysed by Kunz and Moran (1958) and Moran and Gianzero (1979); Rauen and Lastovickova (1995) attempt to quantify the degree of anisotropy using downhole measurements.

Electrical measurements cannot generally distinguish between the various causes of anisotropy. If the measurement resolution is lower than the scale of certain structures (for example a series of isotropic beds) *macroanisotropy* may be observed in the measurements (Maillet, 1947), which is indistinguishable from the effect of a single equivalent (micro-) anisotropic layer.

2.4 Significance of electrical properties

Despite the fact that the electrical resistivity of rocks is controlled to an extent by a combination of petrophysical parameters which may differ between rock types and lithologies, there is a considerable overlap between the resistivity of different rocks (illustrated in Figure 2.1). Discrimination between rocks or lithologies on the basis of resistivity alone is therefore not possible, except in very general terms. Despite this ambiguity, if analysis is restricted, say, to a given formation, geological features such as different rock porosities and porosity styles, fractures, zones with different fluids within them and faults all exhibit quantifiable variations in their electrical properties. A knowledge of variations in resistivity therefore has a variety of applications where the characterisation of the subsurface geology is a requirement. In the context of this thesis, it is noted that numerical modelling plays an important role in the interpretation of electrical data through improved understanding of electric current flow phenomena.

Electrical measurements made on or in the earth can be used to infer the distribution and magnitude of resistivity in the ground away from the measurement location. Survey information can be broadly divided into two categories:

1. quantitative information about resistivity, and hence physical parameters such as porosity, salinity or water saturation (derived indirectly);
2. delineation of anomalous regions or spatial electrical structure. The most important detectable features are a layered electrical structure (due to e.g. water table, bedrock, or geological units), and localised anomalies (due to e.g. cavities, ore bodies or faults).

In practice, many applications make use of a combination of both types of inferences.

The first part of this section (§2.4.1) describes the principles behind quantitative applications of resistivity measurements. The remainder of the section summarises applications of electrical measurements, which have been divided into three categories: surface surveys (§2.4.2), downhole surveys (§2.4.3), and downhole imaging (§2.4.4).

2.4.1 Relationship between resistivity and porosity

The resistivity of the majority of saturated rocks is primarily determined by the resistivity of the saturating fluid. However, the secondary effect of the geometry of the rock matrix (which in turn may be related to porosity) on electrical conduction is one of the key factors utilised when finding applications of resistivity measurements, particularly in the oil industry and in hydrogeology.

Many of the relationships still in use today are based on the empirical relationships proposed by Archie (1942). He termed the ratio of the bulk resistivity of the saturated rock, R_o, to the resistivity of the fluid, R_w, the 'formation factor' (F):

$$F = \frac{R_o}{R_w}. \tag{2.15}$$

For many different saturated rocks, F is found to be constant; this is principally a consequence of the resistivity of the saturating fluid being several orders of magnitude lower than that of the rock matrix. After conducting experiments on saturated sandstone core samples, Archie related F to porosity, ϕ, with what is now named the 'Archie equation':

$$F = \phi^{-m}, \tag{2.16}$$

where m is an empirically derived constant. Archie (1942) found the parameter m to take a value of about 1.3 for unconsolidated sand, increasing to around 1.8–2.0 with more

consolidated sandstones. Subsequent workers also found similar patterns [e.g. Wyllie and Gregory (1953)]; for this reason m is often referred to as the 'cementation exponent' although as Doveton (1986) points out, its value is in fact the consequence of a host of interrelated textural properties. Amongst these, the most important factors are the 'tortuosity' of the pore network (the ratio of pore channel length to straight line length between two points) and in a general sense the geometry of the rock matrix. A great deal of research has been directed towards defining relationships between m and textural properties of potential reservoir rocks. Physical and synthetic grain-packing models (Sen et al., 1981; Grattoni and Dawe, 1991) and analysis of grain shape (Jackson et al., 1978; Atkins and Smith, 1961; Mendelson and Cohen, 1982), in addition to applications of percolation theory (Kirkpatrick, 1973) and network models (Schopper, 1966; Straley, 1976) have identified grain shape, shape sorting and degree of fabric anisotropy as primary controls in sandstones. The porosity structure in carbonates is more complex (Focke and Munn, 1987; Choquette and Pray, 1970) and harder both to simulate and to relate back to empirical constants (Doveton, 1986).

Often a modified version of equation (2.16), first proposed by Winsauer et al. (1952), is used to obtain a better fit with certain data sets by the use of an empirical constant a:

$$F = a\phi^{-m}. \tag{2.17}$$

Archie (1942) also proposed a relation for partially saturated rocks. Pore spaces could be filled with a fluid in addition to pore water, for example gas, or more typically oil. He defined a resistivity index I:

$$I = \frac{R_t}{R_o}, \tag{2.18}$$

where R_t is the resistivity of (rock + water + oil/gas), and found that I was related to the volume fraction of pores containing water (vol. water/vol. pores), S_w, by

$$I = S_w^{-n}. \tag{2.19}$$

The parameter n is termed the 'saturation exponent', and again is derived empirically. It is related to pore geometry and rock texture, and is found to vary between 1.8 and 2.5, although for convenience it is often set to 2 by default.

Combining (2.15), (2.16), (2.18) and (2.19) yields

$$R_t = \frac{R_w}{\phi^m S_w^n}. \tag{2.20}$$

The relation (2.20) is often referred to as 'Archie's law' (in some cases, equation (2.17) is included, adding the extra empirical constant multiplier a to the right hand side of the formula). It is invaluable in the hydrocarbons industry, where it is used routinely to estimate oil reserves in a given reservoir. In finding empirical relationships which fitted his data, Archie was the first person to propose a quantitative relationship between porosity, saturation and resistivity. His empirical findings are generally corroborated by the findings of research intended to derive a physical basis for equation (2.20) (e.g. Madden, 1976; Korvin, 1982).

Archie (1942) originally proposed equation (2.20) to apply to clean (clay-free) sedimentary rocks. Subsequent workers have found it applies equally well to other rock types such as igneous rocks and metamorphosed sediments (Carmichael, 1989); modifications have also been incorporated to take account of the effect of clays in the pore spaces of rocks (Waxman and Smits, 1968; Bussian, 1983). Many authors have pointed out shortcomings of the 'law' (e.g. Herrick and Kennedy, 1994) but equation (2.20) remains an important general description of the relationship between resistivity, porosity and saturation applicable to a wide range of rock types.

2.4.2 Applications of surface measurements

The systematic use of resistivity (and self-potential) methods dates from early this century (Schlumberger, 1920). Electrical measurements are now used routinely to characterise subsurface geology but may also be used to detect other buried targets. Depth of investigation is limited in practical cases to the order of 1 km, since deeper investigations inherently require larger amounts of electric current to be injected into the ground, and also require power cables to stretch over longer distances.

Many applications of electrical surveys attempt, in a general sense, to characterise (commonly shallow) subsurface geology; surveys are typically designed to investigate variation of resistivity with depth or lateral variations over a section of ground. With the advent of more sophisticated measuring equipment and data interpretation, it is possible to infer properties in two or even three dimensions. When the earth is known to be horizontally layered or gently dipping vertical surveys can be used to estimate the depths and resistivities of the various layers. Transverse measurements can be used to map the location of lateral

geological contacts or isolated bodies such as mineralized veins. Fault zones are also associated with changes in electrical properties since they are a focus for fluid flow and weathering which can cause leaching and accumulation of clays.

Some specific applications of surface measurements are outlined below.

Characterisation of deeper geology—Some electrical experiments aimed at investigating deep into the earth's crust have been performed, particularly in the former Soviet Union. Blohm and Flathe (1970) describe an experiment to investigate the structure across the Rhinegraben which used a current source and sink separated by 150 km. Conventional resistivity measurements have been used in combination with other electrical techniques to investigate the electrical properties of the Iceland crust (Hermance and Garland, 1968; Hermance, 1973). Experiments in the USSR generally involve the use of a dipole-dipole configuration (Section 2.3.2) with a current electrode separation of the order of 500 m, allowing measurements down to a depth of 2.5–3 km. In general, however, telluric and magnetotelluric measurements are more convenient for deep surveys.

Engineering applications—resistivity surveys are used routinely in civil engineering investigations where the use of both spatial interpretation (for example to detect underground cavities or to infer the depth of a solid rock foundation), and quantitative values (typically for inference of differing compaction or moisture content or other parameters which may affect the strength of the foundation of constructions such as dams, buildings or roads) is required. Aspinall and Walker (1975) and Owen (1982) provide two examples of locating and mapping buried mine shafts using surface measurements. Owen (1982) found that subsurface cavities could be sensed at significant depths, with the penetration of the electrical survey being dependant upon the size of the cavity, the homogeneity of the overburden and the electrical contrasts involved.

Hydrogeological applications—the location of the water table, delineation of reservoirs or fresh water lenses and monitoring of fluid flow is possible if there is an associated change in electrical properties. Fresh water zones are typically less conductive than saline waters and in addition may be revealed by vertical surveys since they float on top of the more dense saline water (e.g. Bugg and Lloyd, 1976). A typical monitoring application is described by Oteri (1981) who investigates the extent of contamination

of a chalk aquifer by conductive saline water from nearby mine workings. Resistivity values are also used to infer the degree of salinity in the aquifer, and hence quantify the amount of contamination.

Investigation of geothermal areas—changes in conductivity are often associated with geothermal areas due to a variety of phenomena (Thanassoulas, 1991), viz.:

- the conductivity of electrolytic conductors generally increases with temperature;
- conductive solutions form different compositions at different temperatures;
- self-potential anomalies also exist over fluid flow paths due to thermoelectric and electrokinetic coupling;
- host rock conductivity may increase due to hydrothermal alteration;
- host rock conductivity may also be increased due to the effect of mineral deposits in fractures.

Thanassoulas (1991) uses the above characteristics in an attempt to delineate fracture zones and faults in geothermal field in Greece. Such features are important since they can be targeted in the commercial development of a geothermal field.

Prospecting for minerals—minerals which are good conductors may be located and delineated, typically with lateral traverses. Modern techniques usually employ a combination of other geophysical methods in addition to resistivity surveys (in particular induced polarization). Seigel (1967) describes an application where a porphyry-copper deposit in British Columbia is associated with a drop in the measured apparent resistivity. Induced polarization data is used to delineate the body.

Archaeological investigations—lateral traverses and vertical surveys may reveal the location and/or depth of buried man-made features such as wall foundations, ditches, or roads, since these are often composed with materials which differ in composition from the overburden which typically consists of conductive soils or clays [e.g. Papamarinopoulos et al. (1988) use a twin probe array, akin to a dipole-dipole survey, to map the layout of part of an ancient buried town in Greece].

Environmental monitoring—resistivity surveying of contaminated land can be used for location of undesirable leachates, or to track the extent of contaminant fluids below ground. Mazac et al. (1987) use resistivity methods to detect subsurface oil pollution

using a similar approach to that of Oteri (1981): lateral surveys are used to map the extent of contamination and Archie's law (eq. 2.20) is used to quantify the amount of pollution. In this case the presence of hydrocarbons is indicated by an overall increase in resistivity.

2.4.3 Applications of downhole resistivity measurements

The first log of resistivity measurements taken along the length of a borehole was made by Henri Doll in 1927 (Allaud and Martin, 1977). Initially, electrical logs were used in a qualitative way to identify different subsurface geological layers and to located hydrocarbons (which are typically bad electrical conductors and are therefore associated with an increase in measured resistivity).

On the basis of experimental findings, notably those of Archie (1942), quantitative applications of electrical logs became possible. Electrical logs are still vital components of hydrocarbons exploration, since resistivity can be related to porosity and hydrocarbon saturation (see Section 2.4.1). For the same reason, electrical logs are also used widely by hydrogeologists. Porosity itself is now usually derived from downhole sonic velocity, gamma-ray–density, or neutron–gamma-ray measurements (Schlumberger, 1991), although it may still be estimated from resistivity if this data is not available. Once a porosity estimate has been obtained, resistivity measurements can be used with equation (2.20) to obtain an estimate of hydrocarbon saturation, and thus the volume of hydrocarbon present. Due to the relationship between electrical conduction in rocks and the fluids which generally saturate them, indirect information about fluid flow properties and permeability may also sometimes be derived, although [indeed, as Archie (1942) found] it is difficult to quantify in general. Focused electric tools may be used to investigate different regions of interest (Schlumberger, 1984), for example Schlumberger's Dual Laterolog can adjust its focusing to make both deep (several m) and shallow (~ 1 m) measurements while their Microspherically Focused Log is designed to respond primarily to the invaded zone immediately beyond the borehole wall.

Resistivity measurements may also be made between adjacent boreholes, and between boreholes and the surface of the earth. Daniels and Dyck (1984) describe the various possible configurations and report on the testing of selected electrode styles with a view to applying measurement techniques to mineral exploration. Wang et al. (1991) use borehole-to-surface

measurements to investigate the results of a hydraulic fracturing experiment. They were able to infer the direction of propagation of induced fractures, but determination of fracture length was less certain. The principal limiting factors in interpreting the data were identified as the resolving power of the electrical measurements, and the sophistication of the interpretation (inversion) technique. Analysis of downhole electrical array data is generally more complex than for conventional surface measurements, although some modelling has been carried out to aid interpretation (Le Masne and Poirmeur, 1988; Busby and Dabek, 1986).

Cross-borehole resistivity measurements benefit from increased data control, and in such situations electrical tomography becomes possible: the creation of a two- or three-dimensional image of the resistivity distribution of the ground in the region being investigated (Daily and Owen, 1991). Beasley and Tripp (1991) investigate the potential for monitoring an enhanced oil recovery programme using cross-hole tomography, whilst Daily et al. (1992) use similar techniques to investigate underground structure and groundwater movement in the vadose (above the water table) zone.

Qualitative electrical measurements are utilised by the dipmeter logging tool (Allaud and Ringot, 1969; Chauvel et al., 1984), which measures a set (two, four or six) of resistances around the circumference of the borehole wall as the tool is raised. By correlating these resistance measurements, information about structural dip and bedding orientation may be derived. In the case of this tool, calibrated resistivity measurements are not a requirement, since it is only local variations in resistivity that are required to obtain the desired information.

2.4.4 Downhole imaging applications

Over the last decade, dipmeters (see above) have been developed into more sophisticated downhole tools capable of making high resolution electrical resistance measurements over the surface of the borehole wall (Ekstrom et al., 1987; Seiler et al., 1994). These measurements can be combined to produce an electrical image of the borehole wall, which is orientated using readings from three magnetometers and a triaxial accelerometer located on the tool sonde. Applications of downhole electrical imaging can be considered to form a distinct set within the broader range of downhole resistivity measurement applications as a consequence of their unique (high resolution, oriented, spatial) nature.

In the commercial sector, electrical images are used for high-resolution reservoir analysis. In a general sense, features which exhibit a contrast in electrical resistivity may be investigated in detail. In addition, the spatial information contained in an electrical image allows inferences to be made about the geometry of specific structures. Typical examples include:

sedimentary analysis—for example, images allow detailed zonation of units and identification of non-planar bedding surfaces, slumps and cross-bedding;

thin bed analysis—an electrical imaging tool has much higher resolution than conventional logging tools. Consequently, the tool can resolve much narrower beds and identify parameters such as thickness and lamination;

structural dip interpretation—this is akin to the use of the dipmeter, from which imaging tools have evolved. The extra information contained in an electrical image may make it possible to interpret dip in difficult or poor quality intervals, and to provide quality control of such information;

aiding core description—downhole electrical images, which are orientated, can be correlated with rock core (which is not usually oriented and is not accurately depth-located) from the same borehole, allowing accurate core orientation and depth determination. In addition, inferences can be made for intervals where there is little or no core recovery. Interpretation software such as Schlumberger's Diamage package allow interactive manipulation and presentation of scanned-in core photographs alongside borehole images.

Electrical imaging tools were originally developed in response to industry needs; typical 'industry-orientated' applications are outlined by Bourke et al. (1989) and discussed in more detail by Serra (1989). Bourke et al. (1989) broadly classify interpretable features as structural, sedimentary or diagenetic.

Fractures are commonly observed structural features. Open fractures are commonly filled with conductive borehole drilling fluid whilst closed fractures often contain resistive cement; in both these cases a contrast in electrical properties results. An electrical image can provide information about fracture geometry allowing, for example, assessment of whether fractures are open or closed, their orientation and length, and the nature of stress regimes in the formation (Dennis et al., 1987; Pezard and Luthi, 1988; Plumb and Luthi, 1986). When

associated with fracturing, a **fault** (or fault zone) may be identified and characterised using fracture geometry. **Folds** may also be observed, identified as laminations with characteristic structure visible in electrical images.

Bedding surfaces are sedimentary features visible in electrical images (Luthi, 1990), since electrical properties generally vary with parameters such as compaction and grain size. Bedding planes may be cemented, reducing fluid flow and causing an associated increase in resistivity. Other observed sedimentary features detailed by Bourke et al. (1989) include **slumps** and **cross-bedding**, where once again the spatial information contained in an electrical image allows inferences to be made about the geometry of specific structures. **Stylolites**, which are formed by pressure solution processes and are often associated with residual, insoluble, resistive minerals, have also been observed (Serra, 1989).

When electrical images are integrated with conventional logging measurements, more detailed interpretation becomes possible. Electrical image textures can be correlated with log and core data to infer property variations in, for example, grain size and sorting, porosity type (by identifying the presence of e.g. vugs or cementation in bedding), and the presence of bioturbation (Bourke et al., 1989). More detailed analysis of fractures may reveal, for example, whether they are natural or drill-induced (Pezard et al., 1988) and can provide information about fluid flow properties (Dennis et al., 1987).

All the above applications are defined with reference to a commercial environment. Their principal goal is to enhance reservoir characterisation, and in particular provide information that can be used to infer permeability paths and barriers and thus to improve hydrocarbon recovery. It is noted, however, that the use of electrical imaging also has great potential benefits in non-commercial research work. A slimline version of Schlumberger's Formation MicroScanner imaging tool is run routinely in the Ocean Drilling Program. The information obtained is used as a geological aid, where the emphasis shifts to applications like detailed sedimentological evaluation (Pezard et al., 1990; Hiscott et al., 1993), structural analysis and core orientation (MacLeod et al., 1992), and tools are run in a much wider variety of environments than would generally be encountered in industrial applications: for example Brewer et al. (1995) analyse FMS data from a hole in oceanic crust corresponding to pillow lavas and breccias.

Electrical images can also be used in a petrophysical sense if suitable calibration of the resistance data to resistivities is available at the same scale (Hornby et al., 1992);

unfortunately there is currently no downhole resistivity measurement at the same scale as the imaging tools. Bourke et al. (1989) describe how FMS resistance curves can be used to generate high resolution nominal porosity (and even permeability) logs if suitable calibration data is available. Again, such applications are only cautiously implemented since true calibration is not possible without downhole measurements at a high enough resolution. Numerical modelling can provide important quantitative control to help interpretation in this area.

2.5 Summary

This chapter describes a basis for the development of a numerical model of electrical current conduction in rocks and provides a motivation for assessing electrical resistivity properties in 3D.

Resistivity is the dominant electrical property which can be used exclusively to characterise earth properties in numerical simulations of d.c. conduction (§2.1). The mathematical theory which describes electrical flow in 3D has been outlined (§2.2); this provides the theoretical basis for a numerical model.

In addition to a knowledge of the nature electrical flow in rocks, principles of measurement techniques (§2.3) have been reviewed since the numerical modelling is directed towards simulating electrical measurements over and above electrical flow in the earth.

Finally the wealth of potential applications of electrical measurements (§2.4) provides a motivation for developing numerical simulations which can be used to improve understanding and aid interpretation of resistivity measurement data in any one of the applications mentioned. The applications have been categorised as surface, conventional downhole, and downhole imaging. The numerical model described in Section 3.2 has been applied to all three of these areas (§4.1; §4.2; Chap. 5).

CHAPTER 3

Solution of the three-dimensional electrical conduction problem

Chapter 2 describes the nature of electrical conduction in rocks, and the governing equations of electricity that are used to provide a mathematical framework on which to base a numerical model. This framework is embodied in the governing differential equation for electric potential (equation 2.4, §2.2),

$$\nabla \cdot \frac{1}{\rho} \nabla V = -S, \tag{3.1}$$

which is a generalised form of Poisson's equation.

The fundamental problem to be addressed when simulating any electrical flow regime, or the response of any electrode array which uses direct current (d.c.) measurements, is to find the solution of this equation for a given resistivity distribution. This Chapter is split into two parts: the first part reviews the available solution methods, and the second part describes in detail the method used in this research work.

3.1 Review: solution methods for the electrical flow problem

This section reviews the available approaches for addressing the electrical current flow problem. Analytic solutions (reviewed in §3.1.2) of the generalised Poisson equation (3.1) are available only for a limited number of special cases. In order to model more general situations, some form of numerical solution must be used. The principal numerical techniques are outlined in Section 3.1.3.

The work in this thesis builds on an existing numerical model which is formulated using the finite difference approach (Chapter 1). In addition to providing a review of possible solution approaches, this section assesses the suitability of the finite difference method for modelling three dimensional electrical current flow, and compares the method with alternative competing techniques.

3.1.1 Introduction

There is no definitive mathematical solution to equation (3.1). Each problem is specified with a set of boundary conditions (§2.2) which must be satisfied in addition to the governing equation implying that for each set of different boundary conditions a new problem is posed. Given a set of boundary conditions, a general form of a solution might be found, but this would still represent a family of related but different solutions. A particular solution would depend on the resistivity distribution, $\rho(x, y, z)$. Given a specific resistivity function, a wide range of related electric potential distributions, V, would still be possible by having different source magnitudes and locations.

No general expression exists to encompass the infinite number of combinations of boundary conditions and resistivity and source distributions. Even for a given set of boundary conditions, an explicit solution cannot, in general, be found. However a variety of different solution methods, yielding solutions for a variety of different situations, have been determined for certain specific cases. In addition, approaches exist for obtaining solutions in more general cases.

Mathematical solutions to equation (3.1) can be broadly divided into either *analytic* or *numerical* solutions. Analytic solutions may be characterised by the following features:

- the solution consists of an algebraic expression derived from direct mathematical solution of the equation;
- the effect of varying parameters (such as resistivity or source location) can be assessed by inspecting the solution;
- the solution is known everywhere in the region of interest;
- the evaluation of an analytic is usually relatively rapid.

In comparison, numerical solutions may include the following features:

- the solution consists of the values of electric potential at a series of pre-defined points (nodes);
- the effect of varying parameters can in general only be evaluated by obtaining a series of solutions for different situations in order to build up an overall picture;
- the detail of the solution is determined by the distribution of the nodal points, which are the intersections of a grid. Therefore a finely-spaced grid will provide a more detailed solution. The values of a solution between nodal positions are generally found by interpolation.

It can be argued that analytic solutions are exact, whereas numerical solutions are approximate. However, this distinction becomes blurred because analytic solutions may require some form of numerical procedure for final evaluation: for example, a function or integral may be found using an infinite series or some other approximation. It is also worth noting that numerical solutions can in principle be made as accurate as desired by performing calculations to the correct precision, and using a grid with a fine enough mesh. In practice the limits on accuracy for both analytic and numerical solutions may therefore be controlled by the computer (rather than the solution method) employed.

Analytic solutions of equation (3.1) only exist for a few relatively simple situations. Excepting these simplified situations the governing equation cannot be solved directly and a numerical solution has to be applied.

3.1.1.1 Classification of the problem

It is useful to classify the problem expressed by equation (3.1), particularly to aid decisions in the choice and implementation of numerical solution methods. In rectangular cartesian coordinates, equation (3.1) becomes

$$\frac{\partial}{\partial x}\left(\frac{1}{\rho}\frac{\partial V}{\partial x}\right)+\frac{\partial}{\partial y}\left(\frac{1}{\rho}\frac{\partial V}{\partial y}\right)+\frac{\partial}{\partial z}\left(\frac{1}{\rho}\frac{\partial V}{\partial z}\right)=-S\,. \tag{3.2}$$

In two dimensions, equations of the form

$$a\frac{\partial^2 V}{\partial x^2}+2b\frac{\partial^2 V}{\partial x\partial y}+c\frac{\partial^2 V}{\partial y^2}=d$$

are classed as *elliptic* partial differential equations if $b^2 - ac < 0$, where a, b and c are functions of x and y only. Closely associated to equation (3.2) are the equations of Laplace and Poisson [equations (2.8) and (2.7), §2.2] which may be classed as elliptic since they correspond to $a = 1$, $b = 0$ and $c = 1$. The more general form of equation (3.2) may be classed as a *linear self-adjoint* elliptic equation (Mitchell and Griffiths, 1980).

In addition, and more importantly from a computational point of view, problems defined by partial differential equations are classified as either *boundary value* or *initial value* problems. The electrical flow problem as described here is a boundary value problem: the values of electric potential must be found in some region of interest subject to some pre-defined variations in potential along the boundary of the region (Press et al., 1992).

Boundary conditions can take one of three forms (Mitchell and Griffiths, 1980), viz.:

1. Dirichlet conditions. The electric potential, V, is specified at the boundary;
2. Neumann conditions. The component of the potential gradient normal to the boundary, $\partial V/\partial n$, is specified at the boundary;
3. Robbins conditions. A linear combination of the potential gradient and the electric potential [which can be written as $\alpha V + \beta(\partial V/\partial n)$, where α and β are known functions of space] is specified on the boundary.

The problems considered in this work generally involve boundaries which are effectively at infinity, where the electric potential *and* the potential gradient are zero, and either Dirichlet conditions ($V = 0$) or Neumann conditions ($\partial V/\partial n = 0$) can be used.

3.1.1.2 Other applications of the electrical flow equation

The governing equation for electrical flow, and in particular the associated equations of Poisson and Laplace [equations (2.7) and (2.8), §2.2] arise in many physical situations, and are therefore applicable to other problems, principally: potential field theory (gravity and

magnetics); laminar fluid flow; steady-state heat conduction; and flow through porous media (noting that the fluid flow and electrical flow equations are governed by essentially independent parameters).

3.1.2 Analytic solutions

Analytic solutions, although limited to situations involving relatively simple geometries, are extremely valuable in the mathematical analysis of the electrical conduction equation. They provide a basis for the definition of apparent resistivity (§2.3.2), which is useful in determining the resistivity of the ground from measured resistance values, and also goes some way to giving an idea of the nature of anomalies where the resistivity distribution departs from an otherwise predictable structure. In cases where they can be applied, they are generally less computationally intensive than equivalent numerical algorithms.

Analytic solutions are also an invaluable aid to numerical simulations in two ways: firstly, they can be used to verify for numerical approximations; secondly, they may speed up computation by providing a starting point for an iterative solution in the evaluation of a more complex situation.

The following sections outline some analytic results which have been used to enhance and test the numerical modelling described later in this work (chapters 4 and 5). More detail, including an outline of the derivation of the results, can be found in Appendix B. Section 3.1.2.1 outlines the principle of superposition, which is an important result used when calculating the effect of multiple current sources and sinks.

3.1.2.1 Combinations of sources: the principle of superposition

As a result of the linear relationship embodied in Ohm's Law, equation (3.1) is also linear [implying that a linear combination of two known solutions of (3.1) is also a solution]. The resultant effect of multiple source configurations may therefore be deduced by algebraically summing the solutions for the individual sources: this is an important result used in the calculation of potentials for any multiple electrode configuration. The result may be demonstrated as follows: consider the case where there are two current sources, S_1 and S_2. Then from equation (3.1) the electric potentials V_1 and V_2 due to the respective sources satisfy

$$\nabla \cdot \frac{1}{\rho} \nabla V_1 = -S_1, \qquad \text{and} \qquad \nabla \cdot \frac{1}{\rho} \nabla V_2 = -S_2. \tag{3.3}$$

Adding the two equations in (3.3) gives

$$\nabla \cdot \frac{1}{\rho} \nabla V_1 + \nabla \cdot \frac{1}{\rho} \nabla V_2 = -S_1 - S_2. \tag{3.4}$$

Equation (3.4) simplifies to

$$\nabla \cdot \frac{1}{\rho} \nabla (V_1 + V_2) = -(S_1 + S_2), \tag{3.5}$$

so the potential field due to the combined source ($S_1 + S_2$) is ($V_1 + V_2$), i.e. the algebraic sum of the potentials due to the individual fields. In general, if α and β are arbitrary scaling factors (scalars), then the potential field due to an electric source of magnitude ($\alpha S_1 + \beta S_2$) is ($\alpha V_1 + \beta V_2$). This is the *principle of superposition* in d.c. electric field theory [see, for example, Moran and Chemali (1985)].

3.1.2.2 Homogeneous media

If the resistivity of a medium is a constant value and the boundaries of the medium extend to infinity, the governing equation (3.1) may be simplified by considerations of symmetry and can be solved directly by conventional calculus. The following two results are standard results, described in more detail in Appendix B.

Infinite homogeneous medium

The electric potential V at a distance r from a point source emitting a current I located at a point O in an infinite medium of constant resistivity ρ (Figure 3.1, left) is given by (§B.1)

$$V = \frac{\rho I}{4\pi r}. \tag{3.6}$$

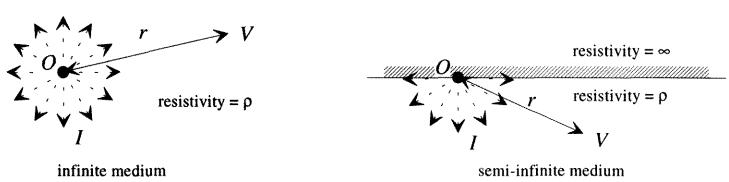

Figure 3.1 Point sources in homogeneous, isotropic media.

This is an idealised situation which represents a buried electrode in a uniform, homogeneous, isotropic earth.

Semi-infinite homogeneous medium

A theoretical representation of an electrode located at the surface of a flat, uniform, homogeneous, isotropic earth is illustrated in right hand part of Figure 3.1. The analytic solution of equation (3.1) for this case, in which a current source of strength I is located on an infinite planar interface between a region of resistivity ρ and a region of infinite resistivity, is (§B.2):

$$V = \frac{\rho I}{2\pi r}. \tag{3.7}$$

3.1.2.3 Solutions to plane interface problems

The method of images

By comparing equations (3.6) and (3.7) it can be seen that a source located at the surface of the earth effectively doubles its magnitude. The earth-air interface acts as a 'current mirror', reflecting current downwards and doubling the electric potential compared with that for the full-space case. The idea of using optical ray theory to treat electric current flow has been developed much further in the *method of images* (Keller and Frischknecht, 1966), the use of which has allowed some of the following results to be obtained. The method of images is only applicable to a limited number of situations, in particular regions separated by plane boundaries, but also anomalous three-dimensional bodies such as a buried sphere (Snyder and Merkel, 1973).

Vertical interface

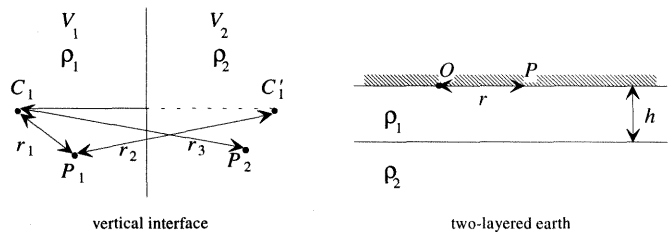

Figure 3.2 Plane interface problems.

The vertical interface problem is illustrated in the left-hand part of Figure 3.2. Denoting the electric potential by V_1 in the region containing the current source, and V_2 in the other region, it can be shown that (§B.4)

$$V_1 = \frac{I\rho_1}{2\pi}\left(\frac{1}{r_1} + \frac{k}{r_2}\right), \qquad \text{and} \qquad V_2 = \frac{I\rho_2}{2\pi}\left(\frac{1-k}{r_3}\right), \tag{3.8}$$

where r_1 and r_2 are the distances from the point of interest to the source and its image respectively, in the first region, and r_3 is the distance to the current source from a point of interest in the second region. The parameter k is the *transmission coefficient*, defined by:

$$k = \left(\frac{\rho_2 - \rho_1}{\rho_2 + \rho_1}\right). \tag{3.9}$$

Two-layered earth

The potential at the earth's surface when a horizontal layer of thickness h and resistivity ρ_1 overlies a region (infinitely deep) of resistivity ρ_2 (Fig. 3.2, right-hand side) can be shown to given by the infinite series (§B.5):

$$V = \frac{I\rho_1}{2\pi r}\left[1 + 2\sum_{m=1}^{\infty} \frac{k^m}{\sqrt{1 + (2mh/r)^2}}\right]. \tag{3.10}$$

Integral solutions

A more fundamental solution for the electric potential in a layered earth can be derived by considering the Laplace/Poisson equation in cylindrical polar coordinates, separating variables, and making use of Bessel functions in the solution (§B.6).

The potential V at the earth's surface ($z = 0$) can be written as

$$V = \frac{I\rho_1}{2\pi r}\left(1 + 2r\int_0^{\infty} K(\lambda) J_0(\lambda r)\mathrm{d}\lambda\right), \tag{3.11}$$

where J_0 is the Bessel function of order zero. The function $K(\lambda)$ (often termed the kernel function of resistivity in this context) depends on the number of layers under consideration. In the two layer case ($n = 2$),

$$K(\lambda) = \frac{-k}{e^{2\lambda h} + k},$$

where h is the top layer thickness and $k = (\rho_2 - \rho_1)/(\rho_2 + \rho_1)$ as in equation (3.9). The solution (3.11) was originally described by Stefanescu et al. (1930). It is equivalent to the infinite series derived from the images method (equation 3.10).

The evaluation of the integral in equation (3.11) requires a numerical approach. This process has been expedited by the use of linear digital filter techniques, pioneered by Ghosh (1971).

3.1.2.4 Other solutions

The most general analytic approach to solving partial differential equations is separation of variables (Gianzero, 1981), which usually results in analytic solutions involving integrals of Bessel functions. The conditions which apply when employing separation of variables imply restrictions on the geometries which can be analysed (Snyder and Merkel, 1973). For example, Grant and West (1965) describe solutions for a single sloping interface, a conducting sphere, an oblate spheroid, and a conducting ribbon. These solutions require the use of exotic coordinate systems and some simplifying assumptions even though the situations, whilst of some geological significance, are relatively simple geometrically. Examples of refined models of a layered earth include those described by Roy and Rao (1977) and Stoyer and Wait (1976).

For borehole situations, Keller and Frischknecht (1966) present a simplified approximation for a highly conductive borehole. This approximation is not valid for porous formations which typically exhibit conductive invaded zones. Other analytic analyses of simplified borehole situations are presented by deWitte and Gould (1959) and Gianzero and Anderson (1982). Gianzero (1981) reviews the various solutions that have been developed for the downhole situation. More recently, Kaufman (1990) has presented a solution for a cased borehole in a homogeneous formation, but a more general analytic solution for a finite-diameter borehole does not exist—other solution approaches have to be taken in this case.

In addition to the homogeneous solutions (equations 3.6 and 3.7), the method of images was favoured for providing analytic test solutions since it is flexible and easy to implement in practice. In more complex scenarios, homogeneous solutions based on a suitable averaged background resistivity are often found to be the most practical means of generating a starting point from which to iterate towards a solution.

3.1.3 Numerical solutions

With the development of computer technology enabling repetitive calculations at ever-increasing speeds and allowing the manipulation of increasingly large arrays of data, numerical solutions have superseded analytic approaches in many areas, including the general electrical current flow problem.

There are a variety of different numerical methods available to solve equation (3.1), which each have different strengths and weaknesses. The following sections outline the principal competing numerical approaches. Of these, the *finite difference method* and the *finite element method* are applicable to arbitrary resistivity distributions, in three dimensions, and are described in more detail than other approaches.

3.1.3.1 Finite difference method

The finite difference (FD) method has been used for electrical resistivity problems in geophysics by a number of workers, including Dey and Morrison (1979), Hermance (1983), James (1985), Mufti (1976; 1978; 1980), and Scriba (1981).

The first step in the application of the FD method to the electrical governing equation (3.1), is to define a *grid* to cover the region of interest (examples of FD grids can be found in subsequent chapters, e.g. Figure 4.1.9). The electric potential function V, which is continuous in the region of interest, is represented by a set of discrete values which are located at the grid intersections or *nodes*. If a continuous function of the potential is required then the potential between nodes is approximated using surrounding nodal values; linear interpolation is usually used.

Although the grid spacing may be non-uniform, the grid itself cannot be completely arbitrary. Each grid line must be parallel to a coordinate direction, so that any grid can be completely described by three arrays, each array storing the intersection points of grid lines along a particular coordinate direction. Usually, rectangular cartesian coordinates are used, although any orthogonal curvilinear system may be used in general. In particular, cylindrical polar coordinates are useful for borehole investigations.

The FD method approximates equation (3.1) at each of the grid nodes. As an example, consider equation (3.1) in rectangular cartesian coordinates (§3.1.1.1):

$$\frac{\partial}{\partial x}\left(\frac{1}{\rho}\frac{\partial V}{\partial x}\right)+\frac{\partial}{\partial y}\left(\frac{1}{\rho}\frac{\partial V}{\partial y}\right)+\frac{\partial}{\partial z}\left(\frac{1}{\rho}\frac{\partial V}{\partial z}\right)=-S\,. \tag{3.2}$$

The basis of the FD method is the expression of the partial derivatives of V using differences of the discrete function values at the nodes. As an example, the partial derivative ($\partial V/\partial x$) can be approximated at a point midway between nodes located at x_0 and x_1 using the *central difference* formula

$$\left.\frac{\partial V}{\partial x}\right|_{x_{\frac{1}{2}}} \approx \frac{V(x_1)-V(x_0)}{x_1-x_0}\,. \tag{3.12}$$

This is illustrated graphically in Figure 3.3.

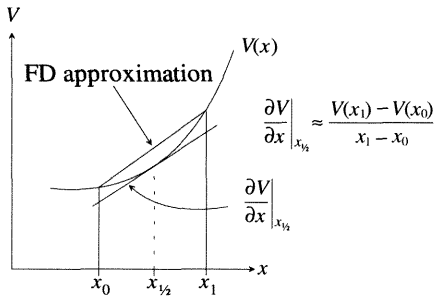

Figure 3.3 Central difference approximation [gradient of the line drawn between $V(x_0)$ and $V(x_1)$] for a first order partial derivative (gradient of the tangent at $x_{1/2}$).

Second order derivatives may be expressed as differences of first order derivatives and so on, allowing in principle any order derivative to be approximated, provided there are enough nodes available. The extension of the above example to three dimensions is straightforward [a full FD formulation of equation (3.1) is described in Section 3.2.1]. The accuracy of the approximation improves as nodes get closer together or as modelled functions become smoother. This is borne out intuitively in Figure 3.3: if the points x_0 and x_1 are moved closer to each other, or if the graph of the function $V(x)$ becomes straighter, then the FD approximation [the gradient of the line drawn between $V(x_0)$ and $V(x_1)$] will converge to the actual value of $\partial V/\partial x$ at $x = x_{1/2}$ (the gradient of the tangent at $x_{1/2}$).

Boundary conditions (§3.1.1.1) are specified on the external nodes of the FD grid. In general, the boundaries in a FD model must coincide with coordinate surfaces, although it is possible to approximate non-aligned boundaries (Mitchell and Griffiths, 1980).

In addition to V, the parameters ρ and S are also specified at each node. Using these, and difference quotients to express partial derivatives (equation 3.12), the electrical governing equation (3.1) may be approximately formulated for each node in terms of the surrounding nodal parameter values.

Specification of resistivity, ρ, by a set of values at nodes is equivalent to discretizing the resistivity distribution in the model region into a series of cells, the size and shape of which are defined by the grid/node locations. In the case of geological models this is, to an extent, observed in reality where resistivity may change abruptly at contacts between different units or beds, for example. Complex resistivity distributions may in principle be simulated, provided a fine enough grid is used.

The discretization of a resistivity distribution is illustrated with a schematic example in Figure 3.4. This shows how a borehole logging tool might be represented using a cylindrical grid (which possesses convenient geometry). Cells in the central part of the model correspond to the logging tool and are surrounded by cells defined to be equivalent to borehole fluid. Outside these cells variations in the model resistivity correspond to simulated variations in the formation resistivity.

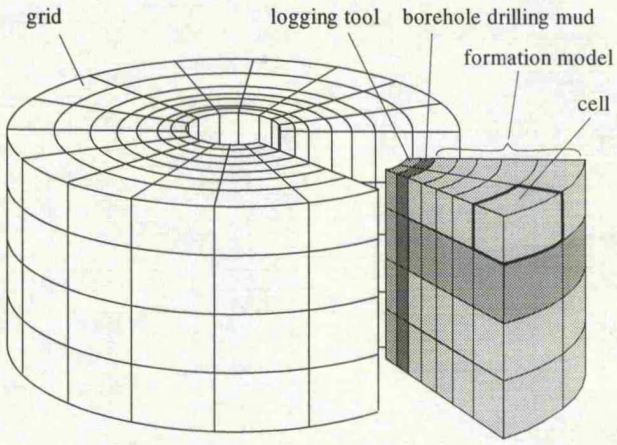

Figure 3.4 Discretization of a resistvity distribution using FD cells.

The set of nodal approximations to equation (3.1) are combined to give a set of simultaneous equations. Expressed in matrix form, the equation set forms a *sparse*, *banded*, matrix. Various numerical procedures exist for solving this kind of problem; they are discussed further in Section 3.5. The solution of the simultaneous equations gives the values of V at the FD grid nodes and thus the simulated electric potential in the modelled region; from these values the simulated response of electrical tools may also be generated.

The FD method can be seen to be applicable to arbitrary geometry, although grid definition is not completely flexible. Model detail is limited by time and space on the computer being used.

A FD formulation of equation (3.1) is described in more detail in Section 3.5.

3.1.3.2 Finite element method

The finite element (FE) method (Zienkiewicz, 1971) has been used for electrical resistivity modelling by Coggon (1971), Bibby (1978) and Sasaki (1994) amongst others. It is also a popular approach for modelling downhole situations (Chang and Anderson, 1984; Luthi and Souhaité, 1990; Chemali et al., 1983, and others).

As with the FD method, the first step in the application of the FE method is to define a grid to cover the region to be modelled. The electric potential function, V, is again represented by a set of discrete nodal values; interpolation is used to give values between nodes. In contrast to the FD method, the FE grid is not constrained by a particular coordinate system. The grid splits the modelled region into a series of elements (hence the method's name). Physical properties are associated with an entire element rather than grid nodes (although a property may vary between vertices of an element if desired). Two-dimensional elements are commonly triangular or rectangular; in 3D they become tetrahedral or cuboid.

The FE method is based on *minimisation of energy*. It can be shown that solving the Poisson equation is equivalent to minimising the total power, ψ, in a d.c. system (Coggon, 1971), which is expressed by the integral

$$\psi = \int_{\vartheta} \left\{ \sigma\left(\nabla V^2\right) + 2V\nabla \cdot \mathbb{J}_s \right\} \mathrm{d}\vartheta \,, \tag{3.13}$$

where V is the electric potential; $\mathbb{J}_s$ represents the contribution from current sources, and σ is conductivity in a region of interest ϑ.

The FE method approximates the minimisation of equation (3.13). The solution involves assuming a form for the resultant potential function by approximating it with local functions over each element (in three dimensions tetrahedral elements are commonly used and a linear variation of the potential is assumed) and formulating the power expression (eq. 3.13) for each element. The equations for each element are combined to give a set of simultaneous equations which can be assembled into a sparse matrix equation, as in the case of the FD method. A

variety of standard approaches exist for solution of the simultaneous equations [see, for example, Press et al. (1992)].

Boundary conditions are automatically incorporated into the minimisation formulation, allowing complex boundary geometry to be catered for by the FE method. In comparison with the FD method, this makes the FE method better suited to modelling Neumann conditions (§3.1.1.1), or situations involving irregular boundary geometries.

As with the FD method, the FE method is capable of modelling situations with arbitrary geometry and resistivity distributions. In terms of grid definition and boundaries the FE method is more flexible, although the situations modelled in this work can be adequately represented using grids and boundaries 'tied' to specific coordinate systems (i.e. rectangular cartesian or cylindrical polar coordinates). The comparison between the FD and FE methods is discussed further in Section 3.1.4.

3.1.3.3 Other methods

The FD and FE methods are the most important solution approaches to modelling the three dimensional electrical conduction problem in the context of this work since they are applicable to problems with arbitrary geometry and resistivity distributions. A variety of other methods have also been used to model electrical flow: these are outlined below.

Integral equation approaches

Integral equation methods are based on the integral representation of the electrical governing equation (eq. 2.9, §2.2.2):

$$V(\mathbf{r}) = \int_{\vartheta} G(\mathbf{r},\mathbf{r}_0) S(\mathbf{r}_0) \mathrm{d}\vartheta_0 . \tag{3.14}$$

The key to using an integral equation approach is to derive an expression for G corresponding to the situation being modelled. There is no general expression for G (which incorporates boundary conditions) although for a full space, for example, it is given by the whole space Green's function:

$$G = \frac{1}{4\pi} \frac{1}{|\mathbf{r} - \mathbf{r}_0|} .$$

The similarity between G and V for the differential equation is apparent (cf. eq. 3.6). In practice, solution of an integral equation problem involves finding G for any anomalous regions in the area of interest.

Once G is known, it is substituted into equation (3.14) which may be converted to a set of algebraic equations (Harrington, 1968) that can be solved by standard numerical techniques. The set of simultaneous equations is in general much simpler than the sets obtained from differential models (such as the FD and FE methods); this is the main advantage of the integral equation approach.

Integral equation methods are discussed in detail by Eskola (1992), and have been applied to electrical resistivity modelling by a number of authors including Daniels (1977) and Straub (1995); Schenkel and Morrison (1994) use integral equation modelling to analyse the response of a resistivity tool in a cased borehole; Beasley and Ward (1986) describe simulation of the mise-à-la-masse technique. The approach is also popular for electromagnetic (Hohmann, 1975; Wannamaker et al., 1984) and magnetotelluric (Ting and Hohmann, 1981) models, which are based on similar principles to those of resistivity simulations.

Lee et al. (1981) use a method which combines aspects of both FE and integral solutions in order to reduce the size and solution time for some electromagnetic simulations. Hermance (1983) uses local integral forms to improve the accuracy of a FD electromagnetic model. In a.c. simulations the accuracy of cerivatives of the electric field and potential, particularly near sharp discontinuities, is more critical than for d.c. resistivity modelling.

Resistor network analogues

Electrical conduction in three dimensions can be approximated by using physical networks of resistors. Such networks have been used to analyse electrical logging tools (Guyod, 1955) but have now been superseded by computers which can duplicate the models without the need to build them. The network analogue is a direct consequence of the current/charge conservation rules expressed in equation 2.2 (§2.2.1). This property is also possessed by the FD formulation of the problem since it is based directly on the conservation equation (see §3.2.3). Zemanian and Anderson (1987) use results for an infinite electrical grid to refine an essentially one-dimensional model used to simulate electrical borehole tools.

Alpha-centre method

The alpha-centre method (Stefanescu and Stefanescu, 1974) produces relatively fast simulations of electrical problems, but is limited to smoothly-varying resistivity distributions between localised conductive bodies. Petrick et al. (1981) use this approach in a 3D inversion scheme. The formulation of the problem moves away from the original electrical governing equation (3.1), so derivation of secondary parameters such as current flow is more difficult.

Fourier methods

Equation (3.1) can be made more tractable by using fourier transformations and solving the transformed problem (Burden and Faires, 1985). As with the alpha-centre method this approach gives fast solutions, but places severe restrictions on the resistivity distributions that can be catered for. Solution approaches based on fourier methods include those by Tripp et al. (1984) and LaBreque and Ward (1990) who apply it to a cross-hole model interpretation.

3.1.4 Summary

Excepting simplified situations, simulation of electrical flow generally requires a numerical approach. Analytic solutions (§3.1.2) are valuable both for verification of numerical methods and for providing good starting points for iterative solutions; the superposition principle (§3.1.2.1) is a useful analytical result allowing the deduction of potential fields for multiple source configurations, or sources of different magnitudes, if the fields due to single sources/sinks are known.

In the context of this work the most important numerical solution approaches are the finite difference method (§3.1.3.1) and the finite element method (§3.1.3.2) which can deal with arbitrary resistivity distributions in three dimensions. Other numerical techniques are in general faster but do not allow enough scope for simulating realistic three-dimensional models (§3.1.3.3). These approaches are useful in other modelling applications, for example resistivity inversion schemes.

The FE method is more flexible than the FD method in terms of grid definition and boundary conditions, and can more easily incorporate sophisticated 'base' functions for approximating highly variable parameters. For modelling the electrical conduction problem such refinements are not essential and the FD method is considered to be suitable for the

purpose of this work. Once the problem has been formulated, both approaches lead to the solution of simultaneous equations which can be expressed as a sparse matrix equations.

Dirichlet boundary conditions are handled well by both the FD and FE methods. The flexibility of the FE method allows Neumann conditions or irregular boundary geometries to be catered for with more ease and accuracy than for the FD method. Typical problems dealt with in this thesis can be expressed without the need for such difficult boundary conditions by using resistive boundaries, effectively locating electrode arrays in large, insulating tanks.

The FD formulation developed has the benefit of being based directly on the generalised Poisson equation, allowing secondary parameters such as current flow, current density and the electric field to be readily deduced. This approach is also directly analogous to a three-dimensional resistor network which is a useful physical reference when analysing any problems with models and ensures that models are physically reasonable. Secondary parameters are not so easily derivable from the FE method which is based on minimisation of energy.

The resistor network analogy of the FD formulation allows it to effectively replace physical resistor networks previously built for simulation purposes (§3.1.3.3). Resistor networks closely simulate the physical process of current conduction and the analogy is invaluable for modelling tools which make use of the measurement and control of current flow. For example, this is exploited to simulate the passively focused current intensity measurements made by electrical imaging devices (Chapter 5).

Following the above discussion, the FD method is identified as a suitable approach for creating a 3D numerical model of electrical current flow in rocks.

3.2 Development of a three dimensional finite difference numerical model

This section describes in detail the formulation and implementation of a FD solution of the three-dimensional electrical conduction problem embodied in equation (3.1). This solution forms the core of the numerical models used in chapters 4 and 5.

3.2.1 Formulation of finite difference equations

Initial models used a grid based on rectangular cartesian coordinates. In such a system, equation (3.1) is written as (eq. 3.2, §3.1.1.1):

$$\frac{\partial}{\partial x}\left(\sigma\frac{\partial V}{\partial x}\right)+\frac{\partial}{\partial y}\left(\sigma\frac{\partial V}{\partial y}\right)+\frac{\partial}{\partial z}\left(\sigma\frac{\partial V}{\partial z}\right)=-S\,.$$

The objective of the FD method is to find the electric potential $V(x, y, z)$ for a modelled region $\Re$. The conductivity distribution $\sigma(x, y, z)$ and source function $S(x, y, z)$ [$S = (\partial q/\partial t)$ represents the location and magnitude of any current sources] are known in $\Re$. In addition, the variation of V at the boundaries of $\Re$ (the boundary conditions) are specified.

Consider a 3D grid consisting of $I \times J \times K$ nodes, where the coordinates of the (i, j, k)th node are denoted by (x_i, y_j, z_k). Consider a typical node (i, j, k). For convenience label (i, j, k) 'P', $(i-1, j, k)$ 'W', $(i+1, j, k)$ 'E', $(i, j-1, k)$ 'S', $(i, j+1, k)$ 'N', $(i, j, k-1)$ 'D' and $(i, j, k+1)$ 'U' (Figure 3.5).

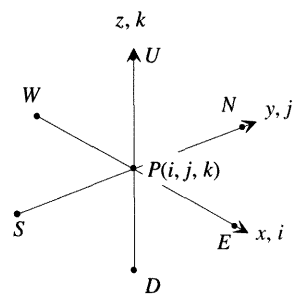

Figure 3.5 Coordinate notation convention.

Equation (3.2) can be approximated using FD quotients for partial derivatives (§3.1.3.1). For simplicity this process is illustrated for a typical node, P, on a one-dimensional grid (Figure 3.6).

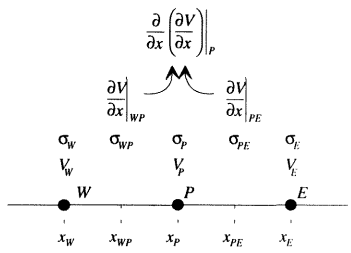

Figure 3.6 Model parameters at a typical node on a one-dimensional grid.

For this example, equation (3.2) reduces to:

$$\frac{\partial}{\partial x}\left(\sigma\frac{\partial V}{\partial x}\right) = -S. \tag{3.15}$$

In order to represent this equation at P, an expression for the partial second derivative $\partial/\partial x(\sigma\partial V/\partial x)$ must be found; this is achieved by using first derivatives calculated *between* the grid nodes, at x_{WP} and x_{PE}:

$$\frac{\partial}{\partial x}\left(\sigma\frac{\partial V}{\partial x}\right)\Bigg|_{x_{WP}} = \frac{\left(\sigma\frac{\partial V}{\partial x}\right)\Big|_{x_{PE}} - \left(\sigma\frac{\partial V}{\partial x}\right)\Big|_{x_{WP}}}{x_{PE} - x_{WP}}. \tag{3.16}$$

The first order derivatives are in turn approximated by difference equations:

$$\left(\sigma\frac{\partial V}{\partial x}\right)\Bigg|_{x_{WP}} = \sigma_{WP}\left(\frac{V_P - V_W}{x_P - x_W}\right); \qquad \left(\sigma\frac{\partial V}{\partial x}\right)\Bigg|_{x_{PE}} = \sigma_{PE}\left(\frac{V_E - V_P}{x_E - x_P}\right). \tag{3.17}$$

Substitution of equations (3.16) and (3.17) into (3.15) yields the FD approximation to equation (3.15) at P:

$$\frac{\sigma_{PE}\left(\frac{V_E - V_P}{x_E - x_P}\right) - \sigma_{WP}\left(\frac{V_P - V_W}{x_P - x_W}\right)}{x_{PE} - x_{WP}} = -S_P. \tag{3.18}$$

The above procedure is easily extended to three dimensions, giving:

$$\frac{\sigma_{PE}\left(\frac{V_E - V_P}{x_E - x_P}\right) - \sigma_{WP}\left(\frac{V_P - V_W}{x_P - x_W}\right)}{x_{PE} - x_{WP}} + \frac{\sigma_{PN}\left(\frac{V_N - V_P}{y_N - y_P}\right) - \sigma_{SP}\left(\frac{V_P - V_S}{y_P - y_S}\right)}{y_{PN} - y_{SP}} + \frac{\sigma_{PU}\left(\frac{V_U - V_P}{z_U - z_P}\right) - \sigma_{DP}\left(\frac{V_P - V_D}{z_P - z_D}\right)}{z_{PU} - z_{DP}} = -S_P. \tag{3.19}$$

The term x_{PE} refers to the x-coordinate midway between nodes P and E, which is the mean of x_P and x_E, i.e. $\frac{1}{2}(x_P + x_E)$. In common with coordinate locations, the inter-nodal variation of most model parameters is found by linear interpolation. An important exception is σ, which is not linearly interpolated for physical reasons (Reece, 1986): consider the case when node P is just below the earth's surface, and node E is just above it. Then σ_P is set to the rock conductivity (a finite number) and $\sigma_E = 0$ as air is (effectively) an electrical insulator. There is no conduction of current across the PE boundary which implies $\sigma_{PE} = 0$. However, linear interpolation gives $\sigma_{PE} = \frac{1}{2}(\sigma_P + \sigma_E) = \frac{1}{2}\sigma_P$, i.e. a non-zero value in general. To overcome this problem resistivity, rather than conductivity, is interpolated. This gives

$$\frac{1}{\sigma_{PE}} = \frac{1}{2}\left(\frac{1}{\sigma_P} + \frac{1}{\sigma_E}\right) \Rightarrow \sigma_{PE} = \frac{2\sigma_P\sigma_E}{\sigma_P + \sigma_E}, \tag{3.20}$$

so in the case of the earth-air interface, equation (3.20) gives $\sigma_{PE} = 0$ as required.

The mistake of averaging conductivity instead of resistivity has been made in published literature (Scriba, 1981). The fact that the FD method has been established for many years is no guarantee of it being implemented correctly.

Kirchhoff's current conservation rule

The source term S_P represents current (emitted at P) per unit volume (§2.2.1), or in the one-dimensional case per unit length, and may be expressed as:

$$S_P = \frac{I_P}{\Delta x_P} = \frac{I_P}{x_{PE} - x_{WP}},$$

where I_P [A] is the magnitude of the current source at P. Substituting this into equation (3.18) and cancelling like terms:

$$\sigma_{PE}\left(\frac{V_E - V_P}{x_E - x_P}\right) - \sigma_{WP}\left(\frac{V_P - V_W}{x_P - x_W}\right) = -I_P.$$

Denoting $(V_E - V_P)$ by ΔV_{PE}, $(V_P - V_W)$ by ΔV_{WP}, $(x_E - x_P)$ by Δx_{PE}, and $(x_P - x_W)$ by Δx_{WP}:

$$\frac{\sigma_{PE}}{\Delta x_{PE}} \Delta V_{PE} - \frac{\sigma_{WP}}{\Delta x_{WP}} \Delta V_{WP} = -I_P \,. \tag{3.21}$$

In one dimension, $(\sigma_{PE}/\Delta x_{PE})$ represents conductance (§A.1), the reciprocal of resistance, so equation (3.21) is equivalent to

$$\frac{\Delta V_{PE}}{R_{PE}} - \frac{\Delta V_{WP}}{R_{WP}} = -I_P \,, \tag{3.22}$$

where R_{PE} is the resistance between P and E; similarly for R_{WP}. On applying Ohm's Law, equation (3.22) can be seen to be a statement of Kirchhoff's current conservation rule (§A.3) for node P and thus the FD formulations expressed in equations (3.18) and (3.19) are equivalent to current conservation rules for electric circuits. Equation (3.19) is therefore analogous to a three-dimensional resistor network with inter-nodal resistances dependent on node spacing and conductivity. This analogy is used in this work in a variety of ways when generating numerical models, most notably for deriving 3D current flow from nodal electric potential values. The resistor network analogy confirms that a physically valid model should use interpolation of resistivity rather than conductivity values between nodes (eq. 3.20), in the same way as resistors are added in series (§A.4).

Boundary conditions

Both Dirichlet and Neumann boundary conditions can be specified for the FD model (§3.1.1.1). The voltage values at the boundaries of the FD grid are generally fixed, and thus Dirichlet conditions are naturally specified at the outer grid surfaces: the initial value of the boundary voltage specified before the start of iteration towards a solution is the boundary condition. Neumann conditions are incorporated in general by a minor modification to the solution algorithm so that the boundary voltage varies as the interior values of V are iterated, in order to preserve the potential gradient specified initially.

The only Neumann condition that needs to be specified for the purposes of this work is that for a resistive boundary (as in the earth-air example above). A model with such boundary conditions is analogous to simulated electrical equipment located in an insulating tank.

Equation (3.19) is used to approximate equation (3.2) at each of the interior nodes of the FD grid. A total of $(I-2)\times(J-2)\times(K-2)$ simultaneous equations are formulated: one for

each node excluding the boundaries. The solution of these equations is discussed in the following section.

3.2.2 Solution of finite difference equations

It is convenient to rearrange equation (3.19) in the form

$$-V_P k_P + V_W k_W + V_E k_E + V_S k_S + V_N k_N + V_D k_D + V_U k_U = -S(dx_P dy_P dz_P) \qquad (3.23)$$

The k's are all known constants which depend upon σ and the node coordinates; $(dx_P \times dy_P \times dz_P)$ is the (known) dimension of the cell surrounding P, so the seven V's are the only unknowns in equation (3.23). In order to find a value of V at each of the grid nodes, the whole set of equations [in $(I-2)(J-2)(K-2)$ unknowns, i.e. the number of internal nodes] must be solved simultaneously.

Direct matrix inversion methods make use of the fact that the equation matrix is *sparse*—i.e. it contains many zero elements. There are a total of $(I-2)(J-2)(K-2)$ unknowns, with seven unknowns (in general) in each equation. This leaves at least $[(I-2)(J-2)(K-2) - 7]$ zero entries per row. A one-dimensional formulation of equation (3.23) produces a *tri-diagonal* matrix with non-zero elements only on the main diagonal and on the diagonals above and below in the equation matrix; this is readily invertable. Two- and three-dimensional formulations produce two and four extra non-zero diagonals (*sparse*, *banded* diagonal matrices) respectively, which are more difficult to invert, and require progressively more computer storage space.

For small matrices ('small' being a computer-dependent definition, but typically when dealing with simplified models such as two-dimensional ones) direct matrix inversion may be used. Tailor-made software packages exist for inversion of sparse matrices (see, for example, Eisenstat et al., 1977). For cases involving larger matrices, which include realistic three-dimensional formulations, iterative processes must be used. The principal iterative methods which may be employed are simultaneous overrelaxation (SOR) (Press et al., 1992) used by Scriba (1981) and alternating direction iteration (ADI) (Gunn, 1964).

James (1985) uses a specialised technique (Polozhii decomposition), which is reported to be efficient and compact, at the expense of full flexibility. Three-dimensional models must be capable of being divided into a number of regions, each of which have resistivity variation in one dimension only. Geological situations which may be approximated on a rectangular grid

using this approach can typically be classed as fault-bounded tectonic blocks. Vertical faults and horsts and grabens are among the list of examples of potential applications given by James (1985).

Dey and Morrison (1979) compare the performance of SOR and ADI with more sophisticated techniques (the incomplete Cholesky-conjugate gradient method and full-banded Cholesky decomposition), finding that these techniques are faster and more accurate than the standard approaches. Full-banded decomposition is particularly useful when many (>15) electric sources are to be simulated, since computations for arbitrary source distributions can be rapidly performed once the matrix inversion has been carried out. These approaches are unfortunately impractical on smaller computers because of memory and storage requirements.

The modelling programs described in this work utilise a hybrid relaxation method (Reece, 1986) which solves for an entire line of nodes simultaneously, and thus iterates by rows (or columns) rather than just node-by-node. This approach is similar to the successive line overrelaxation method described by Varga (1962) and used by used by Mufti (1976), which does not require a great deal of computer memory, and allows models to be small enough to be run on a powerful personal computer (PC) or workstation.

3.2.3 Calculation of resistor values

Since the FD model is analogous to a 3D resistor network (§3.2.1), each cell in the 3-dimensional model resistivity distribution may be represented by three resistors: one in each coordinate direction. The resistor values represent the equivalent resistance of the (isolated) cell in each of the three directions. In Appendix C, relations between the resistance of an elemental cell and its resistivity and geometry are derived; these results are summarised below.

Rectangular cartesian coordinates

The conversion equations for rectangular cartesian coordinates are based on finding expressions for the resistance across opposite ends of a rectangular cell (§C.2) as illustrated in Figure 3.7. Denoting these resistances by R_x, R_y, and R_z in the x, y, and z directions respectively the resistances are given by

$$R_x = \frac{\rho \Delta x}{\Delta y \Delta z}; \qquad R_y = \frac{\rho \Delta y}{\Delta x \Delta z}; \qquad \text{and} \qquad R_z = \frac{\rho \Delta z}{\Delta x \Delta y}.$$

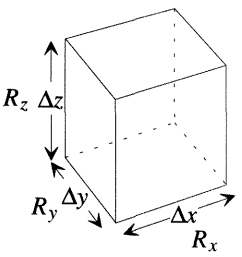

Figure 3.7 Cell geometry in rectangular cartesian coordinates.

Cylindrical polar coordinates

An important modification to the numerical model is to express the problem in cylindrical polar coordinates. Such a coordinate system lends itself to modelling the borehole situation (in the case of an idealised, circular borehole) with the borehole axis coincident with the centre of the FD grid.

The conversion equations for cylindrical polar coordinates (§C.3) express the resistance across opposite ends of a wedge-shaped cell (Figure 3.8). Denoting these resistances by R_r, R_q, and R_z in the radial, tangential, and vertical directions respectively the resistances are given by

$$R_r = \frac{\rho}{\Delta\theta.\Delta z}\ln\left(\frac{r_2}{r_1}\right); \qquad R_\theta = \frac{\rho}{2\Delta z}\left(\frac{r_2 + r_1}{r_2 - r_1}\right)\Delta\theta\,; \quad \text{and} \quad R_z = \frac{\rho\Delta z}{\frac{1}{2}\Delta\theta\left(r_2^2 - r_1^2\right)}.$$

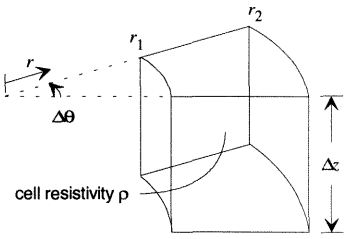

Figure 3.8 Cell geometry in cylindrical polar coordinates.

Using this approach it is possible to account for a cylindrical mesh using internal storage based on a rectangular grid.

3.2.4 Wrapping the grid for cylindrical polar coordinates

The FD model can be modified for cylindrical polar coordinates by 'wrapping' the ends of the originally rectangular mesh back onto themselves (Reece, pers. comm., 1992). This process is illustrated in Figure 3.9. The advantage of this approach, rather than reformulating the FD equations, is that the arrays for internal storage of the FD model remain the same, and the solution algorithm does not need to be greatly modified.

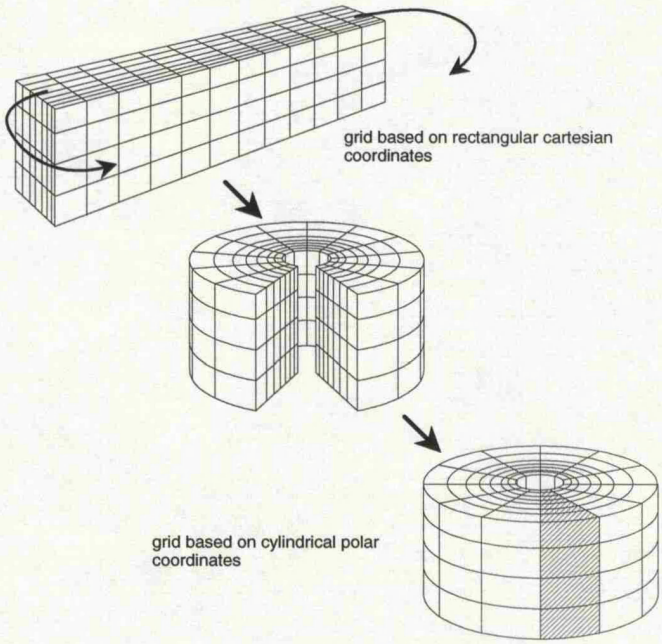

Figure 3.9 Wrapping of a rectangular mesh.

Originally rectangular cells become wedge-shaped and so the conversion equations for cylindrical polar coordinates are used to find resistance values as detailed in the previous section.

In the tangential direction (circling the central axis) nodes that were originally at the opposite ends of the grid come into contact with each other (indicated by the hatching in Figure 3.9). These are fixed boundary nodes in the rectangular grid, but are required to vary freely in the wrapped grid. This is enabled by repeatedly setting the boundary nodes equal to the interior nodes of the opposite side of the grid each time the solution iterates, effectively overlapping the boundary nodes in the tangential direction.

3.2.5 Accuracy and grid definition

The choice of the extent and resolution of a FD grid is compromised by requirements for accuracy (which is improved by finer mesh spacing, implying the need for more nodes) and speed (smaller grids have less nodes, implying fewer computations). An understanding of the parameters governing accuracy is therefore important when considering model development. This section describes theoretical and practical analysis of grid definition and solution accuracy. Grid definition for models described in this work has been implemented using the discussion here as a guide.

3.2.5.1 Discretization errors

The discretization error associated with the FD approximation of partial differential equations can be quantified analytically (Mitchell and Griffiths, 1980).

Consider a two-dimensional formulation of Laplace's equation (eq. 2.8, §2.2) in rectangular cartesian coordinates:

$$\frac{\partial^2 V}{\partial x^2} + \frac{\partial^2 V}{\partial y^2} = 0\,, \tag{3.24}$$

on a rectangular grid with a node spacing of a in the x-direction and b in the y-direction Consider the typical node P illustrated in Figure 3.10.

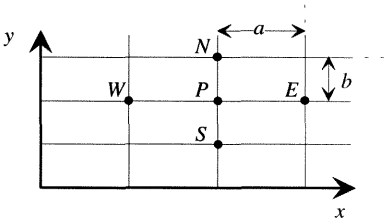

Figure 3.10 Typical node point in a regular two-dimensional grid.

A Taylor expansion may be used to express the potential V_E in terms of that at V_P:

$$V_E = \left(V + a\frac{\partial V}{\partial x} + \frac{a^2}{2}\frac{\partial^2 V}{\partial x^2} + \frac{a^3}{6}\frac{\partial^3 V}{\partial x^3} + \frac{a^4}{24}\frac{\partial^4 V}{\partial x^4} + \ldots + \frac{a^n}{n!}V^{(n)} + \ldots \right)\Bigg|_P . \tag{3.25}$$

Similarly,

$$V_W = \left(V - a\frac{\partial V}{\partial x} + \frac{a^2}{2}\frac{\partial^2 V}{\partial x^2} - \frac{a^3}{6}\frac{\partial^3 V}{\partial x^3} + \frac{a^4}{24}\frac{\partial^4 V}{\partial x^4} - \ldots + \frac{(-a)^n}{n!}V^{(n)} + \ldots \right)\Bigg|_P . \tag{3.26}$$

Adding equations (3.25) and (3.26) gives

$$V_E + V_W - 2V_P = \left(a^2\frac{\partial^2 V}{\partial x^2} + \frac{a^4}{12}\frac{\partial^4 V}{\partial x^4} + \ldots \right)\Bigg|_P . \tag{3.27}$$

Similarly, in the y-direction,

$$V_N + V_S - 2V_P = \left(b^2\frac{\partial^2 V}{\partial y^2} + \frac{b^4}{12}\frac{\partial^4 V}{\partial y^4} + \ldots \right)\Bigg|_P . \tag{3.28}$$

An expression involving the LHS of Laplace's equation as stated in equation (3.24) may be derived by adding [$1/a^2 \times$ eq. (3.27)] to [$1/b^2 \times$ eq. (3.28)]:

$$\frac{1}{a^2}V_E + \frac{1}{a^2}V_W + \frac{1}{b^2}V_N + \frac{1}{b^2}V_S - 2\left(\frac{1}{a^2} + \frac{1}{b^2}\right)V_P = \left\{ \frac{\partial^2 V}{\partial x^2} + \frac{\partial^2 V}{\partial y^2} + \frac{1}{12}\left(a^2\frac{\partial^4 V}{\partial x^4} + b^2\frac{\partial^4 V}{\partial y^4} \right) + \ldots \right\}\Bigg|_P . \tag{3.29}$$

From equation (3.29) it can be seen that the approximation

$$\frac{1}{a^2}V_E + \frac{1}{a^2}V_W + \frac{1}{b^2}V_N + \frac{1}{b^2}V_S - 2\left(\frac{1}{a^2} + \frac{1}{b^2}\right)V_P = 0 \tag{3.30}$$

is equivalent to Laplace's equation with a discretization error [termed 'local truncation error' by Mitchell and Griffiths (1980)] of

$$\frac{1}{12}\left(a^2\frac{\partial^4 V}{\partial x^4} + b^2\frac{\partial^4 V}{\partial y^4} \right) + \ldots . \tag{3.31}$$

Note that equation (3.30) is equivalent to a FD approximation derived from central difference formulae (cf. eq. 3.23, §3.2.2).

The discretization error expressed by equation (3.31) is governed primarily by the grid spacing factors a and b, and to a lesser degree by the variation of the potential function (or to be more specific, its fourth derivative). The truncation error is of the order of a^2 and b^2 for the x- and y-directions, respectively. Accuracy is therefore improved if a and b are reduced, i.e. the grid is made finer. This argument may be extended to define discretization error for three-dimensional grids.

If the grid is not uniform, terms in equations (3.25) and (3.26) will no longer cancel, leading to an error expression involving larger magnitude quantities proportional to $\partial V/\partial x$ and $\partial V/\partial y$. This effect can be reduced by expanding the grid smoothly which reduces the difference between the 'non-cancelling' terms since adjacent grid spacings are of similar magnitude.

The *global* error associated with FD approaches can be analysed in addition to the local truncation error (Mitchell and Griffiths, 1980). Again this is found to decrease as the number of nodes increases and the inter-nodal spacing decreases, but is not specifically dependent on grid geometry and spacing, and will not be considered further.

3.2.5.2 Comparison with analytic solutions

To test the accuracy of the models developed in this work, the FD solution may be compared with the analytical results for certain simplified situations outlined in Section 3.1.2. It is noted that the model cannot be tested for more general cases since analytic solutions do not exist for comparison (indeed, this is the motivation for choosing a numerical technique in the first place).

As an example, test results for the focused surface array described in Section 4.1.4 are outlined below. The FD solution was compared with analytic solutions for the following three situations:

1. a homogeneous, isotropic earth;
2. an isotropic earth with a single horizontal layer;
3. an isotropic earth with a single vertical interface.

Homogeneous, isotropic earth

Figure 3.11 compares the FD solution with the electrical potential derived from equation (3.7) (§3.1.2.2) for a homogeneous, isotropic earth of resistivity 75 ohm-m.

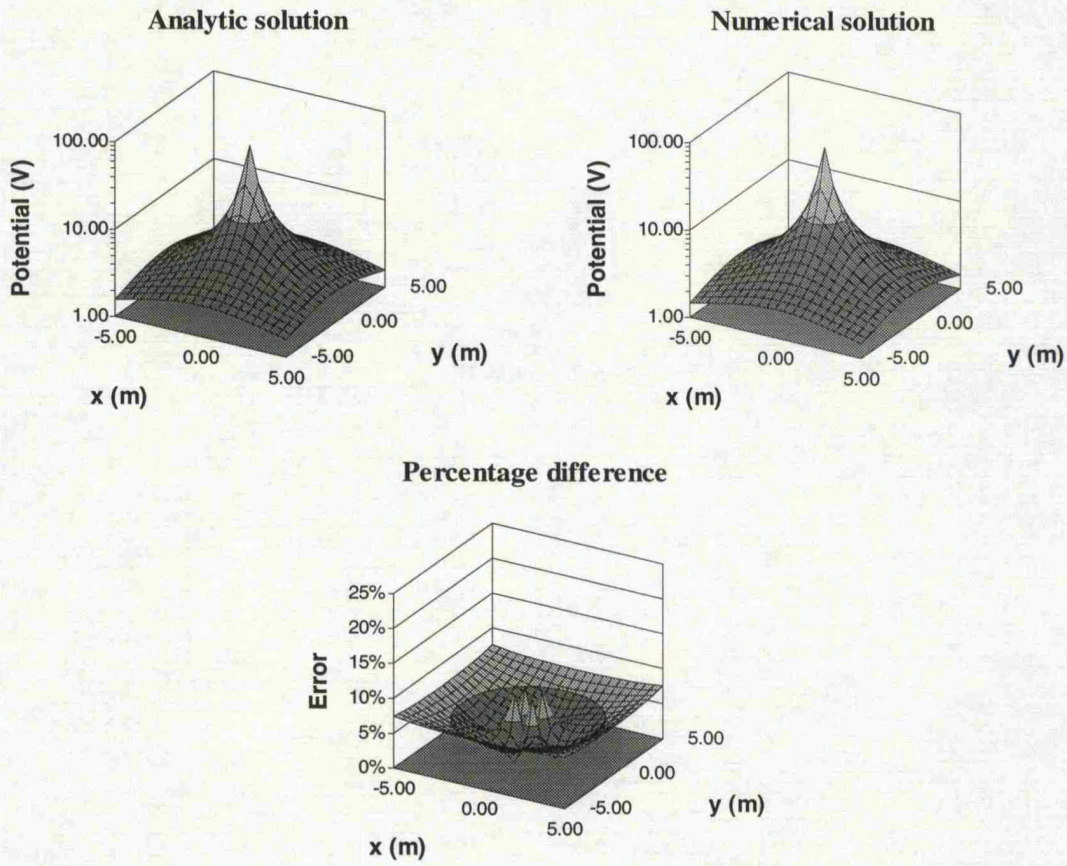

Figure 3.11 Analytic vs. FD solutions for a homogeneous halfspace.

The three plots in Figure 3.11 show parameters for the plane at $z = 0$, for the region -5 m $\leq x, y \leq 5$ m. This region corresponds to a 10 m × 10 m square on the surface of the simulated earth centred around the current injection point [which is located at (0, 0)]. The first two plots show electric potential calculated using equation (3.7) and using the FD model. The voltage is at a maximum at the current injection point, decaying rapidly away from the centre of the square in all directions (a logarithmic scale has been used to improve detail). The solutions can be seen to be similar, and this is confirmed in the third plot which illustrates the difference between the two numerical approaches, expressed as a percentage of the analytic value. The correspondence between the two approaches deteriorates away from the source location: the error approaches 8% near the source location, and also towards the edges of the 10 m × 10 m square shown in the plot.

The focused surface array model calculates focused electric potential and focused apparent resistivity values using the voltages at the locations of eight simulated focusing electrodes [located at (−2, 0), (−1, 0), (1, 0), (2, 0), (0, −2), (0, −1), (0, 1) and (0, 2)]; the errors at these crucial nodes are less than 2%.

Isotropic earth with a single horizontal layer

The analytic solution for an isotropic earth consisting of a single horizontal layer overlying an infinitely deep lower layer is given by equation (3.10) (§3.1.2.3). Figure 3.12 compares the FD solution with the electric potential derived from equation (3.10), for a model consisting of a horizontal layer of resistivity 12 Ω-m, 3.5 m deep, overlying a lower 75 Ω-m layer.

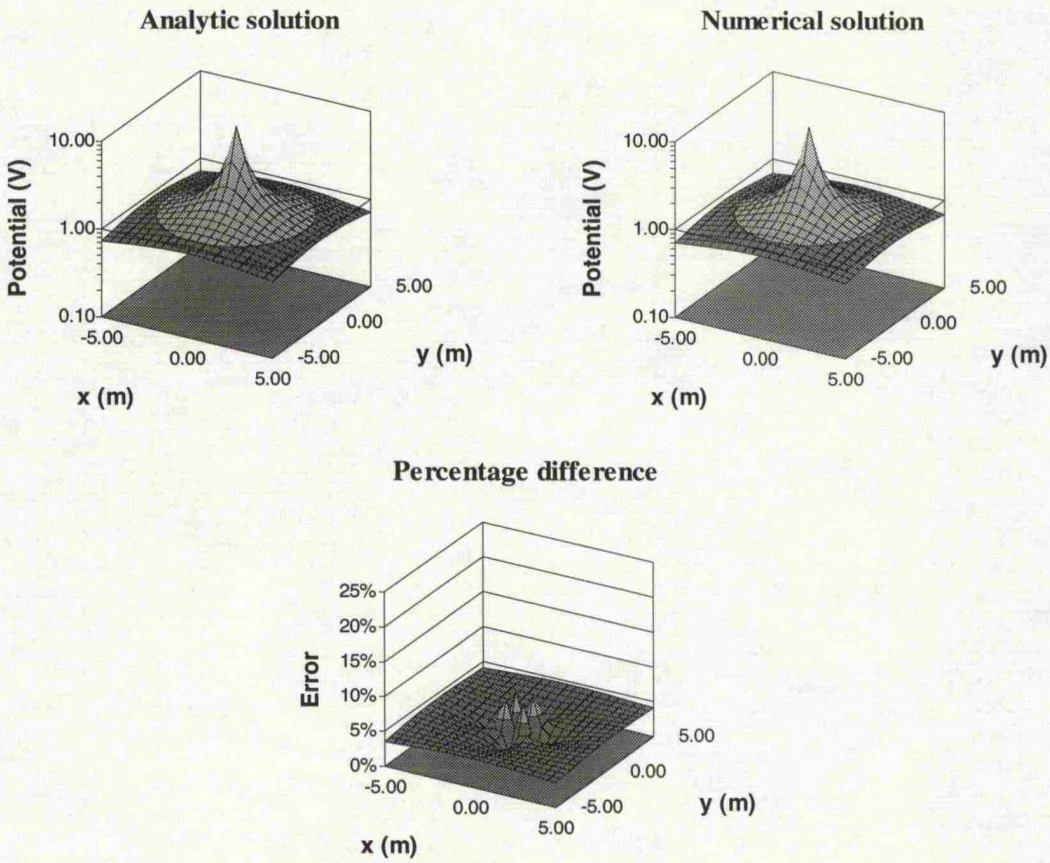

Figure 3.12 Analytic vs. FD solutions for a single-layered earth.

The numerical and analytic solutions for this case can again be seen to be similar, with the percentage difference error typically around 4% rising to nearer 7% in the close vicinity of the source (which is to be expected, since the grid spacing does not become any smaller at the source). The errors at the locations of the eight focusing electrodes are less than 2.5%.

Isotropic earth with a single vertical interface

Figure 3.13 compares the FD solution with the electrical potential derived from equations (3.8) (§3.1.2.3).

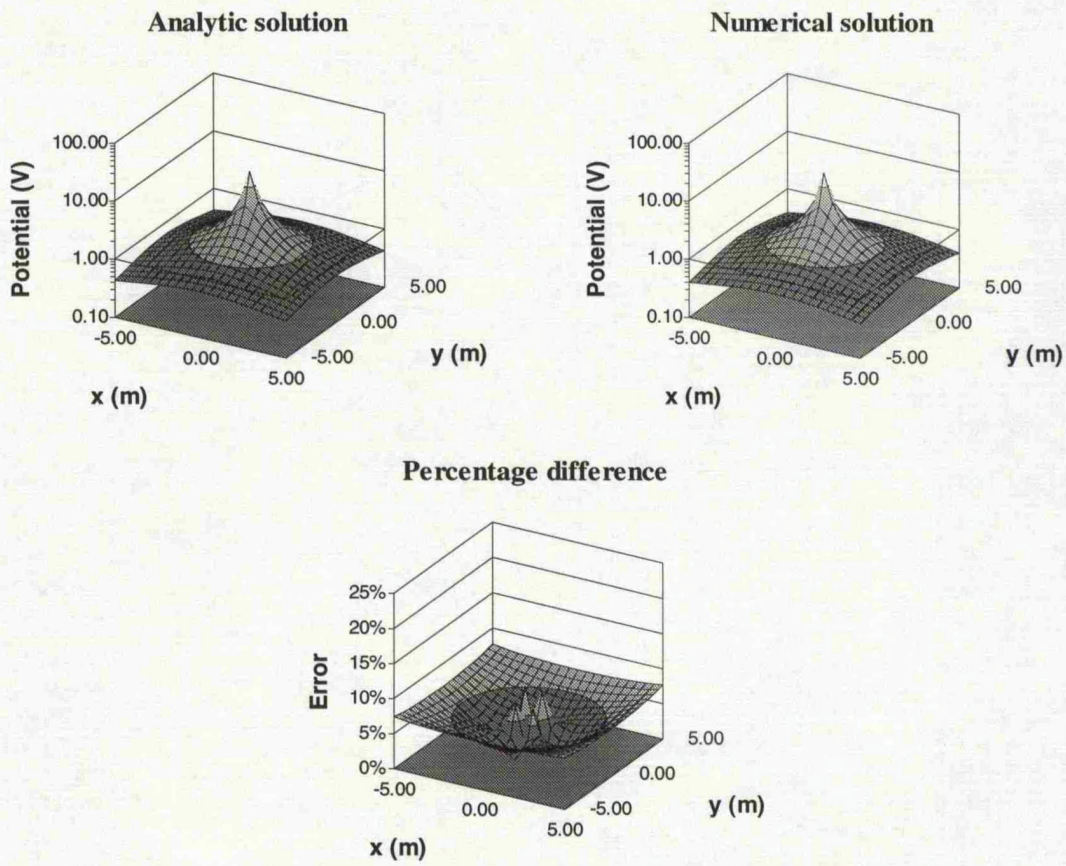

Figure 3.13 Analytic vs. FD solutions for a two-region earth divided by a vertical interface.

The error for the case of the vertical interface is similar to that for the homogeneous halfspace; the error (percentage difference) ranges from 8% near the source location and also the edges of the area shown in the plot, down to less than 2% at the locations of the potential electrodes.

The percentage error in the case of the homogeneous case (Fig. 3.11) and the vertical interface (Fig. 3.13) is seen to increase towards the edge of the modelled region illustrated. There are two reasons for this: firstly, the model grid coarsens at the edge of the 10 m × 10 m square shown in the plots (the full grid is illustrated in Fig. 4.2.2, §4.2.4.2); secondly the *percentage* error can magnify small differences in regions where numerical value of the potential is small (e.g. away from current sources and sinks), since a small *absolute* difference between theoretical and approximated values can still result in a large *proportional* difference (percentage error, e, is calculated using $e = |(V_{analytic} - V_{numerical}) / V_{analytic}| \times 100$).

3.2.5.3 Self consistency

The Kirchhoff error and simulated current flow through the FD resistor network can be monitored during model runs to confirm that any residual error (after iteration) is small and that conservation laws are not being violated (i.e. simulated current flow in the resistor network representing the three dimensional space and the borehole tool is physically reasonable and thus the model is self-consistent).

Numerical models which involve the simulation of artificially induced currents into the grounds can use current sources and sinks to represent current electrodes. The total current flow between simulated electrodes in the mesh is particularly important since this has an important bearing on the magnitude of the calculated geometric factor. The total current flow across any surface dividing the source and sink should be equal to the source/sink value. A vertical section illustrating part of the calculated resistor currents within a FD grid [for an initial simulation of the ODPHT tool (§4.1.4)] is shown in Figure 3.14. The current source is located at $(i, k) = (2, 20)$ and is of magnitude 1/12 (= $0.083\dot{3}$) A, while the sink is at (2, 40) and is of magnitude −1/12 A. The total vertical current flowing across a series of horizontal interfaces is shown in an extra column in the upper table. Where the interface divides the source and sink the total current flow is seen to be close to 0.0833 A as required. In the sink region, the grid spacing increases, and the current flow across boundaries in this region is less accurate (= 0.0835 A); this is a consequence of discretization errors. This loss of accuracy is offset by a decrease in the required computation time, and does not adversely affect the modelled electric potentials in the area of interest. Variation in accuracy is also observed when comparing current flow across the arbitrarily chosen boundaries *a* and *b* (marked in Figure 3.14). The total current across the surface of boundary *a* is found by summing vertical resistor currents for the upper and lower parts of the boundary, and radial currents for the vertical section, as illustrated in Figure 3.15. Again, the current flow (= 0.08332 A) is close to the expected value. Similar calculations give the current flow across surface *b* to be 0.08346 A. This can be used as a check that the grid 'wrapping' technique is operating correctly.

Vertical current flow

kVi	1	2	3	4	5	6	7	8	9	10	11	12	13	14	15	Total vertical current
14	0.00	-6.54E-3	-2.80E-7	-1.80E-7	3.56E-7	1.88E-6	3.61E-6	7.52E-6	1.99E-5	5.06E-5	2.13E-4	7.30E-4	1.98E-3	3.54E-3	0.00	3.65E-06
15	0.00	-6.60E-3	-2.70E-7	-1.20E-7	5.62E-7	2.34E-6	4.28E-6	8.67E-6	2.23E-5	5.49E-5	2.24E-4	7.47E-4	1.99E-3	3.55E-3	0.00	3.62E-06
16	0.00	-6.67E-3	-2.60E-7	-4.00E-8	8.45E-7	2.95E-6	5.13E-6	1.01E-5	2.51E-5	5.97E-5	2.37E-4	7.64E-4	2.01E-3	3.56E-3	0.00	3.59E-06
17	0.00	-6.74E-3	-2.40E-7	8.60E-8	1.26E-6	3.79E-6	6.24E-6	1.19E-5	2.84E-5	6.50E-5	2.49E-4	7.81E-4	2.02E-3	3.57E-3	0.00	3.56E-06
18	0.00	-6.81E-3	-2.10E-7	3.04E-7	1.92E-6	5.00E-6	7.72E-6	1.41E-5	3.22E-5	7.07E-5	2.63E-4	7.98E-4	2.04E-3	3.58E-3	0.00	3.57E-06
19	0.00	-6.88E-3	-1.20E-7	7.40E-7	3.07E-6	6.79E-6	9.68E-6	1.68E-5	3.65E-5	7.68E-5	2.76E-4	8.15E-4	2.05E-3	3.59E-3	0.00	3.45E-06
20	0.00	-6.95E-3	2.23E-7	1.89E-6	5.28E-6	9.45E-6	1.22E-5	2.00E-5	4.11E-5	8.31E-5	2.89E-4	8.31E-4	2.07E-3	3.60E-3	0.00	3.50E-06
21	0.00	7.63E-2	3.76E-6	5.59E-6	9.27E-6	1.29E-5	1.50E-5	2.34E-5	4.59E-5	8.95E-5	3.03E-4	8.47E-4	2.08E-3	3.61E-3	0.00	8.33E-02
22	0.00	7.62E-2	4.11E-6	6.73E-6	1.15E-5	1.56E-5	1.75E-5	2.65E-5	5.06E-5	9.57E-5	3.16E-4	8.63E-4	2.09E-3	3.61E-3	0.00	8.33E-02
23	0.00	7.61E-2	4.20E-6	7.17E-6	1.26E-5	1.73E-5	1.95E-5	2.92E-5	5.48E-5	1.02E-4	3.29E-4	8.79E-4	2.11E-3	3.62E-3	0.00	8.33E-02
24	0.00	7.61E-2	4.23E-6	7.39E-6	1.33E-5	1.86E-5	2.09E-5	3.14E-5	5.86E-5	1.07E-4	3.42E-4	8.93E-4	2.12E-3	3.63E-3	0.00	8.33E-02
25	0.00	7.60E-2	4.25E-6	7.52E-6	1.37E-5	1.94E-5	2.20E-5	3.32E-5	6.18E-5	1.12E-4	3.53E-4	9.07E-4	2.13E-3	3.64E-3	0.00	8.33E-02
26	0.00	7.60E-2	4.27E-6	7.60E-6	1.40E-5	2.00E-5	2.29E-5	3.46E-5	6.45E-5	1.17E-4	3.64E-4	9.21E-4	2.14E-3	3.64E-3	0.00	8.33E-02
27	0.00	7.59E-2	4.27E-6	7.66E-6	1.42E-5	2.04E-5	2.35E-5	3.57E-5	6.68E-5	1.21E-4	3.75E-4	9.33E-4	2.15E-3	3.65E-3	0.00	8.33E-02
28	0.00	7.59E-2	4.28E-6	7.70E-6	1.43E-5	2.08E-5	2.40E-5	3.66E-5	6.87E-5	1.24E-4	3.84E-4	9.45E-4	2.16E-3	3.66E-3	0.00	8.33E-02
29	0.00	7.58E-2	4.28E-6	7.74E-6	1.44E-5	2.10E-5	2.44E-5	3.73E-5	7.03E-5	1.27E-4	3.93E-4	9.56E-4	2.17E-3	3.66E-3	0.00	8.33E-02
30	0.00	7.58E-2	4.29E-6	7.76E-6	1.45E-5	2.12E-5	2.47E-5	3.79E-5	7.16E-5	1.30E-4	4.00E-4	9.65E-4	2.17E-3	3.67E-3	0.00	8.33E-02
31	0.00	7.59E-2	4.29E-6	7.80E-6	1.47E-5	2.16E-5	2.53E-5	3.87E-5	7.35E-5	1.34E-4	4.13E-4	9.82E-4	2.19E-3	3.66E-3	0.00	8.35E-02
32	0.00	7.58E-2	4.29E-6	7.82E-6	1.48E-5	2.18E-5	2.56E-5	3.94E-5	7.50E-5	1.38E-4	4.24E-4	9.97E-4	2.20E-3	3.67E-3	0.00	8.35E-02
33	0.00	7.58E-2	4.29E-6	7.83E-6	1.48E-5	2.19E-5	2.58E-5	3.97E-5	7.57E-5	1.39E-4	4.29E-4	1.01E-3	2.21E-3	3.68E-3	0.00	8.35E-02
34	0.00	7.58E-2	4.29E-6	7.83E-6	1.48E-5	2.19E-5	2.57E-5	3.97E-5	7.56E-5	1.39E-4	4.29E-4	1.01E-3	2.21E-3	3.68E-3	0.00	8.35E-02
35	0.00	7.58E-2	4.29E-6	7.82E-6	1.48E-5	2.18E-5	2.55E-5	3.93E-5	7.48E-5	1.37E-4	4.23E-4	1.00E-3	2.21E-3	3.68E-3	0.00	8.35E-02
36	0.00	7.59E-2	4.29E-6	7.78E-6	1.46E-5	2.15E-5	2.51E-5	3.85E-5	7.29E-5	1.33E-4	4.12E-4	9.88E-4	2.20E-3	3.68E-3	0.00	8.35E-02
37	0.00	7.59E-2	4.28E-6	7.71E-6	1.44E-5	2.10E-5	2.43E-5	3.71E-5	6.98E-5	1.27E-4	3.95E-4	9.69E-4	2.19E-3	3.67E-3	0.00	8.35E-02
38	0.00	7.60E-2	4.26E-6	7.57E-6	1.39E-5	2.00E-5	2.29E-5	3.46E-5	6.49E-5	1.19E-4	3.73E-4	9.44E-4	2.17E-3	3.67E-3	0.00	8.35E-02
39	0.00	7.61E-2	4.17E-6	7.12E-6	1.27E-5	1.77E-5	2.01E-5	3.04E-5	5.73E-5	1.07E-4	3.47E-4	9.14E-4	2.15E-3	3.65E-3	0.00	8.35E-02
40	0.00	7.61E-2	2.19E-6	4.09E-6	7.96E-6	1.22E-5	1.48E-5	2.36E-5	4.71E-5	9.30E-5	3.17E-4	8.81E-4	2.13E-3	3.64E-3	0.00	8.33E-02
41	0.00	-7.02E-3	1.97E-7	1.05E-6	3.24E-6	6.73E-6	9.55E-6	1.67E-5	3.68E-5	7.89E-5	2.87E-4	8.44E-4	2.10E-3	3.63E-3	0.00	-5.27E-06
42	0.00	-6.87E-3	1.03E-7	5.94E-7	1.97E-6	4.45E-6	6.74E-6	1.24E-5	2.91E-5	6.67E-5	2.57E-4	8.06E-4	2.07E-3	3.61E-3	0.00	-5.33E-06
43	0.00	-6.66E-3	6.50E-8	3.76E-7	1.26E-6	2.93E-6	4.56E-6	8.65E-6	2.13E-5	5.21E-5	2.18E-4	7.45E-4	2.02E-3	3.59E-3	0.00	8.72E-06
44	0.00	-6.27E-3	3.90E-8	2.28E-7	7.66E-7	1.79E-6	2.82E-6	5.41E-6	1.37E-5	3.51E-5	1.57E-4	6.36E-4	1.91E-3	3.51E-3	0.00	3.81E-06

Horizontal (radial) current flow

kVi	1	2	3	4	5	6	7	8	9	10	11	12	13	14	15
14		0.00	6.46E-5	6.47E-5	6.45E-5	6.43E-5	6.39E-5	6.32E-5	6.21E-5	5.98E-5	5.54E-5	4.36E-5	2.65E-5	1.08E-5	0.00
15		0.00	6.61E-5	6.62E-5	6.60E-5	6.57E-5	6.52E-5	6.43E-5	6.29E-5	6.01E-5	5.53E-5	4.29E-5	2.58E-5	1.04E-5	0.00
16		0.00	6.78E-5	6.79E-5	6.76E-5	6.72E-5	6.64E-5	6.53E-5	6.35E-5	6.03E-5	5.51E-5	4.22E-5	2.51E-5	1.01E-5	0.00
17		0.00	6.98E-5	6.99E-5	6.95E-5	6.88E-5	6.77E-5	6.62E-5	6.40E-5	6.03E-5	5.46E-5	4.13E-5	2.44E-5	9.73E-6	0.00
18		0.00	7.23E-5	7.23E-5	7.17E-5	7.06E-5	6.88E-5	6.68E-5	6.42E-5	5.99E-5	5.39E-5	4.04E-5	2.36E-5	9.36E-6	0.00
19		0.00	7.58E-5	7.56E-5	7.43E-5	7.21E-5	6.95E-5	6.69E-5	6.38E-5	5.92E-5	5.29E-5	3.93E-5	2.27E-5	8.99E-6	0.00
20		0.00	8.37E-5	8.02E-5	7.64E-5	7.24E-5	6.90E-5	6.61E-5	6.28E-5	5.81E-5	5.17E-5	3.81E-5	2.19E-5	8.62E-6	0.00
21		0.00	7.30E-5	7.27E-5	7.15E-5	6.92E-5	6.67E-5	6.41E-5	6.10E-5	5.64E-5	5.02E-5	3.68E-5	2.10E-5	8.24E-6	0.00
22		0.00	6.66E-5	6.66E-5	6.61E-5	6.49E-5	6.32E-5	6.12E-5	5.85E-5	5.43E-5	4.84E-5	3.53E-5	2.01E-5	7.85E-6	0.00
23		0.00	6.13E-5	6.13E-5	6.10E-5	6.04E-5	5.92E-5	5.77E-5	5.56E-5	5.19E-5	4.63E-5	3.38E-5	1.91E-5	7.45E-6	0.00
24		0.00	5.65E-5	5.65E-5	5.63E-5	5.59E-5	5.51E-5	5.40E-5	5.23E-5	4.91E-5	4.41E-5	3.21E-5	1.81E-5	7.05E-6	0.00
25		0.00	5.20E-5	5.20E-5	5.18E-5	5.15E-5	5.10E-5	5.01E-5	4.88E-5	4.61E-5	4.16E-5	3.04E-5	1.71E-5	6.65E-6	0.00
26		0.00	4.76E-5	4.77E-5	4.75E-5	4.73E-5	4.69E-5	4.62E-5	4.51E-5	4.29E-5	3.89E-5	2.85E-5	1.60E-5	6.23E-6	0.00
27		0.00	4.34E-5	4.35E-5	4.33E-5	4.32E-5	4.29E-5	4.23E-5	4.15E-5	3.96E-5	3.61E-5	2.66E-5	1.49E-5	5.82E-6	0.00
28		0.00	3.93E-5	3.93E-5	3.92E-5	3.91E-5	3.89E-5	3.85E-5	3.78E-5	3.62E-5	3.32E-5	2.46E-5	1.38E-5	5.40E-6	0.00
29		0.00	3.53E-5	3.53E-5	3.52E-5	3.51E-5	3.50E-5	3.46E-5	3.41E-5	3.28E-5	3.02E-5	2.25E-5	1.27E-5	4.97E-6	0.00
30		0.00	5.49E-5	5.49E-5	5.48E-5	5.47E-5	5.44E-5	5.39E-5	5.31E-5	5.12E-5	4.73E-5	3.56E-5	2.01E-5	7.94E-6	0.00
31		0.00	5.41E-5	5.42E-5	5.42E-5	5.41E-5	5.38E-5	5.33E-5	5.28E-5	5.13E-5	4.78E-5	3.68E-5	2.14E-5	8.65E-6	0.00
32		0.00	3.04E-5	3.04E-5	3.04E-5	3.04E-5	3.03E-5	3.00E-5	2.98E-5	2.91E-5	2.76E-5	2.22E-5	1.38E-5	5.89E-6	0.00
33		0.00	6.83E-6	6.84E-6	6.84E-6	6.85E-6	6.86E-6	6.86E-6	6.92E-6	7.01E-6	7.14E-6	7.27E-6	5.98E-6	3.11E-6	0.00
34		0.00	-1.67E-5	-1.68E-5	-1.67E-5	-1.67E-5	-1.65E-5	-1.63E-5	-1.60E-5	-1.51E-5	-1.32E-5	-7.61E-6	-1.79E-6	3.19E-7	0.00
35		0.00	-4.06E-5	-4.06E-5	-4.06E-5	-4.04E-5	-4.01E-5	-3.96E-5	-3.89E-5	-3.71E-5	-3.33E-5	-2.22E-5	-9.47E-6	-2.46E-6	0.00
36		0.00	-6.49E-5	-6.49E-5	-6.49E-5	-6.47E-5	-6.41E-5	-6.31E-5	-6.19E-5	-5.88E-5	-5.28E-5	-3.61E-5	-1.70E-5	-5.21E-6	0.00
37		0.00	-9.03E-5	-9.03E-5	-9.02E-5	-8.97E-5	-8.86E-5	-8.69E-5	-8.47E-5	-7.98E-5	-7.11E-5	-4.91E-5	-2.42E-5	-7.92E-6	0.00
38		0.00	-1.18E-4	-1.18E-4	-1.17E-4	-1.16E-4	-1.14E-4	-1.11E-4	-1.07E-4	-9.92E-5	-8.75E-5	-6.09E-5	-3.11E-5	-1.06E-5	0.00
39		0.00	-1.52E-4	-1.50E-4	-1.47E-4	-1.43E-4	-1.37E-4	-1.32E-4	-1.25E-4	-1.15E-4	-1.01E-4	-7.13E-5	-3.75E-5	-1.32E-5	0.00
40		0.00	-1.62E-4	-1.60E-4	-1.57E-4	-1.53E-4	-1.47E-4	-1.41E-4	-1.35E-4	-1.25E-4	-1.11E-4	-7.99E-5	-4.35E-5	-1.57E-5	0.00
41		0.00	-1.47E-4	-1.47E-4	-1.47E-4	-1.46E-4	-1.43E-4	-1.40E-4	-1.36E-4	-1.28E-4	-1.16E-4	-8.69E-5	-4.89E-5	-1.81E-5	0.00
42		0.00	-2.10E-4	-2.09E-4	-2.09E-4	-2.08E-4	-2.07E-4	-2.05E-4	-2.02E-4	-1.93E-4	-1.79E-4	-1.39E-4	-8.08E-5	-3.06E-5	0.00
43		0.00	-3.89E-4	-3.89E-4	-3.89E-4	-3.89E-4	-3.87E-4	-3.85E-4	-3.82E-4	-3.74E-4	-3.58E-4	-2.97E-4	-1.86E-4	-7.40E-5	0.00
44		0.00	-7.06E-4	-7.05E-4	-7.05E-4	-7.05E-4	-7.04E-4	-7.03E-4	-7.01E-4	-6.95E-4	-6.79E-4	-6.18E-4	-4.39E-4	-1.92E-4	0.00

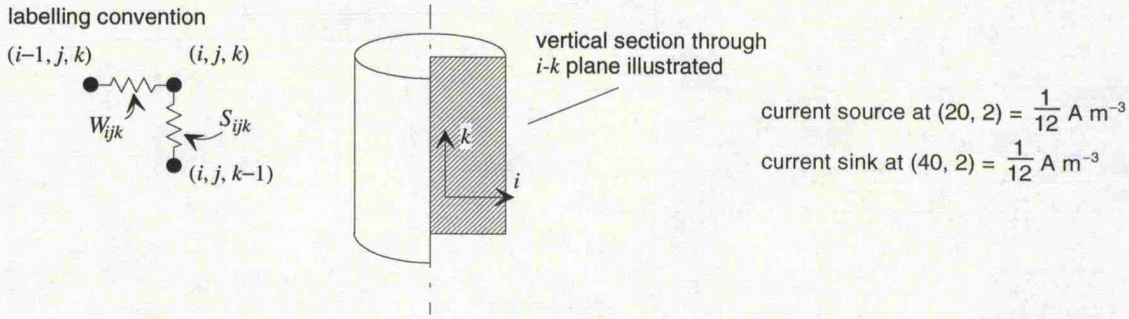

Figure 3.14 Current flow through branches in the FD grid.

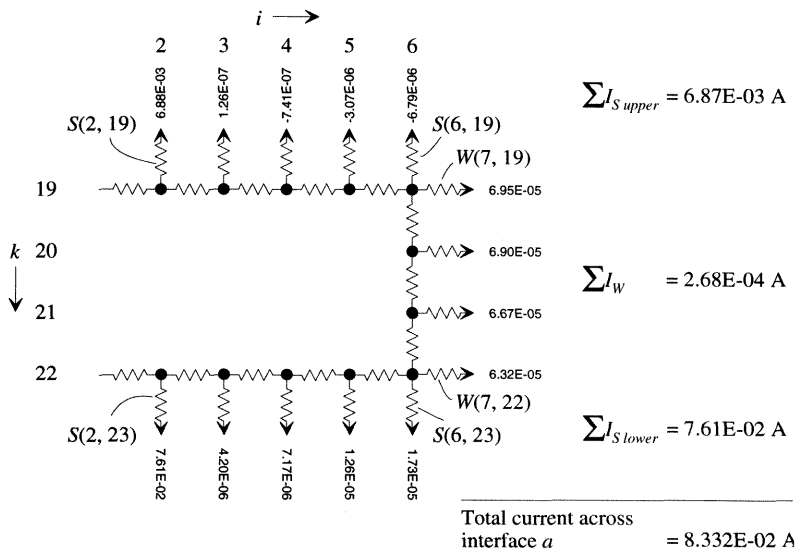

Figure 3.15 Calculating current flow across boundary *a*.

3.2.6 Anisotropy

The equivalence of the FD model representation of a three-dimensional resistivity distribution to an electrical resistor network (§3.2.1) provides a natural basis for the representation of electrical anisotropy.

A typical node in a rectangular grid will have resistors connecting it in each of the three, orthogonal coordinate directions. Resistors can therefore be used to represent the resistivity in each of the coordinate directions, as indicated in Figure 3.16. With suitable orientation of the grid axes, the resistor directions may coincide with the principal components of anisotropy, and these components can be substituted directly into the equations summarised in Section 3.2.3.

In cases where the FD grid is not aligned with the principal components of anisotropy, the principal components can be resolved to give their respective contributions to the resistivity in each of the grid coordinate directions. This procedure would be required by default when using cylindrical grids since the radial resistors are not parallel to any one direction.

Although the most general case of anisotropy (eq. 2.11, §2.2.3) cannot be simulated using this approach, cases where the electric field and current density are parallel can be catered for.

This includes many physical situations, including cases which commonly arise in geology where anisotropy can be approximately represented by a transverse and a longitudinal value (§2.1.2).

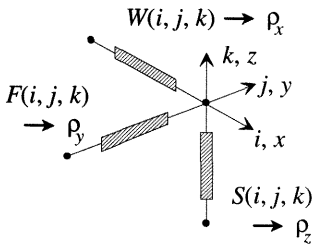

Figure 3.16 Using resistors to represent components of anisotropic resistivity.

3.2.7 Simulation of electrical arrays

The operation of electrical arrays (current electrodes) which introduce artificial electric currents into the ground can be simulated by locating a current source and sink in the model at the earth's surface or in the centre of a borehole. Potential electrodes are not catered for specifically since the electric potential is known everywhere in the model and every node can thus in principle be a voltage measurement location.

Current sources are located at nodes, whereas resistivity interfaces are located midway between nodes. Adjustments must be made to the model in order to accurately represent a source located at the earth's surface (rather than buried half the inter-nodal distance into the ground). Using the resistor network analogy, it is easily demonstrated that resistances in the horizontal plane should be doubled since the cells at the model earth's surface are representing half earth and half air and therefore conduct across only half the cell's surface area. Vertical resistances remain unaltered.

In order to simulate a survey involving different current source locations (i.e. to simulate tool motion in the case of a downhole model, or to cater for relocation of a surface array) it is necessary to run a series of related numerical models. This process is expedited by using the solution for a previous position as the start point for the present location. It is found that in order to simulate the motion of a fixed electrode array it is convenient to effectively move the resistivity distribution relative to the FD grid rather than vice-versa. This means that source and sink locations have a fixed position relative to the grid, which is preferable because

primary discretization effects are related to the grid spacing in the source/sink vicinity rather than the spacing around any resistivity variations (§3.2.5.1).

The running time of models is highly dependent on the model size and the number of positions run. Models run on a 486DX 66MHz PC with 8Mb of RAM can take anything from less than a minute for two-dimensional focused log simulations (§4.1) to more than twelve hours for a detailed electrical imaging run (Chap. 5).

3.2.8 Summary

This section has described in detail the implementation of the three-dimensional FD numerical method which is the basis of all the numerical models used in this work.

The finite-difference formulation of the problem (§3.2.1) is based on the direct solution of the generalised Poisson equation. As a result, numerical models are closely related to a physical representation of the conduction problem by a 3D network of resistances (§3.2.3) allowing secondary parameters such as current flow to be readily derived from the models, which solve for the electric potential field (the primary parameter).

An iterative scheme based on the successive line overrelaxation method is used to solve the simultaneous equations generated by the FD formulation (§3.2.2) which does not require a great deal of computer memory (but by the same token does not minimise solution time) allowing the modelling programs to run on powerful PC's or workstations.

The model is sufficiently flexible to cater for envisaged modelling applications. In principle, arbitrary resistivity distributions can be represented by using sufficiently fine grids; modifications are also made to incorporate cylindrical grids for downhole simulations (§3.2.4). Adequate boundary conditions may be specified at the outer surfaces of the FD grid (§3.2.1). Anisotropy can be incorporated (§3.2.6).

A study of theoretical controls on discretization errors and model accuracy (§3.2.5) is used to provide practical guidelines for grid definition. Coarsening of grids away from areas of interest can be used to model larger regions while remaining with in practical limits on the number of nodes. Testing shows accuracy to be good in regions of interest, for cases which can be compared with analytic solutions. Other practical aspects for the modelling of moving electrical arrays, both at the surface and downhole, have been outlined.

This chapter has reviewed the available solution methods for the three-dimensional electrical conduction problem. The FD method has been identified as a numerical approach which is capable of modelling both 3D current flow and the measurements made by resistivity electrode arrays tools in arbitrary resistivity distributions.

The following chapters (4 and 5) describe the application of models based on the FD method (as described in Section 3.2) to both surface and downhole measurements.

CHAPTER 4

Results: focused measurements

This chapter describes the application of the model described in Chapter 3 to two focused electrode arrays. Both measurements are actively focused, one using five electrodes at the earth's surface (§4.1) and the other using three electrodes downhole (§4.2).

In the first example ideas used in numerical models of focused measurements are applied to the generation of a novel field measurement which was tested in the field. A numerical model is developed to simulate this focused surface array and to aid in the interpretation of the field data.

The second example is a model of a focused borehole tool. Whilst the focusing principle is the same, the geometry of the problem is different, requiring a revised numerical model to be developed. In this example, a numerical model is developed to enable the geometric factor (a characteristic of the tool measurement) of a specific focused borehole tool (the Ocean Drilling Program High Temperature tool) to be calculated.

In addition to demonstrating applications of the numerical model, these simulations serve to develop and test the model towards more sophisticated downhole applications. Operational details of both arrays are known, enabling the systems to be closely simulated, providing a good testing environment.

The first part of this chapter introduces some common concepts of the active focusing technique used in both numerical models.

4.0 Introduction

The purpose of focused electrical measurements is to control the region in which current flows, and thus to constrain the region to which a measurements applies.

Focused electrical measurements are routinely made in borehole geophysics. Most electrical resistivity logging tools operate by measuring a resistance between two electrodes; this resistance is dependent upon the properties of the volume of material through which the electric current generated by the tool flows. The principal aim of focusing the current emitted by a tool is to constrain the shape and location of the volume of rock through which current flows, and therefore to constrain the region of measurement of the tool. This gives improved vertical resolution and readings more representative of specific beds, taken away from the invaded zone (Ellis, 1987).

Focusing is achieved in the downhole case by using extra focusing (or guard) electrodes. A typical electrode arrangement which uses this technique is illustrated in Figure 4.0.1. The magnitude of the focusing currents is varied so that the potential difference between them and the sensing electrode is zero. Their magnitudes depend on the current flow (and consequently the resistivity distribution) in the tool region.

In the borehole case, the unfocused electrode currents typically travel preferentially in the conductive borehole mud and also close to the borehole. The focused sensing currents are forced further into the formation rather than travelling directly up the borehole, therefore travelling through less borehole fluid and less of the invaded zone.

Focusing the measurement

Figure 4.0.2 illustrates a typical device with a central sensing current electrode $A0$ and two focusing electrodes $A1$ and $A2$. In order to enable active focusing in electrical measurement devices, a feedback system is employed to control the magnitude of the focusing currents; this is achieved by using the pairs of *potential electrodes* ($M1$, $M1'$) and ($M2$, $M2'$).

Different methods are used to focus electrical currents. In the case of the work reported in this thesis, focusing is achieved by making the potential difference across each of the potential electrode pairs zero—this implies that there is no current flow between adjacent potential electrodes and the sensing current from $A0$ is constrained to flow perpendicular to the tool

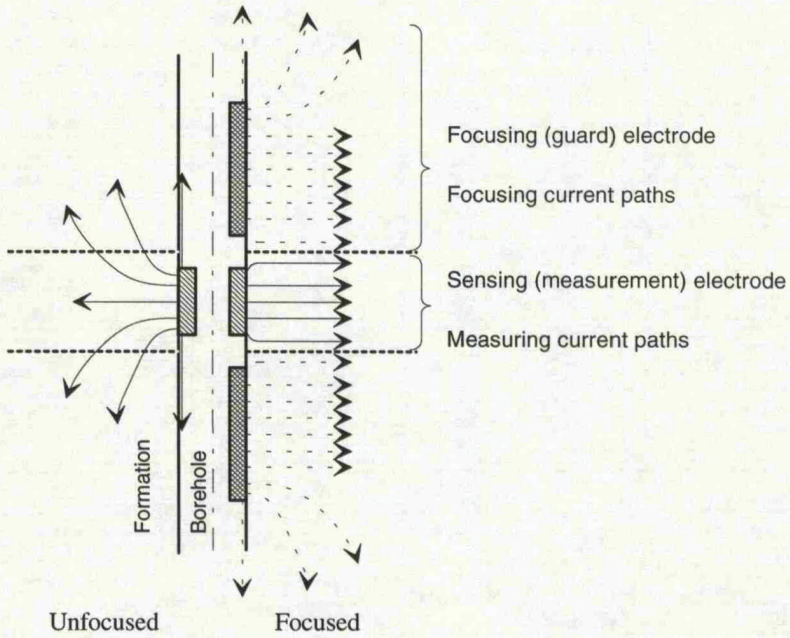

Figure 4.0.1 Focused versus unfocused electrode measurements.

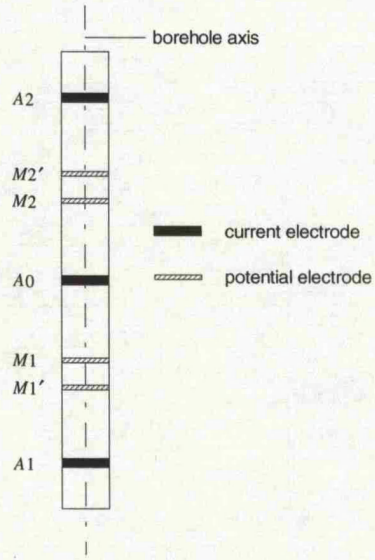

Figure 4.0.2 Current and potential electrodes used by focusing devices.

orientation (this idea is illustrated schematically in Figure 4.1.1, §4.1). The focused potentials of each electrode pair are *independent* of each other, allowing the measurement device to compensate for non-symmetrical resistivity distributions. Mathematically, the focusing conditions for the device illustrated in Figure 4.0.2 may be expressed as

$$V_{M1} = V_{M1'}, \text{ and}$$

$$V_{M2} = V_{M2'}.$$

There is no condition relating V_{M1} to V_{M2}.

There are critics of focused measurements, notably Roy (1982) who argues that such measurements are unnecessary. His assertion that any focused measurement can be constructed from a series of normal (single-electrode, unfocused) logs is correct—indeed it is the basis of both numerical models described in this Chapter, and also used to generate the focused field measurements described in Section 4.1. However, his interpretation of the measurement involves the use of an apparent resistivity factor which effectively defocuses the measurement (Jackson, 1976; 1981), and with this in mind it is not surprising that the focused measurements appear to be worthless.

The benefit of actively focused measurements in the field is their provision of a raw measurement which is much closer to the true formation values than equivalent unfocused readings; since their inception in the 50's (Doll, 1951) they have continued to be applied widely both in commercial and research fields. Numerical modelling of focused electrode arrays enhances the assessment and interpretation of such measurements.

4.1 Focused surface array

The work described in this section forms part of a project involving geophysical fieldwork carried out in Saarland, Germany. A novel resistivity technique involving a 'dual laterolog' focused surface array proposed by Jackson (1981) was implemented and tested in the field. The following sections describe the measurement method and interpretation of data acquired.

The focused field measurement is based on a numerical algorithm which is described in Section 4.1.2.2. This algorithm is also used by a numerical model developed to simulate the measurement.

As well as providing an opportunity to work with real field data, the focused surface array allows the testing of a numerical model in a simpler geometry than is required for modelling down-hole situations (i.e. rectangular cartesian coordinates rather than cylindrical polar coordinates). Numerical simulations enhance analysis and interpretation of the focused measurement data.

4.1.1 Outline of project

As part of a collaborative project between the BGS and Saarberg, the Saarland state coal company (which derives its funding jointly from the Saarland government and the German Federal government) fieldwork was carried out in Saarland, Germany in the summer of 1993 and 1994. The project itself was jointly funded by Saarberg and the CEC (Commission of European Communities—European Coal and Steel Community).

The project aimed to assess the relative merits of different geophysical techniques in mapping faults at the earth's surface, with a view to developing an optimum methodology for tracing fault lines. When mining works cut through fault planes, faults can often be reactivated resulting in slippage at the earth's surface, which in turn may cause undesirable structural damage.

Known fault intersections found in underground workings were extrapolated upwards to identify where faults might reach the surface, and on this basis a number of test sites were proposed for investigation, each approximately 100 m × 100 m.

A variety of geophysical techniques were employed to map each of the test sites, including low-frequency (VLF) and conventional (EM) electromagnetics, resistivity (including the BGS RESCAN system), seismics, and ground-penetrating radar.

The resistivity measurements used to create focused measurements were made with the BGS RESCAN resistivity measuring equipment. This is a computer-controlled multi-electrode resistivity measurement system (Meldrum et al., 1994; Jackson et al., 1989). In view of its lack of mobility and large number of measurements, it was envisaged that RESCAN would provide relatively high-resolution characterisation of the electrical properties of a specific location rather than being used as a prospecting tool. It was hoped that this would aid the electrical methods by providing a more detailed picture of the electrical properties along a fault and the surrounding area, and thus give an insight into any electrical characteristics associated with the faulting (or perhaps due other associated processes such as alteration, weathering or fluid-flow).

RESCAN is capable making four-electrode measurements, where one electrode introduces an artificially generated current into the earth, one electrode provides a current return, and the remaining pair of electrodes measure a potential difference. Electrodes in a grid may be addressed independently allowing a variety of different array styles to be employed. The work described here is concerned specifically with the development and testing of the focused surface array resistivity measurement.

The 'focused surface array' forms part of the suite of different survey styles carried out by the RESCAN d.c. earth resistivity measurement system. It is essentially a pole-pole type measurement: a single electrode injects measurement current creating a voltage field which is measured using a single potential electrode; both the current return and the potential reference electrodes are located some distance away from the survey area, effectively at infinity. The focused array proposed by Jackson (1981) requires four independently controlled focusing currents in addition to the measurement current that are used to constrain the volume of earth through which the measurement current flows. The RESCAN system cannot simultaneously emit multiple currents but the focused measurement may be reconstructed from a set of conventional pole-pole measurements (see §4.1.2.2). This is the principal difference between the focused measurement and the other survey styles used by RESCAN.

4.1.2 The focused measurement

This section describes some theoretical aspects of the focused measurement.

4.1.2.1 Measurement principles

The focused surface array makes resistivity measurements using similar principles to those of the laterolog and microlaterolog focused electric borehole tools (Doll, 1951; 1953).

The principles used in making focused downhole logging measurements (§4.0) may be developed for surface measurements. Figure 4.1.1 illustrates the operation of a typical focused surface array schematically. The central electrode is the *sensing electrode*, the current from which is used to make resistivity measurements; this is surrounded by *focusing electrodes* which emit current with the intention of constraining the region of earth through which the measurement (sensing) current flows.

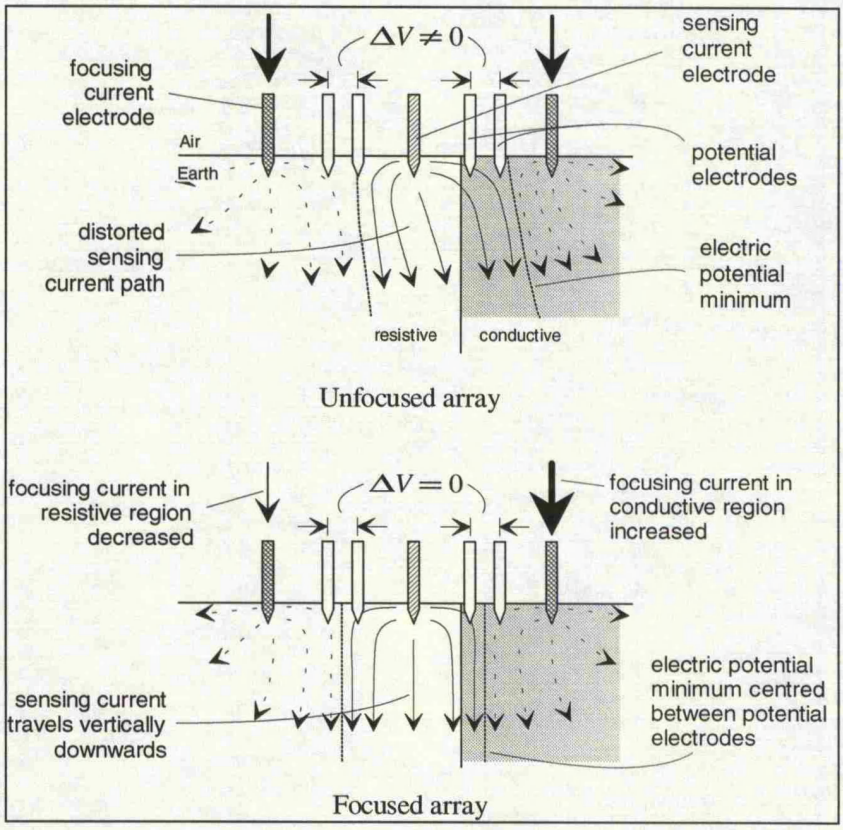

Figure 4.1.1 Focusing currents over a conductive/resistive boundary (schematic).

At the surface of the earth, the maximum focusing effect would be achieved by using a ring-shaped electrode surrounding the measurement electrode, as is the case with the

microlaterolog. However, Jackson (1981) shows that four orthogonal electrodes in a cross shape around the measurement electrode can still achieve a significant focusing effect. Such an arrangement has an additional benefit since the focusing currents may be adjusted independently of each other, allowing compensation for lateral inhomogeneities in the electrical properties of the earth (as illustrated in the lower part of Figure 4.1.1).

An implementation of a focused surface array proposed by Jackson (1981), similar in principle to that of the Laterolog 7 borehole tool (Doll, 1951), but using four focusing electrodes, is illustrated in Figure 4.1.2. In this arrangement, P is the *measurement* current electrode, while N, S, E and W are the *focusing* current electrodes. The current electrodes simultaneously inject current into the ground (which returns to a common electrode located effectively at infinity), and the magnitudes of the focusing currents are adjusted to achieve focusing. Active focusing of the array is achieved by monitoring the measurements made by four pairs of potential electrodes: N_1 and N_2, S_1 and S_2, E_1 and E_2 and W_1 and W_2.

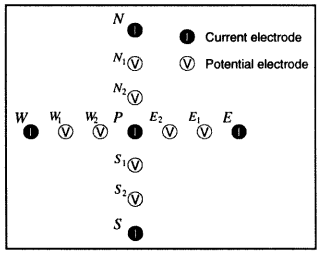

Figure 4.1.2 Electrode configuration (schematic) for a 'double laterolog' focused array proposed by Jackson (1981).

Focusing the array

The focusing conditions outlined in Section 4.0 for the array shown in Figure 4.1.2 are:

$$V_{N_1} = V_{N_2},\ V_{S_1} = V_{S_2},\ V_{E_1} = V_{E_2} \text{ and } V_{W_1} = V_{W_2}. \qquad (4.1.1)$$

4.1.2.2 Synthetic focusing

Focused electric borehole tools operate by continually adjusting the magnitude of the focusing currents using electronic feedback loops to ensure that the tool remains correctly focused. These principles have been applied to surface arrays (Apparao et al., 1969; Apparao and Roy, 1971) but are not used extensively in surface geophysics.

The RESCAN measurement system can only allow current to flow out of a single electrode at any one time. In order to produce a focused measurement, a hybrid approach using physical measurements in conjunction with numerical processing techniques is taken, using ideas originally developed for numerical simulations of focused borehole tools. In such models, focusing current magnitudes are determined theoretically rather than by simulating the electronic balancing process, which is less expensive in terms of time.

The principles involved in simulating focused electric *borehole* tools has been described in detail by Gianzero (1981) and Moran and Chemali (1985). Jackson (1981) investigates the response of various focused *surface arrays*, including a combination of two surface laterologs at 90° to each other which is equivalent to the focused surface array being described in the present work. Parra and Owen (1990) develop a methodology to create focused surface measurements from readings taken with a single line of current electrodes. Theoretical approaches involve the combination of electric potentials, computed for individual current electrodes, in a weighted sum to derive the potential that would exist if all current electrodes were simultaneously emitting current (superposition of electric potentials is discussed in Section 3.1.2.1). The relative weighting of the contributions from individual electrodes are calculated so that focusing conditions are satisfied.

The approach of Moran and Chemali (1985), which uses the concept of *transfer impedances* in conjunction with the principle of superposition, is developed in §D.1 to derive an expression for a focused surface measurement created from individual unfocused measurements made using a surface electrode array. In equation (D.6), the superposed focused electric potential at a potential electrode B, Vf_B, is shown to be given by an equation of the form

$$Vf_B = \left(Z_{PB} + Z_{NB}Bf_N + Z_{SB}Bf_S + Z_{EB}Bf_E + Z_{WB}Bf_W\right)I_P, \qquad (4.1.2)$$

where I_P is current emitted from the central, sensing electrode and terms of the form Z_{AB} are transfer impedances determined by measuring the electric potential at electrode B when unit current is emitted from electrode A. The terms of the form Bf_A are balance factors pertaining to current electrode A; these express the relative magnitude of each of the four focusing currents required to focus the array, and are determined by solving a set of simultaneous equations (as detailed in §D.1) involving the transfer impedances.

The theoretical investigation described by Parra and Owen (1990) is a similar synthetic focusing technique, designed with a view to increasing the depth of investigation of pole-dipole measurements in order to improve location of sub-surface cavities. Their system involves using multiple focusing electrodes along a single line only, and focusing current magnitudes are symmetrical about a central measurement electrode. Whilst such an arrangement would be useful in detecting anomalies in an otherwise homogeneous medium, it is unsuitable for the (three dimensional) situations encountered in the field areas described here, where non-symmetrical focusing is required to counteract the effect of lateral inhomogeneities. Hence for this work, an electrode configuration similar to that illustrated in Figure 4.1.2 has been used.

4.1.2.3 Apparent resistivity

In Section 2.3.2 the general expression for apparent resistivity, ρ_a, is given as (eq. 2.13):

$$\rho_a = \mathrm{G}(\mathbf{r})\frac{\Delta V}{I}. \tag{4.1.3}$$

In the case of a pole-pole measurement, the p.d. ΔV is measured between a near electrode and a distant reference electrode where the electric field is effectively zero. The measured p.d. therefore closely approximates the absolute potential V. In this case, equation (2.14) for the geometric factor, G, can be written as:

$$\frac{I}{V_h}\rho_h = \mathrm{G}(\mathbf{r}), \tag{4.1.4}$$

where V_h is the electric potential in a homogeneous half-space of resistivity ρ_h. For the focused array, V_h, may be determined analytically. For a single current source, the electric potential V_h at a distance r from the source is given by (eq. B.7, §B.2):

$$V_h = \frac{\rho_h I}{2\pi r}.$$

In the case of the focused array, there are five current sources: N, S, E, W and P, emitting currents I_N, I_S, I_E, I_W, and I_P respectively, so the 'homogeneous' electric potential is found by using superposition (§3.1.2.1), i.e. summing the contribution from each source:

$$V_h = \frac{\rho_h I_N}{2\pi r_N} + \frac{\rho_h I_S}{2\pi r_S} + \frac{\rho_h I_E}{2\pi r_E} + \frac{\rho_h I_W}{2\pi r_W} + \frac{\rho_h I_P}{2\pi r_P}, \tag{4.1.5}$$

where r_N, r_S, r_E, r_W and r_P are the distances from the respective current sources N, S, E, W and P to the point of interest. The magnitudes of the currents I_N, I_S, I_E and I_W are chosen so that they focus the array (Section 4.1.2.1) for the homogeneous case. In the case of a symmetrical array, they will be some constant proportion Bf of the sensing current I_P, i.e.

$$I_N = I_S = I_E = I_W = Bf \cdot I_P. \tag{4.1.6}$$

Substituting equations (4.1.6) and (4.1.5) into (4.1.4), we arrive at

$$G = \frac{2\pi}{I_P \rho_h \left(\frac{Bf}{r_N} + \frac{Bf}{r_S} + \frac{Bf}{r_E} + \frac{Bf}{r_W} + \frac{1}{r_P} \right)} I_P \rho_h, \tag{4.1.7}$$

and thus substituting equation (4.1.7) in equation (4.1.3), we obtain an expression for the apparent resistivity of a focused array:

$$\rho_a = \frac{V}{I_P} \cdot \frac{2\pi}{\left(Bf \left(\frac{1}{r_N} + \frac{1}{r_S} + \frac{1}{r_E} + \frac{1}{r_W} \right) + \frac{1}{r_P} \right)}. \tag{4.1.8}$$

where V [V] is the electric potential at the point of interest, I_P [A] is the measurement current magnitude, r_N, r_S, r_E, r_W and r_P [m] are the distances from the respective current sources N, S, E, W and P to the point of interest, and Bf is an analytically determined *balance factor* which is the relative proportion of the focusing currents to the measurement current required to balance the focused array *for a homogeneous half-space*. [The quantity Bf is found by solving the set of simultaneous equations (D.4) using transfer impedances derived by substituting equation (B.7) (the electric potential in a homogeneous halfspace) into equation (D.1)]. The geometric factor, G, is a function of position, array geometry, and I_P only, and is not (as Roy, 1982 assumed) related to the magnitude of the balance currents.

It is noted that the measurement current flow is constrained by the surrounding balance currents, so the apparent resistivity should be indicative of the properties of a column of ground directly below the central sensing electrode of the focusing star configuration. This property of the apparent resistivity is used to define the objectives of the focused measurement outlined in Section 4.1.2.5 below.

4.1.2.4 Summary: focused measurement technique

Using the ideas described in sections 4.1.2.2 and 4.1.2.3 above, it can be seen that a synthetically focused measurement may be 'reconstructed' from sets of independent RESCAN measurements, made for the measurement electrode and the four focusing electrodes, by numerically balancing and superposing the readings (Figure 4.1.3). For each of the five current positions, the electric potential is measured at the eight potential electrodes, resulting in 40 measurements which are then combined to produce a focused measurement.

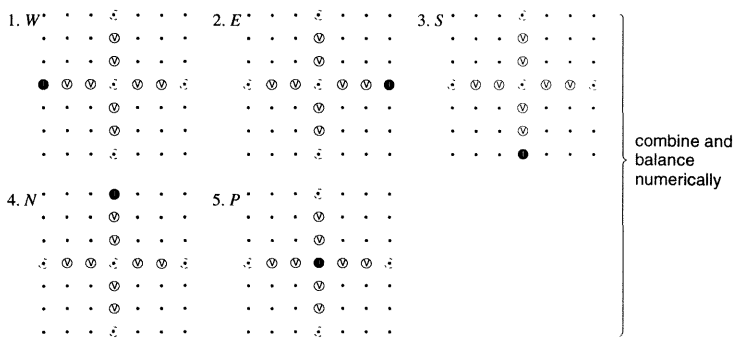

Figure 4.1.3 Superposition of RESCAN measurements.

In summary, a focused measurement is obtained as follows (refer to Figure 4.1.2 which illustrates the electrode labelling conventions, and §D.1 which details the focusing equations):

1. With the current source located at N (and current sink at infinity), measure the electric potential at the eight potential electrodes (N_1, N_2, S_1, S_2, E_1, E_2, W_1, and W_2). Calculate the corresponding transfer impedances Z_{NN_1}, Z_{NN_2}, Z_{NS_1}, Z_{NS_2}, Z_{NE_1}, Z_{NE_2}, Z_{NW_1} and Z_{NW_2} using equation (D.1);
2. Repeat (1) for current sources located at S, E, W and P;
3. Substitute the transfer impedance values obtained into the set of simultaneous equations (D.4) and solve for I_N, I_S, I_E and I_W using e.g. Gaussian elimination;
4. Derive the focused potential distribution for the eight potential electrodes using equation set (D.6);
5. Use the focused electric potentials to give eight focused apparent resistivity measurements, one for each potential electrode, using equation (4.1.8).

4.1.2.5 Measurement objectives

In common with other electrical measurements, the focused measurement will respond to changes in resistivity of the earth. Contrasts in the resistivity of shale and sandstone layers could be readily identified, allowing a fault line to be located where these two rock types lie on either side of the fault.

There are two envisaged advantages of using a focused measurement, which stem from the fact that the region of measurement is constrained by the focusing:

1. enhanced depth of investigation in comparison with equivalent unfocused measurements—allowing, for example, penetration of overburden to investigate structure deeper in the earth;
2. accurate lateral placement of conductive/resistive boundaries. Conventional measurements are often distorted by preferential current flow in conductive zones, since standard methods (before inversion) do not take account of such effects when attributing an apparent resistivity measurement to a region of earth. The focused measurement can reduce distortion effects at the measurement (rather than interpretation) stage, by forcing the measurement region to remain below the measurement electrode, as illustrated in Figure 4.1.1.

4.1.3 Fieldwork and data acquisition

This section gives an overview of the initial results of the fieldwork carried out in Saarland, in addition to describing aspects of data acquisition and processing. The general approach to interpretation of the focused measurement is also outlined. This section precedes a more detailed description of the numerical model used to aid interpretation, and detailed descriptions of the results and interpretation of data from two specific survey areas that have been used as case studies.

4.1.3.1 Survey areas investigated

The focused array was run in addition to other measurement styles on the RESCAN electrode grid. The focused measurement was not carried out at every site where RESCAN was deployed, but was made at a total of five sites, as detailed in Table 4.1.1.

Year	Site name	Notes
1993	1.2	Three adjoining grids, labelled 1.2a, 1.2b and 1.2c. Lines 4, 5, 6, 7, and 8 on 1.2a Lines 5, 6, and 7 on 1.2b Line 6 on 1.2c
	1.4	Line 6 only
	2.1	Lines 4, 5, 6, 7, and 8.
1994	3.1	Line 6 only
	3.2	Two adjoining grids, labelled 3.2a and 3.2b Line 6 only on both.

Table 4.1.1 Sites where focused measurements were carried out

The electrode grid was a rectangular array of 20 × 11 electrodes which were spaced at 1 m intervals at all sites. A focusing star with a 6 m span was used, allowing a total of 14 measurement positions along the longer axis of the grid and 5 positions in the perpendicular direction (Figure 4.1.4).

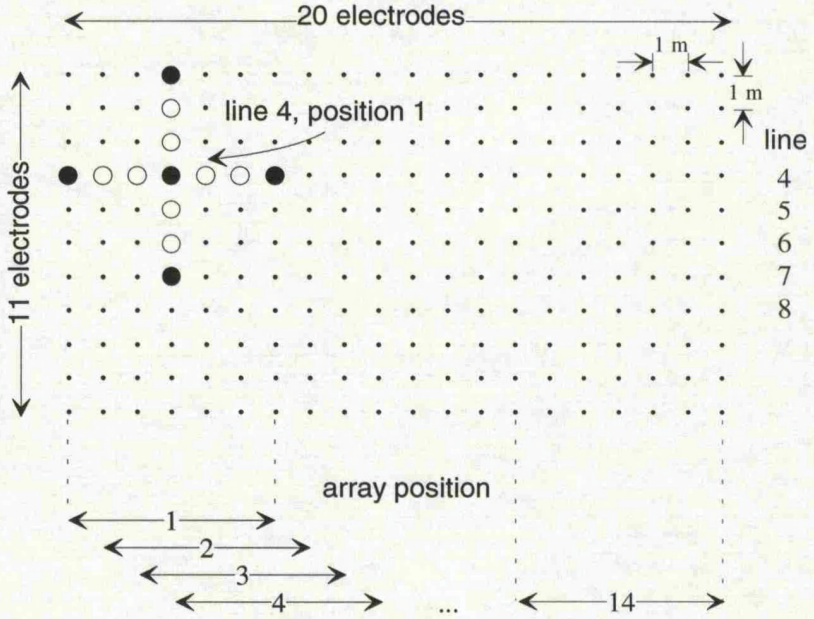

Figure 4.1.4 RESCAN electrode grid and focused array positions.

In the field, surveys were arranged as a series of 14 measurements along the long axis of the electrode array. As indicated in Table (4.1.1), at some sites (e.g. Site 2.1) a series of parallel surveys were conducted, enabling a two-dimensional array of focused measurements to be built up. At other locations only one line was run due to time restrictions. At sites 1.2 and 3.2, wide anomalies were indicated by other survey techniques, and measurements were

made on overlapping adjacent grids in order to try to cover a wider lateral range (Figure 4.1.5).

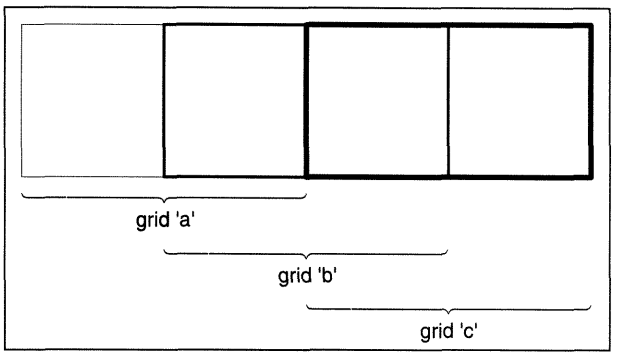

Figure 4.1.5 Adjacent grids.

4.1.3.2 Measurement data

The raw data provided by the RESCAN measurement equipment consist of a series of resistance measurements which are then given coordinates using data in a position file. The resistance measurements are converted to focused apparent resistivities using the technique summarised in Section 4.1.2.4. The balance factors required to satisfy the focusing conditions are also output for reference. For comparison, defocused and conventional pole-pole apparent resistivity values have also been calculated from the same data sets.

The focused apparent resistivity (§4.1.2.3) is calculated using

$$\rho_a = \frac{V}{I_P} \cdot \frac{2\pi}{\left(Bf\left(\frac{1}{r_N} + \frac{1}{r_S} + \frac{1}{r_E} + \frac{1}{r_W} \right) + \frac{1}{r_P} \right)}, \tag{4.1.8}$$

where V is a superposed electric potential calculated by combining the voltages due to current sources *adjusted in magnitude to satisfy the focusing conditions*. The defocused apparent resistivity is calculated with the formula

$$\rho_a = \frac{V_a}{I_P} \cdot \frac{2\pi}{\left(Bf\left(\frac{1}{r_N} + \frac{1}{r_S} + \frac{1}{r_E} + \frac{1}{r_W} \right) + \frac{1}{r_P} \right)}, \tag{4.1.14}$$

where V_a is the superposed electric potential calculated using current sources of fixed magnitude *equal* to those required for a homogeneous half-space (i.e. focusing conditions will *not* in general be satisfied, except in the case of a uniform, homogeneous earth). The pole-pole apparent resistivity is calculated using

$$\rho_a = \frac{V_P}{I_P} \cdot 2\pi r_P, \tag{4.1.15}$$

where V_P is the electric potential due to the measurement electrode only (i.e. the focusing electrodes are effectively inactive).

4.1.3.3 Focused apparent resistivity traverses

The results of focused apparent resistivity traverses are presented in Appendix E on a site-by-site basis. On each page, focused, defocused and pole-pole data are plotted for a single line. For each apparent resistivity type, four apparent resistivity curves (*W*, *E*, *S*, and *N*) have been superimposed, corresponding to calculations using the potential on electrodes W_2, E_2, S_2 and N_2 respectively. The vertical scale (apparent resistivity) is logarithmic. The horizontal scale refers to the relative position of the focusing star in the electrode array (as illustrated in Figure 4.1.4). This can be related to site coordinates by referring to the relevant field reports (Greenwood et al., 1993; Meldrum and Williams, 1995).

In the lower half of each page, the calculated balance factors required for focusing are plotted. A plot of the normalised balance factors for the orthogonal current electrode pairs *W*-*E* and *N*-*S* is also included to aid analysis of balance variation. The normalised balance factor for the *W*-electrode, Bf_W' is calculated using

$$Bf_W' = \left| \log\left(\frac{Bf_W}{Bf_h} \right) \right|,$$

where Bf_W is the (non-normalised) *W*-balance factor and Bf_h is the analytically calculated balance factor for a homogeneous medium. Similarly for the *E*, *S* and *N* balance factors. The normalised balance factors express the relative increase or decrease of a balance current relative to the homogeneous balance factor, Bf_h. A normalised balance factor of 2 would correspond to a reduction to 50% or an increase to 200% of Bf_h.

It should be noted that no compensation has been made in the plots in Appendix E for occasional erroneous readings which manifest themselves as sudden jumps in the apparent resistivity curves (e.g. Site 1.2a, Line 4 position 4 m, or Site 3.2a position 5 m).

4.1.3.4 Interpretation methodology

Interpretation of the electrical properties in the region of the electrode array initially centres on the focused apparent resistivity traverses; however important information can also be gained by inspecting the magnitude of the focusing currents, or in the case of the synthetically focused array, the calculated balance factors required to focus the array.

Numerical models of the response of the focused array to specific simplified geological models have been used to provide a quantitative guide to the response to key situations. It is noted that as a further step, models may be 'fine-tuned' to simulate specific field situations in order to confirm any inferences made, but the models considered in this work have not been extended beyond a low level of complexity.

Apparent resistivity data

The primary data source is the focused apparent resistivity traverse. Changes in apparent resistivity can be used to infer changes in the electrical properties of the earth which can be caused by faulting (e.g. where two rock types of differing resistivity lie alongside each other). More detailed information may be derived by analysis of the relationship between the focused, de-focused and pole-pole traverses (although in practice the de-focused measurement was not found to be of much assistance in data interpretation). The focused measurement is taken to be indicative of the resistivity of a cylindrical region directly below the central, sensing electrode (Section 4.1.2.5), due to the constraining effect of the balance currents. The focused current may also penetrate further into the ground than a conventional unfocused measurement, giving an indication of electrical resistivity properties deeper into the earth.

Focusing balance factors

The variation of the focusing currents (calculated balance factors) is often more sensitive to changes in resistivity than the focused apparent resistivity measurement itself (see §4.1.5 and §4.1.6). When one side of the array is in a conductive medium, current will tend to flow preferentially into that medium, and the focusing current on the conductive side will increase to counteract this effect. Conversely, the focusing current required on the resistive side is

reduced since the sensing current already has a tendency to flow away from that region. In this way, lateral inhomogeneities such as faults are expected to disturb the balance currents as was illustrated schematically in Figure 4.1.1.

Compensation for bad readings

Many experimental precautions are taken to improve the accuracy of resistance readings made with the RESCAN equipment (Jackson et al., 1989; Meldrum et al., 1994). Multiple readings are taken for a given measurement position, and the waveform of the current being passed can also be monitored. An electronic filter is available if large amplitude 50 Hz frequency electrical noise is found to be present at any site. In the Saarland fieldwork, an initial 'ground truth' survey was carried out at each site to ensure good electrical contact between each of the electrodes and the earth. This and other experimental procedures are detailed by Meldrum and Williams (1995).

These built in precautions in the RESCAN measurement procedure ensured that the majority of resistance readings were of a good quality. However, some more subtle problems came to light only after processing was carried out. This caused some spurious readings in the focused apparent resistivity data.

Each focused apparent resistivity is arrived at using 40 resistance measurements. On some lines, a handful of readings were evidently inaccurate. An attempt was made to smooth these erroneous readings by comparison with the measurements taken in their immediate surroundings. Rather than adjust processed apparent resistivity values, raw RESCAN resistance data were manipulated, with the aim of allowing error-free readings in any set of 40 measurements to preserve any natural trends in the data.

4.1.4 Numerical modelling

This section describes the development of the three-dimensional finite difference model to analyse both apparent resistivity profiles and variations in balance current magnitudes in order to aid and enhance interpretation.

The fundamental aspects of a model suitable for simulating d.c. electrical problems using the finite difference method were described in Chapter 3. The next step in generating a model for a specific application is to define a suitable grid and to choose appropriate boundary

conditions at the edges of this grid. Once this has been achieved, the grid is used as a framework on which to set up a physical resistivity model.

4.1.4.1 Finite difference grid

As discussed in Section 3.2.5, the choice of the extent and resolution of a finite difference grid is compromised by requirements for accuracy and speed. In the case of the focused array, the most crucial region of the model is in the immediate vicinity of the current injection point, since the electric potentials calculated here are used to generate the focused measurement. Unfortunately, this is also the most difficult area to model accurately because the electric potential varies most rapidly around a current source or sink.

The region to be modelled in the case of a surface measurement is a semi-infinite half-space, since the earth may be considered to extend to infinity laterally and with depth (at the measurement scales considered here), and is bounded above by air which is electrically insulating. In practice, the electric potential approaches zero a finite distance away from the current source, and the model grid need only extend as far as where the voltage and its derivative (the potential gradient) are to all intents and purposes zero. This is checked by inspecting the values of voltage at the boundary. As an additional check, the difference between applying conductive (Dirichlet) or resistive (Neumann) boundaries should be minimal in the region of interest.

By following the guidelines outlined above, a rectangular mesh was used to represent a 160 m × 80 m × 80 m region of earth, with mesh spacing (and therefore model resolution) down to 0.5 m in the region of the focused array measurement electrodes (Figure 4.1.6). Away from the source region, the grid is expanded since the potential gradient changes much less rapidly between nodes. It was not found to be necessary to place as large a number of nodes at the sink location as at the source [verified by testing of the model (§4.1.4.3)].

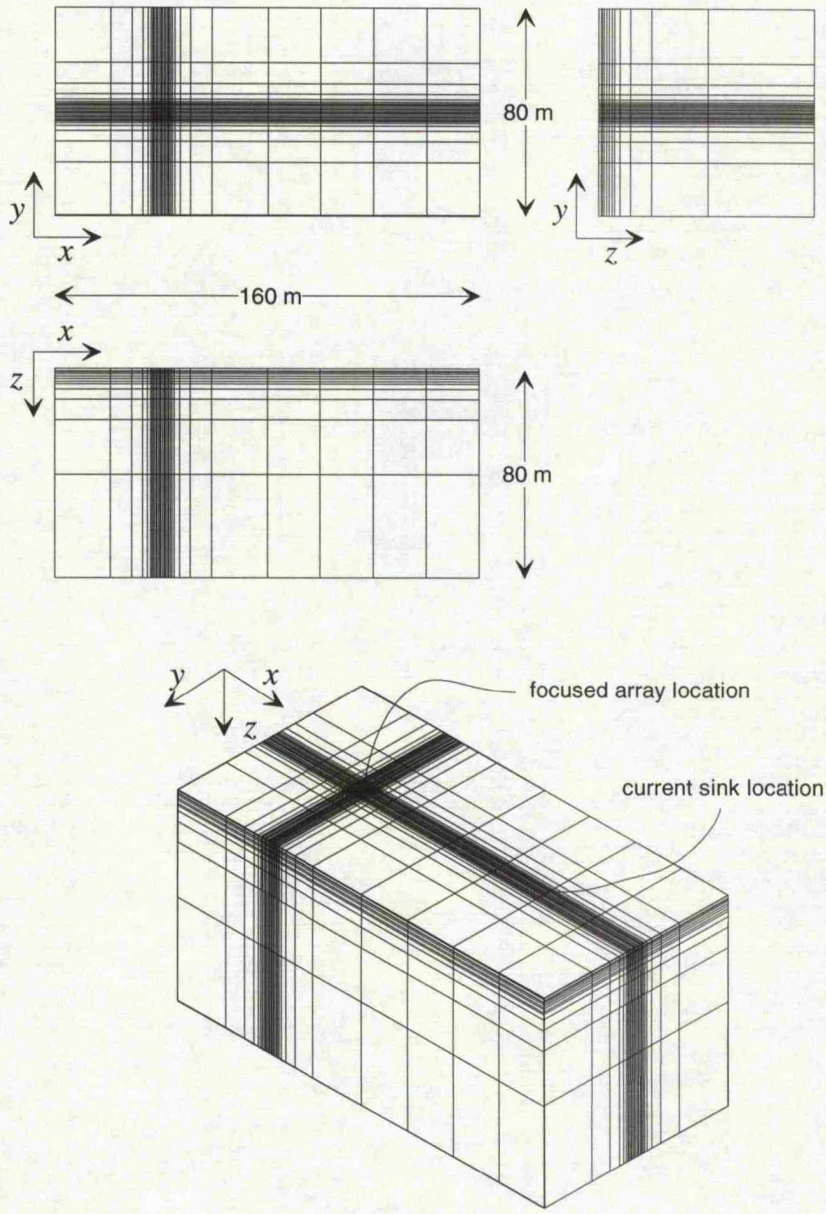

Figure 4.1.6 Model grid used in simulations of the focused surface array.

4.1.4.2 Boundary conditions

The model grid was chosen to extend sufficiently away from the source and sink to prevent boundary conditions from greatly affecting the numerical solution. In practice, this meant ensuring that the electric potential and potential gradient at the boundaries are small. Both conductive (Dirichlet) and resistive (Neumann) outer boundaries were tested (the results are not reported here). The solutions for both methods were similar, and satisfactorily accurate (§4.1.4.3). For these models, conductive boundaries were preferred as they give slightly more accurate and faster converging solutions in the cases tested.

4.1.4.3 Testing of the model

To demonstrate the accuracy of the model, the finite difference solution was compared with theoretical results for a selection of simplified situations where an analytic solution exists for comparison. This is described in detail in Chapter 3 (§3.2.5.2).

In the case of the focused array, the most crucial region of the model is the immediate vicinity of the current injection point, since the electric potentials calculated here are used to generate the focused measurement. This is also the most difficult area to model accurately because the electric potential varies most rapidly around a current source or sink.

For the three cases tested (a homogeneous, isotropic earth; an isotropic earth with a single horizontal layer; and an isotropic earth with a single vertical interface), the percentage difference between analytic and numerical solutions at the locations of the eight simulated potential electrodes is found to be in the region of 2–2.5%.

The model is considered to offer good accuracy in the region of most interest, for the cases tested. Whilst this is a far from rigorous test, it does at least provides a basis for assuming the model will provide a reasonable approximation for more complex situations. It is noted that accuracy could in principle be increased to any level desired by expanding the boundaries of the mesh and including more nodes in the region of the source and the sink, but this would be at the expense of increased computation times.

4.1.4.4 Simulated focused measurements

The numerical model works on a similar principle to the method of focusing described in Section 4.1.2.2 above. For a given resistivity model, the electric potential due to a single current source (with the sink located effectively at infinity) is calculated. This process is repeated five times for each of the source locations in the focusing star; the five calculated electric potentials are then combined in a weighted sum so that the focusing conditions are satisfied. The combined electric potential may then be used to derive a focused apparent resistivity.

The modelled electric potential is used to create data files with an identical format to the measurement file generated by RESCAN in the field. This allows the similarity between real and modelled focused measurements to be exploited since the modelled focused apparent

resistivity can be generated using the same program code as that used for the field data processing.

Typical models simulated surveys where the focused array is moved along an 8 m line (details of simulating tool motion are given in §3.2.7). The grid employed (§4.1.4.1) allowed steps of 0.5 m to be simulated (compared with 1 m in the field, since this was the fixed electrode spacing used in all the surveys concerned with focused measurements).

4.1.5 Case study: Site 2.1

4.1.5.1 Apparent resistivity traverses

Focused measurements were made on lines 4, 5, 6, 7 and 8 at Site 2.1. All the traverses exhibit a trend in apparent resistivity (ρ_a) from a lower value of around 60 Ω-m at the western end of the grid to 300 Ω-m at the opposite side, in agreement with data from other electrical surveys. Subsequent trenching at this site has indicated that the lower resistivity region is shale, whilst more resistive sandstone lies at the eastern end of the array.

Taking Line 7 as an example (Figure 4.1.7), the focused array shows a steep increase in ρ_a values between 3 and 6 m, whilst the increase in ρ_a values for the pole-pole measurements is not so pronounced

4.1.5.2 Focusing balance factors

Again, taking Line 7 as an example (Figure 4.1.8), the *W-E* balance factors exhibit the largest variation, indicating that the principle variation in electrical properties is parallel to this direction. The most notable feature is a drop in the *E* value around 3 m followed by a rise in the *W* value at 6 m. The normalised *W-E* values (Figure 4.1.9) indicate that the anomaly is symmetrical and centred about 4.5 m. The inference here is that moving from left to right, the *E* factor drops as it encounters resistive material (which the sensing current tends to naturally avoid) and the *W* factor rises once the array is centred over a more resistive zone (since the sensing current must be prevented from flowing preferentially back into the conductive zone). This is confirmed by numerical models.

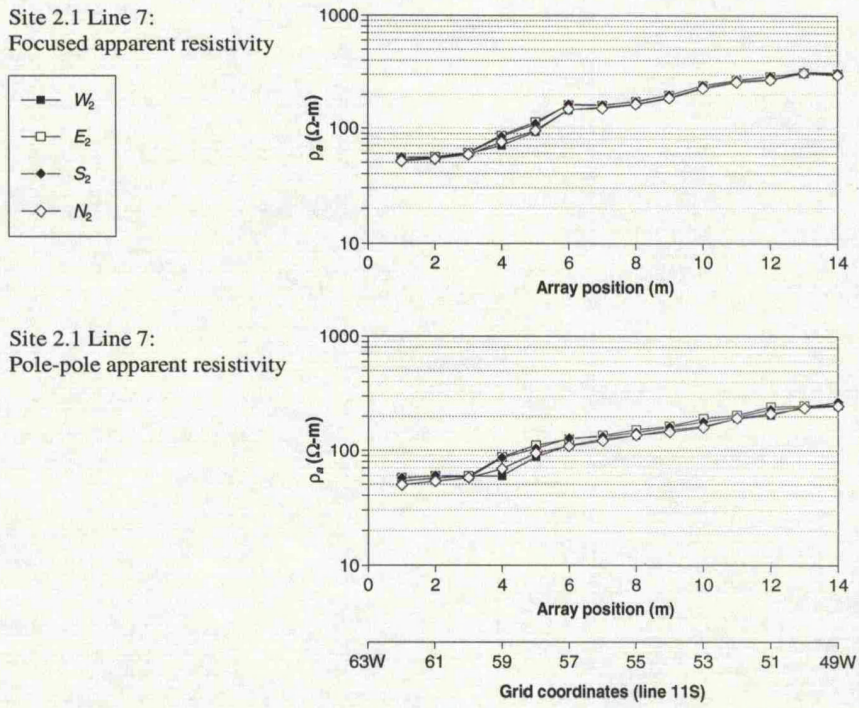

Figure 4.1.7 Site 2.1, Line 7: Apparent resistivity traverses.

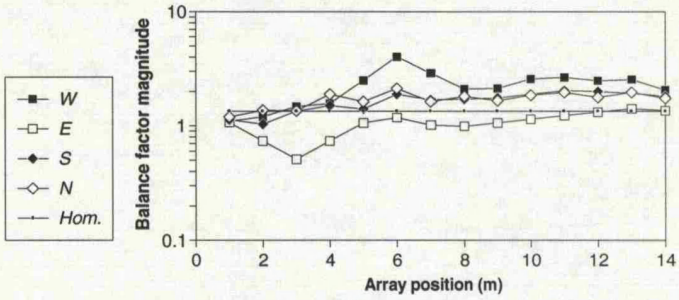

Figure 4.1.8 Site 2.1, Line 7: Focusing balance factors.

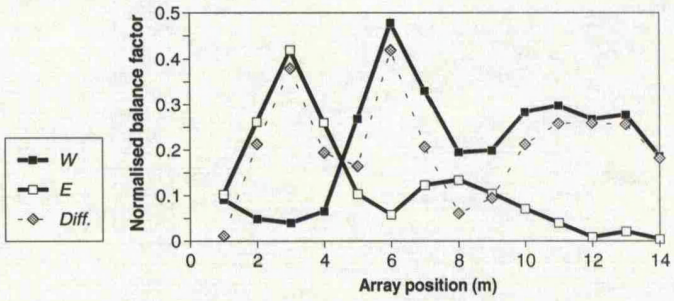

Figure 4.1.9 Site 2.1, Line 7: Normalised *W-E* balance factors.

4.1.5.3 Numerical modelling

Apparent resistivity traverses for a numerical model of a simple earth consisting of two regions of resistivity 50 Ω-m and 300 Ω-m, separated by a vertical, planar interface (Figure 4.1.10) are presented in Figure 4.1.11.

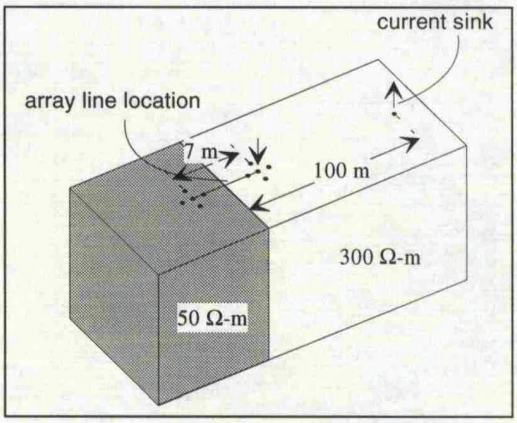

Figure 4.1.10 Idealised model of a vertical interface.

In addition to the four apparent resistivity (ρ_a) curves the model earth resistivity has also been superimposed for comparison. To reflect the grid spacing and the fact that parameters are interpolated between nodes, the model resistivity is not vertical, but varies steeply between adjacent nodes located at –0.25 and +0.25 m. The simulated focused array was modelled traversing a span of 7 m, with measurements being taken every 0.5 m.

Comparison of the model data (Figure 4.1.11) with the field data (Figure 4.1.7) (especially between array positions 2–8 m) reveals a similar trend in focused, de-focused and pole-pole ρ_a traverses, although the model values are generally too high. Considerable weight is added to the plausibility of the model when the simulated focusing current data (Figures 4.1.12 and 4.1.13) are compared with the corresponding field data (Figures 4.1.8 and 4.1.9). It is noted that although the apparent resistivity traverses are asymmetric about the vertical interface, the focusing current data is close to being symmetrical. The asymmetry of the ρ_a traverses is therefore considered to be inherent in the measurement and not caused by, say, the approximation of the vertical contact by an interpolated (near-vertical) slope.

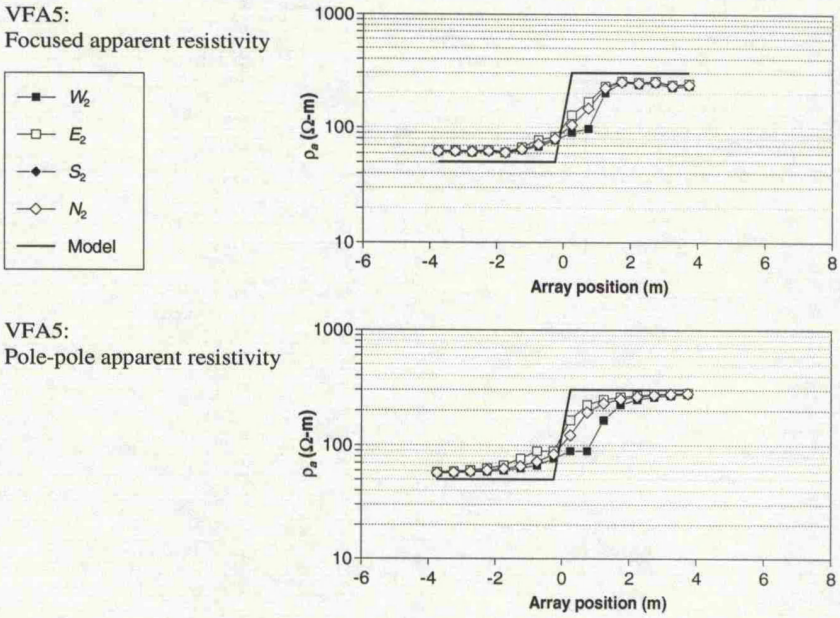

Figure 4.1.11 Vertical interface model results: Apparent resistivity traverses.

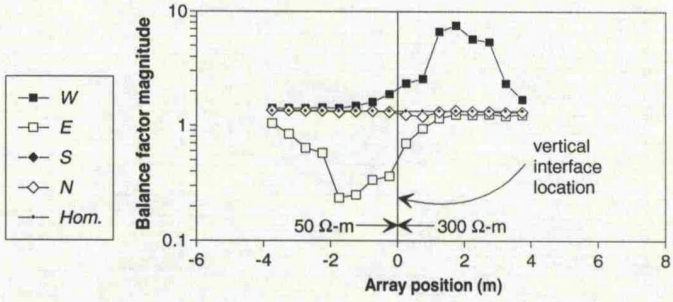

Figure 4.1.12 Vertical interface model results: Focusing balance factors.

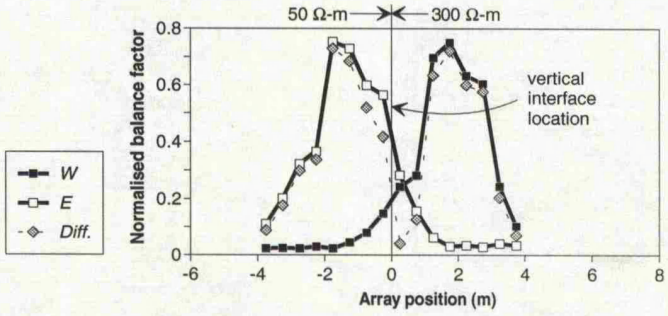

Figure 4.1.13 Vertical interface model results: Normalised *W-E* balance factors.

4.1.5.4 Interpretation

The close correspondence between numerical models and field data indicates a near-surface conductive–resistive contact in the survey area. Field apparent resistivity values are in the range 45–180 Ω-m compared with model values of 60–250 Ω-m indicating that the model 50/300 resistivity contrast is too high. Measured balance current anomaly peaks are also smaller than those modelled. A crossover point in the *W-E* balance factors almost coincides with the model fault location, being shifted about 0.5 m towards the resistive region. Models with lower resistivity contrasts indicate crossovers would be likely to be shifted by around 0.3 m towards the resistive zone in the case of the field data. The resulting inferred anomaly location is plotted in Figure 4.1.14.

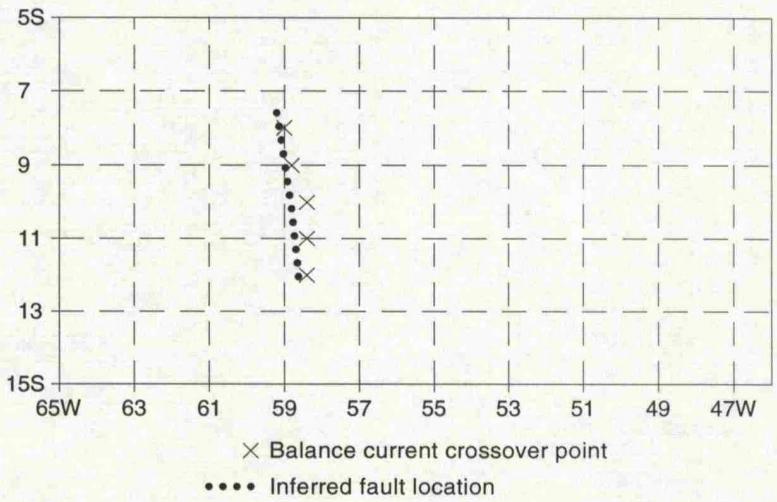

Figure 4.1.14 Site 2.1: Inferred surface location of fault line.

4.1.6 Case study: Site 1.4

4.1.6.1 Apparent resistivity traverses

Smoothed apparent resistivity data are shown in Figure 4.1.15. The histogram at the top of the figure indicates that most of the data points remain unaffected, with the largest correction being applied to the reading for position 4 m where nearly 10 (25%) of the 40 RESCAN measurements used to generate an apparent resistivity at this point have been altered. The effect of the smoothing can be seen by comparison with the raw data in Appendix E.

The focused apparent resistivity varies from a minimum of 90 Ω-m around 3–5 m up to 200 Ω-m, whereas the pole-pole data are much flatter, remaining around 200 Ω-m along the

entire line. Other resistivity data acquired at this site, in particular the half-schlumberger measurements, indicated the presence of a resistive covering which obscured deeper variations in resistivity. This was consistent with the site location on a valley floor, where recent alluvial cover would be expected. The focused measurement is apparently able to sense some of the deeper variation, whereas the pole-pole measurement seems to be responding to the surface cover only.

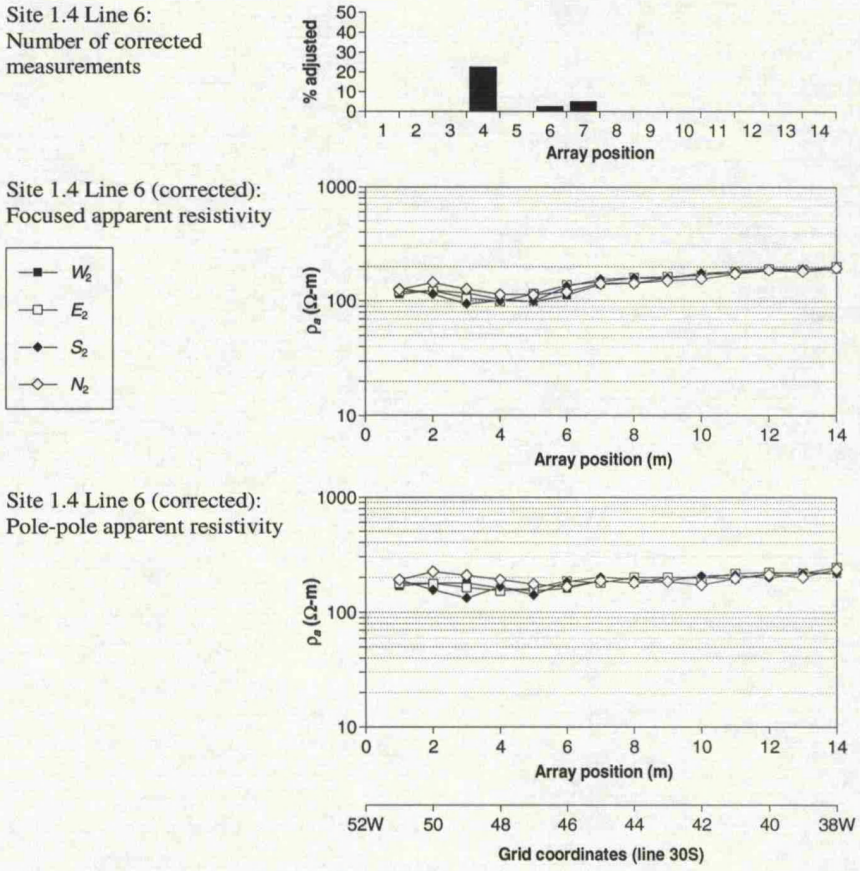

Figure 4.1.15 Site 1.4, Line 6: Corrected apparent resistivity traverses.

4.1.6.2 Focusing balance factors

The focusing balance factors exhibit relatively little variation (Figure 4.1.16) in contrast to that seen at Site 2.1. The largest variation corresponds with the low apparent resistivity values around 3–5 m.

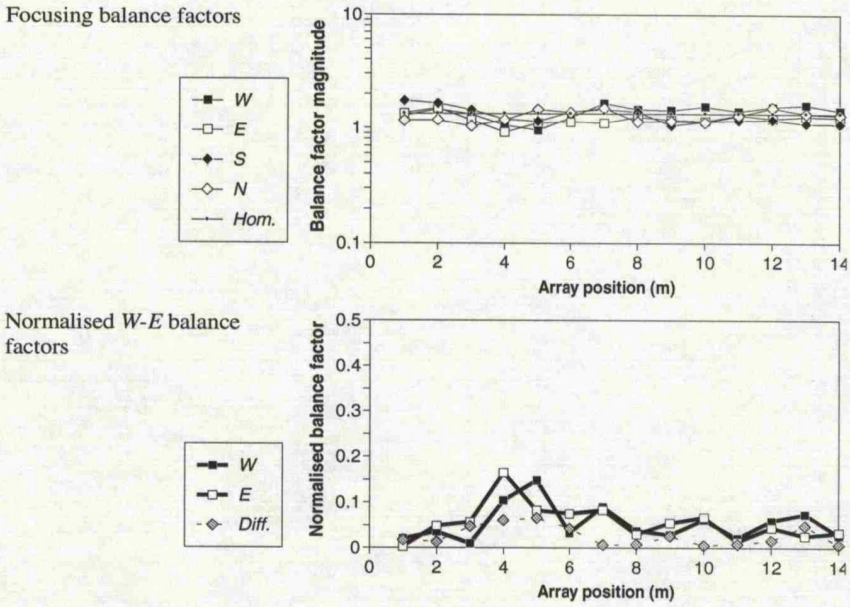

Figure 4.1.16 Site 1.4, Line 6: Focusing balance factors.

4.1.6.3 Numerical modelling

The proposal that the variance between pole-pole and focused apparent resistivity data was caused by the presence of a resistive overburden was tested with the model illustrated in Figure 4.1.17.

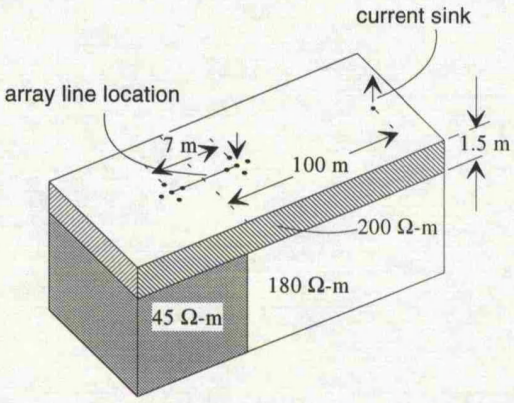

Figure 4.1.17. Idealised model of a vertical interface with overburden.

Apparent resistivity traverses generated by the numerical model are shown in Figure 4.1.18. Model and field resistivity traverses show close agreement in the region 4–10 m; in particular the pole-pole curve is seen to be flatter than the focused curve, with a ρ_a value reflecting the resistivity of the 200 Ω-m overburden.

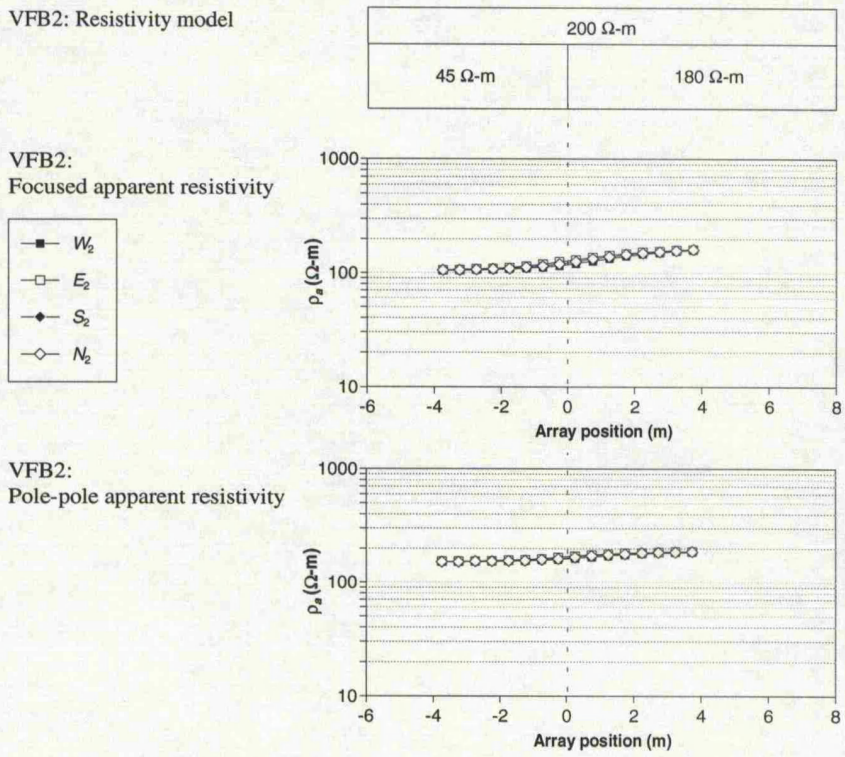

Figure 4.1.18 Site 1.4 model results: Apparent resistivity traverses.

The variation in balance currents (figures 4.1.19 and 4.1.20) is not so easily matched with field data, although the magnitude of the current variations is similar, and the absence of a large 'cross-over' anomaly (observed at Site 2.1) is confirmed.

4.1.6.4 Interpretation

Close agreement in apparent resistivity values between field and model data indicate that the resistivity of the units in the overburden model are plausible. In addition, this model accounts for the mismatch between pole-pole and focused apparent resistivity values, and indicates that the expected variation in balance currents is small in magnitude.

On the basis of the model described above, the alluvial overburden is interpreted as being of the order of 1.5m thick, damping the response of more conductive layers below. A change in resistivity between 45 Ω-m and 180 Ω-m indicating a possible fault plane is tentatively located at array position 6 m (= 46W on Line 30S).

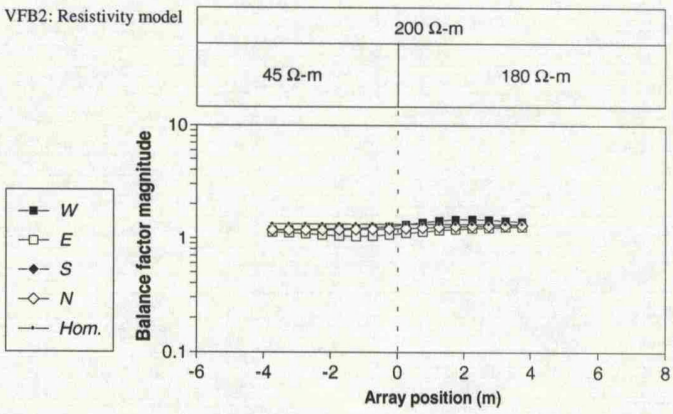

Figure 4.1.19 Site 1.4 model results: Focusing balance factors.

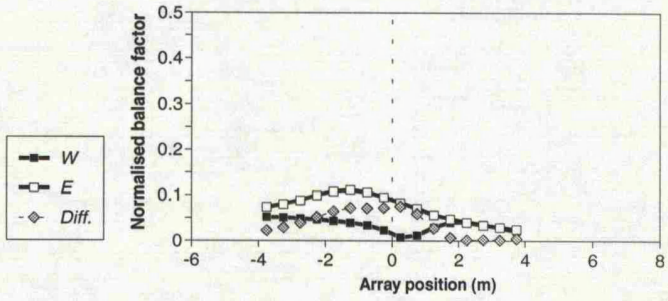

Figure 4.1.20 Site 1.4 model results: Normalised *W-E* balance factors.

4.1.7 Discussion

The two case studies described in Sections 4.1.5 and 4.1.6 provide examples of interpretations that have been verified by numerical modelling. They can therefore be used as a guide for interpreting data from other field areas.

Figure 4.1.21 is a presentation of data from Sites 1.2 a, b and c, Line 6 (which Line 20N referred to the local site coordinates), combined on the same plot. The three sites overlapped by 5 m, allowing confirmation of the repeatability of the RESCAN measurements: the average difference in overlapping data points was less than 5%. A conductive anomaly is seen between 84W and 76W, but the picture becomes clearer when the balance currents are plotted (Figure 4.1.22). The normalised *W-E* balance factors show cross-overs at 85.5W, 82.5W, 79.5W, 76.5W and 69.5W, all similar in shape and magnitude to the single crossover seen at Site 2.1. Hence a series of near-surface discontinuities is inferred, probably due to a series of faults

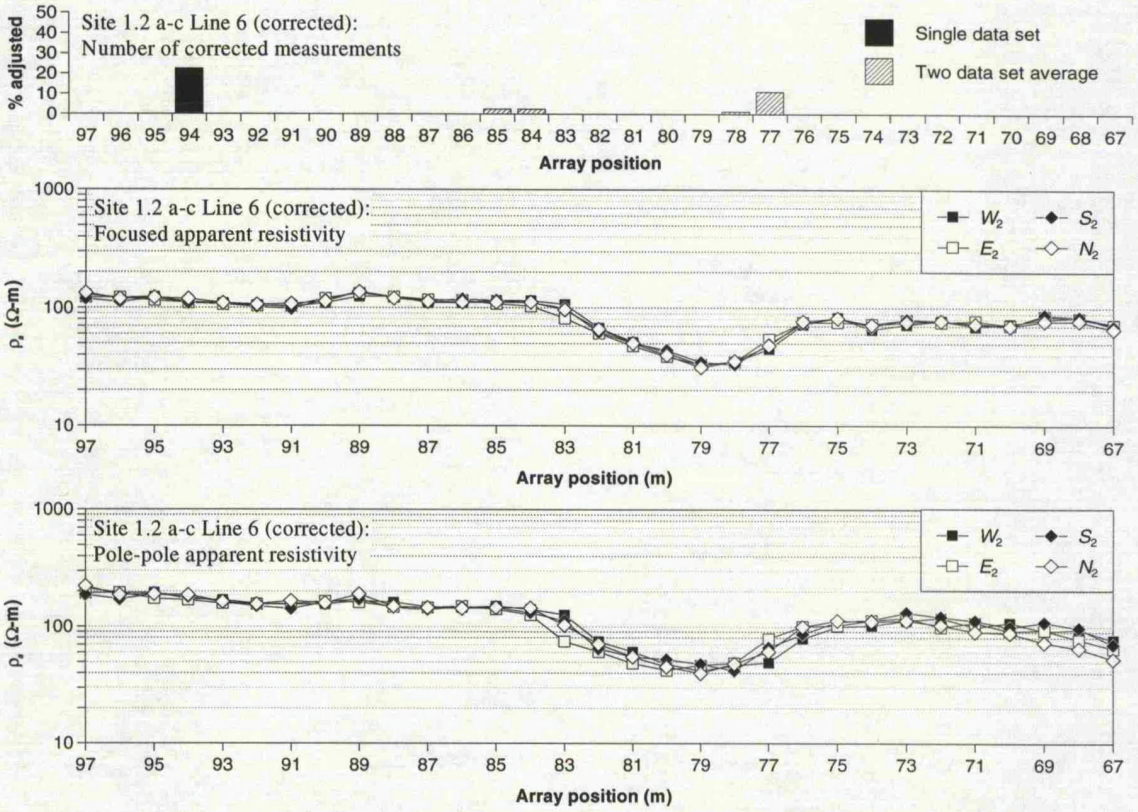

Figure 4.1.21 Site 1.2 a, b and c, Line 6: Apparent resistivity traverses.

causing two blocks of conductive rock to contact at the surface with a more resistive background zone.

A similar pattern occurs at Site 3.2 (Appendix E), although the data at this site are more noisy. A cross-over in the normalised *W-E* balance factors is present at position 9.5 m on grid *b*, and other steps in resistivity could be placed at 12 or 14 m. The anomaly at 3-4 m may be due to a handful of erroneous measurements; smoothing would help to confirm this. At this site, it is noticeable that the variation in *S-N* balance factors is similar in magnitude to the *W-E* factors, indicating some variation in properties perpendicular to, as well as parallel to the array.

In contrast to the variation seen at other field areas, no anomalies are visible at Site 3.1 (Appendix E). This may be due to too small a resistivity contrast, or too deep an overburden. The site location was on a hillside, suggesting that the former reason is more likely since the overburden is unlikely to be very thick.

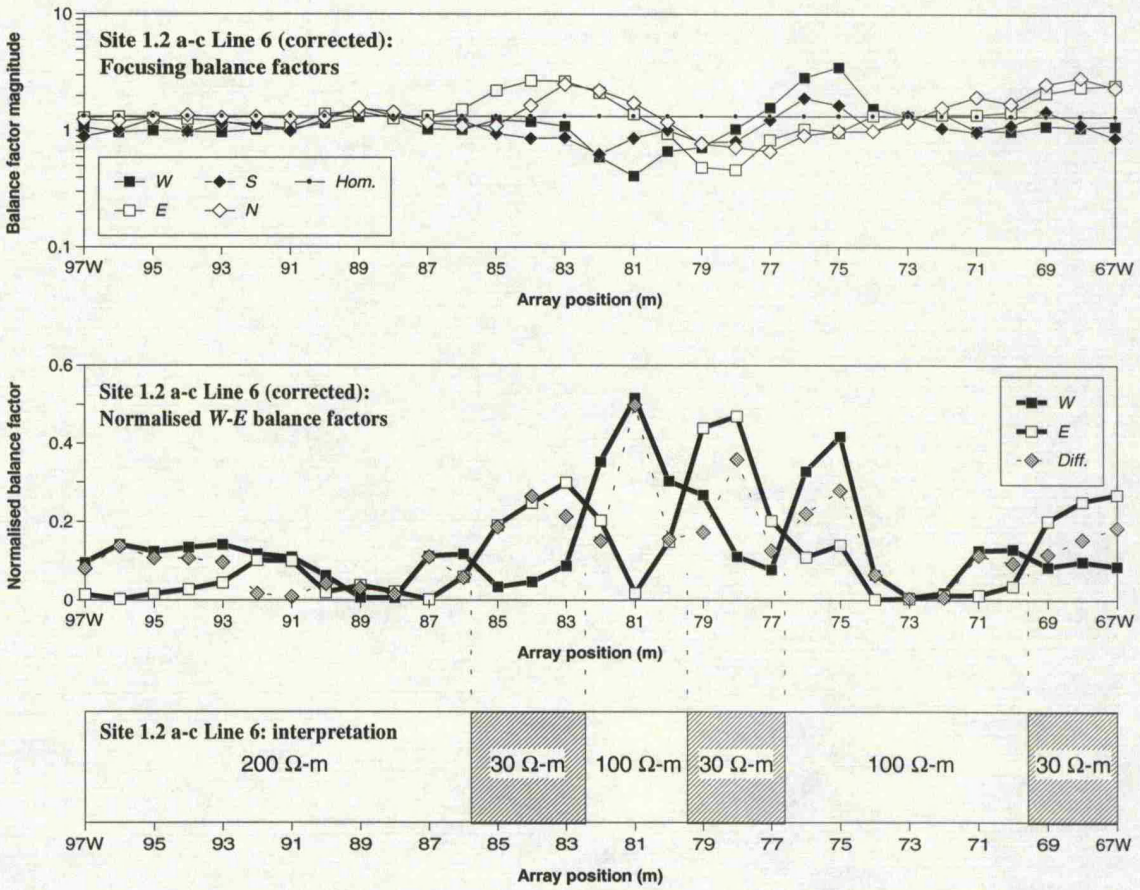

Figure 4.1.22 Site 1.2 a, b and c, Line 6: Focusing balance factors.

4.1.8 Conclusions

4.1.8.1 Synthetic focused measurement

The objectives of the focused measurement were to enhance depth of investigation and to accurately locate lateral conductive/resistive boundaries (§4.1.2.5). Both of these have been achieved, demonstrating the synthetic focusing method works in practice as well as in theory. In addition, the normalised balance currents have been shown to provide an additional response characteristic of faulting. The focused survey seems to give best results where an electrical resistivity contrast is present close to the earth's surface (as at Site 2.1, §4.1.5). In such cases, analysis of variation in synthetic focusing balance factors allows accurate location of subsurface lateral discontinuities, and thus enhances the detection and delineation of faults.

In order to create numerical models it was found that data from other survey styles, particularly the half-Schlumberger measurements, were helpful in giving an overall picture of the electrical structure in the region of interest. Focused apparent resistivity traverses, whilst providing less variable apparent resistivity values than pole-pole measurements, do not necessarily directly correspond to the resistivity of the earth. In addition, the coverage of the focused measurement is more limited than the half-schlumberger style. From this point of view, the best potential application of the data is as an extra constraint on existing data, rather than a unique survey style.

The focusing technique is seen to be robust enough to successfully produced synthetic focused measurements despite a degree of noise in the raw field data. In cases where anomalous measurements were observed, they could often be replaced using interpolation from the surrounding resistance measurements. The synthetic focusing technique appears to be more sensitive than conventional spreads in terms of the magnitude of anomalous values. However, these generally appear to be caused by systematic measurement errors rather than experimental noise, and so the technique could act as a quality control on the measurement data.

The number of measurements required to generate a focused measurement meant that the survey is relatively inefficient in terms of time. A survey run of 14 positions on a single line takes around 90 minutes, depending on the measurement frequency. Following the ideas outlined above, it may be possible to include the necessary focused pole-pole measurements in another survey style allowing more data to be generated from a single survey.

Although the focused array described here allowed focusing in two directions, many of the anomalies encountered were essentially uni-directional. In such situations, focusing could be restricted to one direction only (using just two focusing current electrodes). This would require only 12 measurements per focusing array location, a reduction of 70% (reducing the survey time for a single line to 25–30 minutes. However, some variation perpendicular to the array was seen at sites 1.2 and 3.2, and in this case bi-directional focusing is assumed to be superior, although no attempt to interpret these variations has been made at this stage.

4.1.8.2 Numerical modelling

The principal objective of the work described in this section was to provide a basis on which to develop numerical models for further modelling applications. Satisfactory operation of both

the focusing technique (which has been proven to be robust enough to cope with a certain amount of noise in the input potential values) and the finite difference model (which matches analytic solutions closely in the region of interest) has been demonstrated.

This part of the research work also illustrates the direct application of numerical model to the interpretation of field data. Field data at certain sites has been used to infer near-surface faulting; the model is able to verify these proposals. In addition, comparison of field results with numerical simulations can quantify fault location and overburden depth in favourable conditions.

4.1.8.3 Integration of other field measurements

In addition to d.c. resistivity measurements, a suite of other geophysical data was acquired during the Saarland project (§4.1.1). The combination of this data into an integrated geophysical interpretation for each survey area would provide additional support for the initial interpretations presented in sections 4.1.5 and 4.1.6. Whilst the importance of this final step is recognised, it was not directly in line with the aims of this PhD and it was consequently not pursued. An overall report of the findings of the fieldwork (Peart et al., 1996) shows that interpretations derived from other survey data are in agreement with the inferences made from the focused surface array measurements. The amalgamated survey measurements provide an inviting data set for future study.

The focusing technique has been demonstrated to operate well in the case of a surface array, based on a rectangular grid. The next section describes the development of the numerical model to cater for a borehole resistivity device, located in a borehole, and modelled using a cylindrical grid.

4.2 Simulation of ODP high temperature tool

4.2.1 Introduction

The work described in this section is the result of a project to model the basic characteristics of a new focused resistivity logging tool designed by Peter Jackson at the British Geological Survey and engineered by CSM Associates, for use in the Ocean Drilling Program (ODP).

The tool is designed to operate in high temperature conditions sometimes encountered in ODP drill-holes: hence the acronym ODPHT (Ocean Drilling Program High Temperature) tool. The tool is especially useful for logging boreholes drilled in hydrothermal systems which are typically permeated by highly saline/mineralized fluids. In addition to the high temperature environment in such drillholes, borehole fluids can be highly conductive; a focused measurement is necessary in order to counteract the short-circuiting effect of conductive boreholes. Another special feature of the tool is its exceptionally narrow diameter: it is intended to be operated whilst a diamond coring system is in place in the borehole, which presents a severe constraint on the tool diameter since it must be able to pass through a core barrel with an internal diameter of only 56 mm.

The principal objective of the modelling in this case is to assess the geometric factor of the tool which compensates for tool geometry and primary borehole effects on the tool measurement (standard results cannot be used due to the narrow sonde diameter). The geometric factor facilitates the conversion of a raw resistance measurement into an apparent resistivity value (see §2.3.2), which is the primary parameter required by ODP scientists for interpretation of the focused log. When considering a numerical simulation, only relatively straight-forward resistivity models are needed in order to derive the geometric factor. The modelling also provides an opportunity to test the performance of a 'wrapped' grid (based on cylindrical polar coordinates) in solving the electrical flow problem.

The principles of modelling a focused resistivity measurement (outlined in §4.0) are adapted for the case of a downhole device based on cylindrical polar coordinates. The ODPHT tool has only two focusing current electrodes so although the geometry of the problem is more complex the actual focusing simulation is simpler than in the case of the focused surface array described in Section 4.1.

The ODPHT tool emits sensing and focusing currents simultaneously and uses electronic feedback systems to achieve focusing dynamically as the measurement is made, in contrast to the focused surface measurement made using RESCAN, which was generated by combining measurements made from individual electrodes (§4.1.2.4). The superposition approach for modelling the focused measurement is therefore only used in the numerical model of the tool, as opposed to the focused surface array work where superposition is used to generate both field and model focused measurements.

Since the details of tool operation were available, the numerical model could be developed to mirror the tool operation (this is not possible in the case of the electrical imaging models described in Chapter 5).

4.2.2 Tool description

The prototype ODPHT tool is illustrated in Figure 4.2.1. Further tool details are presented by Halladay (1994). The mode of operation of the ODPHT tool follows the theory of the Laterolog 7 borehole tool (Doll, 1951). Electric current, which is used to make a resistivity measurement, is emitted from the central *sensing electrode* $A0$. This current flows into the formation and back to a common current return (V_{ref}) located 7 m above $A0$. The sensing current flow direction is constrained by the effect of additional currents emitted by the two *balance electrodes* $A1$ and $A2$. The magnitude of these two currents is adjusted using electronic feedback loops to keep the potential measured at $M1$ equal to that at $M1'$, and also the potential at $M2$ equal to that at $M2'$. This is intended to force the sensing current to flow normal to the axis of the tool, through a disc-shaped region, giving improved vertical resolution and improved depth of investigation.

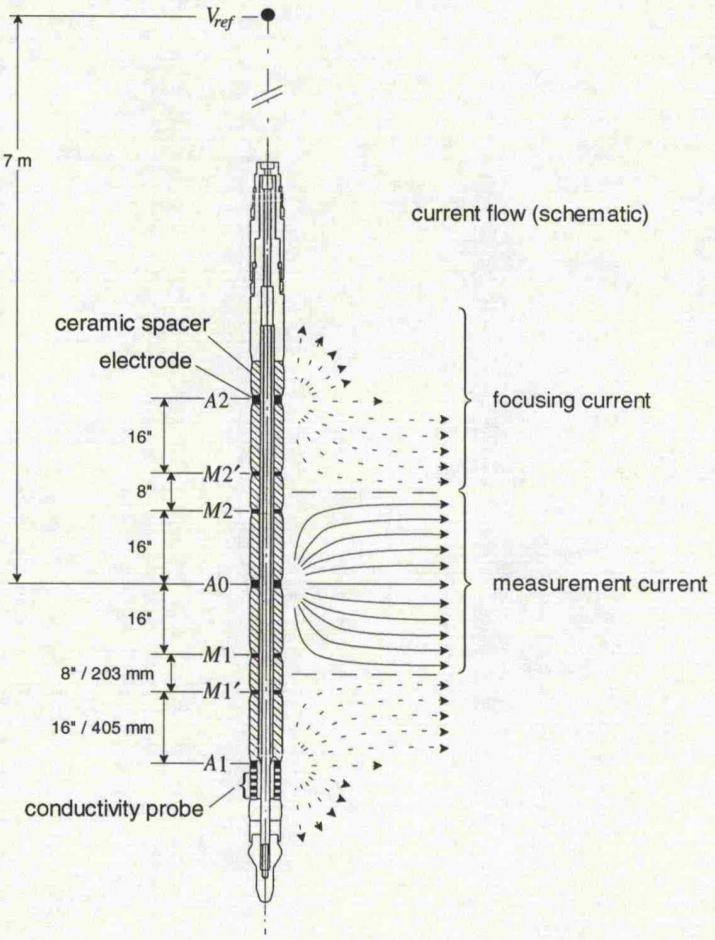

Figure 4.2.1 ODPHT tool configuration and focused current flow (schematic).

4.2.3 Numerical simulation of the focused measurement

Focused electric borehole tools (including the ODPHT tool) operate by continually adjusting the magnitude of the focusing currents using electronic feedback loops to ensure that the tool remains correctly focused (see above). In this case (in contrast to the focused surface array), synthetic focusing (§4.1.2.2) is used only for numerical simulation of the tool measurement.

4.2.3.1 Superposed focused electric potential

The principles involved in simulating focused electric borehole tools have been described in detail by Gianzero (1981) and Moran and Chemali (1985). Using the approach of Moran and Chemali (1985), and following the derivation of focusing equations for the focused *surface*

array, expressions for the superposed focused electric potential (Vf) measured on each of the ODPHT tool potential electrodes are derived in §D.2. These are:

$$\left.\begin{aligned} Vf_{M1} &= (Z_{A0M1} + Z_{A1M1}Bf_{A1} + Z_{A2M1}Bf_{A2})I_{A0} \\ Vf_{M1'} &= (Z_{A0M1'} + Z_{A1M1'}Bf_{A1} + Z_{A2M1'}Bf_{A2})I_{A0} \\ Vf_{M2} &= (Z_{A0M2} + Z_{A1M2}Bf_{A1} + Z_{A2M2}Bf_{A2})I_{A0} \\ Vf_{M2'} &= (Z_{A0M2'} + Z_{A1M2'}Bf_{A1} + Z_{A2M2'}Bf_{A2})I_{A0} \end{aligned}\right\}. \tag{4.2.1}$$

In equation (4.2.1), terms of the form Bf_R are balance factors which are functions of the transfer impedances (denoted by the terms Z_{AnMn}). The transfer impedances are determined by measuring the voltage at each of the potential electrodes while current is being emitted from a single current electrode only; thus the superposed focused electric potential is arrived at by calculating potentials where current is emitted from a *single electrode only* at any one time. This is the principal advantage in using this approach in numerical simulations of focused measurements, since the model can proceed without any a priori knowledge of the relative magnitudes of the measurement and balancing currents, avoiding the need for extra iteration in the solution process. Since there are only two unknowns in the focused potential expression, Bf_{A1} and Bf_{A2}, it is appropriate to derive explicit expressions (given in §D.2) for the balance factors in terms of the transfer impedances, rather than solve the simultaneous equations each time the balance factors are calculated.

4.2.3.2 Apparent resistivity and geometric factor

In Section 4.1.2.3 (eq. 4.1.3), the geometric factor G was introduced in the relationship

$$\rho_a = G\frac{V}{I}.$$

In the case of the ODPHT tool, V [V] corresponds to a potential difference measured between two points on the tool/logging cable and I [A] is the magnitude of the measurement current (which is independent of the variable balance currents). The purpose of the geometric factor is to convert the raw resistance measurement of the logging tool ($R_{tool} = V/I$) to a more meaningful parameter: ρ_a [Ω-m], the apparent resistivity, which is equal to the true resistivity in the case of a homogeneous, isotropic formation.

An analytic expression is derived for the apparent resistivity of the focused surface array in Section 4.1.2.3. This is not possible in the case of a borehole tool since an analytic solution

for the geometry of an electric tool situated in a borehole does not exist (§3.1.2.4). In this case, some sort of numerical evaluation of the electric potential for the homogeneous case must be used.

One approach is to use the finite difference method to create a model of the borehole, tool and surrounding formation. Using this model, the expected measured tool resistance, R_{tool}, for a known formation resistivity, ρ_f, may be determined. Rearranging equation (4.1.3) and substituting these parameters, the geometric factor may be determined from the relation

$$G = \frac{\rho_f}{R_{tool}}. \tag{4.2.2}$$

Using equation 4.2.2 in conjunction with the results of numerical models, it is possible to derive a value for the geometric factor for a given electrode location. In comparison with the geometric factor of the focused surface array there is an additional degree of freedom in the form of the borehole/formation resistivity contrast. Values of G must therefore also be determined for a variety of such resistivity contrasts.

4.2.4 Finite difference model

The development of the numerical model for simulating the ODPHT tool follows a similar pattern to that described for the focused surface array (§4.1.4). The principal difference between the two models is the geometry of the finite difference grid. In the case of the focused surface array, a grid based on rectangular cartesian coordinates is used, whereas a cylindrical grid is more appropriate for the simulation of a borehole tool. In order to derive geometric factors relatively simple resistivity distributions are required which represent a borehole located in a homogeneous, isotropic medium extending (effectively) to infinity in all directions. Grid definition away from the borehole does not therefore have to be sophisticated.

4.2.4.1 Boundary conditions

The region to be modelled is a three-dimensional volume, centred on the borehole tool, which may be considered to extend to infinity in all directions. As outlined in Section 4.1.4.1, the region covered by the finite difference grid is chosen to extend only to the point where the electric potential generated by the modelled tool approaches zero; this is found by inspecting the value of the electrical potential at the boundaries of test grids. With grid boundaries

located sufficiently far away from source/sink locations, the nature of the boundary conditions chosen for the finite difference model is not crucial. In practice, resistive (Neumann) boundaries were chosen in preference to conductive (Dirichlet) boundaries as these give faster convergence, although the end results using either condition are very similar.

4.2.4.2 Finite difference grid

The determination of the size and shape of the finite difference grid required to model the ODPHT tool is compromised by the conflicting demands of accuracy and speed (§3.2.5). The most crucial area of the grid is that part which represents the surface of the borehole tool, since this is where the voltages used to generate an apparent resistivity and geometric factor are located.

The homogenous case used for determining tool geometric factors is axisymmetric and so there is no need in principle to have many nodes in the tangential direction, circling the borehole axis. The problem can in principle be reduced to a purely two-dimensional one, since variation in electric potential will only take place in the radial and vertical directions. However, this part of work aims to develop a model which can be used to simulate current flow and tool geometry in three dimensions, for more complex simulations, and so the application of a 3-D model to a 2-D problem provides a useful stepping stone in the model development. Model results can be checked for symmetry to verify the wrapping process is working properly.

Figure 4.2.2 illustrates a vertical section through the finite difference grid developed for modelling the ODPHT tool. The left-hand edge of the section is the tool/borehole axis, located at $r = 0$. As illustrated in the blown up part of the figure, nodes are closely spaced in the region of the tool. The vertical locations of the respective electrodes $A1$, $M1$, $M1'$, $A0$, $M2'$, $M2$ and $A2$ are $z = -1$, -0.6, -0.4, 0, 0.4, 0.6 and 1.0 m respectively. The current return electrode (V_{ref}) is located at $z = 7$ m; grid spacing here is wider than for the source electrodes since this is not found to significantly affect the calculated potentials in the region of interest (i.e. the region from which values used for calculating geometric factors are taken).

In this idealised model the tool radius is set at 0.028 m, located midway between nodes placed at 0.018 m and 0.038 m in the radial direction. The borehole radius is 0.145 m, corresponding to a diameter of 29 cm or approximately 11.5 in which is a typical value for

ODP holes. The tool sonde is represented by resistive cells located between $z = -1.7$ and $z = 2.3$ m.

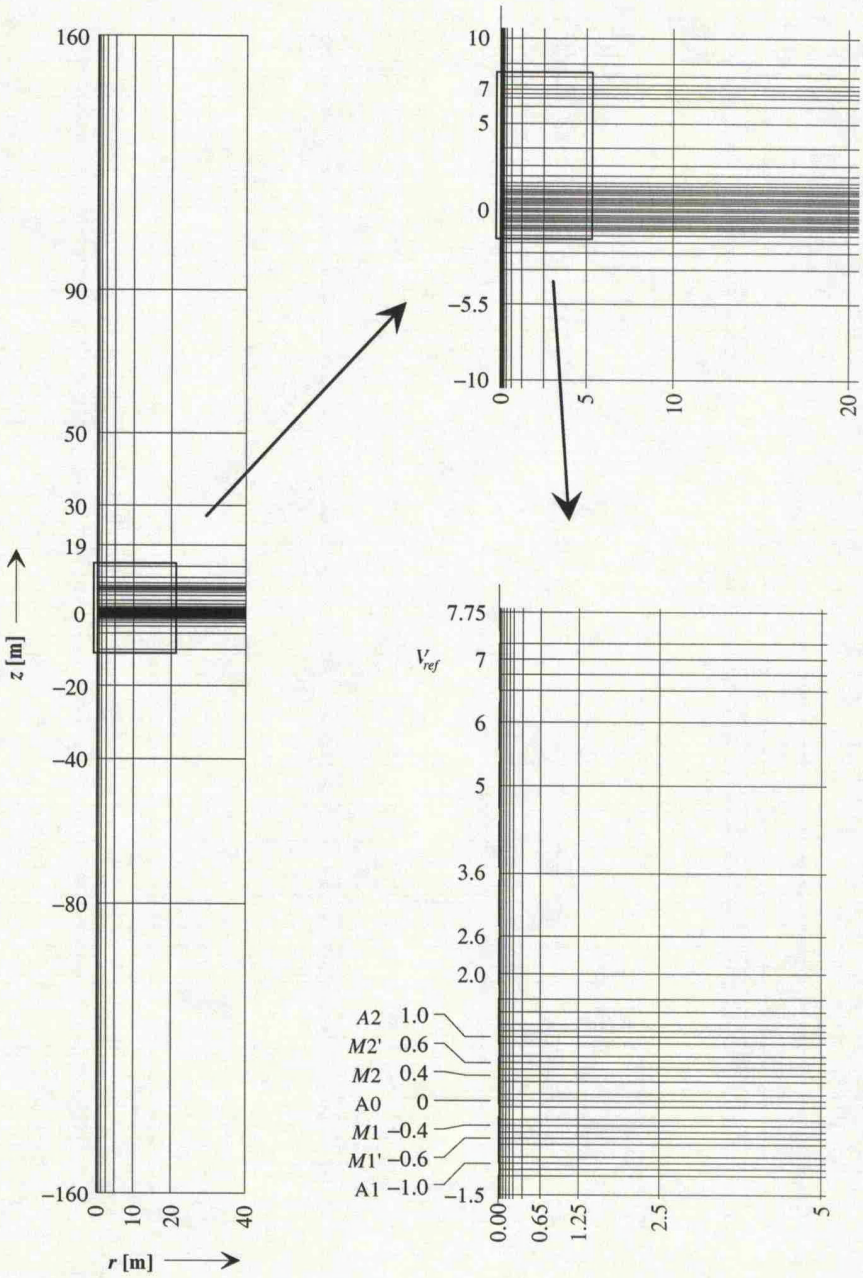

Figure 4.2.2 Vertical section through finite difference grid used for ODPHT simulation.

4.2.4.3 Testing of the model

Once a suitable finite difference grid has been defined, the model can be tested against known analytic solutions. Close agreement was found in the case of a homogeneous region (with no borehole) containing a source and a sink located at various points in the grid, and for the case of a horizontally layered earth (again, with no borehole). The details of this are not reported

here, but the testing is similar to the example given in Section 3.2.5.2. Note that there is no suitable analytic solution available for the electric potential in an earth containing a borehole (§3.1.2.4)—hence the need for a numerical approach to the problem.

Self-consistency

The Kirchhoff error and simulated current flow through the finite difference resistor network can be monitored during model runs to confirm that any residual error is small and that conservation laws are obeyed (a specific example is given in §3.2.5.3). This ensures that the model is self-consistent (i.e. it obeys the conservation principles on which the electrical conduction equations are based) and can be used to confirm that the grid 'wrapping' technique is not introducing unwanted errors.

4.2.5 Results

4.2.5.1 Two-dimensional modelling

Initial models confirmed the assumption that there is no variation in the electric potential in the azimuthal direction. This provides some confirmation that the wrapping routine operates correctly. Since there is no current flow azimuthally, it is not necessary for any relaxation of the calculated voltage values in this direction, and so the finite difference algorithm was modified to miss out iterations in the azimuthal direction, considerably reducing solution times.

With this modification, the three dimensional finite difference model effectively represents a two-dimensional problem by a segment as illustrated in Figure 4.2.3. The magnitude of any current source in the region is reduced in proportion to the size of the wedge: for example, a source of magnitude 1 A m^{-3} in a segment subtending an angle of 30° would have an equivalent strength of 12 A m^{-3} when the full 360° contribution is taken into account.

The angle subtended by the wedge is arbitrary in principle. This was tested by a series of models which are summarised in Table 4.2.1. Each model has a different number of azimuthal nodes, as indicated in the second row; this is the input parameter in the finite difference model which defines the angle subtended by the '2D' segment. The geometric factor was calculated using a formation resistivity of 1000 Ω-m.

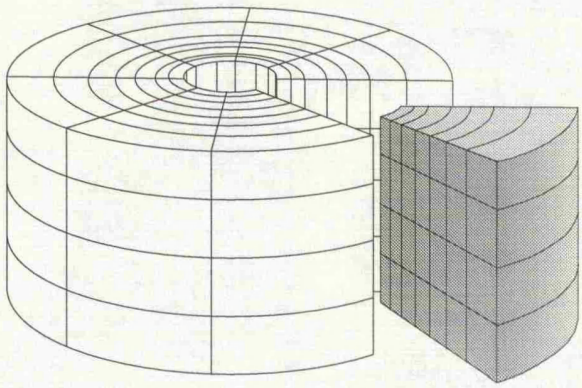

Figure 4.2.3 Wedge representing 2D model.

Model		SV01	SV02	SV03	SV04
Calculated balance factors	Bf_{A1}	18.183	21.801	21.515	21.515
	Bf_{A2}	240.652	288.799	284.982	284.982
No. azimuthal nodes		7	21	31	61
Wedge angle		90°	20°	12.86°	6.21°
Source strength		1/4	1/18	1/28	1/58
Calculated geometric factor	G_{M1}	0.932	0.777	0.788	0.788
	G_{M2}	0.932	0.777	0.788	0.788

Table 4.2.1 Results of series of models investigating effect of varying number of azimuthal nodes.

4.2.5.2 Geometric factors

Table 4.2.2 shows a range of geometric factors derived from models of the ODPHT tool operating in differing borehole/formation resistivity contrasts. The six runs *WB*01–*WB*06 correspond to respective borehole-formation resistivities of 0.025:1000; 0.25:1000; 2.5:1000; 25:1000; 0.025:1; and 2.5:10 (Ω-m in each case). For each run, the simulated potentials on the tool electrodes are given; following the derivation in §D.2 these are used to calculate the transfer impedances below, which in turn are used to calculate simulated focused balance factors. Finally, a value for the geometric factor is calculated, using equation 4.2.2. The potential on either voltage electrode pair (*M*1 or *M*2) may be used, hence the reason for two values of G for each model. A summary of the geometric factor calculations is given in Table 4.2.3.

Run	*WB*01			*WB*02			*WB*03		
Source location	*A*0	*A*1	*A*2	*A*0	*A*1	*A*2	*A*0	*A*1	*A*2
V_{A1}	0.367	0.677	0.212	2.800	5.701	1.416	17.739	41.467	7.597
$V_{M1'}$	0.376	0.495	0.219	3.097	4.144	1.656	22.777	29.599	11.130
V_{M1}	0.380	0.421	0.222	3.249	3.544	1.780	25.538	25.686	13.051
V_{A0}	0.423	0.274	0.229	3.911	2.352	2.033	35.093	18.334	17.239
V_{M2}	0.240	0.127	0.237	2.321	1.170	2.296	22.900	11.510	21.957
$V_{M2'}$	0.166	0.054	0.241	1.703	0.582	2.432	18.813	8.264	24.548
V_{A2}	0.018	-0.093	0.283	0.476	-0.588	3.059	11.095	2.048	33.746
V_{ref}	-2.166	-2.258	-1.954	-17.385	-17.833	-15.828	-89.054	-88.459	-82.909
Transfer impedances									
I_{A0}	1	1	1	1	1	1	1	1	1
$Z_{A0M1'}$, $Z_{A1M1'}$, $Z_{A2M1'}$	2.541	2.753	2.173	20.482	21.977	17.484	111.831	118.058	94.039
Z_{A0M1}, Z_{A1M1}, Z_{A2M1}	2.545	2.680	2.176	20.634	21.377	17.608	114.592	114.145	95.960
$Z_{A0M2'}$, $Z_{A1M2'}$, $Z_{A2M2'}$	2.332	2.312	2.194	19.088	18.415	18.260	107.867	96.723	107.457
Z_{A0M2}, Z_{A1M2}, Z_{A2M2}	2.406	2.386	2.191	19.706	19.003	18.124	111.954	99.969	104.866
Solution coefficients									
γ_1, α_1, β_1	-0.004	-0.074	0.004	-0.153	-0.600	0.123	-2.761	-3.913	1.921
γ_2, α_2, β_2	-0.074	0.073	-0.004	-0.617	0.588	-0.136	-4.087	3.247	-2.591
Balance factors									
Bf_{A1}, Bf_{A2}		24.322	498.906		10.797	51.325		3.845	6.396
I_{A0}	1			1			1		
Focused electric potential									
Vf_{M1}, Vf_{M2}		1153.394	1153.381		1155.142	1155.106		1167.245	1167.054
$Vf_{M1'}$, $Vf_{M2'}$		1153.394	1153.381		1155.142	1155.106		1167.245	1167.054
R_t	1000			1000			1000		
Geometric factor (*M*1, *M*2)		**0.867**	**0.867**		**0.866**	**0.866**		**0.857**	**0.857**

Run	*WB*04			*WB*05			*WB*06		
Source location	*A*0	*A*1	*A*2	*A*0	*A*1	*A*2	*A*0	*A*1	*A*2
V_{A1}	65.105	217.570	24.466	0.065	0.218	0.024	0.676	8.705	0.243
$V_{M1'}$	96.635	122.090	37.356	0.097	0.122	0.037	1.220	1.792	0.349
V_{M1}	117.840	100.410	45.574	0.118	0.100	0.046	1.784	1.226	0.426
V_{A0}	212.390	67.850	66.920	0.212	0.068	0.067	8.689	0.676	0.673
V_{M2}	116.160	44.850	97.860	0.116	0.045	0.098	1.771	0.417	1.212
$V_{M2'}$	94.107	35.781	118.740	0.094	0.036	0.119	1.201	0.334	1.775
V_{A2}	60.827	21.118	212.630	0.061	0.021	0.213	0.644	0.215	8.695
V_{ref}	-231.130	-228.390	-225.040	-0.231	-0.228	-0.225	-6.244	-6.244	-6.215
Transfer impedances									
I_{A0}	1	1	1	1	1	1	1	1	1
$Z_{A0M1'}$, $Z_{A1M1'}$, $Z_{A2M1'}$	327.765	350.480	262.396	0.328	0.350	0.262	7.464	8.036	6.564
Z_{A0M1}, Z_{A1M1}, Z_{A2M1}	348.970	328.800	270.614	0.349	0.329	0.271	8.028	7.470	6.641
$Z_{A0M2'}$, $Z_{A1M2'}$, $Z_{A2M2'}$	325.237	264.171	343.780	0.325	0.264	0.344	7.445	6.577	7.990
Z_{A0M2}, Z_{A1M2}, Z_{A2M2}	347.290	273.240	322.900	0.347	0.273	0.323	8.016	6.661	7.428
Solution coefficients									
γ_1, α_1, β_1	-21.205	-21.680	8.218	-0.021	-0.022	0.008	-0.564	-0.566	0.077
γ_2, α_2, β_2	-22.053	9.069	-20.880	-0.022	0.009	-0.021	-0.571	0.083	-0.563
Balance factors									
Bf_{A1}, Bf_{A2}		1.650	1.773		1.650	1.773		1.159	1.186
I_{A0}	1			1			1		
Focused electric potential									
Vf_{M1}, Vf_{M2}		1371.298	1370.635		1.371	1.371		24.559	24.541
$Vf_{M1'}$, $Vf_{M2'}$		1371.298	1370.635		1.371	1.371		24.559	24.541
R_t	1000			1			10		
Geometric factor (*M*1, *M*2)		**0.729**	**0.730**		**0.729**	**0.730**		**0.407**	**0.407**

Table 4.2.2 Results of geometric factor calculations.

Run	borehole: formation resistivity contrast	Ratio	G (average)	Balance current ratios (*A*0:*A*1:*A*2)
*WB*01	0.025:1000	0.000,025	0.867	1:24.322:498.906
*WB*02	0.25:1000	0.000,250	0.866	1: 10.797: 51.325
*WB*03	2.5:1000	0.002,500	0.857	1: 3.845: 6.396
*WB*04	25:1000	0.025	0.730	1:1.650:1.773
*WB*05	0.025:1	0.025	0.730	1:1.650:1.773
*WB*06	2.5:10	0.250	0.407	1:1.159: 1.186

Table 4.2.3 Summary of geometric factor calculation results.

4.2.6 Discussion

The results from investigating the effect of different width wedges confirms that the angle subtended by the segment of the finite difference grid has little effect on the calculated model potentials. Referring to Table 4.2.1 it is apparent that the calculated balance factors and the derived geometric factor show no variation (to 3 d.p.) for angles less than 20°. For larger angles, calculated values are seen to depart from the steady values of narrower sections. The geometry of the 'wedge' may be coming into play with a wide difference in the orientation of opposing faces of the finite difference cells and significant curvature of the radial faces introducing discretization errors. On inspection of calculated potential values it was noted that a small difference in voltage caused a much wider variation in calculated geometric factor, magnifying any discretization effects.

The wrapping method for generating a cylindrical polar grid may be considered successful for the case of an azimuthally symmetrical model, since the symmetry is preserved in the calculated voltages, and these match values calculated using the modified 'wedge' solution algorithm. It is noted that a two-dimensional model would be the ideal choice for this application, although the model simulations have been used in the development of a three-dimensional model in this instance.

Although the model is azimuthally symmetrical, it does not exhibit vertical symmetry about the central current electrode. This is apparent on inspection of the calculated balance factors in Table 4.2.3, particularly in the case of runs *WB*01, *WB*02 and *WB*03. In run *WB*01, the magnitude of the upper electrode (*A*2) current is calculated to be nearly 500 times that of the measurement current, whilst the current magnitude of the lower electrode (*A*1) increases by a factor of 24.3. This is due in part to the proximity of the current return [located 7 m from

*A*0, as compared with around 100 m for the focused surface array (§4.1)], but is principally caused by highly conductive borehole fluid (0.025 Ω-m) which magnifies the effect of the current sink and tends to 'drag' the measurement current upwards towards the sink. The focusing is working hard to reach balanced voltages on the potential electrodes, but this is still achieved [as can be seen from the calculated potential pairs (V_{fM1}, $V_{fM1'}$) and (V_{fM2}, $V_{fM2'}$)]. Focusing is much easier in cases where the borehole/formation contrast is lower, as can be seen, for example, in run *WB*04, where balance factors are around 1.7 and are approximately equal since the potential becomes more symmetrical about *A*0.

In conclusion, the ODPHT tool has been successfully simulated, allowing the calculation of geometric factors which can be used by ODP logging scientists to transform raw measurement data into more meaningful resistivity values. The geometric factors would normally be verified by testing of the tool. This typically involves running the tool in test wells where a suite of conventional log data is available for comparison, and possibly measuring the response of the tool whilst suspended in a tank of water. Unfortunately such data was not available for this project, precluding any practical verification of the numerical model.

The model development goals stated at the beginning of this section have been achieved, providing a basis for the development of more sophisticated simulations of electrical borehole devices. The following chapter describes one such simulation: that of a downhole electrical imaging tool.

CHAPTER 5

Results: electrical imaging

5.1 Introduction

This chapter describes the application of the finite difference model developed in Chapter 3 to the numerical simulation of electrical imaging tools. After introducing imaging tools and their principles of operation, the elements of a numerical model of such tools are described. This model is then used to simulate some specific, geologically relevant situations.

Detailed information regarding both the operation and simulation of imaging tools is not available from the service companies which have developed this technology, presumably to protect their commercial interests. The information that is available in the public domain includes an overview of tool function and image generation, and the barest details of theoretical modelling which has been used to analyse tool response. This is not enough on its own to be able to create a tool simulation using standard modelling techniques. However, published information can been used to infer the basic principles of tool operation, and a numerical model has been developed which aims to simulate these principles by making use of some of the properties of the finite difference model described in Chapter 3.

This model is then compared with the limited amount of published simulation data, and some (more widely available) field data, firstly to validate it and subsequently to help characterise the first-order response of imaging tools, with the intent of providing an insight into the nature of the measurements made by this important branch of downhole logging devices.

5.2 Electrical imaging tools

5.2.1 Tool description and operating principles

Downhole electrical imaging has become possible with the development of Schlumberger's Formation MicroScanner (FMS) (Lloyd et al., 1986; Ekstrom et al., 1987; Boyeldieu and Jeffreys, 1988; Luthi and Souhaité, 1990) and Formation MicroImager (FMI) tools (Bourke, 1992); more recently equivalent devices have since been produced by Western Atlas and Halliburton [Electrical Micro Imaging (EMI) tool (Seiler et al., 1994)]. These modified dipmeter-style tools provide detailed images related to variations in the resistivity of the borehole wall. A schematic representation of a typical imaging tool is shown in Figure 5.2.1 which illustrates the important elements of these wireline devices. Measurements are made on the surface of passively focused metal pads which are pressed against the face of the borehole wall using sprung arms as the tool is drawn upwards. (The FMS has two or four pads, whilst the FMI has eight pads [Bourke, 1992]; the EMI has six pads [Seiler et al., 1994]). The pad measurements correspond to readings from an array of electrical buttons located centrally on each pad surface (as illustrated in Figure 5.2.1), and are used to generate an electrical image of the borehole wall. In the case of the FMS, the buttons are circular with a diameter of 5 mm and are arranged in rows so that they overlap. This gives the FMS a potential tool resolution of 2.5 mm at the appropriate logging speed.

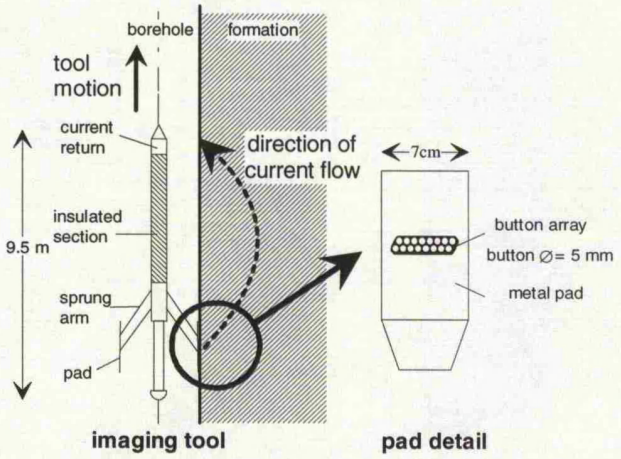

Figure 5.2.1 Downhole electrical imaging tool (schematic). Dimensions and pad detail refer to the FMS.

Figure 5.2.1 also illustrates the flow direction of current generated by the tool. The imaging buttons, pad face, and lower part of the tool body are at a higher electric potential relative to a return electrode located near the top of the tool body. Currents are thus induced to flow out of the buttons, through the formation, and back to the tool; these are passively focused to flow directly into the formation (rather than along the borehole) by the metal pad surrounding the buttons, and the lower part of the tool. The current emitted by the tool is varied to compensate for variations in the formation resistivity (Bourke et al., 1989): in resistive zones, the current is increased to keep current levels at an optimum level for measurements to be made; conversely current flow is reduced in the presence of conductive zones to avoid saturation of the electric signal. Currents through each button are recorded enabling a current density map of the surface of the button array to be produced; this is then converted to resistance values which are used to generate an electrical image of the borehole wall—the tool can be thought of as producing a picture of the borehole wall as seen by an electrical eye. Ideally, such an image is obtained from measurements with a very shallow depth of investigation, although it is evident that the currents used to make measurements flow a finite depth into the formation. Tool readings are influenced primarily by current flow close to the pads, where current density is highest, although Bourke et al. (1989) report that modelling by Trouiller (1988) and others indicates that the depth of investigation of the tool can be as much as 25 cm in a homogeneous formation with a smooth borehole. In practice, formation heterogeneities can reduce the depth penetration to as little as 2.5 cm and the focusing effect of the tool further reduces depth of investigation. A three-dimensional (3D) numerical simulation is one way of quantifying the depth of investigation of imaging tools in different geological settings

5.2.2 Data acquisition and processing

Since the numerical models developed for this work are intended to simulate not only the tool operation but in addition the generation of electrical images, an appreciation of the data acquisition and processing procedure used to translate raw tool measurements into downhole images is required.

Details of the processing procedure in the case of Schlumberger's FMS/FMI are given by Serra (1989), with some further discussion in Bourke et al. (1989) and Harker et al. (1990).

The latter authors divide the process by which raw tool data are used to generate images of the borehole wall into three steps: data restoration, image generation and image enhancement.

Data restoration involves correcting the raw measurement data for varying measurement conditions. A speed correction is made using vertical accelerometer data which removes 'saw-tooth' artifacts in the images caused by incorrectly aligned button measurements resulting from any mismatch in the measured cable speed and the actual tool speed (which typically occurs when the tool sticks). The gain and offset of individual buttons is equalised to compensate for differing responses to resistivity variations, and effects due to borehole rugosity and eccentricity. This removes stripy features in the images (note that the button measurements are not actually calibrated). Finally a correction is made to allow for variation in the tool focusing current.

Image generation is the mapping of current intensity measurements to grayscale values (of pixels) or other colour scales, thus allowing the measured resistance curves to be converted into a two-dimensional image. The usual convention is to represent conductive (high current) values by dark tones and resistive (low current) values by light tones. Common colour schemes are variations from brown to yellow or a rainbow (blue through green and yellow to red).

Image enhancement involves re-scaling the generated image (i.e. modifying the mapping of measurements to grayscale values). Schlumberger typically use static normalisation (where a particular scale of values is applied to a long interval of data), dynamic normalisation (where images are scaled over a moving window, typically 1 m in length), or dynamic histogram normalisation (which emphasises fine variations in button current intensity), depending on what kind of features are being analysed.

5.2.3 Applications of electrical imaging

The applications and significance of electrical imaging have already been outlined in Section 2.4.3. Downhole electrical imaging provides a connection between geological interpretation and conventional log analysis. Numerical modelling can be of benefit by characterising the nature of the measurement and its expected response, and also opens up the possibility of more quantitative petrophysical information being derived from electrical images.

It is noted that much of the imaging tool application relies on interpretation of images which can be strikingly similar to what would be seen by the naked eye. Numerical modelling is one way of verifying or dissuading the use of conventional 'optical intuition' in the interpretation process.

5.3 Simulation of electrical imaging tools

Reported simulation of electrical imaging tools has been exclusively in-house, carried out with proprietary software (Ekstrom et al., 1987; Luthi and Souhaité, 1990; Trouiller, 1988). The present work represents an attempt at modelling such tools outside the commercial environment.

Information regarding simulation of electrical imaging tools in the public-domain is limited; in addition many details of tool specification, method of operation, and data acquisition and processing are also restricted to in-house engineers and scientists. It is not therefore viable to aim to produce the detail of previously reported modelling, or to attempt to simulate a specific device in detail. Instead, the more fundamental characteristics of such tools aim to be assessed, with the intention of investigating first order measurement effects. In creating models of imaging devices, certain assumptions have been made with regards to operational details; these have been translated into numerical simulations which make use of some of the properties of the finite difference method to simulate the electric button measurements used to generate synthetic electrical images.

5.3.1 Introduction

Numerical models of the FMS have been described by Ekstrom et al. (1987) and Luthi and Souhaité (1990). Results of in-house modelling by Trouiller (1988) are reported by Bourke et al. (1989), but no detail of the models used are given. Even in the case of the modelling described by Ekstrom et al. (1987), little detail is given about the technique used, other than to say it utilises a 3D finite element model with a flexible grid consisting of about 50,000 nodes. These features are also present in the model used by Luthi and Souhaité (1990), although it is larger, consisting of about 70,000 nodes, but the response of a single button only is simulated. Chang and Anderson (1984) give some details of the method used, and describe how the grid

is automatically generated by considering (estimated) discretization error. It seems likely that the model described by Ekstrom et al. (1987) is also based on the same principles.

In common with the models described in the literature, and as described in Section 3.2, the model presented here is a forward model, as illustrated in Figure 5.3.1. For a given model the grid geometry and resistivity distribution are pre-defined. Tool characteristics are also specified (e.g. diameter, length, location and magnitude of current source and sink). The model then calculates the electric potential we would expect in a formation with a resistivity distribution matching that specified in the simulation. Since the solution includes the potentials on the surface of the tool, a simulated tool response, and thus a simulated electrical image can be generated.

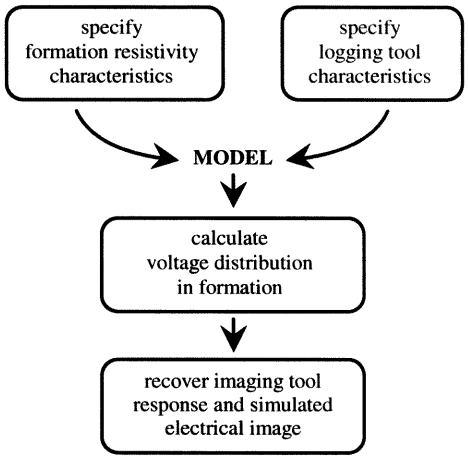

Figure 5.3.1 Flow diagram to illustrate a forward model for simulating electrical imaging.

The model used here differs from those previously described in several respects. As described earlier, it is based on the finite difference method, although it is also 3D with a similar number of mesh nodes. The mesh itself is also flexible within the constraints of the cylindrical polar coordinate system although it is not automatically generated. The model attempts to simulate current flow in the borehole region surrounding the whole imaging tool, not just the pad region.

In general the finite difference method is less flexible, but simpler, than the finite element method used in the simulations of Ekstrom et al. (1987) and Luthi and Souhaité (1990). The full flexibility of a finite element mesh is not always required: the model described here could

easily accommodate the meshes described by Chang and Anderson (1984), for example. In addition, the models presented here are deliberately restricted to simple situations with a view to illustrating the fundamental tool characteristics.

Perhaps the most important aspect of the numerical model is the simulation of the current flowing from the passively focused button electrodes. Although the physical dimensions of the buttons and surrounding pad have been published (e.g. Ekstrom et al., 1987), the method of controlling, focusing, and measuring the current flowing from them has not. Information concerning methods of simulating this process is equally limited. Section 5.3.2 describes how the button measurements are simulated by making specific use of the way the electrical flow problem is formulated in the finite difference method.

5.3.2 Simulation of electrical imaging buttons

The electrical imaging buttons are micro electrodes which independently inject current into the formation (the buttons are illustrated schematically in Figure 5.2.1). The button currents are measured and form the basis of the downhole electrical image. The current flow from the buttons is passively focused by current from the tool pad; to generate a reasonable replication of the imaging tool measurement, the focusing mechanism must also be represented. Focusing is achieved by ensuring that the tool pad and buttons are at the same potential: this implies that current flow from the buttons will be normal to the pad, directly into the formation (rather than 'short-circuiting' up the borehole). The focusing is termed 'passive' since there is no attempt to vary focusing currents to compensate for the effect of formation heterogeneities (as opposed to the focusing described in Chapter 4).

In order to simulate the electric buttons, direct use is made of the resistor analogy of the finite difference approximation (Section 3.2.3). A single resistor in the finite difference grid is used to represent an individual imaging button. Once a resistivity model has been specified, the finite difference method is used to calculate the electric potential across each button resistor. To calculate the current intensity associated with each model button, Ohm's law is applied. The simulated button current intensities are thus intended to be generated from a theoretical process which is similar to the way the actual tool operates (notwithstanding any assumptions that have been made about tool function).

In the FD model, given nodes cannot, in general, be held at a fixed potential. The exception is the boundary of the grid. One of the boundaries of the wrapped grid coincides with the axis of the borehole, and therefore conveniently runs down the centre of the logging tool. Passive focusing is simulated by translating the fixed boundary potential at the centre of the grid to the grid cells representing the surface of the imaging tool pads, using very low resistance inter-nodal connections. The button resistors form part of the connection between boundary and pad, but must be finite in order for a measurable potential difference to be present across them. With these low resistance connections in place, the electric potential at the simulated pad surface will be very close to that of the boundary, which may be fixed to a constant value ensuring the surface of the pad approximates an equipotential surface.

The implementation of simulated electric buttons is illustrated schematically in Figure 5.3.2, which shows a vertical section through part of the finite difference grid in the simulated imaging tool's pad region. The radial nodes of a typical row have been labelled $A_1 \ldots A_6$ for convenience. The potential of the boundary node A_1 is set at 100 V. Radial resistances between the boundary and A_5 are set close to zero (actually 1×10^{-10} Ω to prevent division by zero errors in the solution algorithm). Note that nodes A_2, A_3 and A_4 are not needed for the button simulation; they are used to represent the imaging tool body and borehole fluid further up and down the grid. The vertical resistances and tangential resistances (which are normal to the plane in Figure 5.3.2 and are not illustrated) connecting nodes $A_2 \ldots A_5$ are set effectively to infinity (in practice to an equivalent resistivity of 1×10^{30} Ω-m) ensuring current flows independently through individual buttons. The electric potential at A_5 is thus virtually the same as the boundary value of 100 V. The radial resistor connecting A_5 to A_6 is the button resistor and is set to a small value ΔR to ensure that the potential A_6 is still close to 100 V. The current I_b flowing through this button resistor is given by Ohm's law:

$$I_b = \frac{V_5 - V_6}{\Delta R}.$$

The real imaging button current data generated by the FMS/FMI is corrected for variations in the pad focusing current (Section 5.2.2). In the simulation described here, the equivalent process is the normalisation of I_b to a button resistance R_b, using

$$R_b = \frac{V_6}{I_b}. \tag{5.1}$$

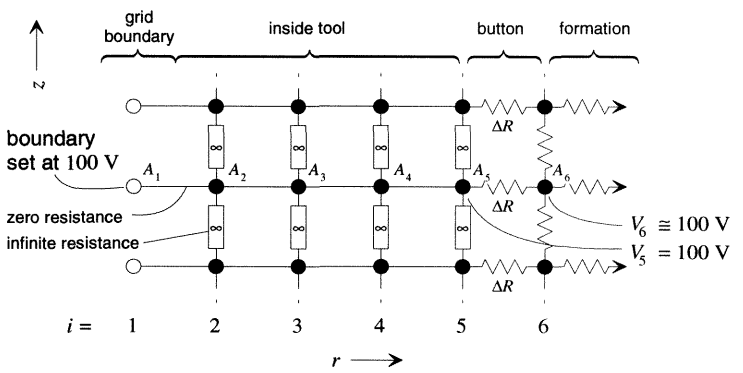

Figure 5.3.2 Representation of passively focused imaging tool button using FD grid resistors.

Note that V_6 represents absolute potential, relative to infinity (approximated by the boundary of the model).

In practice, it was found necessary to make ΔR equal to 1 Ω in order for the potential drop across this resistor big enough to be measurable (i.e. to prevent numerical underflow). Testing shows the potential at A_6 is still found to be close to 100 V, preserving the simulated passive focusing effect.

5.3.3 Boundary conditions

In the electrical imaging tool model, boundary conditions are used to generate current flow, as opposed to the models described in Chapter 4 which use current sources and sinks. This allows simulation of passive focusing to be accommodated, as described in Section 5.3.2 above. Electrical currents are generated by having a voltage drop between the tool pads and the current return, which is located at the top of the tool body. This is illustrated schematically in Figure 5.3.3. The portion of the grid boundary which corresponds to the lower part of the imaging tool is set to a positive potential (100 V) with respect to the top part of the tool (which is set to 0 V). Other boundaries are made highly resistive, so no current can flow through them; this is analogous to locating a tool within an electrically insulating tank. Thus the model has a mixture of Dirichlet and Neumann boundary conditions (illustrated in Figure 5.3.3).

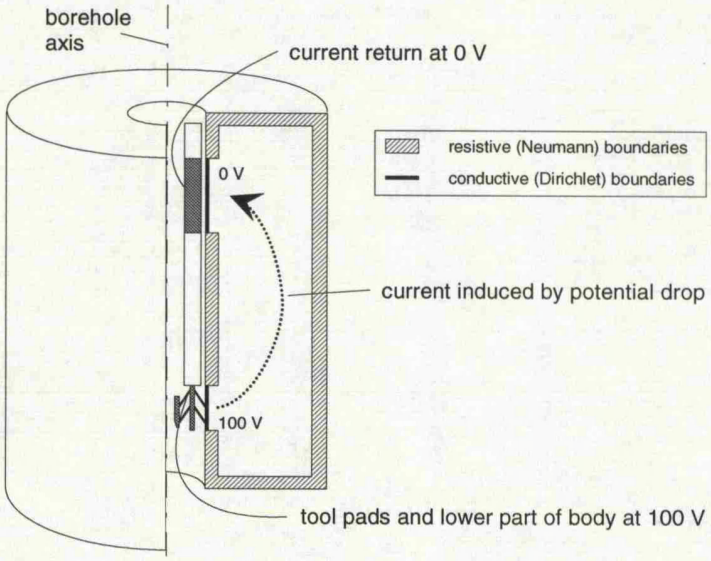

Figure 5.3.3 Schematic vertical section through a model of an electrical imaging tool illustrating boundary conditions used to generate current flow.

5.3.4 Finite difference grid

By experimentation the model grid is defined to extend three metres from the top, bottom and axis of the simulated imaging tool, using the principles outlined in Section 3.2.5. The tool is located between $z = -0.16$ and $z = 7$ m; in Figure 5.3.4 the location of the tool pad and simulated buttons corresponds to a dense packing of grid nodes centred around $z = 0$ m. There are 17 radial nodes and 47 vertical nodes. Where azimuthal variation is important, up to 91 azimuthal nodes (including those used for wrapping) are used giving a total grid size of 72,709 nodes; this is reduced when symmetrical models are to be investigated.

The locations of the grid nodes are defined to match the published dimensions of the Formation MicroScanner (Ekstrom et al., 1987). The simulated tool is azimuthally symmetrical: rather than simulate four individual pads, a single 360° ring of electric buttons is effectively present. This allows full borehole coverage, and provides an adequate approximation to a real tool: given the other simplifying assumptions in the model, it was not thought important to try to incorporate the extra detail of individual imaging pads.

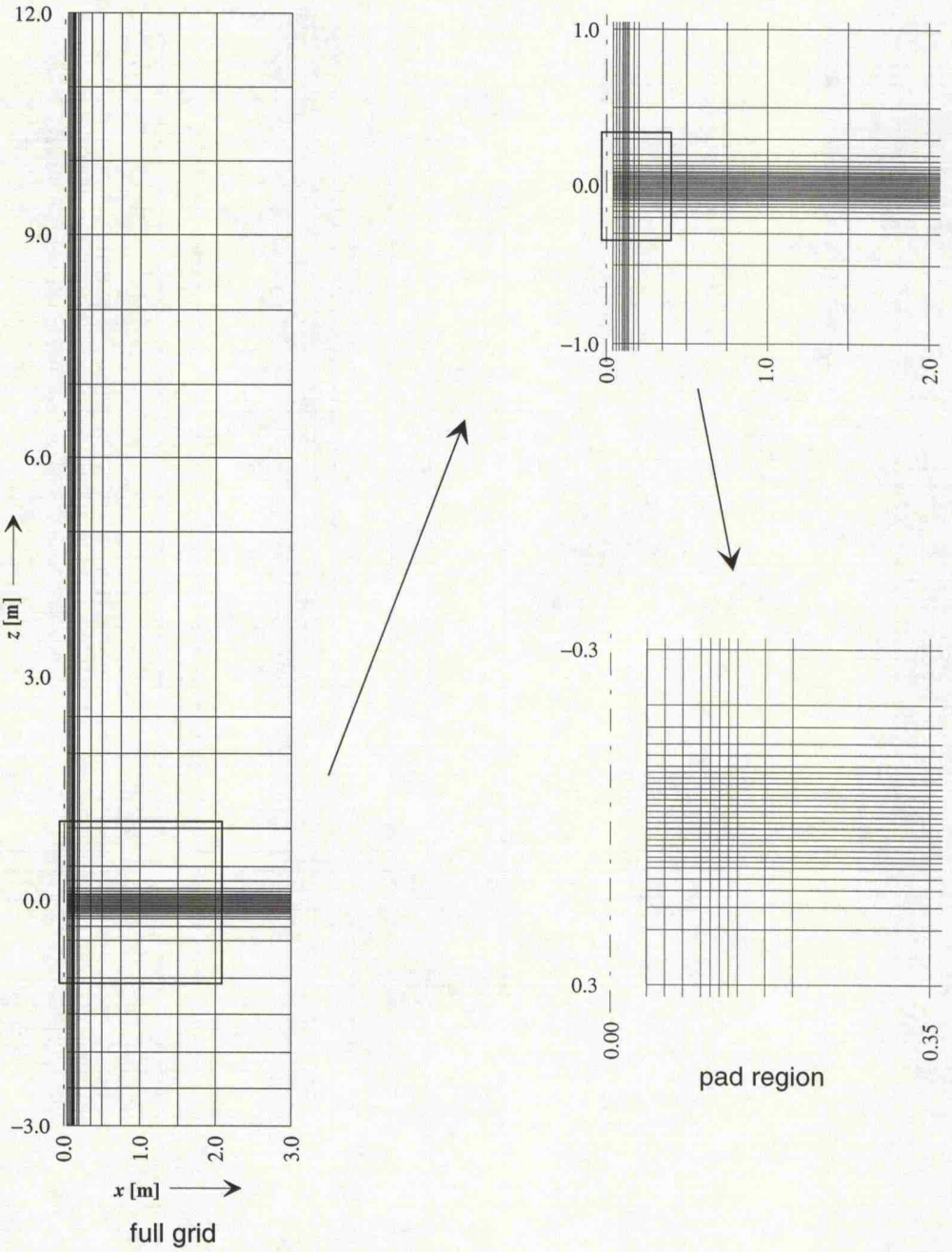

Figure 5.3.4 Vertical section through grid used in finite difference simulation of electrical imaging tools.

5.3.5 Generation of electrical images

The process by which downhole images are generated from raw tool resistance measurements has been outlined in Section 5.2.2. Any true simulation of a specific logging tool would require detailed knowledge of these procedures, but not all such information is publicly available.

Certain processing steps are not applicable to the idealised situation represented by the numerical model: there is no need to make a speed correction or gain and offset correction since tool motion is uniform and imaging buttons are identical; other sources of measurement noise such as borehole rugosity and contact resistances are also absent.

Static and dynamic normalisation has not been carried out on simulation data in the generation of grayscale images since simulations have been run over relatively small intervals. Where grayscale images have been generated, data imaging software has been used to create an appropriate colour or grey scale.

Perhaps the most crucial processing step is compensation of the variation of the focusing current (controlled by what is termed the 'EMEX' voltage by Schlumberger). Clearly the compensation procedure depends on the method used to vary focusing current; in the numerical model this is achieved by fixing the voltage between the tool pads and the current return (Section 5.3.3). In this case, current normalisation is easily implemented by converting measured button currents into resistances using equation 5.1.

5.3.6 Testing

The finite difference model used for the FMS is based on the cylindrical grid of the ODPHT model described in Section 4.2. Section 4.2.4.3 refers the testing of this grid using known analytic solutions for simplified resistivity distributions. Note that there is no suitable analytic solution available for the electric potential in an earth containing a borehole, or even an idealised electrical device located in a homogeneous region (§3.1.2.4)—hence the need for a numerical approach to the problem.

Section 4.2.4.3 also describes how a model may be tested for self-consistency by monitoring current flow through the finite difference grid and analysing Kirchhoff error. Similar procedures have been adopted in the case of the electrical imaging model, with accurate results as required.

Beyond this, rigorous testing of the model is not possible. However, simulation data may be compared with published results to provide confirmation that the modelling is producing reasonable results. This is described in the next section.

5.4 Application of the numerical model

Numerical modelling has been carried out with the intention of investigating some simple geometries with some geological significance. The results presented here involve relatively simple situations with a view to illustrating the fundamental tool characteristics. In addition, initial models aim to test the simulation which has been developed.

The models follow a progression, starting with cases which aim to demonstrate the validity of the numerical model, and moving on to potential applications of the quantitative numerical simulation. In view of the fact that information concerning both the operation of electrical imaging tools and the simulation of such tools is restricted (as described in Section 5.2), it is not viable to rigorously demonstrate that any model closely simulates an actual tool. However, model output can be compared with reported tool responses to various situations, and a less direct test is thus made.

5.4.1 Sequence of horizontal layers

A section of downhole data from ODP Leg 126, Hole 793B is illustrated in Figure 5.4.1. The section corresponds to thick turbidite beds exhibiting classic grading of particles: the largest pebbles are found at the base of each bed with particles fining upwards and becoming clays at the top. The particle grading is typically associated with a change in resistivity: the clay-rich parts of each bed are observed to be more conductive. This is due to a combination of surface conduction effects associated with clays (see §2.1.3) and a high porosity typically observed in clay-rich marine sediments (Ellis, 1987; Taylor, Fjioka et al., 1990). A trend in resistivity values from high (at a layer base) to low (at the top of the layer) is apparent on conventional resistivity log data (on the left of the figure). An FMS image from the same section is presented on the right of the figure (finer, more conductive beds appear as darker bands).

At present, downhole resistivity measurements are not available on the same scale as electrical images, but in this case the relatively thick beds allow the conventional resistivity data to be used as a control on the interpreted resistivity of the formation. Using the conventional (quantitative, calibrated, but lower resolution) resistivity measurements, a model consisting of a series of horizontal layers (illustrated in Fig. 5.4.2) is created. The location and resistivity of each model layer is shown in the left hand plot of Figure 5.4.2.

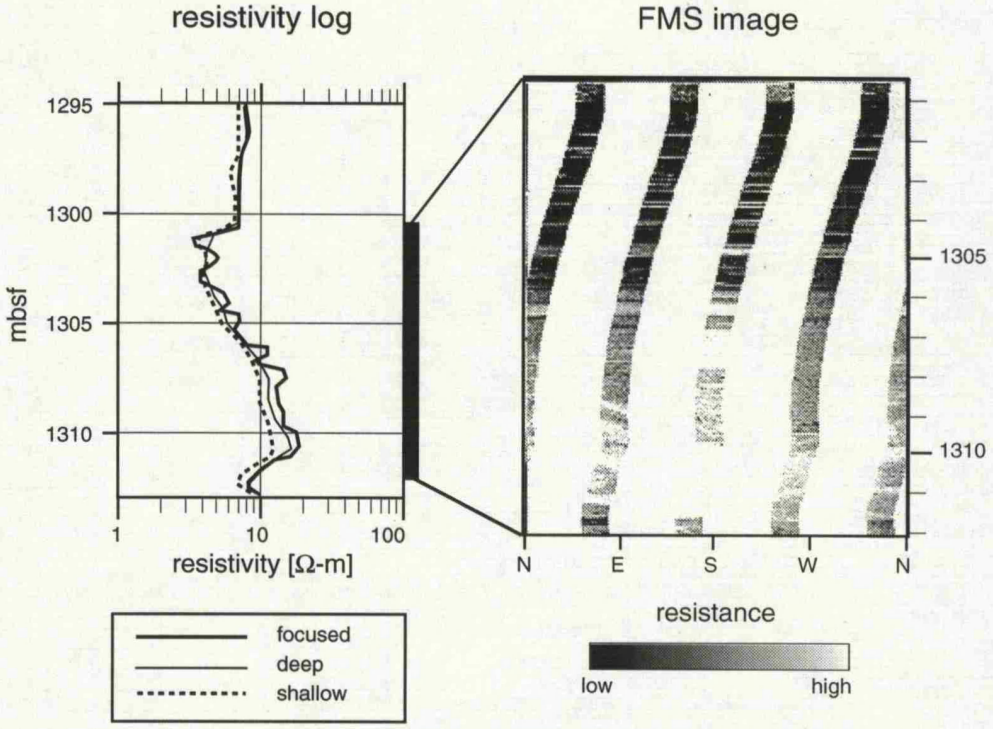

Figure 5.4.1 Resistivity and FMS data from ODP Hole 793B.

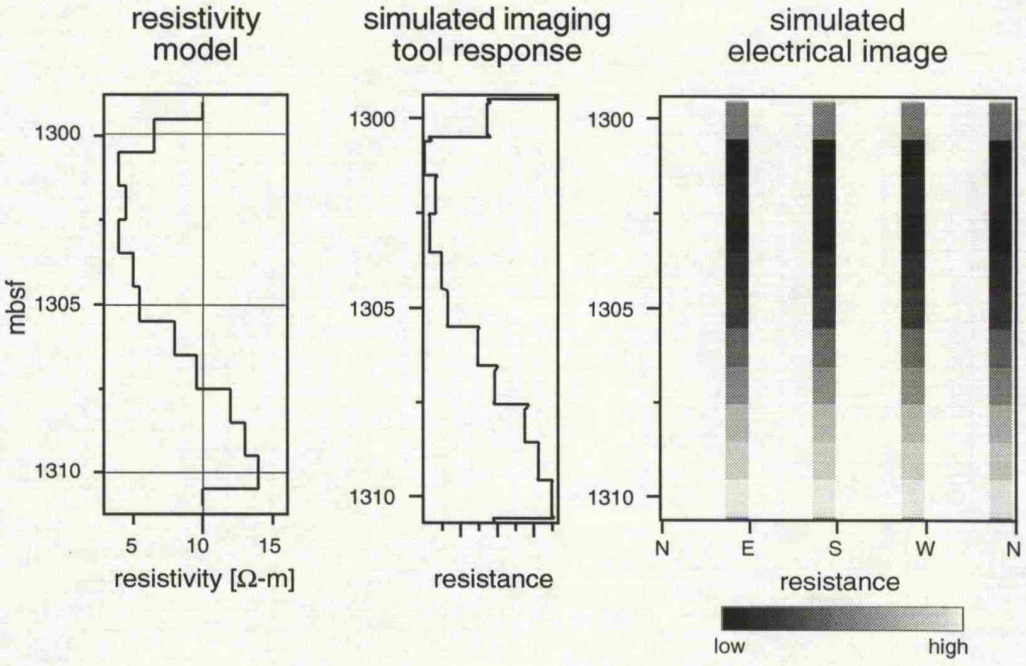

Figure 5.4.2 Numerical simulation of data from ODP Hole 793B.

A borehole diameter of 0.29 m is specified to match caliper data. The drilling fluid occupying the borehole, which is sea water in the case of the ODP, has a resistivity of 0.3 Ω-m. This is used as the input to the electrical imaging model, which generates the synthetic electrical image shown on the right. The modelled image shows general agreement with the ODP data, as would be expected. Note that the fine detail picked up by the FMS is not present in the model and is not therefore expected in model results. This illustrates the difference in resolution between FMS and conventional resistivity logging measurements. Although this does not constitute a rigorous test, experiments such as this provide evidence that the numerical model is at least viable.

5.4.2 Offhole resistive anomalies

Figure 5.4.3 shows a set of results for a different model in which a horizontal, conductive (blue) zone has a resistive (red) anomaly within it. Such a resistivity model can find geological relevance if interpreted as e.g. dolomitic porosity structure, a gas-filled cavity within a conductive bed, solution breccia, or mineral infilling.

The fracture is 15 mm deep, and the resistive anomaly is a cube with sides of 5 mm. The resistive feature is effectively modelled at different distances from the borehole wall. The anomaly is initially absent (top), but is then introduced intersecting the borehole wall (middle) and finally at 5 mm away from the borehole wall (bottom). It can be seen that the resistive feature contributes an anomaly to the tool response even when it does not intersect the borehole wall.

Resistive anomalies on a similar scale to that modelled above have been observed in ODP data. A section of FMS image from ODP hole 835B, which is located in the Lau Basin, near Tonga in the Pacific Ocean (Parson et al., 1992) is shown in Figure 5.4.4. This interval corresponds to a turbidite layer consisting of clayey nannofossil ooze. The layer itself is very uniform, exhibiting very little sedimentary structure; this is reflected in conventional log curves over the interval, and also in the recovered core. The FMS image shows much more variation than might be expected, and is characterised by resistive spots (most abundant on the second pad trace). These anomalies are thought to be caused by clumps of foraminifera fossils which are composed of resistive calcite, and have dimensions of the order of up to 5 mm (Rothwell, pers. comm., 1995). The modelling illustrated in Figure 5.4.3 confirms that such a

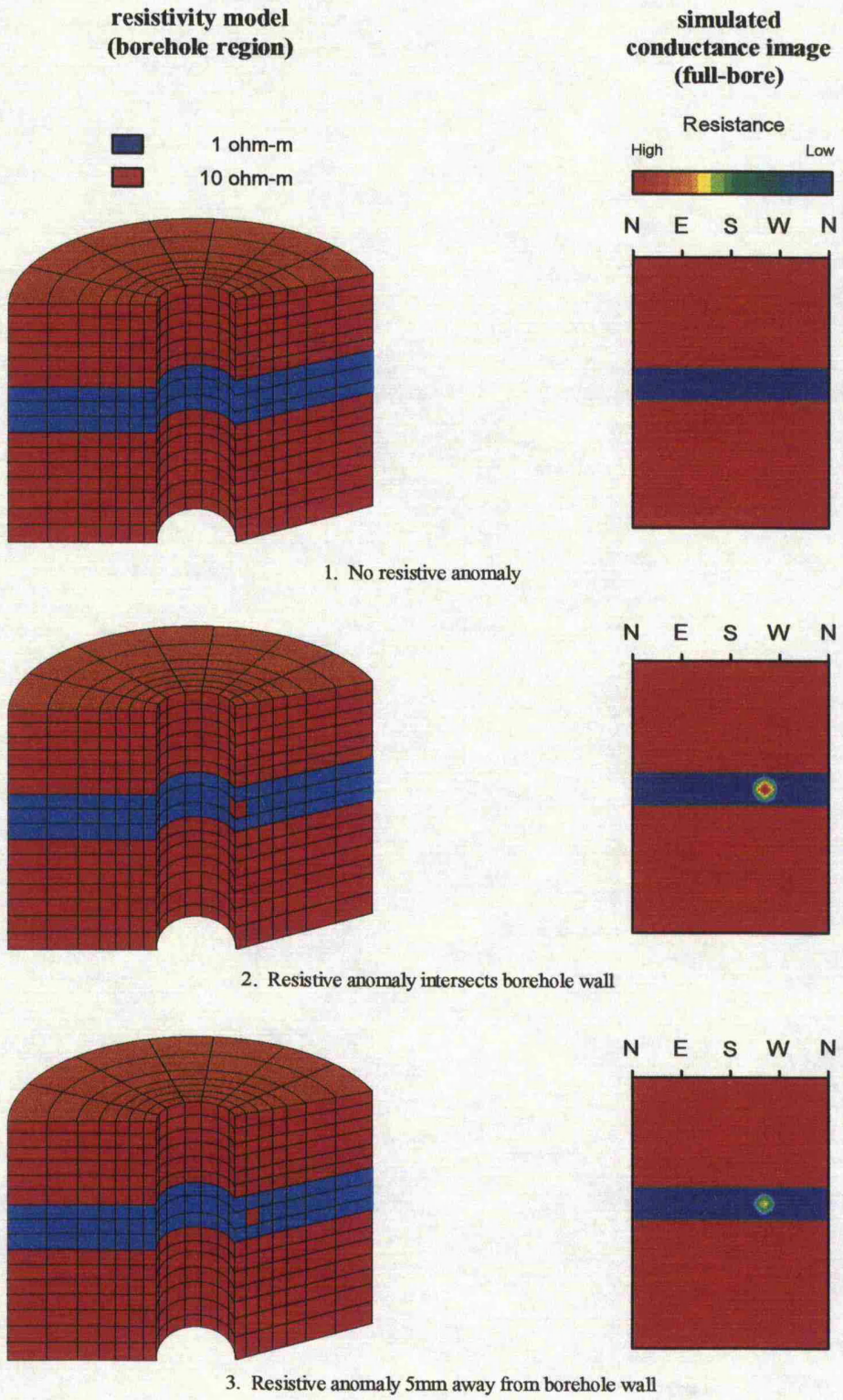

Figure 5.4.3 Simulated electrical imaging tool responses to a resistive anomaly within a conductive zone.

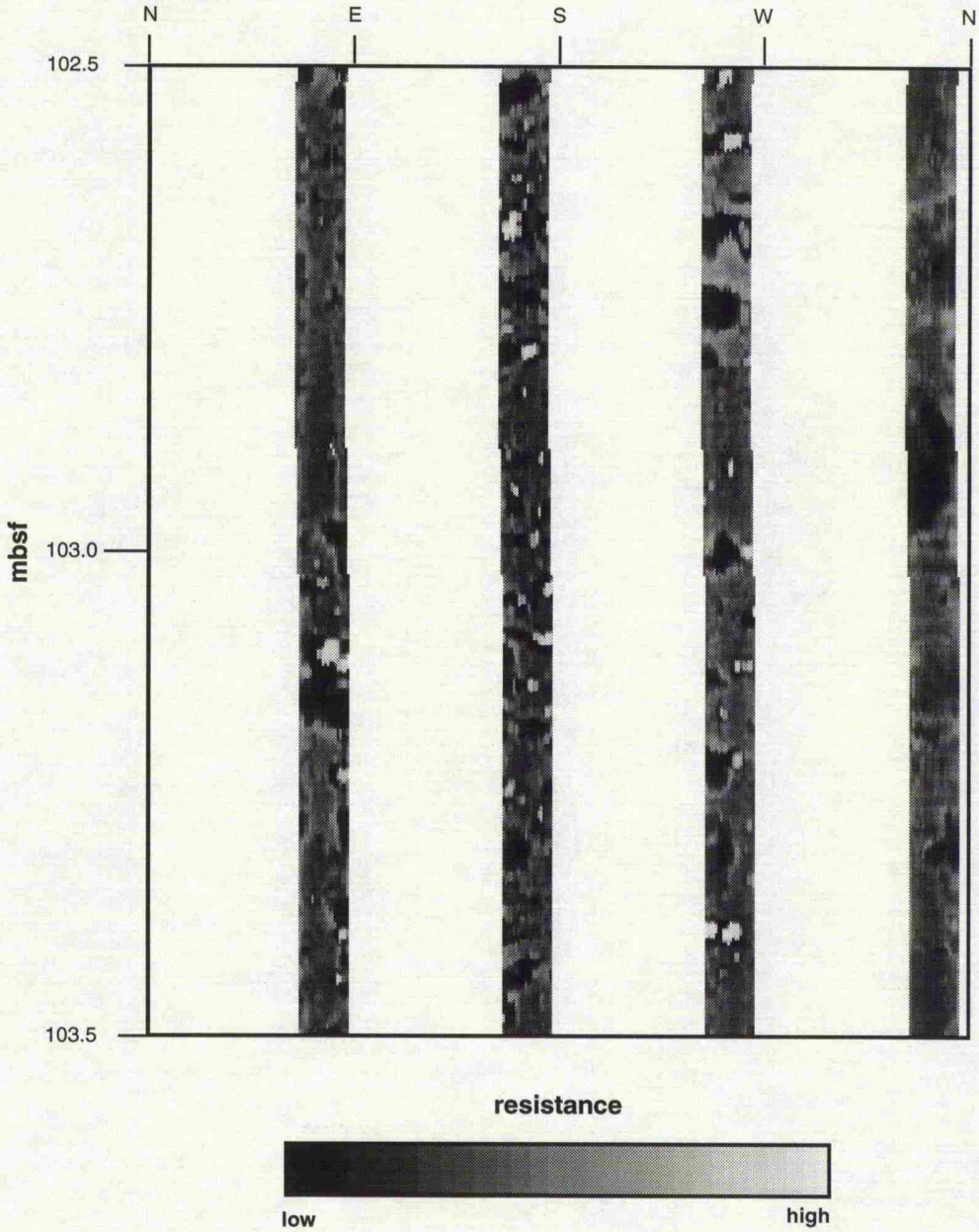

Figure 5.4.4 Resistive anomalies observed on FMS image from ODP Hole 835B.

proposal is reasonable, and in addition suggests that the less bright spots may be caused by fossils located a few mm away from the borehole wall. It is noted that the depth of investigation modelling described in Section 5.4.4 extends the present model, by looking at different resistivity contrasts and anomaly depths, and adds more weight to the hypothesis that highly resistive features are causing the observed image anomalies.

5.4.3 Dipping, resistive layer

Steeply dipping, thin resistive layers are reported to cause halo-like anomalies on electrical images, and provide a good example of a case when there is a mismatch between electrical and optical images, as illustrated in Figure 5.4.5. Such situations can arise when cemented fractures intersect the borehole. Examples of such effects occurring in FMS measurements are given by Serra (1989); similar effects in the EMI response are reported by Seiler et al. (1994), and are shown in Figure 5.4.9.

Bourke (1989) reports that modelling by Trouiller (1988) indicates that the anomaly is caused by distortion of the current flow of the FMS when it encounters the resistive layer, counteracting the focusing effect of the tool, as illustrated in Figure 5.4.6. The tool senses the presence of the resistive plane before it actually contacts the borehole wall, causing anomalously high readings on one side of the fracture intersection which result in the pale 'halo' or 'aureole' seen in some electrical images.

A finite difference model has been set up which aims to replicate the halo effect. Unfortunately, the geometry of a dipping plane does not conveniently coincide with that of the cylindrical polar grid—this situation illustrates one of the limitations of the finite difference grid. A dipping layer is set up by using a 'staircase' effect as illustrated in 5.4.7. To further simplify model definition, the resistivity distribution was chosen to be azimuthally symmetrical, so in three dimensions it actually represents a cone (rather than a plane) intersecting the borehole.

Results of the modelling are shown in Figure 5.4.8. On the left of the Figure, the relative location of the dipping anomaly is shown for comparison with the simulated imaging tool response, which is on the right of the figure. In this diagram, the imaging tool response has been shown as a raw resistance curve to emphasise the asymmetry of the simulated response. The curve exhibits a steep variation on the lower side of the intersection, whilst it decays

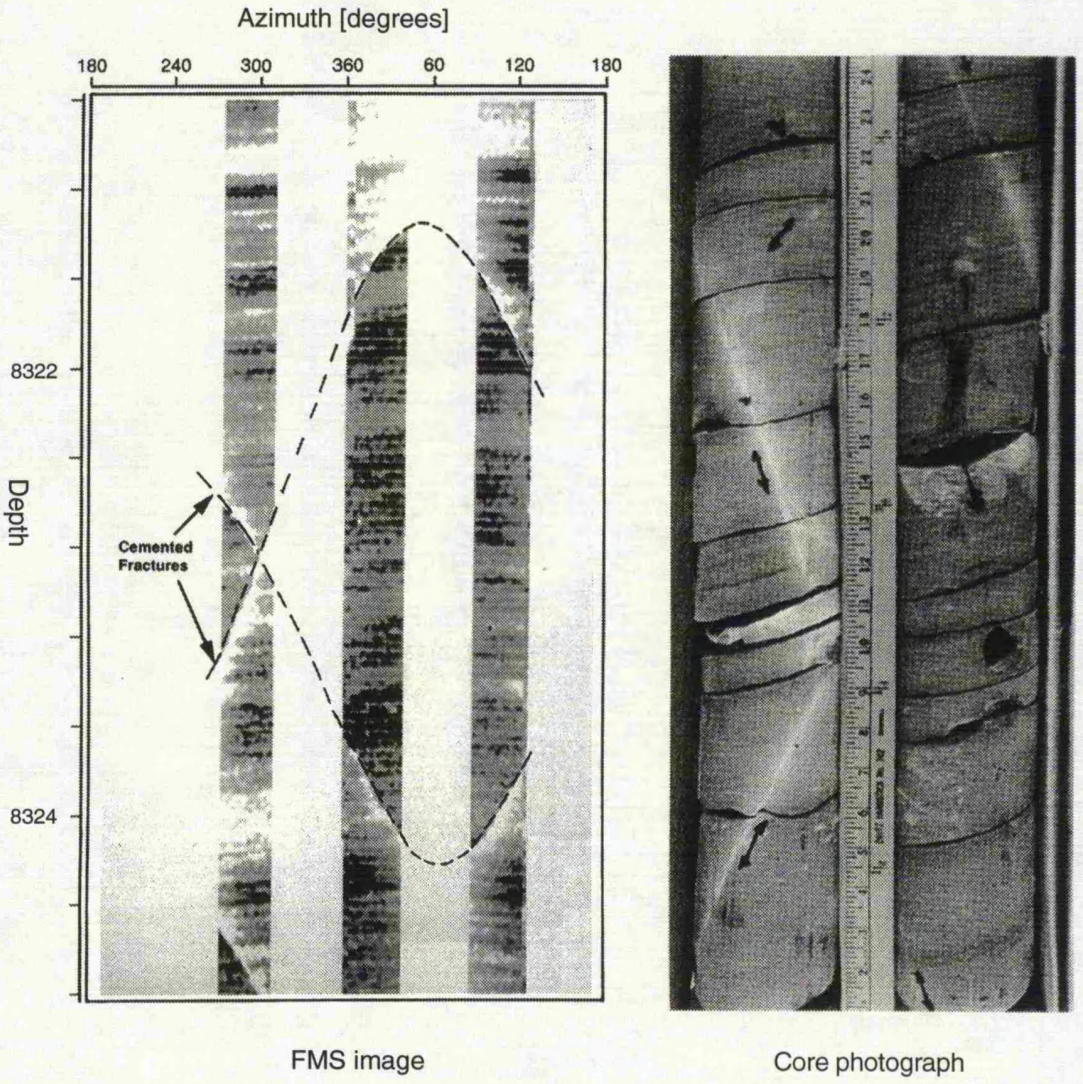

Figure 5.4.5 FMS image of steeply dipping, conjugate cemented fractures exhibiting halo effect, with corresponding core photographs (after Serra, 1989).

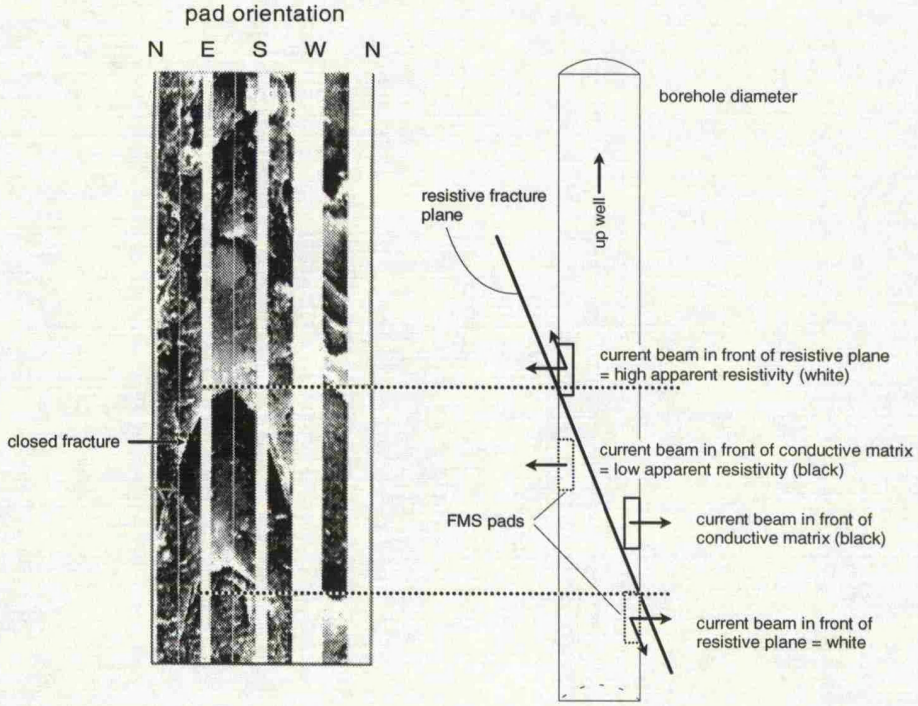

Figure 5.4.6 Illustration of distortion of current flow of the FMS in the presence of a dipping resistive fracture (after Serra, 1989).

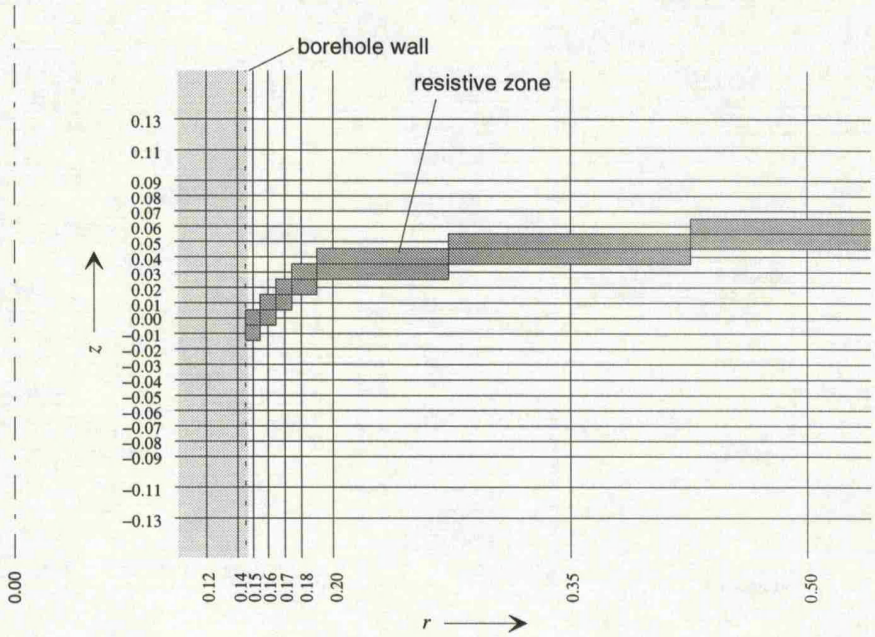

Figure 5.4.7 Vertical section through an azimuthally symmetrical approximation to a dipping plane: a resistive 'cone'.

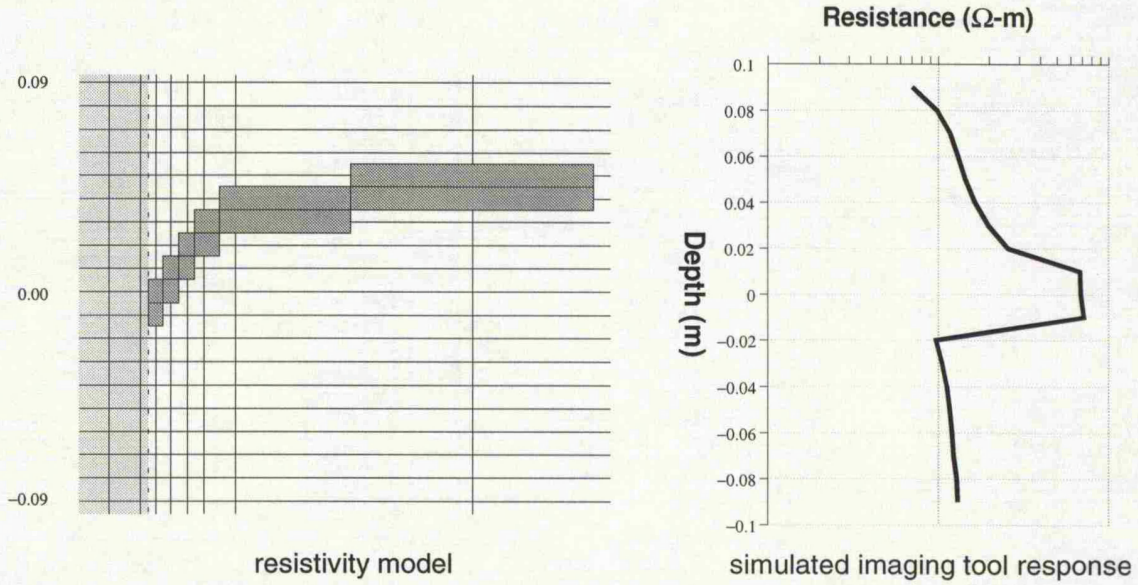

Figure 5.4.8 Finite difference model of a resistive cone: results.

much more slowly on the upper side. When converted to a grayscale image this corresponds to a pale halo which is similar in appearance to those seen on electrical images, as can be seen in Figure 5.4.9.

5.4.4 Depth of investigation

A series of model simulations have been performed to investigate the nature of the imaging tool response to small, near-hole anomalies as illustrated in the upper half of Figure 5.4.10. This model series is intended to quantify the simulated tool response with respect to:

1. distance of the anomaly from the borehole;
2. formation/anomaly resistivity contrast (for both conductive and resistive features).

The anomaly was chosen to be a cube with sides of 1 cm. For the case of a conductive anomaly within a resistive formation, the formation resistivity was set to 1000 Ω-m while the cube resistivity given values of 100, 10, 1 and 0.1 Ω-m. In the case of a resistive anomaly in a conductive formation, the formation was set to 0.3 Ω-m, and cube resistivities of 1, 10, 100 and 1000 Ω-m were modelled. In cases the where cube was more resistive than the formation, a resistive shoulder was introduced in order to make the model more physically relevant: without the shoulder, there would effectively be no borehole, and the simulation would be

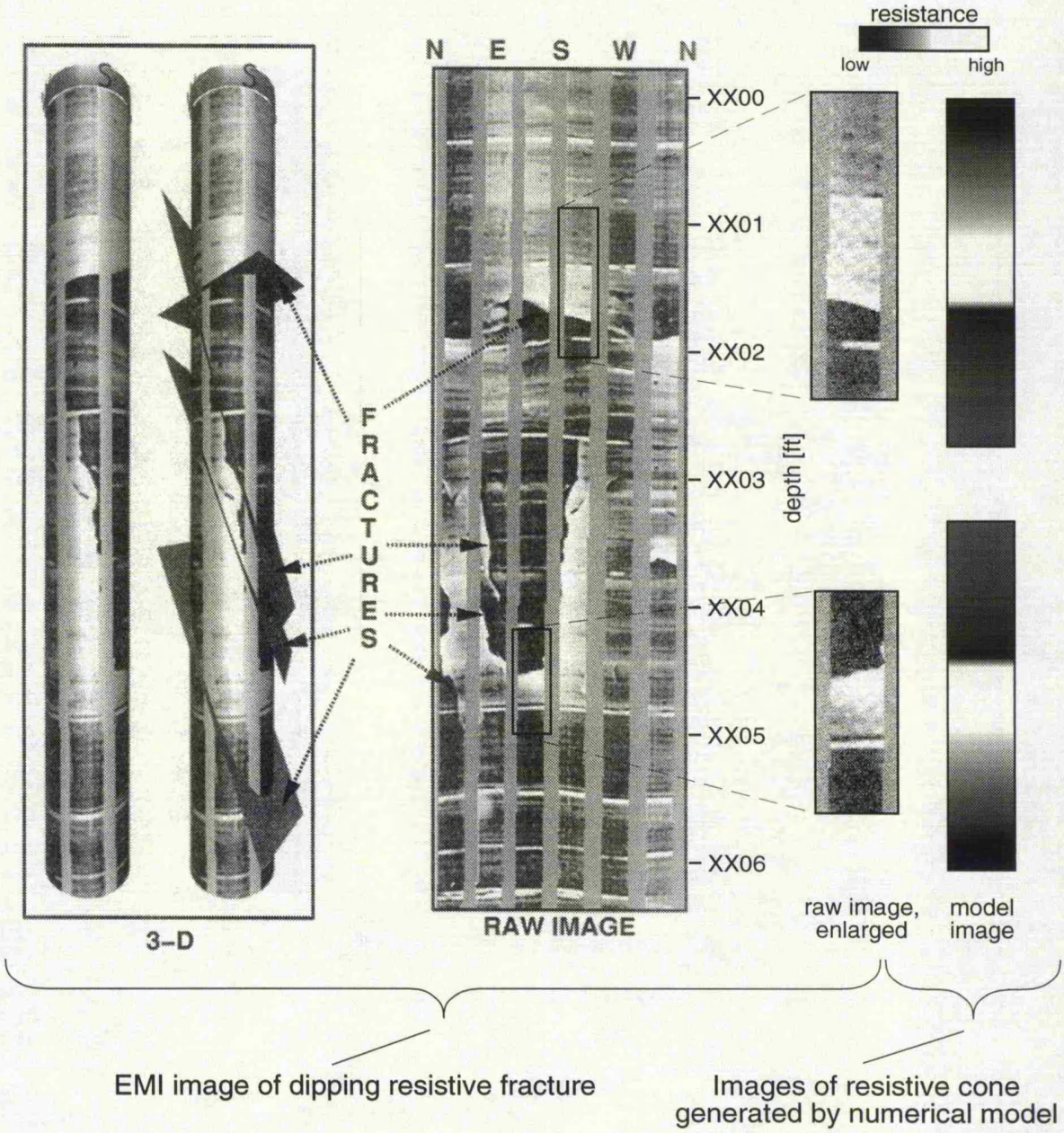

Figure 5.4.9 EMI response to dipping resistive fracture (*left and centre*), after Seiler et al., (1994), compared with images from model of resistive cone intersecting borehole (*right*).

analogous to running the tool in a tank of water. In addition, the shoulder improves current flow back to the current return, and aids the passive focusing of the tool.

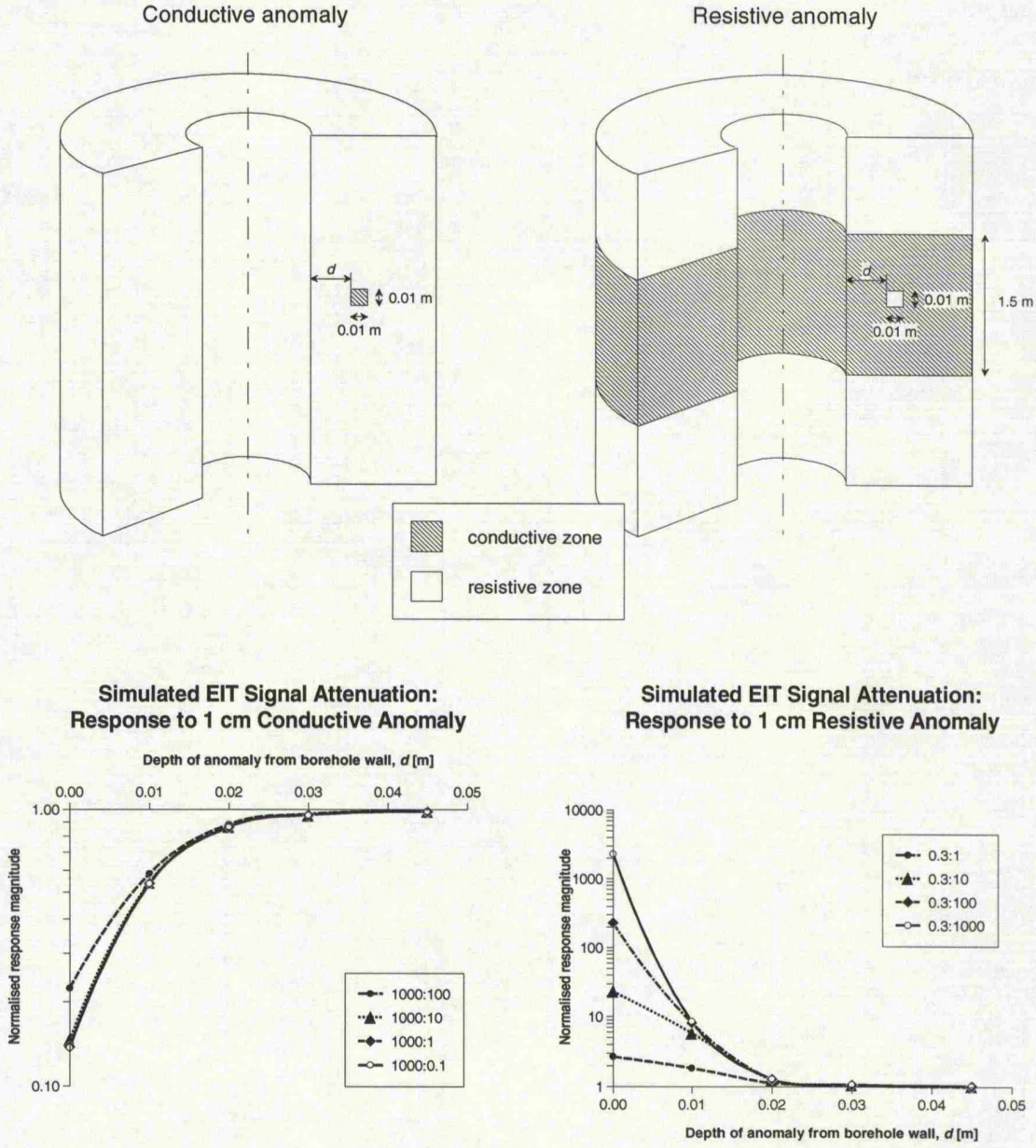

Figure 5.4.10 Investigation of imaging tool response to near-hole anomalies.

The imaging tool responses have been summarised in the two graphs in the lower part of Figure 5.4.10. The normalised response magnitude is the maximum measured button resistance expressed as a proportion of the 'background' tool response when there is no anomaly present. The tool is seen to give the strongest response to features within 2 cm of the borehole wall, for both resistive and conductive anomalies, irrespective of resistivity contrast.

The variation in response to resistive versus conductive features is not symmetrical. Both graphs show data for a variation in resistivity contrast of four orders of magnitude, but the conductive anomaly response is not seen to vary once the contrast is above 100:1, whilst, for the range of contrasts modelled, the resistive response continues to increase as the contrast increases. This is because the resistive anomaly forms a barrier to current flow and as the resistance of the anomaly increases, successively larger potential differences across opposite ends of the cube will be required in order to enable current to flow. The reverse is not true of a highly conductive cube: a threshold value is reached (around 100:1 in the above model) where the potential drop across the cube becomes very small in comparison to the drop across the rest of the formation; beyond this stage variations in the conductivity of the cube have little effect on the potential distribution in the formation, and the tool is effectively sensitive only to the more resistive formation. It is noted that in the case of a resistive anomaly, a threshold is reached in cases where the cube does not contact the borehole wall—for example, the response to contrasts of 0.3:100 and 0.3:1000 can be seen to be similar for an anomaly located 1 cm from the borehole wall. As the anomaly becomes more resistive, current will tend to bypass it in favour of travelling through the more conductive formation: beyond a certain value, virtually no current will pass through the resistive cell, and further increases in resistivity will have little effect on the overall current flow and potential distribution.

It is further noted that the above results for resistive anomalies provide more information to support arguments that clumps of fossils are the possible cause of the white spots observed in Figure 5.4.4, as discussed in Section 5.4.2.

5.4.5 Deepening conductive fracture

Figure 5.4.11 shows slices through a set of simplified physical models, each exhibiting a horizontal conductive layer of finite radial extent. Such a feature could be interpreted, for example, as a fluid-filled fracture, a shale bed within a sandstone, or a porous layer within a tight rock.

The models are azimuthally symmetric and, from top to bottom, exhibit an increase in depth into the formation of the conductive layer. In three dimensions, the model represents a horizontal conductive disc or annulus, the diameter of which increases in each step of the model, from 0.02 m to 2.4 m. The vertical depth of the feature is 0.02 m. The resistivity contrast between rock and fluid is 10:1. On the right of the Figure the simulated response of

the numerical model is shown for each situation. For this model, which is effectively 2-dimensional, it is more instructive to present the response as a resistance curve rather than an unwrapped image of the borehole wall (which would appear as a horizontal stripe). In the case of the shallowest layer, a shouldering effect is observed either side of the conductive zone. This effect rapidly dies off as the conductive layer extends further into the formation, so that responses for a 5 cm depth feature and a 2.4 m depth feature are virtually identical. This suggests that, for example, gleaning information about whether or not a fracture is connected away from the borehole zone using an imaging tool would be difficult. In addition, it may be possible to infer when conductive features are very shallow by looking for shouldering effects at the edge of the response they produce.

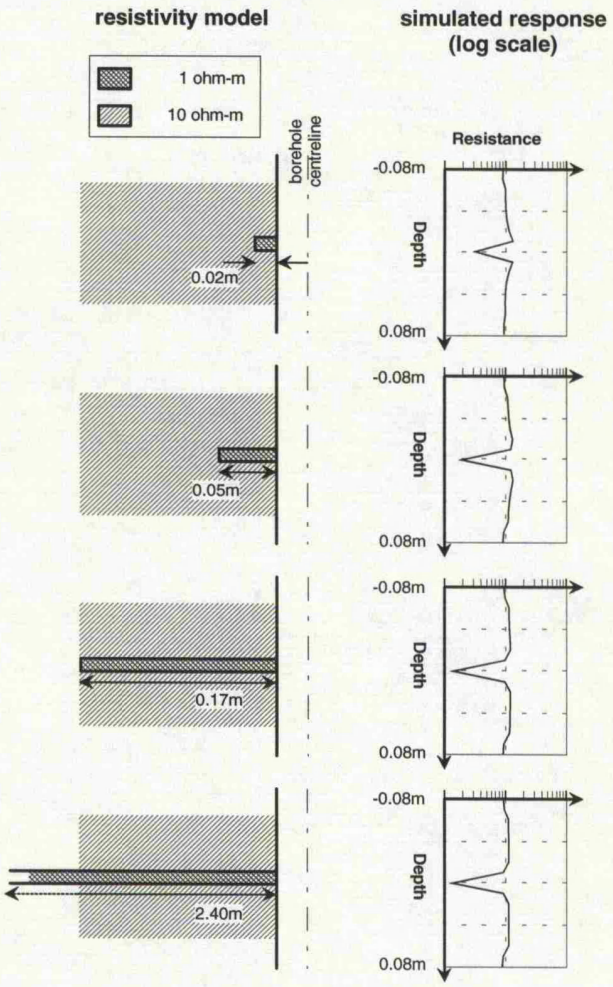

Figure 5.4.11 Simulated electrical conductance tool responses to a deepening conductive, horizontal layer (using a logarithmic resistance scale).

Figure 5.4.12 presents the same data as in Figure 5.4.11, but using more intermediate steps. A linear scale has been used for the resistance measurements to emphasise the shouldering effect, which can be seen to be pronounced at shallow depths but falls off as the radial extent of the conductive layer increases.

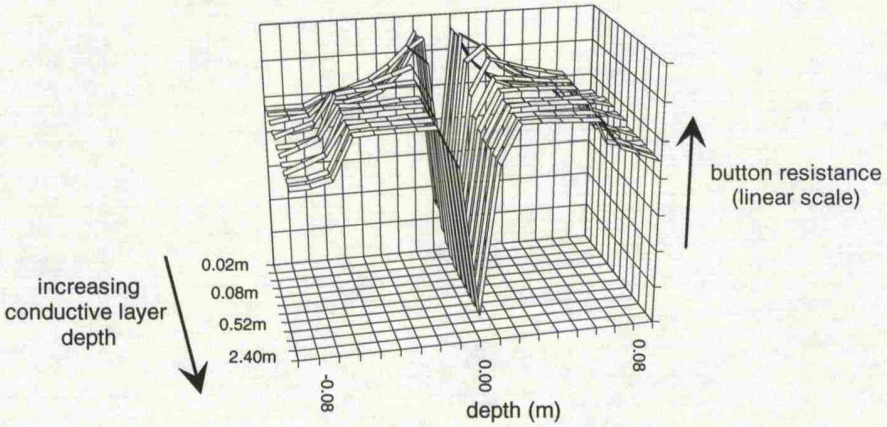

Figure 5.4.12 Simulated electrical conductance tool responses to a deepening conductive, horizontal layer (using a linear resistance scale).

On an electrical image, a shouldering effect on a shallow conductive feature would appear as a pale zone at the border of the dark conductive region. Such a feature may be present in the FMS image in Figure 5.4.13, which corresponds to a metre interval in ODP Hole 835B (see Section 5.4.2). Core recovered from this depth consists of clayey nannofossil ooze, and does not exhibit any features on a similar scale to the larger dark zones present in the electrical images. Pale fringing is observed at the edges of a conductive feature present on the eastern pad trace (enlarged on the right of Figure 5.4.13); the above models suggest that this is therefore a shallow feature and could be caused by poor pad contact on the borehole wall resulting in a thin layer of (conductive) borehole fluid between the pad and the borehole wall. This provides another example of a mismatch between electrical and optical images.

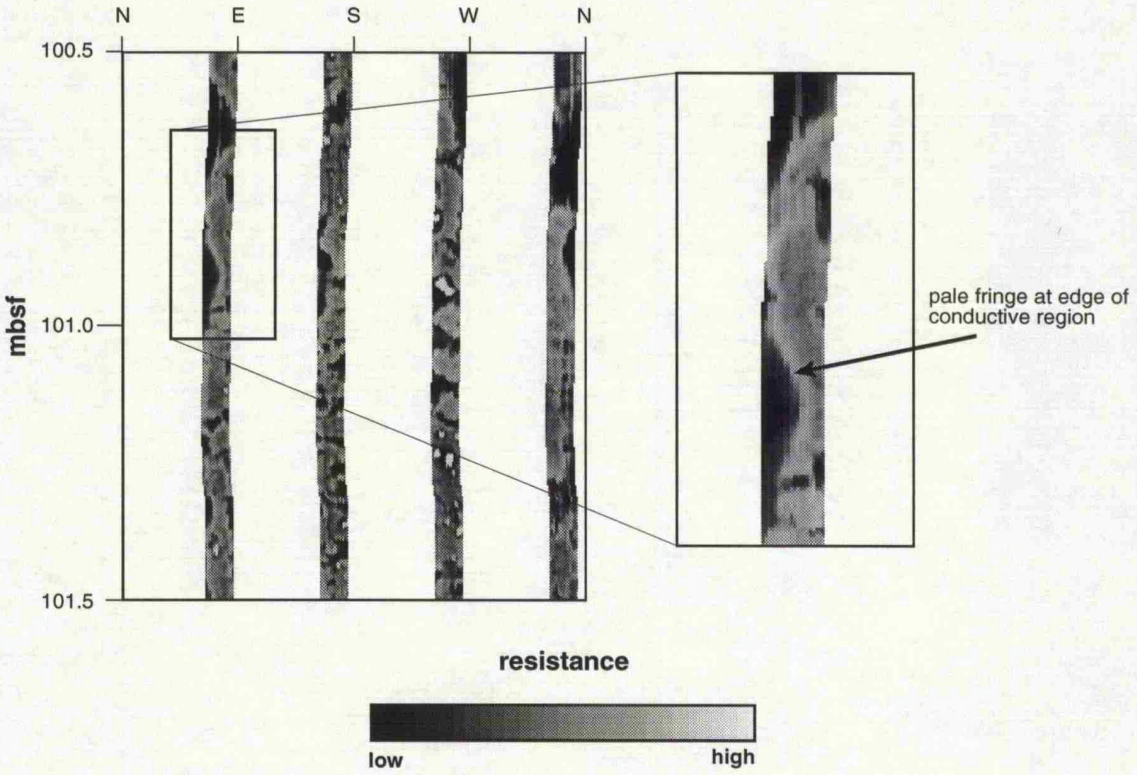

Figure 5.4.13 Pale fringing observed at edges of conductive feature observed on FMS image from ODP Hole 835.

5.5 Discussion

The initial goal of the modelling applications presented in Section 5.4 was to provide evidence that the numerical model is valid. In the horizontal layer model (Section 5.4.1) it was shown that the simulated imaging tool response is similar in a general sense to actual data, but comparison was made at a lower resolution than the real tool response. In order to make a comparison at higher resolutions more information about how the tool varies current and how the raw measurement data is processed would (ideally) be required. Even if such information was available, calibration (and thus quantification) of the raw tool data could still prove extremely difficult due to the nature of the measurement itself which suffers from inherent problems such as the contact effects on the buttons where the tool measurement is made.

The model of a cone (Section 5.4.3), intended to approximate a dipping fracture, illustrates the limitations of the finite difference method, which is constrained by the coordinate system on which it is based when generating a resistivity distribution. Despite this, it is noted that the representation of a slanting line on a non-aligned grid is no different to the use of pixels on a screen or dots on a printed page to create an image. Using this analogy, it can be seen that so long as the finite difference grid is fine enough, any oblique feature may be adequately approximated. In addition, the depth of investigation models (Section 5.4.4) indicate that the electrical images do not pick up features more than a few cm away from the borehole, so in principle a grid could still be coarsened away from the tool pad region without loosing accuracy. The modelling described in Section 5.4.3 successfully reproduced halo effects seen in actual images of an oblique, resistive feature (Figure 5.4.9) indicating that the simulation is capable of handling these kinds of models.

Modelling results presented in Section 5.4.4 indicate a tool depth of investigation of a similar order of magnitude to published information (Bourke et al., 1989), although in general image sensitivity seems shallower than maximum depths reported in the literature. The results are considered reasonable in the absence of detail on how reported tool depth of investigation has been arrived at (for example, details of the modelling of Trouiller [1988] have not been published). The way the pad current is focused is particularly crucial in influencing the depth to which current travels into the formation. Precise inferences cannot be made unless more information about tool characteristics becomes available.

The depth of investigation modelling confirms reported findings that the tool response to conductive versus resistive anomalies is not symmetrical (Bourke et al., 1989). In Section 5.4.4 considerations of variation of electric potential and current flow within the formation were used to explain the observed model results. The simulated tool is not sensitive to variations in conductivity once a certain threshold is exceeded. It is interesting to note that in reality the actual tool can suffer current saturation in conductive regions, although the cause of the phenomenon may be due to power limitations of the tool, which are not simulated in the model.

It is worth noting that the electric potential field is known throughout the whole volume of formation covered by the model. This enables parameters such as current flow to be investigated in three dimensions in the whole borehole region rather than just specific points on the surface of the tool (which would be the case in a field test), allowing confirmation of ideas such as those proposed in Section 5.4.4. As an example, Figure 5.5.1 illustrates the modelled electric potential and current flow for an imaging tool located near a narrow, conductive event (as described in Figure 5.4.11). A series of vertical sections through the simulation is shown. The left and central images illustrate the simulated electric potential over the whole model. In the central image, the pad region is indicated by red colouring (high potential) and the potential can be seen to decay away to violet (low potential) further up the borehole wall where the current return is located. On the right hand side, a blow up of the pad region illustrates the simulated current flow out of the pad. The passive focusing mechanism of the pad and lower part of the tool manifests itself as high current flow in the conductive borehole fluid. Higher current flow is apparent in the centre of the pad, which is where the conductive feature in the resistivity model is located. The electrical image is generated from these currents.

This additional 3-D information enables the modeller to appreciate exactly how the tool is behaving under specified conditions: for example, the amount of passive focusing that is being applied is evident from inspection of the current flow up and down the simulated borehole.

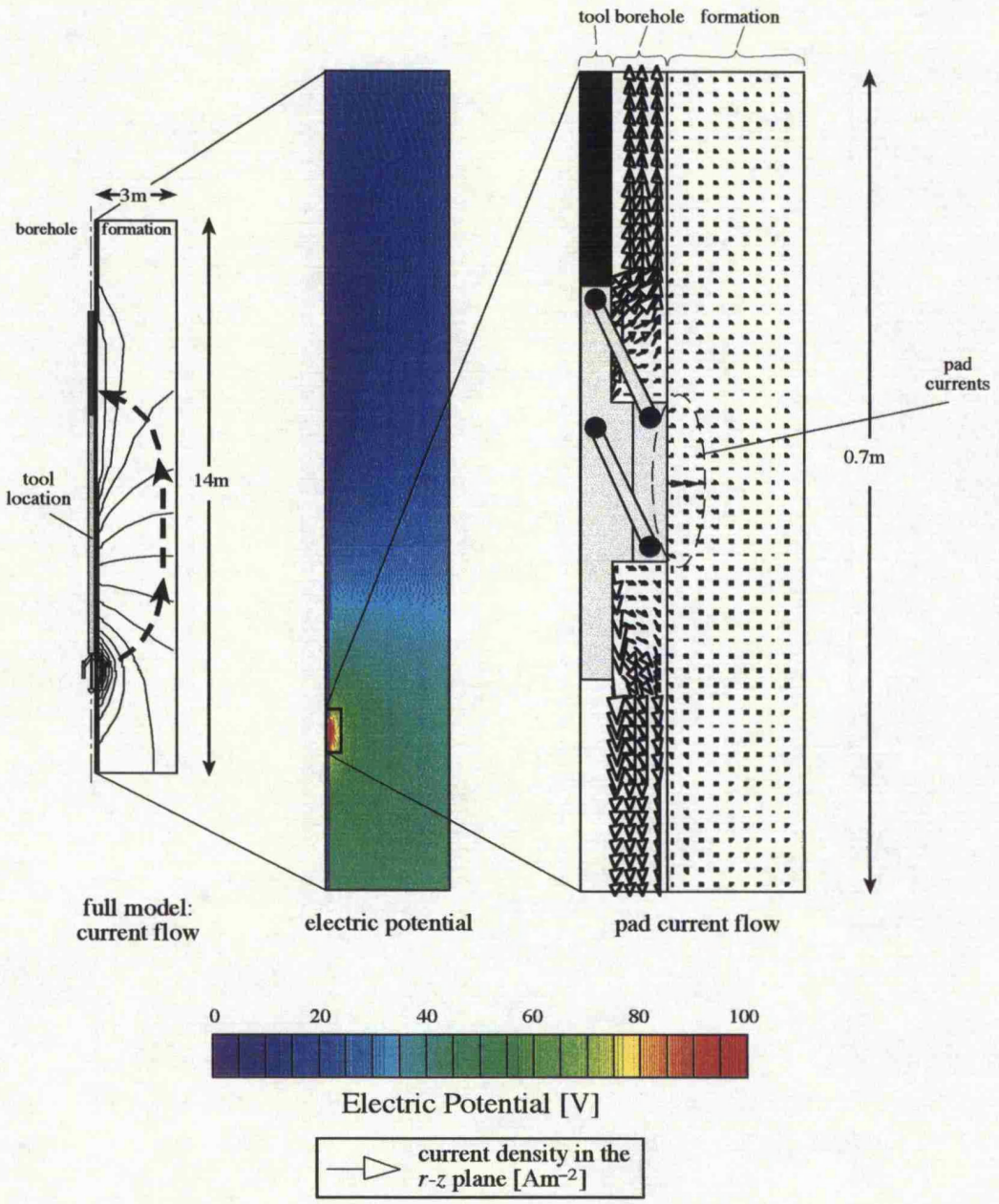

Figure 5.5.1 Vertical sections through a simulation of an imaging tool located near a narrow, conductive event.

5.6 Summary and conclusions

As stated in the introduction, the simulation only addresses primary effects of the electrical imaging process, due to the lack of availability of detailed information on the tool construction and signal processing techniques. One avenue to explore with a numerical model is to try to simulate closely real tool data over specific intervals of interest, at a high resolution. A more rigorous test would involve using button resistance data to create a more detailed resistivity model. Button measurements are not calibrated to resistivity, but could be calibrated at a lower resolution with conventional logs.

A useful modelling enhancement would be to enable oblique bodies to be modelled by using interpolation between grid cells which are partially intersected by resistivity distributions that are not aligned with the grid coordinates (§5.5). Averaging between cells may be used to smooth the jagged edges—Ohm's Law can be used as a physical basis for the derivation of an interpolation law. Automatic generation of models involving dipping planes based on cylindrical meshes could be incorporated into the model. Such models would (hopefully) reproduce the sinusoidal features observed when planar features intersect the borehole at an oblique angle (see, for example, Fig. 5.4.6).

Modelling can help to constrain the possible geological and geometrical effects that could give rise to an electrical image of interest. One example is an FMS image from ODP Leg 133 (Jackson et al., 1993) where a hint of possible structure in a carbonate reef is observed (Figure 5.6.1). Work such as that described in Section 5.4.4 can add weight to speculation about how deep into the formation the measurement may be sensing, and the possible geometry of the feature of interest.

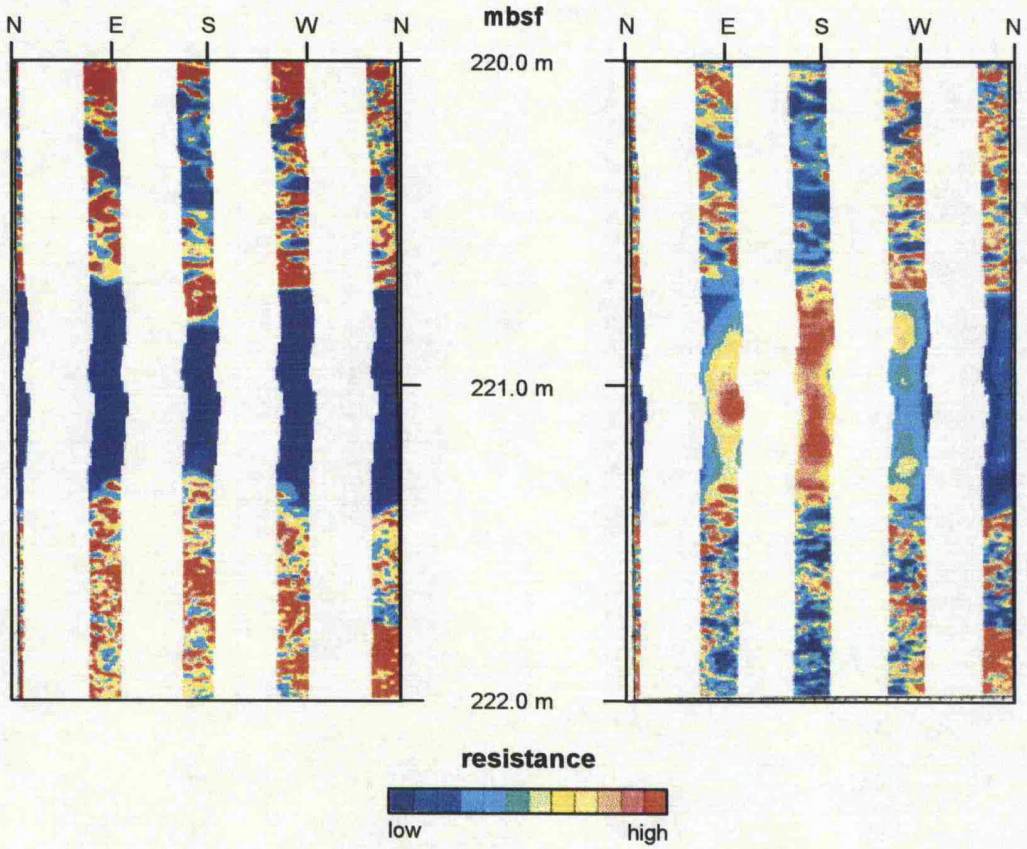

Figure 5.6.1 FMS image data from ODP Leg 133.

The numerical model described in this chapter has been seen to produce viable results in test situations, and in addition has provided an insight into the way imaging tools are likely to respond to simple geometries which may approximate geological situations. Understanding such features, especially at high resolutions of a few millimetres, is important in validating the interpretation of downhole images in terms of their geological significance. Whilst the limitations of numerical modelling of this kind are recognised, a forward model is often most useful when applied to fundamental situations. The modelling allows an appreciation of first order effects generated by the measurement technique, rather than finer anomalies which might be caused by specific geometry of a particular tool. The results serve to emphasise that tools such as the FMS and EMI are electrical rather than optical imaging devices. In particular, in the models presented here such tools are seen to have small but finite depths of investigation which in certain situations may lead to images which are at variance with conventional visual interpretations of borehole wall features.

CHAPTER 6

Conclusions

In Chapter 1 research objectives were introduced which involved elements of numerical model *development* and model *application.*

6.1 Assessment of model development

The initial models developed aimed to simulate ('actively') focused electrical measurements (Chapter 4). In Section 4.1, the focusing technique is applied to field data, and is seen to be robust enough to successfully produce synthetic focused measurements despite a degree of noise in the raw data set. The synthetic focusing technique is also successfully applied to the numerical model: theoretical potential distributions satisfy the focusing conditions as required. The model is able to reproduce characteristics seen in field data, and agrees well with analytic solutions used to test its accuracy.

Chapter 4.2 describes the development of the model to cater for downhole situations by simulating a novel focused borehole tool: the Ocean Drilling Program High Temperature (ODPHT) tool. Both the 'wrapping' method and the modification of the focusing algorithm for a cylindrical grid were successfully implemented, with current conservation laws being obeyed and symmetry in the model being preserved. Focusing is achieved even in unfavourable conditions (e.g. a highly conductive borehole). The three dimensional (3D) model also matches results from a modified two-dimensional scheme. Derived geometric factors are sensitive to small changes in the calculated electric potential, which can be caused when the number of azimuthal nodes is very low. This effect is thought to be caused by discretization errors.

In Chapter 5, the development of the model to simulate downhole electrical imaging devices is described. This requires the modelling of a passive focusing mechanism, which is achieved by considering the resistor network that is analogous (§3) to the numerical model. Investigation of current flow in the model and the results of various model applications (§6.2) indicate that the model is operating correctly.

In all cases the accuracy of the numerical models have been demonstrated by comparison with analytic results. In addition to these rigorous tests in idealised scenarios the model gains credence from the fact that the simulation results match characteristics in the actual field data.

The FD method is one of many possible solution strategies for simulating electrical current flow (Chapter 3); which one is chosen for a specific problem depends on the problem itself and the compromise between speed, accuracy and computer power required. Of the possible solution approaches, the finite element method is the only other technique that is versatile enough for this work. While the finite element method has advantages such as the possibility of arbitrary grid node locations and irregular grid boundaries, these are not required for modelling measurements made by electrode arrays. Boundary conditions are typically regular and are easily catered for with the FD method; the only disadvantage is the inclusion of unnecessary nodes due to grid restrictions (see e.g. §4.1). Additional features of the FD approach which have benefited numerical models are its direct relationship with the generalised Poisson equation (§2) and the 3D resistor network analogy which allows current flow to be easily derived (from the primary parameter: electric potential) in any model. Models are generally limited in complexity only by grid size and solution time.

The benefit of 3D modelling has been demonstrated despite the relative simplicity of the models described in this work. Increased complexity may introduce detail that is of little help when interpreting field data, especially when the effect of noise is taken into account. There are a wide range of basic features (for example a point source rather than a line source, or an isolated resistive feature rather than a resistive plane) many of which have been addressed by the modelling in this work, that can only be properly represented in three dimensions.

6.2 Assessment of model application

The application of the numerical model has been expanded alongside the model development (Chapters 4 and 5). The modelling of the ODPHT tool (§4.2) was restricted to basic models in order to determine the tool's geometric factor, but simulations have been used to address a wider range of problems in Section 4.1 and Chapter 5.

The numerical model is used in the case of fieldwork in Germany (§4.2) as an interpretational aid by attempting to reproduce the principal features seen in field data. In cases where there are shallow subsurface contacts between rocks of contrasting resistivity the

modelling is particularly successful, demonstrating that the focused measurement provides enhanced fault detection. The simulations also serve to provide guidelines for areas of application where the use of the focused surface array would be beneficial.

In the case of the electrical imaging simulations (Chapter 5), the emphasis of the modelling shifts to characterising the tool response, and verifying that the model is a valid one (since some of the operational details of imaging devices are not available). The model is validated by comparison of simulation results with data from well-constrained situations. There are a variety of potential applications of the imaging simulations: mismatches between electrical and optical images can be identified; the 3D response of the imaging tool can be investigated in terms of its current flow characteristics and consequent imaging response; interpretation (or speculation as to the nature) of specific features can be confirmed or discredited.

Chapter 2 gives an indication of the wide range of possible applications of resistivity measurements. Numerical simulations can play an important part in any one of them. Even within this thesis, simulations of various focused measurement devices have been used to investigate a range of different applications both on the earth's surface and in downhole environments.

6.3 Recommendations for further work

The numerical model, which models the flow of artificially induced d.c. electricity in 3D, could be extended in a variety of different directions:

- existing models of specific measurement devices could be enhanced;
- the basic model could be applied to different devices;
- general model improvements, for example: more efficient solution algorithms for the FD equations, or the explicit inclusion of geological information such as anisotropy or bed dip and thickness as input parameters;
- the modelling (computer) program could be improved;
- the modelling and interpretation of more complex geology could be attempted.

Each of these ideas are discussed below.

Development of existing model applications

The modelling of the field data carried out in Germany (§4.1) only attempted a reconstruction of basic features based on vertical contacts with or without an overburden. More sophisticated models could easily be defined involving, for example, dipping fault planes or conductive features in inferred fault zones to simulate the presence of clay or water. No use of non-d.c. resistivity field measurements has been made in the case studies presented in sections 4.1.5. and 4.1.6. In addition to verifying independently derived interpretations, different geophysical measurements often complement each other by filling in the gaps inevitably left when any one method is considered in isolation. The full potential of these data can only be realised if they are integrated more closely with each other to provide an interpretation based on all available survey information.

The calculation of geometric factors for the ODPHT tool (§4.2) makes only minimal use of the 3D FD model. More complex geological models can be readily defined and simulated using the existing program. Tool characteristics and response could be assessed and could prove especially useful for investigating performance in the envisaged operating conditions of high salinity (and thus high conductivity) borehole fluids. Using a similar approach to that of the focused surface array interpretation, specific logging data could also be interpreted by comparison with suitable models.

The sophistication of the electrical imaging tool simulation (§5), based to a large extent on Schlumberger's FMS tool, is limited by the availability of information in the public domain. Use of information that is currently confidential would allow a more detailed model to be constructed and evaluated. Imaging tools have been engineered by other service companies (e.g. Halliburton, Western Atlas). When and if suitable information becomes available, models of these tools could also be created using existing program code.

Use can be made of existing FMS data to investigate model versus tool response at a higher resolution than has been tried at present. Raw button measurement curves could be calibrated at intervals (at a lower resolution) using conventional, quantitative resistivity measurements. A resistivity model of the formation could then be generated based on this information and used to test the simulation at the same resolution as the button measurement curves.

Work has begun to include dipping planes in the numerical model. Extending this approach, input for modelling of bodies of arbitrary geometry, structural discontinuities, or specific fracture geometries could be incorporated into the model.

Extension to new model applications

There are many different resistivity measurement devices which make use of d.c. electricity, reflecting the wide variety of applications of electrical measurements (Chapter 2). Any one of these can in principle be simulated using the basic numerical model as a start point. The model can be applied to surface and downhole, focused and unfocused arrays, at both conventional and micro scales.

Development of the numerical model

The basic formulation and solution of the 3D electrical flow problem using the finite difference method and the resistor network analogy has been shown to operate successfully. Different solution methods for the simultaneous equations generated could be compared with the hybrid relaxation method used at present. A wide variety of alternatives exist; which one is best depends on computer power and desired model size, solution time, and accuracy required (§3).

The resistivity models described here are presently defined by specifying a resistivity value for each node of the FD grid. The program could be made more specific to geological applications by allowing input of parameters such as bed thickness and dip, and using internal routines to calculate nodal resistivities from this information. A similar approach could be used to allow anisotropy (§2 and §3) to be included as an explicit parameter.

Development of computer modelling code

The FORTRAN programs used in the modelling are still at an experimental stage. The code could be modularised, providing building blocks for a more general modelling application program. It would also benefit from an enhanced user interface to simplify the process of data input, grid generation, and output/visualisation.

This project has made use of properties specific to the finite difference method, but there is, in principle, no reason why a different solution approach could not be incorporated. A modular approach to program development would be able to take advantage of any

improvements to existing methods, or allow a equation solver for a specific problem to be included without major modifications.

Extension to more sophisticated interpretation

Although there are valid reasons for restricting the complexity of forward models, more detailed problems would provide interpretational aids and 3D analysis directly applicable to field data. A future goal of this kind of modelling is to enable closer integration of simulation and field data.

In the long term, more sophisticated modelling routines could be included in data visualisation software (such as Schlumberger's Diamage or Z&S's Review) allowing quantitative interpretation of field data direct comparison with numerical results. Constraints could be placed on possible interpretations of specific features by automatic or interactive design of models which attempt to replicate observed measurement characteristics.

Quantitative analysis of electrical measurements has a role to play in any one of the wide range of applications of resistivity techniques. It is hoped that the work in this thesis will eventually aid geoscientists in the interpretation of electrical data, perhaps by leading to the development of tools on the workstations of the future.

Appendices

APPENDIX A

Fundamental relations in electrical conduction

A.1 Definitions in current electricity

This section defines electric current, potential difference, resistance, resistivity, conductance, conductivity, and current density from first principles. SI Units are given for each quantity. These parameters are used to develop the vector equations for describing 3D electric current flow given in §2.2.1. Since the finite difference model is analogous to a resistor network (§3.2.1) any of the parameters listed below can be related to the model and interpreted in the context of a 3D simulation: for example current density (eq. A.5) can be deduced from model potentials and inter-nodal resistance values.

When an electrical potential difference is applied to a typical electrical conductor it sets up an electric field within the conductor, and an electric current passes through it. The current consists of the systematic drift of (positively or negatively charged) mobile charge-carriers which are influenced by an electric force due to the field; the direction of the current is taken to be the direction in which positively-charged carriers move. Using the SI Units measurement convention, the fundamental quantity in electricity is electric current, which is measured in amperes [A] (Whelan and Hodgson, 1978). Current (I) is related to charge (Q) by the definition

$$I = \frac{\mathrm{d}Q}{\mathrm{d}t}$$

where ($\mathrm{d}Q/\mathrm{d}t$) is the rate of flow of charge past a given cross-section. Time (t) is in seconds [s] and Q is measured in coulombs [C].

Consider a material which has a constant cross-sectional area A and length l, through which a current I flows (Figure A.1). By definition, the potential difference (or voltage) V_{ab} (volts [V]) between the ends a and b is

$$V_{ab} = \frac{W_{ab}}{Q} \tag{A.1}$$

where W_{ab} (joules [J]) is the work that would be done in moving a charge Q from a to b.

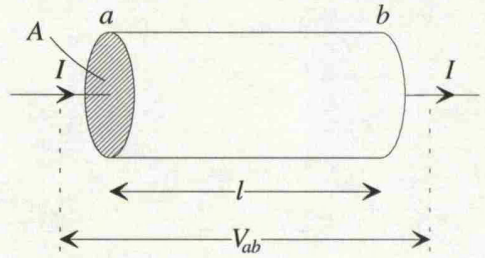

Figure A.1 To define V, R, ρ, σ and J.

Resistance R (ohms [Ω]) is defined by

$$R = \frac{V}{I}. \tag{A.2}$$

The definition of resistance stems from Ohm's law which states that for many materials, particularly metallic conductors,

$$V \propto I \Rightarrow R \text{ is constant}.$$

This should not be confused with equation (A.2) which is a definition of R and does not necessarily imply that R is independent of I and V (Whelan and Hodgson, 1978). Materials which obey Ohm's law are termed *linear* conductors, reflecting the nature of the I–V relationship.

The resistance of a given material is dependent upon its physical dimensions and in general will be directly proportional to the length l, and inversely proportional to the cross-sectional area A, of the material. It is desirable to define a property of the material which is independent of its size and shape: such a property is the resistivity ρ, (ohm-metres [Ω-m]) defined by

$$\rho = \frac{AR}{l}. \tag{A.3}$$

The resistivity of a material is a physical property which describes how difficult it is to pass a current through a unit length of that material, of unit cross-section. The reciprocal of resistivity is termed conductivity, σ (siemens/metre [S m^{-1}]), so

$$\sigma = \frac{1}{\rho} = \frac{l}{AR}. \tag{A.4}$$

The name 'mho' is sometimes used as a synonym for siemen.

The electric current density, J, over a cross-section of area A (and at any point in the prismatic conductor of Figure A.1) is defined by

$$J = \frac{I}{A}. \tag{A.5}$$

A.2 Generalisation of Ohm's law

Ohm's law in its original form applied to electric circuits. This section discusses the generalisation of the law to describe current flow in three dimensional space, as used in §2.2.1 and §2.2.3. The generalised version relates the electric field E (rather than potential difference V) to current density J (rather than current I).

The electric field, E

If a (test) charge Q_0 [coulombs, C] has a force **F** [newtons, N] exerted upon it by virtue of its position in an electric field, then the electric field **E** [N C^{-1}] is defined as

$$\mathbf{E} = \frac{\mathbf{F}}{Q_0}. \tag{A.6}$$

Now consider moving the charge Q_0 a distance δx within the field, where δx is chosen to be in the direction of the action of **F**. The work δW done in moving Q_0 will be (magnitude of force)×(distance moved), i.e.

$$\delta W = -F\delta x. \tag{A.7}$$

From equation (A.1) there will be an associated change in potential δV at the location of Q_0:

$$\delta V = \frac{\delta W}{Q_0}. \tag{A.8}$$

Combining equations A.6, A.7 and A.8,

$$E = -\frac{\delta V}{\delta x},$$

and in the limit as $\delta x \to 0$ we arrive at the relation

$$E = -\frac{\mathrm{d}V}{\mathrm{d}x}. \tag{A.9}$$

An alternative unit for E is seen to be the volt per metre [V m^{-1}].

Ohm's Law

Consider a small volume of material in the form of a box (rectangular prism), with sides of length δx, δy and δz (Figure A.2). A current I passes through the material; for convenience let the box be orientated so that the current direction is parallel to the side of length δx. The potential difference between opposite faces of the box in the direction of current flow is δV.

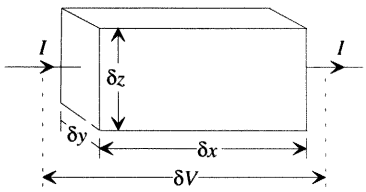

Figure A.2 To describe current flow in a volume of material.

Equation (A.3) for this box is

$$\rho = \frac{\delta y \delta z R}{\delta x}, \tag{A.10}$$

where R is obtained from equation (A.2). Expressing R in terms of V and I and including this in (A.10) we have

$$\rho = \frac{\delta y \delta z \delta V}{\delta x I}, \tag{A.11}$$

but from (A.5) and (A.9)

$$J = \frac{I}{\delta y \delta z} \text{ and } E = -\frac{dV}{dx},$$

so making δx very small,

$$\lim_{\delta x \to 0}\left(\frac{\delta y \delta z \delta V}{\delta x I}\right) = \frac{\delta y \delta z}{I}\frac{\mathrm{d}V}{\mathrm{d}x} = -\frac{J}{E}$$

and hence from (A.11)

$$E = \rho J\,. \tag{A.12}$$

Since $\sigma = 1/\rho$ (equation A.4) equation (A.12) may also be stated as

$$J = \sigma E\,. \tag{A.13}$$

Ohm's law and current density in three dimensions

Equation (A.5) defines current density in electric circuits. The components of the electric field **E** can be denoted by (E_x, E_y, E_z). Equation (A.9) can easily be generalised to describe each of the electric field components in three-dimensions:

$$E_x = -\frac{\partial V}{\partial x};\ E_y = -\frac{\partial V}{\partial y};\ E_z = -\frac{\partial V}{\partial z},. \tag{A.14}$$

which in combination gives the relationship stated in Chapter 2 (equation 2.1):

$$\mathbf{E} = -\nabla V\,,$$

where ∇ is the del-operator, which equals $(\partial/\partial x)\mathbf{i} + (\partial/\partial y)\mathbf{j} + (\partial/\partial z)\mathbf{k}$ in rectangular cartesian coordinates (Bourne and Kendall, 1977). Similarly, in order to describe the flow of electricity in three dimensional space, the electric current density J is expressed as a vector quantity **J**:

$$\mathbf{J} = J_x\mathbf{i} + J_y\mathbf{j} + J_z\mathbf{k}\,, \tag{A.15}$$

where (J_x, J_y, J_z) are the components of current density and (**i**, **j**, **k**) are the unit vectors in the (x, y, z) -coordinate directions, respectively.

Applying (A.14) and (A.15) to the Ohm's law expressions (A.12) and (A.13) we arrive at a generalised Ohm's law applicable to conduction in three-dimensional space:

$$\boxed{\mathbf{E} = \rho\mathbf{J}};\ \text{or}$$

$$\boxed{\mathbf{J} = \sigma\mathbf{E}}. \tag{A.16}$$

This is the version of Ohm's law stated in Chapter 2 [equation (2.3)]. It assumes that the conducting medium is isotropic, i.e. the resistivity is independent of direction and may be represented by a scalar value.

Maxwell's equations

Maxwell's equations [see, for example, Stratton (1941)] summarise the fundamental relations in electricity and magnetism in the form of a set of vector equations. They can

therefore be used as an alternative starting point for defining relationships in current electricity.

Equation (2.1), the vector form of equation (A.9), can be arrived at from Maxwell's equations as follows: Maxwell's equation, relating electric field strength $\mathbf{E}$[V m^{-1}] and magnetic flux density $\mathbf{B}$[Vs m^{-2}] is

$$\nabla \times \mathbf{E} = -\frac{\partial \mathbf{B}}{\partial t}.$$

For direct current situations, in which the magnetic field is constant,

$$\frac{\partial \mathbf{B}}{\partial t} = \mathbf{0},$$

so that

$$\nabla \times \mathbf{E} = \mathbf{0}. \tag{A.17}$$

Equation (A.17) implies that the electric field is conservative and can be expressed as the (vector) gradient of a scalar potential function:

$$\mathbf{E} = -\nabla V. \tag{2.1}$$

Ohm's law, as expressed in equation (A.16), may also be derived from Maxwell's equations, and is commonly used as an extra relationship in combination with the other equations.

A.3 Kirchhoff's rules

Kirchhoff's rules express the laws of conservation of charge and conservation of energy for electric circuits (Whelan and Hodgson, 1978). In Section 3.2.1 the finite difference formulation of the generalised Poisson equation is shown to be equivalent to the first rule, as stated below.

Rule 1 (conservation of charge): the algebraic sum of currents at a junction plus the magnitude of any current source at that junction is equal to zero:

$$\sum I + S = 0.$$

Rule 2 (conservation of energy): around any closed loop, the algebraic sum of the e.m.f's is equal to the algebraic sum of the products of current and resistance:

$$\sum \xi = \sum IR.$$

A.4 Generalisation of resistor addition

Due to the resistor network analogy of the numerical models described in this work (§3.2.1) concepts from resistor networks can be applied during model development. Resistor addition may be used in fine-tuning of resistivity models.

The effective resistance of two resistors in series is derived using Ohm's law and conservation of charge considerations. Consider two resistors, R_1 and R_2, connected in series (Figure A.3), across which there are respective p.d.'s of V_1 and V_2. Conservation of charge dictates that the current though each resistor must be the same, I. Denote the total resistance provided by R_1 and R_2 by R.

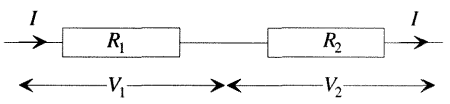

Figure A.3 Resistors in series.

Applying Ohm's law (equation A.2) to R_1 and R_2:

$$R_1 = \frac{V_1}{I};\ R_2 = \frac{V_2}{I}. \tag{A.18}$$

Applying Ohm's law to the total effective resistance R:

$$(V_1 + V_2) = IR;$$

$$R = \frac{V_1}{I} + \frac{V_2}{I};$$

substituting equations (A.18), $$R = R_1 + R_2. \tag{A.19}$$

The same principle can be applied to adjacent 3D cells, with respective resistivities ρ_1 and ρ_2, lengths l_1 and l_2, and cross-sectional areas A_1 and A_2 (Figure A.4). Substituting equation (A.3) into equation (A.19) for this case:

$$R = \frac{\rho_1 l_1}{A_1} + \frac{\rho_2 l_2}{A_2}. \tag{A.20}$$

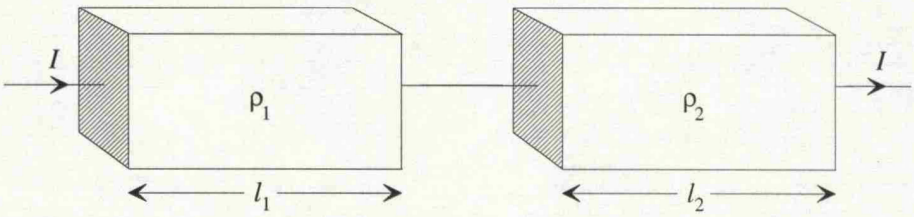

Figure A.4 Resistance of 3D cells in series.

The above result (eq. A.20) is extended in Appendix C which develops relationships relating FD model cell geometry and resistivity to inter-nodal resistances in the analogous 3D resistor network.

It is noted that equation (A.20) requires the same current I to flow through both cells since equation (A.19), on which it is based, assumes conservation of charge. In circumstances where the current flow is not parallel over both the cells some may flow through the cell sides. On physical grounds, therefore, the relationship (A.20) is in general only approximate, becoming more accurate when cells are small and/or current flow is parallel.

APPENDIX B

Analytic solutions of the electrical conduction equation

This appendix describes (in more detail than in Section 3.1.2) the derivation of some of the fundamental analytic solutions to equation (2.4) (§2.2.1):

$$\nabla \cdot \frac{1}{\rho} \nabla V = -S.$$

B.1 Infinite homogeneous medium

Consider the case where a point source emitting a current I is located at a point O in an infinite medium of constant resistivity ρ. In this case, it is convenient express equation (2.4) in spherical polar coordinates (r, θ, ϕ) since this coincides with symmetry in the electrical field. In this system, for constant ρ, equation (2.4) becomes

$$\frac{1}{r^2}\frac{\partial}{\partial r}\left(r^2 \frac{\partial V}{\partial r}\right) + \frac{1}{r^2 \sin\theta}\frac{\partial}{\partial \theta}\left(\sin\theta \frac{\partial V}{\partial \theta}\right) + \frac{1}{r^2 \sin^2\theta}\frac{\partial^2 V}{\partial \phi^2} = -\rho S.$$

Due to symmetry, the partial derivatives $\partial V/\partial\theta$ and $\partial V/\partial\phi$ vanish, giving

$$\frac{1}{r^2}\frac{\partial}{\partial r}\left(r^2 \frac{\partial V}{\partial r}\right) = -\rho S, \tag{B.1}$$

where r is distance from O. Consider a region which does not include the point source (O); for this region $S = 0$. Multiplying each side of equation (B.1) by r^2 and integrating with respect to r:

$$\left(r^2 \frac{\mathrm{d}V}{\mathrm{d}r}\right) = A. \tag{B.2}$$

Integrating once more,

$$V = -\frac{A}{r} + B. \tag{B.3}$$

The parameter V is commonly defined so that as $r \to \infty$, $V \to 0$; This implies $B = 0$ in (B.3). By symmetry, current flows out from the source location in all directions, and by conservation principles the total current I crossing a spherical surface centred on O will be $4\pi r^2 J$ where J is current density (§A.1). Using Ohm's law as stated in equation (A.13) (§A.2) for the radial direction:

$$I = -4\pi r^2 \frac{1}{\rho} E. \tag{B.4}$$

Using $E = -(dV/dr)$ (equation A.9, §A.2) and combining (B.2) and (B.4),

$$A = -\frac{I\rho}{4\pi},$$

so that in equation (B.3) the electric potential in a infinite homogeneous medium is found to be

$$V = \frac{\rho I}{4\pi r}. \tag{B.5}$$

Equation (B.5) was formulated for a region which does not contain the current source (O). In practice this region can be made to include all space except O itself, which is a singularity (i.e. the current density there is theoretically infinite).

B.2 Semi-infinite homogeneous medium

Consider a current source of strength I located on an infinite planar interface between a region of resistivity ρ and a region of infinite resistivity.

Following the above approach of §B.1, equation (2.4) reduces to the general solution

$$V = -\frac{A}{r}. \tag{B.6}$$

In this case, the condition $\partial V/\partial z = 0$ applies at the earth-air interface, since there is no current flow out of the earth (z is the vertical coordinate direction). Substituting $r = \sqrt{x^2 + z^2}$ into equation (B.6):

$$V = -A\left(x^2 + z^2\right)^{-\frac{1}{2}}.$$

Differentiating:

$$\frac{\partial V}{\partial z} = \frac{1}{2}A\left(x^2 + z^2\right)^{-\frac{3}{2}} \cdot 2z = Az\left(x^2 + z^2\right)^{-\frac{3}{2}}.$$

At $z = 0$ the condition $\partial V/\partial z = 0$ is clearly satisfied.

In this case current flows out from the source location in all downward directions, since no current passes into the air. The total current I crossing a *hemispherical* surface centred on O, is $2\pi r^2 J$. Following a similar argument to that outlined above (§B.1), the electric potential in a semi-infinite homogeneous medium is found to be:

$$V = \frac{\rho I}{2\pi r}. \tag{B.7}$$

B.3 Plane boundary

Consider two regions of resistivity ρ_1 and ρ_2 separated by a plane boundary (Figure B.1). A current source, C_1, of magnitude I is located in the first region. When using the method of images (§3.1.2.3) the boundary between the two regions is regarded as a semi-transparent 'current mirror'. The electric potential in the first region is a combination of that due to a reflection from the plane boundary plus the direct contribution from the source itself. An image source C_1' in the second region symmetrically placed with respect to the boundary and C_1 is used to represent the effect of current reflections on the plane boundary.

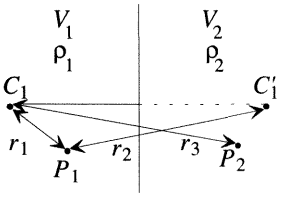

Figure B.1 Current source near a plane boundary.

In this situation, the potential V_1 at a point P_1 in the first region can be shown to be (Telford et al., 1990):

$$V_1 = \frac{I\rho_1}{4\pi}\left(\frac{1}{r_1} + \frac{k}{r_2}\right),$$

where k is the transmission coefficient, defined by:

$$k = \left(\frac{\rho_2 - \rho_1}{\rho_2 + \rho_1}\right), \tag{B.8}$$

and r_1 and r_2 are the distances from P_1 to the source and its image respectively. The potential V_2 at a point P_2 in the second region can be shown to be

$$V_2 = \frac{I\rho_2}{4\pi}\left(\frac{1-k}{r_3}\right),$$

where r_3 is the distance to the current source from P_2.

B.4 Isotropic earth with a single vertical interface

Using the method of images, and following the derivation outlined above, the potential V_1 at a point of interest in the region containing the current source can be shown to be (Keller and Frischknecht, 1966):

$$V_1 = \frac{I\rho_1}{2\pi}\left(\frac{1}{r_1} + \frac{k}{r_2}\right), \tag{B.9}$$

where k is the transmission coefficient, defined as in equation (B.8), and r_1 and r_2 are the distances to the source and its image respectively. The potential V_2 in the other region can be shown to be

$$V_2 = \frac{I\rho_2}{2\pi}\left(\frac{1-k}{r_3}\right), \tag{B.10}$$

where r_3 is the distance to the current source from a point of interest in the second medium.

B.5 Two-layered earth

Using the method of images, the potential at the earth's surface due to two horizontal layers can be shown to given by the infinite series (Telford et al., 1990)

$$V = \frac{I\rho_1}{2\pi r}\left[1 + 2\sum_{m=1}^{\infty}\frac{k^m}{\sqrt{1+(2mh/r)^2}}\right], \tag{B.11}$$

where r is distance from current source, h is the depth of the top layer and k is defined as in equation (B.8).

B.6 Integral solutions for layered earth

The potential V_j in the jth layer of a stratified earth consisting of $(n - 1)$ layers lying upon an infinitely-deep base layer is (Koefoed, 1979):

$$V_j = \begin{cases} \int_0^\infty \left[A_j(\lambda)e^{-\lambda z} + B_j(\lambda)e^{\lambda z}\right]J_0(\lambda r)\mathrm{d}\lambda, & 1 < j < n; \\ \int_0^\infty A_n(\lambda)e^{-\lambda z}J_0(\lambda r)\mathrm{d}\lambda, & j = n; \\ \frac{I\rho_1}{2\pi}\int_0^\infty e^{-\lambda z}J_0(\lambda r)\mathrm{d}\lambda + \int_0^\infty A_1(\lambda)\left(e^{-\lambda z} + e^{\lambda z}\right)J_0(\lambda r)\mathrm{d}\lambda, & j = 1. \end{cases} \tag{B.12}$$

where r and z are the radial (horizontal) and vertical distances from the current source (located at the origin), respectively. The function J_0 is the Bessel function of order zero, which is a known quantity. The terms A_j and B_j are constants which depend upon the number of layers, n, and are evaluated using the continuity conditions [equations (2.5) and (2.6), §2.2.1] across layer boundaries

$$V_{j-1} = V_j,$$

and

$$\frac{1}{\rho_{j-1}}\frac{\partial V_{j-1}}{\partial z} = \frac{1}{\rho_j}\frac{\partial V_j}{\partial z}.$$

In particular, the potential V at the earth's surface ($z = 0$) can be written as

$$V = \frac{I\rho_1}{2\pi r}\left(1 + 2r\int_0^\infty K(\lambda)J_0(\lambda r)\mathrm{d}\lambda\right), \tag{B.13}$$

where $K(\lambda)$ (often termed the *kernel function of resistivity* in this context) depends on the number of layers under consideration. In the two layer case ($n = 2$),

$$K(\lambda) = \frac{-k}{e^{2\lambda h} + k},$$

where h is the top layer thickness and $k = (\rho_2 - \rho_1)/(\rho_2 + \rho_1)$ as in equation (B.8).

APPENDIX C

Resistivity to resistance conversions

The finite difference model described in this work is analogous to a 3D resistor network (§3.2.1). This appendix derives relations between the resistance of elemental cells and their resistivity and geometry. These relationships are used to convert three-dimensional resistivity distributions into resistance values for internal storage in computer models.

C.1 Introduction

The models used in this thesis represent 3D resistivity distributions by dividing a region of interest into a series of discrete cells of constant resistivity (§3.1.3.1). Each cell is centred on a node of the finite difference grid. The size of each cell is governed by the grid spacing, whilst the general shape of a cell is determined by the coordinate system on which the grid is based.

In the modelling programs developed and used for this work, resistivity values are represented by three (independent) 3D arrays of conductance values, one array for each coordinate direction. In combination, the three arrays are analogous to a 3D network of resistors which connect the nodes of the finite difference grid (Figure C.1). The value of a given resistor represents the effective resistance of adjacent cells between the two nodes it connects (see §A.4).

Notation

The three nodal (grid) coordinates are denoted by i, j and k; these respectively represent the x, y and z directions in rectangular cartesian coordinates and the r, θ and z directions in cylindrical polar coordinates. The physical coordinates of the nodes in 3D space are recorded in three 1D arrays: X, Y and Z. The three 3D conductance arrays are labelled W, F and S.

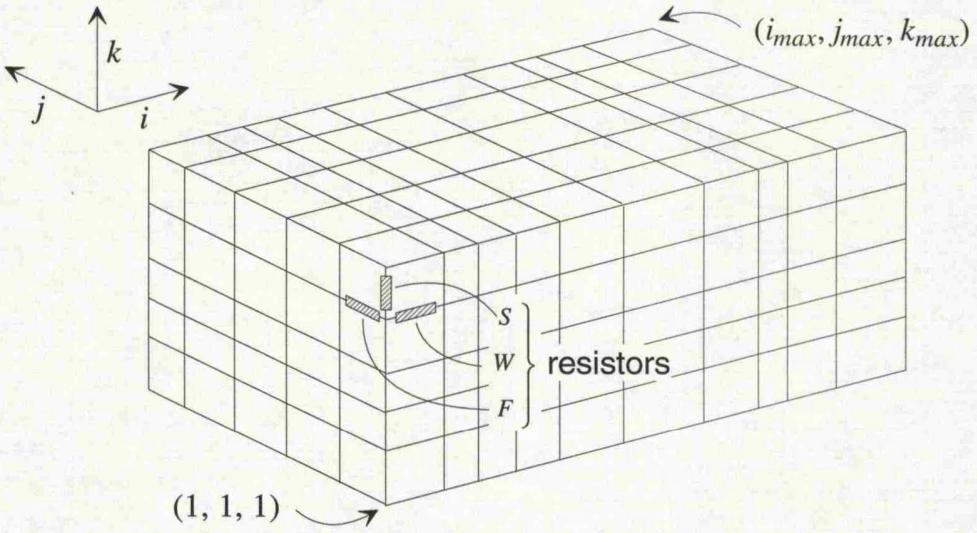

Figure C.1 The finite difference grid: a 3D resistor network.

As indicated in Figure C.1, the nodal coordinates range from (1, 1, 1) to $(i_{max}, j_{max}, k_{max})$, resulting in a grid with $(i_{max} - 1)\times(j_{max} - 1)\times(k_{max} - 1)$ nodes. Thus the arrays X, Y and Z have dimension (i_{max}), (j_{max}) and (k_{max}) respectively, and the arrays W, F and S each have dimension $(i_{max} \times j_{max} \times k_{max})$.

To compress notation when coding routines in FORTRAN, the following convention has been adopted to refer to the resistors: in the i-direction, the resistor W_{ijk} joins node $(i - 1, j, k)$ to node (i, j, k). Similarly, the resistor F_{ijk} joins node $(i, j - 1, k)$ to node (i, j, k) and S_{ijk} joins node $(i, j, k - 1)$ to node (i, j, k) (Figure C.2). Note that W_{1jk}, F_{i1k} and S_{ij1} are thus undefined.

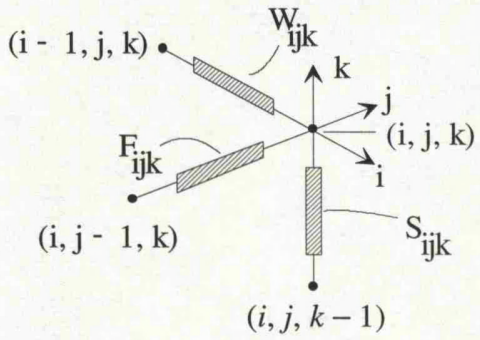

Figure C.2 W, F and S resistors.

Mesh alignment

Two basic mesh alignments are catered for in the numerical models. The first is based between nodes (around resistors), the second around nodes. This is illustrated in Figure C.3 for a one-dimensional mesh.

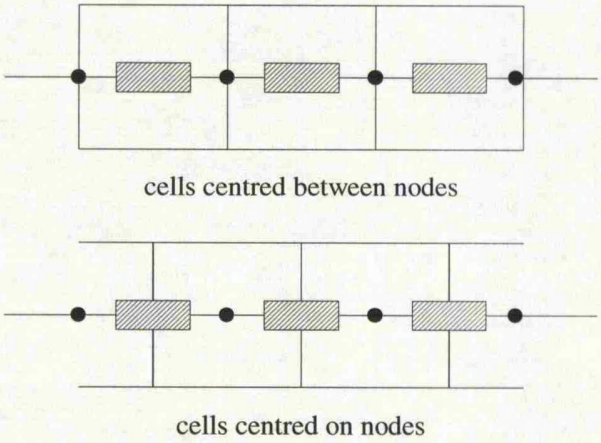

Figure C.3 Alternative mesh alignments.

The following two sections derive formulae for converting three-dimensional model resistivity distributions into resistances, firstly for rectangular cartesian coordinates, and secondly for cylindrical polar coordinates. In both cases, general 'cell' formulae are used to develop expressions for W, F and S values for both mesh alignments illustrated in Figure C.3.

C.2 Rectangular Cartesian coordinates

C.2.1 Cell formulae

The definition of resistivity (eq. A.3, §A.1)

$$R = \rho L/A \tag{C.2.1}$$

can be applied to the unit cell illustrated in Figure C.4 in each of the coordinate directions. This gives:

$$R_x = \frac{\rho \Delta x}{\Delta y \Delta z}, \tag{C.2.2}$$

$$R_y = \frac{\rho \Delta y}{\Delta x \Delta z}, \tag{C.2.3}$$

and

$$R_z = \frac{\rho \Delta z}{\Delta x \Delta y}, \tag{C.2.4}$$

where R_x, R_y and R_z are the resistances across opposite faces of the cell in the x-, y- and z-directions respectively.

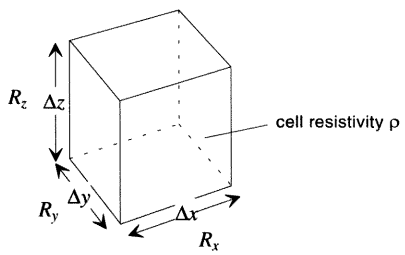

Figure C.4 Dimensions and resistances of an elemental cell in a rectangular cartesian grid.

C.2.2 Resistance of cells centred between nodes

Equations (C.2.2), (C.2.3) and (C.2.4) are easily modified to relate to a resistor in the finite difference grid.

In the x-direction, from equation (C.2.2),

$$\boxed{\frac{1}{W_{ijk}} = \frac{\rho_{cell} \Delta x}{\Delta y \Delta z}}, \qquad 2 \le i \le i_{max}, \tag{C.2.5}$$

where

$$\Delta x = X_i - X_{i-1}, \quad 2 \le i \le i_{max}; \tag{C.2.6}$$

$$\Delta y = \begin{cases} \frac{1}{2}\left(Y_{j+1} - Y_{j-1}\right), & 1 < j < j_{max}; \\ Y_{j+1} - Y_j, & j = 1; \\ Y_j - Y_{j-1}, & j = j_{max}. \end{cases} \tag{C.2.7}$$

$$\Delta z = \begin{cases} \frac{1}{2}\left(Z_{k+1} - Z_{k-1}\right), & 1 < k < k_{max}; \\ Z_{k+1} - Z_k, & k = 1; \\ Z_k - Z_{k-1}, & k = k_{max}. \end{cases} \tag{C.2.8}$$

In the y-direction, from equation (C.2.3),

$$\boxed{\frac{1}{F_{ijk}} = \frac{\rho_{cell}\Delta y}{\Delta x \Delta z}}, \qquad 2 \le j \le j_{max}, \tag{C.2.9}$$

where

$$\Delta x = \begin{cases} \frac{1}{2}(X_{i+1} - X_{i-1}), & 1 < i < i_{max}; \\ X_{i+1} - X_i, & i = 1; \\ X_i - X_{i-1}, & i = i_{max}. \end{cases} \tag{C.2.10}$$

$$\Delta y = Y_j - Y_{j-1}, \quad 2 \le j \le j_{max}; \tag{C.2.11}$$

and Δz is defined as in equation (C.2.8).

In the z-direction, from equation (C.2.4),

$$\boxed{\frac{1}{S_{ijk}} = \frac{\rho_{cell}\Delta z}{\Delta x \Delta y}}, \qquad 2 \le k \le k_{max}, \tag{C.2.12}$$

where

Δx is defined as in equation (C.2.10);

Δy is defined as in equation (C.2.7); and

$$\Delta z = Z_k - Z_{k-1}, \quad 2 \le k \le k_{max} \tag{C.2.13}$$

C.2.3 Resistance between cells centred on nodes

In this case a given resistivity values is associated with one node of the 3D network. The interconnecting resistors are weighted averages of the resistivities of the pairs of nodes they connect (§A.4). The resistivity associated with the node (i, j, k) is ρ_{ijk}.

The resistance $(1/W_{ijk})$ is found by summing two component resistors R_1 and R_2, which represent the adjoining halves of the cells surrounding the nodes $(i-1, j, k)$ and (i, j, k) respectively.

From equation (C.2.2),

$$R_1 = \frac{\rho_1 \cdot \frac{1}{2}\Delta x}{\Delta y \Delta z}, \text{ and } R_2 = \frac{\rho_2 \cdot \frac{1}{2}\Delta x}{\Delta y \Delta z}, \tag{C.2.14}$$

where Δx, Δy and Δz are defined by equations (C.2.6), (C.2.7), and (C.2.8) respectively.

Summing the component resistors R_1 and R_2 in equation (C.2.14):

$$\boxed{\frac{1}{W_{ijk}} = \frac{\frac{1}{2}(\rho_1 + \rho_2)\Delta x}{\Delta y \Delta z}}, \quad 2 \le i \le i_{max}. \tag{C.2.15}$$

Similarly, expressions for resistances in the y- and z-directions may be found by summing component resistors expressed using equations (C.2.3) and (C.2.4) respectively.

In the y-direction,

$$\boxed{\frac{1}{F_{ijk}} = \frac{\frac{1}{2}(\rho_1 + \rho_2)\Delta y}{\Delta x \Delta z}}, \quad 2 \le j \le j_{max}, \tag{C.2.16}$$

where Δx and Δy are now defined by equations (C.2.10) and (C.2.11) respectively, and Δz is given by (C.2.8) as above.

In the z-direction,

$$\boxed{\frac{1}{S_{ijk}} = \frac{\frac{1}{2}(\rho_1 + \rho_2)\Delta z}{\Delta x \Delta y}}, \quad 2 \le k \le k_{max}. \tag{C.2.17}$$

In this case, Δx, Δy and Δz are defined by equations (C.2.10), (C.2.7), and (C.2.13) respectively.

C.2.4 Summary

Table C.1 summarises the formulae for deriving resistances of cells in rectangular cartesian coordinates.

	cell formula	cell centred on resistor	cell centred on node
x-resistance	$R_x = \frac{\rho \Delta x}{\Delta y \Delta z}$	$\frac{1}{W_{ijk}} = \frac{\rho_{cell} \Delta x}{\Delta y \Delta z}$	$\frac{1}{W_{ijk}} = \frac{\frac{1}{2}(\rho_1 + \rho_2)\Delta x}{\Delta y \Delta z}$
y-resistance	$R_y = \frac{\rho \Delta y}{\Delta x \Delta z}$	$\frac{1}{F_{ijk}} = \frac{\rho_{cell} \Delta y}{\Delta x \Delta z}$	$\frac{1}{F_{ijk}} = \frac{\frac{1}{2}(\rho_1 + \rho_2)\Delta y}{\Delta x \Delta z}$
z-resistance	$R_z = \frac{\rho \Delta z}{\Delta x \Delta y}$	$\frac{1}{S_{ijk}} = \frac{\rho_{cell} \Delta z}{\Delta x \Delta y}$	$\frac{1}{S_{ijk}} = \frac{\frac{1}{2}(\rho_1 + \rho_2)\Delta z}{\Delta x \Delta y}$

Table C.1 Resistance formulae for cylindrical polar coordinates.

C.3 Cylindrical polar coordinates

In cylindrical polar coordinates, a typical cell is wedge-shaped, bounded by arc-shaped surfaces in the radial direction, non-parallel planes radiating from the centre of the grid in the tangential direction, and parallel, horizontal planes in the vertical direction (Figure C.5).

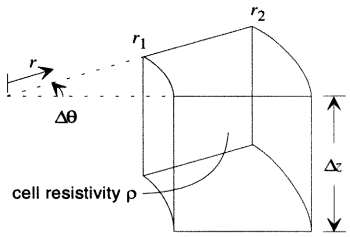

Figure C.5 Typical cell surrounding a node in a cylindrical polar grid.

C.3.1 Cell formulae

This section describes the formulation of expressions for the resistance of a cell, defined in cylindrical polar coordinates, in each of the coordinate directions. The coordinate directions are termed *radial* (r), *tangential* (θ) and *vertical* (z) (Figure C.6), and the corresponding resistances are R_r, R_θ and R_z respectively. Calculations are based on $R = \rho L/A$ (eq. A.3, §A.1).

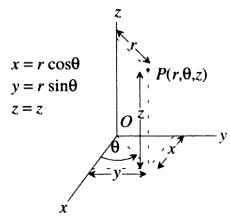

Figure C.6 Cylindrical polar coordinates.

C.3.1.1 Radial resistances

As can be seen from Figure C.7, the width of a typical cell in the radial direction is not constant, varying from $r_1\Delta\theta$ to $r_2\Delta\theta$ (measuring arc lengths). The total resistance between the two curved faces may be found by summing the contributions of elemental slices.

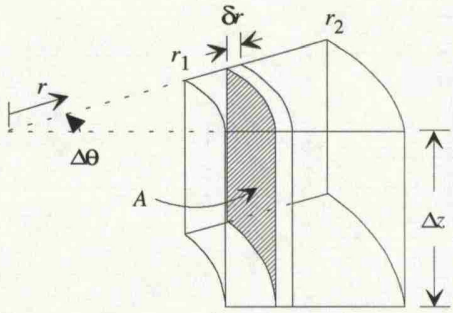

Figure C.7 Elemental slice for the radial direction.

Across the slice of width δr the cross-sectional area A is assumed to remain approximately equal to $r.\Delta\theta.\Delta z$. The resistance of this slice in the radial direction is found by substitution into equation (C.2.1)

$$= \rho \times \delta r / r\Delta\theta\Delta z.$$

Summing from $r = r_1$ to r_2, and taking the limit as $\delta r \to 0$:

$$R_r = \int_{r_1}^{r_2} \frac{\rho dr}{r.\Delta\theta.\Delta z}$$

i.e.

$$\boxed{R_r = \frac{\rho}{\Delta\theta.\Delta z} \ln\left(\frac{r_2}{r_1}\right)}. \qquad \text{(C.3.1)}$$

C.3.1.2 Tangential resistances

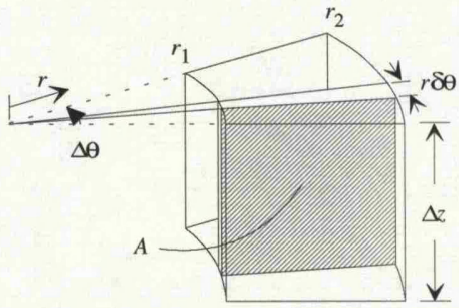

Figure C.8 Elemental slice for the tangential direction.

Referring to Figure C.8, the area A is constant at $(r_2 - r_1)\,\Delta z$, but the 'length' from $\theta = 0$ to $\theta = \Delta\theta$ is more difficult to define (Figure C.9).

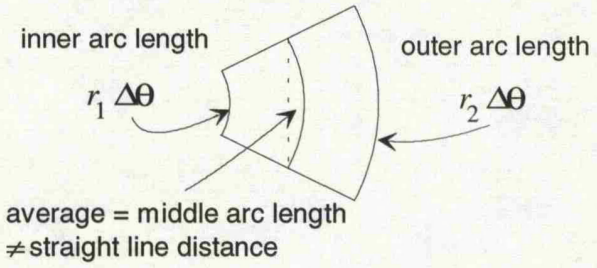

Figure C.9 Defining cell length.

Arc lengths are chosen rather than straight-line distances. Note that the smaller $\Delta\theta$ gets, the closer the end faces get to becoming parallel and the better the approximation gets. Taking the middle arc length, i.e. $\frac{1}{2}(r_1 + r_2)\Delta\theta$, the resistance of the elemental slice will be

$$\cong \rho \times \frac{\frac{1}{2}(r_1 + r_2)\delta\theta}{(r_2 - r_1)\Delta z}.$$

Summing from $\theta = 0$ to $\Delta\theta$, and taking the limit as $\delta\theta \to 0$:

$$R_\theta = \int_0^{\Delta\theta} \frac{\rho(r_2 + r_1)}{2\Delta z(r_2 - r_1)}\,\mathrm{d}\theta$$

i.e.

$$\boxed{R_\theta = \frac{\rho}{2\Delta z}\left(\frac{r_2 + r_1}{r_2 - r_1}\right)\Delta\theta}. \qquad \text{(C.3.2)}$$

C.3.1.3 Vertical resistances

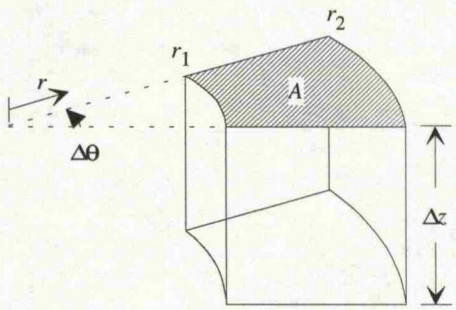

Figure C.10 Measuring resistance in the vertical direction.

Refer to Figure C.10, the area of a sector = $\frac{1}{2}r^2\theta$

$$\Rightarrow \qquad A = \tfrac{1}{2}r_2^2\Delta\theta - \tfrac{1}{2}r_1^2\Delta\theta = \tfrac{1}{2}\Delta\theta\left(r_2^2 - r_1^2\right).$$

This remains constant.

$$\therefore \qquad \boxed{R_z = \frac{\rho \Delta z}{\frac{1}{2}\Delta\theta\left(r_2^2 - r_1^2\right)}}. \qquad \text{(C.3.3)}$$

C.3.2 Resistance of cells centred between nodes

C.3.2.1 Radial resistances

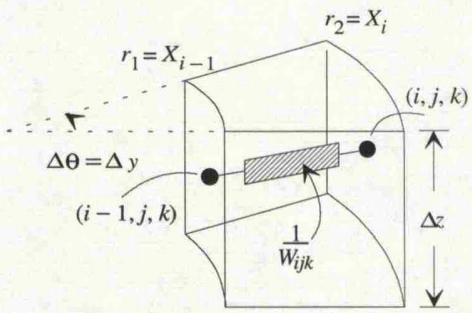

Figure C.11 Cell associated with a radial resistor.

Substituting the parameters of a cell of uniform resistivity ρ_{cell}, tangential dimension Δy and height Δz (Figure C.11) into equation (C.3.1):

$$\boxed{\frac{1}{W_{ijk}} = \frac{\rho_{cell}}{\Delta y . \Delta z} \ln\left(\frac{X_i}{X_{i-1}}\right)}, \qquad 2 \le i \le i_{max}, \qquad \text{(C.3.4)}$$

where

$$\Delta y = 2\pi \,/\, \left(j_{max} - 3\right); \qquad \text{(C.3.5)}$$

$$\Delta z = \begin{cases} \frac{1}{2}\left(Z_{k+1} - Z_{k-1}\right), & 1 < k < k_{max}; \\ Z_{k+1} - Z_k, & k = 1; \\ Z_k - Z_{k-1}, & k = k_{max}. \end{cases} \qquad \text{(C.3.6)}$$

In calculating Δy, the three nodes used to 'wrap' the mesh have been taken into account. In calculating Δz, the following assumptions have been made:

1. The FD cell boundaries lie exactly half-way between nodes;
2. At the extremities of the network, the cell extends outwards to the same extent as it does inwards (Figure C.12).

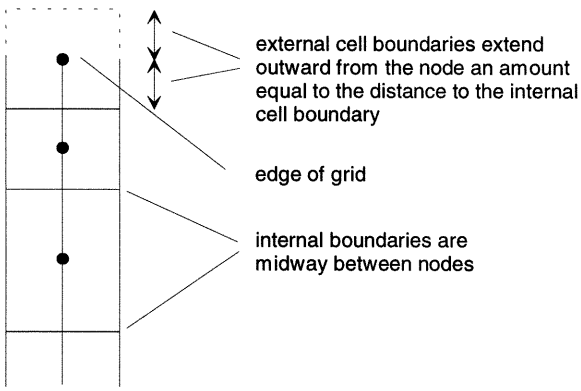

Figure C.12 End cells.

C.3.2.2 Tangential resistances

Consider the cell of uniform resistivity ρ_{cell}, illustrated in Figure C.13. It has tangential dimension Δy and height Δz, and is located from x_1 to x_2 in the radial direction. The location x_1 is midway between the ith and $i-1^{st}$ nodes, whilst x_2 is midway between the $i+1^{st}$ and i^{th} nodes [cf. Δz for the radial resistances (eq. C.3.6)]

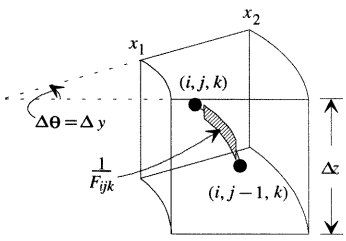

Figure C.13 Cell associated with a tangential resistor.

Substituting these parameters into equation (C.3.2):

$$\boxed{\frac{1}{F_{ijk}} = \frac{\rho_{cell}}{2\Delta z}\left(\frac{x_2 + x_1}{x_2 - x_1}\right)\Delta y}. \tag{C.3.7}$$

In this case,

$$x_1 = \begin{cases} \frac{1}{2}\left(3X_i - X_{i+1}\right), & i = 1; \\ \frac{1}{2}\left(X_{i-1} + X_i\right), & 1 < i \le i_{max}; \end{cases} \tag{C.3.8a}$$

$$x_2 = \begin{cases} \frac{1}{2}\left(X_i + X_{i+1}\right), & 1 \le i < i_{max}; \\ \frac{1}{2}\left(3X_i - X_{i-1}\right), & i = i_{max}. \end{cases} \tag{C.3.8b}$$

The dimensions Δy and Δz are defined as for the radial resistances (equations (C.3.5) and (C.3.6) respectively).

C.3.2.3 Vertical Resistances

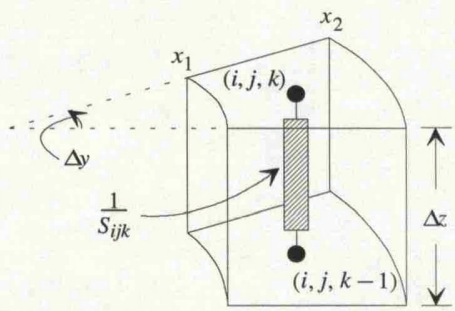

Figure C.14 Cell associated with a vertical resistor.

Consider the cell of uniform resistivity ρ_{cell}, illustrated in Figure C.14, with tangential dimension Δy and height Δz, and is located from x_1 to x_2 in the radial direction. Substituting these parameters into equation (C.3.3):

$$\boxed{\frac{1}{S_{ijk}} = \frac{2\rho_{cell}\Delta z}{\Delta y\left(x_2^2 - x_1^2\right)}}, \tag{C.3.9}$$

where x_1 and x_2 are defined by equation (C.3.8), Δy is defined by equation (C.3.5), and

$$\Delta z = Z_k - Z_{k-1}, \qquad 2 \le k \le k_{max}. \tag{C.3.10}$$

C.3.3 Resistance between cells centred on nodes

The value of inter-connecting resistors in the 3D grid are weighted averages of the resistivities of the pairs of nodes they connect. The resistivity associated with the node (i, j, k) is denoted by ρ_{ijk}.

C.3.3.1 Radial resistances

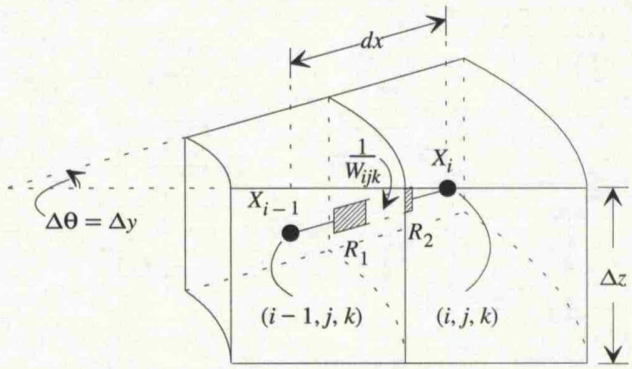

Figure C.15 Adjoining cells in the radial direction.

Referring to Figure C.15, the resistance $1/W_{ijk}$ is found by summing two component resistors R_1 and R_2, which represent adjoining halves of the cells surrounding the nodes $(i-1, j, k)$ and (i, j, k) respectively.

Let $dx = X_i - X_{i-1}$, then in equation (C.3.1):

$$R_1 = \frac{\rho_{i-1jk}}{\Delta y.\Delta z} \ln\left(\frac{X_{i-1} + \frac{1}{2}dx}{X_{i-1}}\right) \tag{C.3.11}$$

$$R_2 = \frac{\rho_{ijk}}{\Delta y.\Delta z} \ln\left(\frac{X_i}{X_{i-1} + \frac{1}{2}dx}\right). \tag{C.3.12}$$

Substituting equations (C.3.11) and (C.3.12) into the relation $1/W_{ijk} = R_1 + R_2$, and noting that $X_{i-1} + \frac{1}{2}dx = \frac{1}{2}(X_{i-1} + X_i)$:

$$\boxed{\frac{1}{W_{ijk}} = \frac{1}{\Delta y.\Delta z}\left\{\rho_{i-1jk} \ln\left(\frac{X_{i-1} + X_i}{2X_{i-1}}\right) + \rho_{ijk} \ln\left(\frac{2X_i}{X_{i-1} + X_i}\right)\right\}}, \quad 2 \le i \le i_{max}. \tag{C.3.13}$$

The variables Δy and Δz are defined as in equations (C.3.5) and (C.3.6) respectively.

C.3.3.2 Tangential resistances

Refer to Figure C.16. Using equation (C.3.2) to express the two component resistors R_1 and R_2, which represent adjoining halves of the cells surrounding the nodes $(i, j-1, k)$ and (i, j, k) respectively:

$$R_1 = \frac{\rho_{ij-1k}}{2\Delta z}\left(\frac{x_2 + x_1}{x_2 - x_1}\right) \times \frac{1}{2}dy, \tag{C.3.14}$$

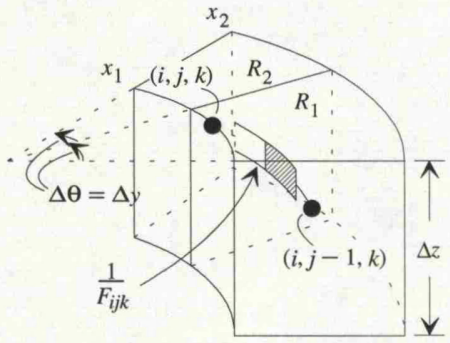

Figure C.16 Adjoining cells in the tangential direction.

and
$$R_2 = \frac{\rho_{ijk}}{2\Delta z}\left(\frac{x_2 + x_1}{x_2 - x_1}\right) \times \tfrac{1}{2}\, dy\,. \tag{C.3.15}$$

Substituting equations (C.3.14) and (C.3.15) into $1/F_{ijk} = R_1 + R_2$:

$$\boxed{\frac{1}{F_{ijk}} = \frac{\Delta y}{4\Delta z}\left(\frac{x_2 + x_1}{x_2 - x_1}\right)\left(\rho_{ij-1k} + \rho_{ijk}\right)}. \tag{C.3.16}$$

Again, Δy and Δz are defined as in equations (C.3.5) and (C.3.6) respectively. The positions x_1 and x_2 can be calculated from equations (C.3.8a) and (C.3.8b).

C.3.3.3 Vertical resistances

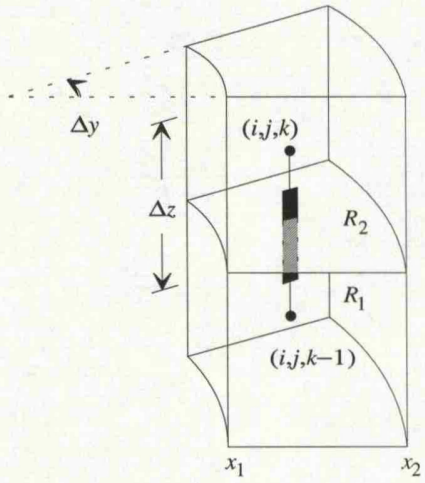

Figure C.17 Adjoining cells in the vertical direction.

Refer to Figure C.17. Using equation (C.3.3) to express the two component resistors R_1 and R_2, which represent adjoining halves of the cells surrounding the nodes $(i, j, k-1)$ and (i, j, k) respectively:

$$R_1 = \frac{\rho_{ijk-1} \cdot \frac{1}{2}\Delta z}{\frac{1}{2}\Delta y\left(x_2^2 - x_1^2\right)}; \tag{C.3.17}$$

$$R_2 = \frac{\rho_{ijk} \cdot \frac{1}{2}\Delta z}{\frac{1}{2}\Delta y\left(x_2^2 - x_1^2\right)}. \tag{C.3.18}$$

Substituting equations (C.3.17) and (C.3.18) into $1/S_{ijk} = R_1 + R_2$:

$$\boxed{\frac{1}{S_{ijk}} = \frac{\Delta z\left(\rho_{ijk-1} + \rho_{ijk}\right)}{\Delta y\left(x_2^2 - x_1^2\right)}.} \tag{C.3.19}$$

As before, x_1 and x_2 are defined as in equation (C.3.8),.and Δy is defined as in (C.3.5). However, Δz is now defined by equation (C.3.10).

C.3.4 Summary

Table C.2 summarises the formulae for deriving resistances of cells in cylindrical polar coordinates.

	cell formula	cell centred on resistor	cell centred on node
Radial resistance	$R_r = \frac{\rho}{\Delta\theta.\Delta z}\ln\left(\frac{r_2}{r_1}\right)$	$\frac{1}{W_{ijk}} = \frac{\rho_{cell}}{\Delta y.\Delta z}\ln\left(\frac{X_i}{X_{i-1}}\right)$	$\frac{1}{W_{ijk}} = \frac{1}{\Delta y.\Delta z}\left\{\begin{array}{l}\rho_{i-1jk}\ln\left(\frac{X_{i-1}+X_i}{2X_{i-1}}\right)\\ +\rho_{ijk}\ln\left(\frac{2X_i}{X_{i-1}+X_i}\right)\end{array}\right\}$
Tangential resistance	$R_\theta = \frac{\rho}{2\Delta z}\left(\frac{r_2+r_1}{r_2-r_1}\right)\Delta\theta$	$\frac{1}{F_{ijk}} = \frac{\rho_{cell}}{2\Delta z}\left(\frac{x_2+x_1}{x_2-x_1}\right)\Delta y$	$\frac{1}{F_{ijk}} = \frac{\Delta y}{4\Delta z}\left(\frac{x_2+x_1}{x_2-x_1}\right)\left(\rho_{ij-1k}+\rho_{ijk}\right)$
Vertical resistance	$R_z = \frac{\rho\Delta z}{\frac{1}{2}\Delta\theta\left(r_2^2-r_1^2\right)}$	$\frac{1}{S_{ijk}} = \frac{2\rho_{cell}\Delta z}{\Delta y\left(x_2^2-x_1^2\right)}$	$\frac{1}{S_{ijk}} = \frac{\Delta z\left(\rho_{ijk-1}+\rho_{ijk}\right)}{\Delta y\left(x_2^2-x_1^2\right)}.$

Table C.2 Resistance formulae for cylindrical polar coordinates.

APPENDIX D

Simulated focused measurement equations

This appendix describes theoretical expressions for the magnitude of the focusing currents required to focus two specific electrode configurations, and expressions for the focused electric potential in each case. Section D.1 derives an expression for a surface electrical array (see §4.2); Section D.2 derives equivalent expressions for the ODP high-temperature focused resistivity tool (see §4.1).

D.1 Focused surface array

The focused surface array electrode configuration, described in Section 4.1.2.1, is illustrated in Figure D.1. It consists of a measurement current electrode: P; four focusing current electrodes: N, S, E, and W, and eight potential electrodes: N_1, N_2, S_1, S_2, E_1, E_2, W_1, and W_2. The magnitudes of the focusing currents are adjusted to satisfy conditions on the measured potential at the potential electrodes, and are dependent on the array geometry, the magnitude of the measurement current, and the resistivity distribution in the earth.

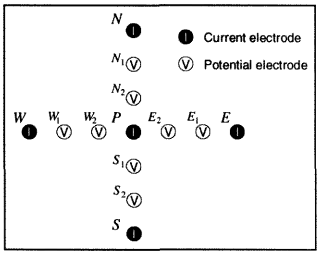

Figure D.1 Focused array electrode configuration (schematic).

Transfer impedances

Consider an electrode A emitting a current I_A, which causes a potential V_B at an electrode B. The *transfer impedance*, Z_{AB}, between A and B is defined by

$$Z_{AB} = \frac{V_B}{I_A}. \tag{D.1}$$

The transfer impedance Z_{AB} can be seen to be equal to the voltage at B when a unit current source is positioned at A.

Each of the current electrodes N, S, E, W and P has 8 transfer impedances associated with them, one for each potential electrode. For electrode N, these are denoted by Z_{NN_1}, Z_{NN_2}, Z_{NS_1}, Z_{NS_2}, Z_{NE_1}, Z_{NE_2}, Z_{NW_1} and Z_{NW_2}; similarly for electrodes S, E, W and P. The impedances Z_{NN_1}, Z_{NN_2}, Z_{NS_1}, Z_{NS_2}, Z_{NE_1}, Z_{NE_2}, Z_{NW_1} and Z_{NW_2} are determined by measuring the voltage at each of the potential electrodes while current is being emitted from electrode N only. Similarly, transfer impedances for the other four current electrodes can be found, giving a total of 5 × 8 = 40 transfer impedances for the focused array that are determined by making measurements where current is only emitted from a *single electrode* at any one time.

The transfer impedances can be used to express the voltage that would exist at each of the potential electrodes if all current electrodes were simultaneously emitting current. This is done by using superposition: for example the voltage V_{N_1} at N_1 is given by algebraically summing the contributions from I_N, I_S, I_E, I_W and I_P. The full expressions are:

$$\left.\begin{aligned}
V_{N_1} &= I_N Z_{NN_1} + I_S Z_{SN_1} + I_E Z_{EN_1} + I_W Z_{WN_1} + I_P Z_{PN_1} \\
V_{N_2} &= I_N Z_{NN_2} + I_S Z_{SN_2} + I_E Z_{EN_2} + I_W Z_{WN_2} + I_P Z_{PN_2} \\
V_{S_1} &= I_N Z_{NS_1} + I_S Z_{SS_1} + I_E Z_{ES_1} + I_W Z_{WS_1} + I_P Z_{PS_1} \\
V_{S_2} &= I_N Z_{NS_2} + I_S Z_{SS_2} + I_E Z_{ES_2} + I_W Z_{WS_2} + I_P Z_{PS_2} \\
V_{E_1} &= I_N Z_{NE_1} + I_S Z_{SE_1} + I_E Z_{EE_1} + I_W Z_{WE_1} + I_P Z_{PE_1} \\
V_{E_2} &= I_N Z_{NE_2} + I_S Z_{SE_2} + I_E Z_{EE_2} + I_W Z_{WE_2} + I_P Z_{PE_2} \\
V_{W_1} &= I_N Z_{NW_1} + I_S Z_{SW_1} + I_E Z_{EW_1} + I_W Z_{WW_1} + I_P Z_{PW_1} \\
V_{W_2} &= I_N Z_{NW_2} + I_S Z_{SW_2} + I_E Z_{EW_2} + I_W Z_{WW_2} + I_P Z_{PW_2}
\end{aligned}\right\}. \tag{D.2}$$

A set of simultaneous equations may be formulated by substituting the set of equations (D.2) into the following *focusing conditions* (eq. 4.1.1, §4.1.2.1):

$$\left.\begin{aligned}
V_{N_1} &= V_{N_2} \\
V_{S_1} &= V_{S_2} \\
V_{E_1} &= V_{E_2} \\
V_{W_1} &= V_{W_2}
\end{aligned}\right\} \tag{D.3}$$

The unknowns are the balance currents I_N, I_S, I_E and I_W. Rearranging the result of substituting (D.2) into the four equations (D.3):

$$\left.\begin{array}{l} I_N\left(Z_{NN_1}-Z_{NN_2}\right)+I_S\left(Z_{SN_1}-Z_{SN_2}\right)+I_E\left(Z_{EN_1}-Z_{EN_2}\right)+I_W\left(Z_{WN_1}-Z_{WN_2}\right)=-I_P\left(Z_{PN_1}-Z_{PN_2}\right) \\ I_N\left(Z_{NS_1}-Z_{NS_2}\right)+I_S\left(Z_{SS_1}-Z_{SS_2}\right)+I_E\left(Z_{ES_1}-Z_{ES_2}\right)+I_W\left(Z_{WS_1}-Z_{WS_2}\right)=-I_P\left(Z_{PS_1}-Z_{PS_2}\right) \\ I_N\left(Z_{NE_1}-Z_{NE_2}\right)+I_S\left(Z_{SE_1}-Z_{SE_2}\right)+I_E\left(Z_{EE_1}-Z_{EE_2}\right)+I_W\left(Z_{WE_1}-Z_{WE_2}\right)=-I_P\left(Z_{PE_1}-Z_{PE_2}\right) \\ I_N\left(Z_{NW_1}-Z_{NW_2}\right)+I_S\left(Z_{SW_1}-Z_{SW_2}\right)+I_E\left(Z_{EW_1}-Z_{EW_2}\right)+I_W\left(Z_{WW_1}-Z_{WW_2}\right)=-I_P\left(Z_{PW_1}-Z_{PW_2}\right) \end{array}\right\} . \quad \text{(D.4)}$$

Balance current magnitudes

The solution of the set of simultaneous equations (D.4) is expressed in terms of the sensing current, I_P, and the pre-calculated transfer impedances, and may be expressed as

$$\left.\begin{array}{l} I_N = Bf_N I_P \\ I_S = Bf_S I_P \\ I_E = Bf_E I_P \\ I_W = Bf_W I_P \end{array}\right\} , \quad \text{(D.5)}$$

where Bf_R is the 'balance factor' for the Rth electrode—that is, the magnitude of the balance current relative to the measurement current required for focusing to be achieved.

It is noted that the conditions required to focus the array are independent of array geometry (i.e. the distance between and location of the electrodes is arbitrary in principle, although it is usually preferable to have a uniform, symmetrical configuration).

Focused electric potential

The focused potential distribution is found by summing the contribution from the four current electrodes (eq. D.2), each contribution being weighted according to the balance factors in eq. D.5. Substituting (D.5) into (D.2):

$$\left.\begin{array}{l} Vf_{N_1} = \left(Z_{PN_1} + Z_{NN_1}Bf_N + Z_{SN_1}Bf_S + Z_{EN_1}Bf_E + Z_{WN_1}Bf_W\right)I_P \\ Vf_{N_2} = \left(Z_{PN_2} + Z_{NN_2}Bf_N + Z_{SN_2}Bf_S + Z_{EN_2}Bf_E + Z_{WN_2}Bf_W\right)I_P \\ Vf_{S_1} = \left(Z_{PS_1} + Z_{NS_1}Bf_N + Z_{SS_1}Bf_S + Z_{ES_1}Bf_E + Z_{WS_1}Bf_W\right)I_P \\ Vf_{S_2} = \left(Z_{PS_2} + Z_{NS_2}Bf_N + Z_{SS_2}Bf_S + Z_{ES_2}Bf_E + Z_{WS_2}Bf_W\right)I_P \\ Vf_{E_1} = \left(Z_{PE_1} + Z_{NE_1}Bf_N + Z_{SE_1}Bf_S + Z_{EE_1}Bf_E + Z_{WE_1}Bf_W\right)I_P \\ Vf_{E_2} = \left(Z_{PE_2} + Z_{NE_2}Bf_N + Z_{SE_2}Bf_S + Z_{EE_2}Bf_E + Z_{WE_2}Bf_W\right)I_P \\ Vf_{W_1} = \left(Z_{PW_1} + Z_{NW_1}Bf_N + Z_{SW_1}Bf_S + Z_{EW_1}Bf_E + Z_{WW_1}Bf_W\right)I_P \\ Vf_{W_2} = \left(Z_{PW_2} + Z_{NW_2}Bf_N + Z_{SW_2}Bf_S + Z_{EW_2}Bf_E + Z_{WW_2}Bf_W\right)I_P \end{array}\right\} , \quad \text{(D.6)}$$

where Vf_R is the theoretical focused electric potential at electrode R. These focused electric potentials may be used to calculate a focused apparent resistivity, as described in Section 4.1.2.3.

D.2 ODPHT tool

Consider the downhole tool electrode configuration illustrated in Figure D.2. As described in Section 4.2.2, this focusing tool consists of a measurement current electrode: $A0$; two focusing current electrodes: $A1$ and $A2$, and four potential electrodes: $M1$, $M1'$, $M2$ and $M2'$. As with the focused surface array, the magnitudes of the focusing currents are adjusted to satisfy conditions on the voltage at the potential electrodes, and are dependent on the electrode geometry of the tool, the magnitude of the measurement current, and the resistivity distribution in the formation surrounding the borehole.

Transfer impedances

Following the discussion in Section D.1, $3 \times 4 = 12$ transfer impedances can be defined from equation (D.1). For example, the four transfer impedances associated with electrode $A0$ are

$$Z_{A0M1} = \frac{V_{M1}}{I_{A0}};\ Z_{A0M2} = \frac{V_{M2}}{I_{A0}};\ Z_{A0M1'} = \frac{V_{M1'}}{I_{A0}} \text{ and } Z_{A0M2'} = \frac{V_{M2'}}{I_{A0}}; \tag{D.7}$$

similar expressions for transfer impedances for electrodes $A1$ and $A2$ may also be written down.

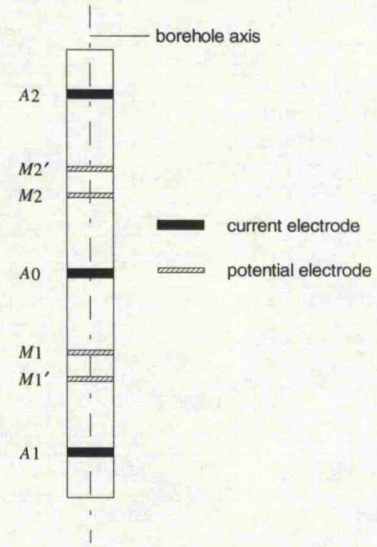

Figure D.2 ODPHT electrode arrangement (schematic).

Using superposition, if all current electrodes were simultaneously emitting current, the electric potentials at each of the potential electrodes would be given by

$$\left.\begin{aligned} V_{M1} &= I_{A0}Z_{A0M1} + I_{A1}Z_{A1M1} + I_{A2}Z_{A2M1} \\ V_{M1'} &= I_{A0}Z_{A0M1'} + I_{A1}Z_{A1M1'} + I_{A2}Z_{A2M1'} \\ V_{M2} &= I_{A0}Z_{A0M2} + I_{A1}Z_{A1M2} + I_{A2}Z_{A2M2} \\ V_{M2'} &= I_{A0}Z_{A0M2'} + I_{A1}Z_{A1M2'} + I_{A2}Z_{A2M2'} \end{aligned}\right\}, \tag{D.8}$$

where *IAn* denotes the current emitted by electrode *An*.

Equations (D.8) are substituted into the *focusing conditions* $V_{M1} = V_{M1'}$ and $V_{M2} = V_{M2'}$ to obtain two simultaneous equations:

$$\left.\begin{aligned} I_{A0}Z_{A0M1} + I_{A1}Z_{A1M1} + I_{A2}Z_{A2M1} &= I_{A0}Z_{A0M1'} + I_{A1}Z_{A1M1'} + I_{A2}Z_{A2M1'} \\ I_{A0}Z_{A0M2} + I_{A1}Z_{A1M2} + I_{A2}Z_{A2M2} &= I_{A0}Z_{A0M2'} + I_{A1}Z_{A1M2'} + I_{A2}Z_{A2M2'} \end{aligned}\right\} \tag{D.9}$$

There are two unknowns: I_{A1} and I_{A2}. Equations (D.9) can be rearranged to give:

$$\left.\begin{aligned} I_{A1}(Z_{A1M1} - Z_{A1M1'}) + I_{A2}(Z_{A2M1} - Z_{A2M1'}) &= -I_{A0}(Z_{A0M1} - Z_{A0M1'}) \\ I_{A1}(Z_{A1M2} - Z_{A1M2'}) + I_{A2}(Z_{A2M2} - Z_{A2M2'}) &= -I_{A0}(Z_{A0M2} - Z_{A0M2'}) \end{aligned}\right\} \tag{D.10}$$

Balance current magnitudes

The two simultaneous equations (D.10) can be solved by elimination, giving

$$I_{A1} = Bf_{A1} I_{A0}, \text{ and } I_{A2} = Bf_{A2} I_{A0}, \tag{D.11}$$

where

$$Bf_{A1} = \left(\frac{\beta_2 \gamma_1 - \beta_1 \gamma_2}{\alpha_1 \beta_2 - \alpha_2 \beta_1} \right), \text{ and } Bf_{A2} = \left(\frac{\alpha_1 \gamma_2 - \alpha_2 \gamma_1}{\alpha_1 \beta_2 - \alpha_2 \beta_1} \right),$$

and where

$$\begin{aligned}
\alpha_1 &= Z_{A1M1} - Z_{A1M1'}; \\
\alpha_2 &= Z_{A1M2} - Z_{A1M2'}; \\
\beta_1 &= Z_{A2M1} - Z_{A2M1'}; \\
\beta_2 &= Z_{A2M2} - Z_{A2M2'}; \\
\gamma_1 &= -(Z_{A0M1} - Z_{A0M1'}); \text{ and} \\
\gamma_2 &= -(Z_{A0M2} - Z_{A0M2'}).
\end{aligned}$$

The solution (D.11) is expressed in terms of I_{A0}, and the pre-calculated transfer impedances. It is noted that these results are independent of the tool's electrode geometry.

Focused electric potential

Substituting equation (D.11) into (D.8), a set of equations expressing the focused electric potential at each of the potential electrodes results:

$$\left.\begin{aligned}
Vf_{M1} &= (Z_{A0M1} + Z_{A1M1} Bf_{A1} + Z_{A2M1} Bf_{A2}) I_{A0} \\
Vf_{M1'} &= (Z_{A0M1'} + Z_{A1M1'} Bf_{A1} + Z_{A2M1'} Bf_{A2}) I_{A0} \\
Vf_{M2} &= (Z_{A0M2} + Z_{A1M2} Bf_{A1} + Z_{A2M2} Bf_{A2}) I_{A0} \\
Vf_{M2'} &= (Z_{A0M2'} + Z_{A1M2'} Bf_{A1} + Z_{A2M2'} Bf_{A2}) I_{A0}
\end{aligned}\right\}. \tag{D.12}$$

In equation (D.12) , terms of the form Vf_R refer to the theoretical focused electric potential at electrode R. These focused electric potentials may be used to calculate a focused apparent resistivity and to derive a geometric factor for the tool (§4.2.3.2).

APPENDIX E

Focused apparent resistivity field data

This appendix contains focused apparent resistivity data acquired in Saarland, Germany, in August 1993 and September 1994. Resistivity traverses (focused, defocused and pole-pole measurements) and focusing balance factors are presented on a site-by-site basis (see §4.1.3). The table below lists the survey sites where focused measurements were made. Refer to the relevant field reports (Greenwood et al., 1993; Meldrum and Williams, 1995) for more details.

Year	Site name	Notes
1993	1.2	Three adjoining grids, labelled 1.2a, 1.2b and 1.2c. Lines 4, 5, 6, 7, and 8 on 1.2a Lines 5, 6, and 7 on 1.2b Line 6 on 1.2c
	1.4	Line 6 only
	2.1	Lines 4, 5, 6, 7, and 8.
1994	3.1	Line 6 only
	3.2	Two adjoining grids, labelled 3.2a and 3.2b Line 6 only on both.

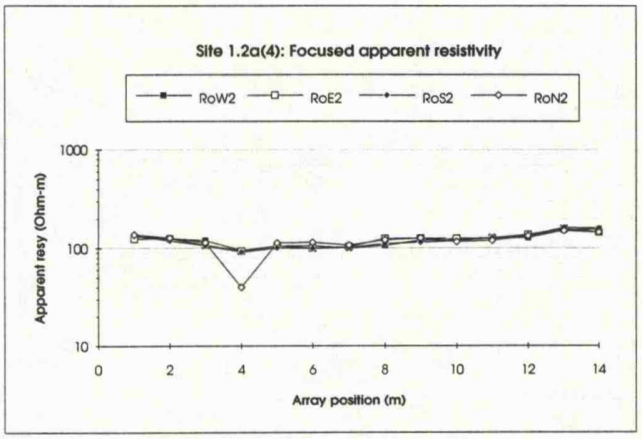
Site 1.2a(4): Focused apparent resistivity
RoW2
RoE2
RoS2
RoN2
Apparent resy (Ohm-m)
1000
100
10
0
2
4
6
8
10
12
14
Array position (m)

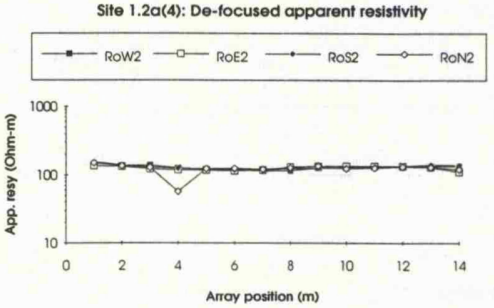
Site 1.2a(4): De-focused apparent resistivity
RoW2
RoE2
RoS2
RoN2
App. resy (Ohm-m)
1000
100
10
0
2
4
6
8
10
12
14
Array position (m)

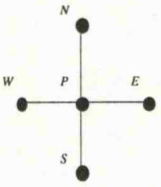
N
W
P
E
S

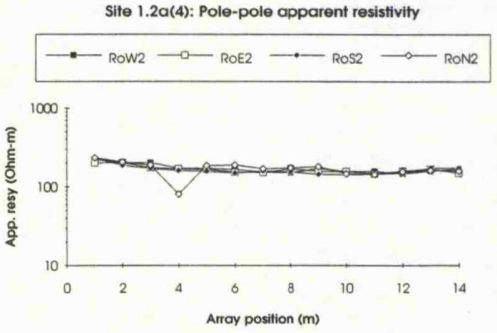
Site 1.2a(4): Pole-pole apparent resistivity
RoW2
RoE2
RoS2
RoN2
App. resy (Ohm-m)
1000
100
10
0
2
4
6
8
10
12
14
Array position (m)

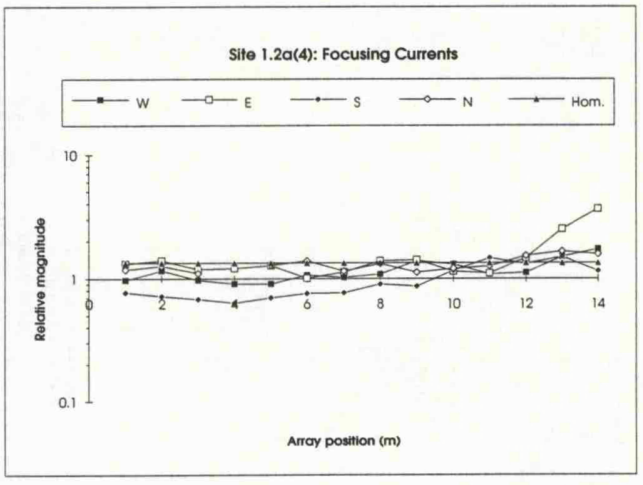
Site 1.2a(4): Focusing Currents
W
E
S
N
Hom.
Relative magnitude
10
1
0.1
0
2
4
6
8
10
12
14
Array position (m)

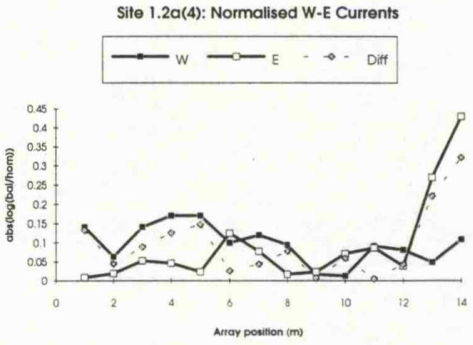
Site 1.2a(4): Normalised W-E Currents
W
E
Diff
abs(log(bal/hom))
0.45
0.4
0.35
0.3
0.25
0.2
0.15
0.1
0.05
0
0
2
4
6
8
10
12
14
Array position (m)

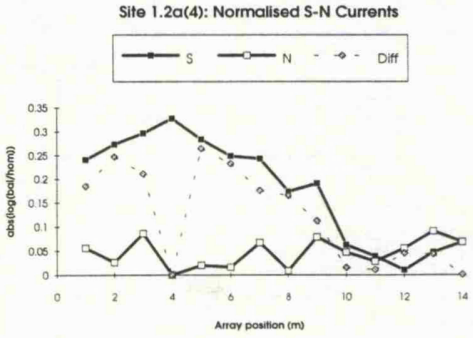
Site 1.2a(4): Normalised S-N Currents
S
N
Diff
abs(log(bal/hom))
0.35
0.3
0.25
0.2
0.15
0.1
0.05
0
0
2
4
6
8
10
12
14
Array position (m)

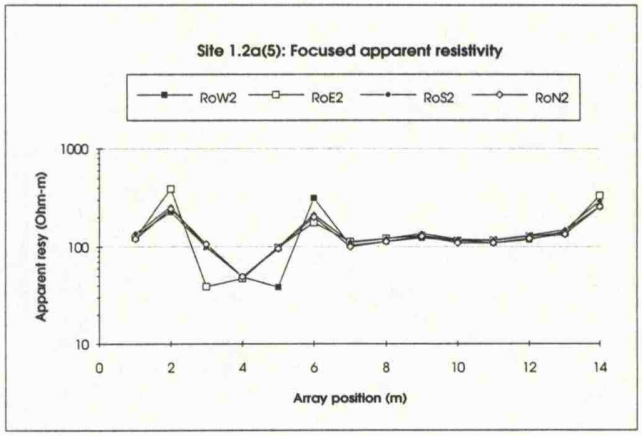
Site 1.2a(5): Focused apparent resistivity
RoW2
RoE2
RoS2
RoN2
Apparent resy (Ohm-m)
1000
100
10
0
2
4
6
8
10
12
14
Array position (m)

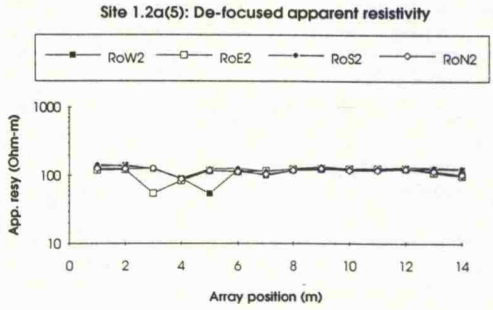
Site 1.2a(5): De-focused apparent resistivity
RoW2
RoE2
RoS2
RoN2
App. resy (Ohm-m)
1000
100
10
0
2
4
6
8
10
12
14
Array position (m)

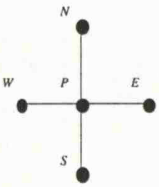
N
W
P
E
S

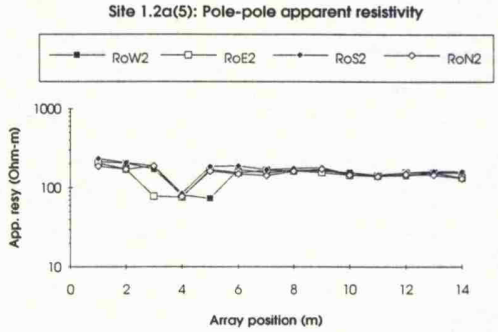
Site 1.2a(5): Pole-pole apparent resistivity
RoW2
RoE2
RoS2
RoN2
App. resy (Ohm-m)
1000
100
10
0
2
4
6
8
10
12
14
Array position (m)

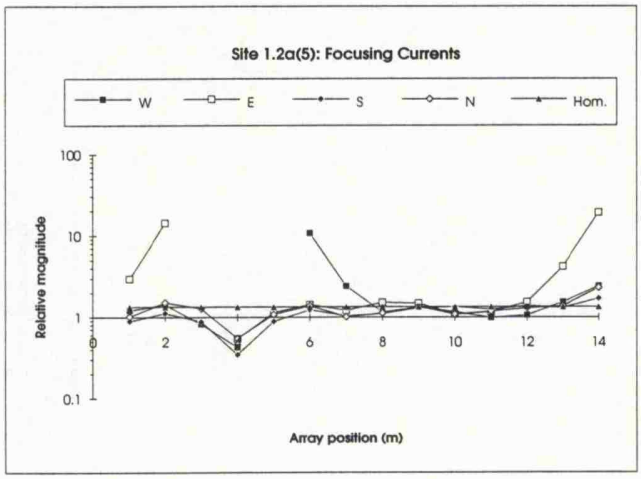
Site 1.2a(5): Focusing Currents
W
E
S
N
Hom.
Relative magnitude
100
10
1
0.1
0
2
6
8
10
12
14
Array position (m)

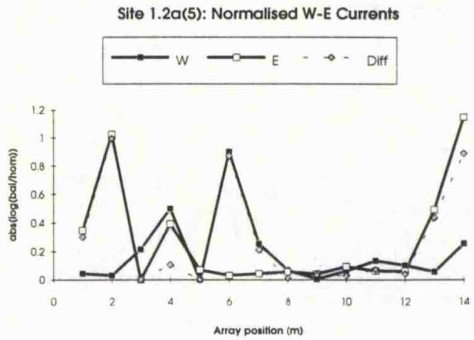
Site 1.2a(5): Normalised W-E Currents
W
E
Diff
abs(log(bal/hom))
1.2
1
0.8
0.6
0.4
0.2
0
0
2
4
6
8
10
12
14
Array position (m)

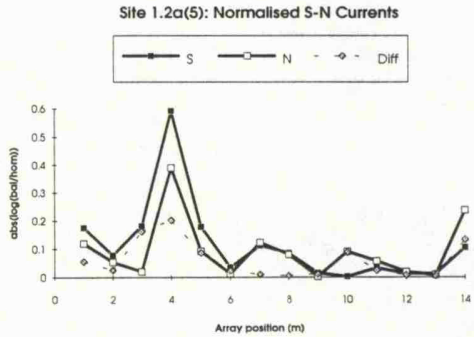
Site 1.2a(5): Normalised S-N Currents
S
N
Diff
abs(log(bal/hom))
0.6
0.5
0.4
0.3
0.2
0.1
0
0
2
4
6
8
10
12
14
Array position (m)

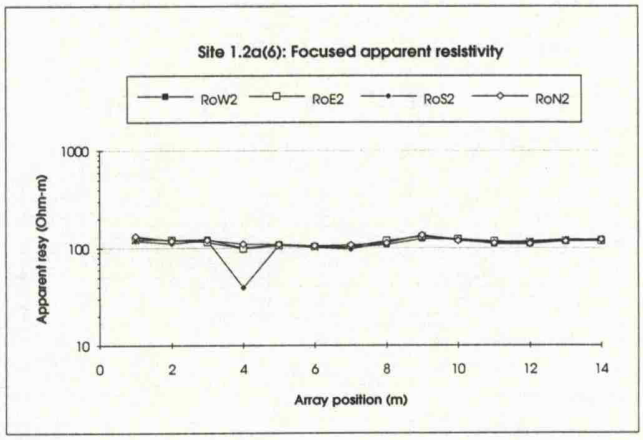
Site 1.2a(6): Focused apparent resistivity
RoW2
RoE2
RoS2
RoN2
Apparent resy (Ohm-m)
1000
100
10
0
2
4
6
8
10
12
14
Array position (m)

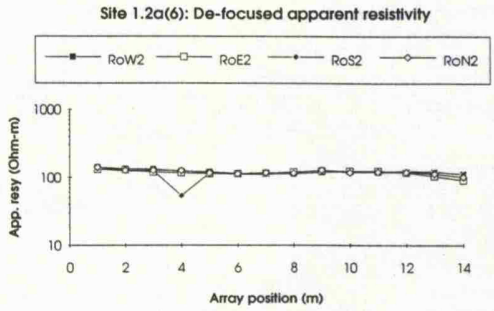
Site 1.2a(6): De-focused apparent resistivity
RoW2
RoE2
RoS2
RoN2
App. resy (Ohm-m)
1000
100
10
0
2
4
6
8
10
12
14
Array position (m)

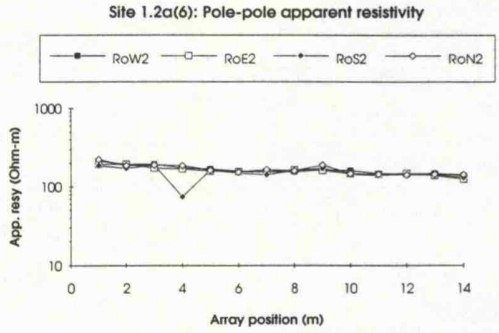
Site 1.2a(6): Pole-pole apparent resistivity
RoW2
RoE2
RoS2
RoN2
App. resy (Ohm-m)
1000
100
10
0
2
4
6
8
10
12
14
Array position (m)

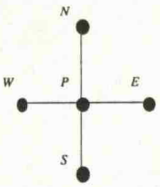
N
W
P
E
S

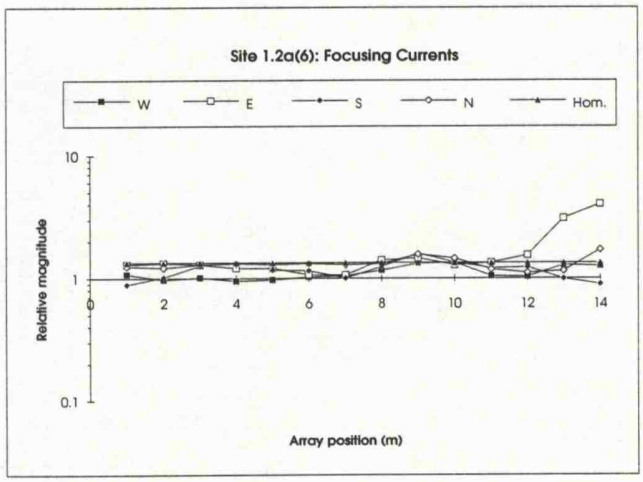
Site 1.2a(6): Focusing Currents
W
E
S
N
Hom.
Relative magnitude
10
1
0.1
0
2
4
6
8
10
12
14
Array position (m)

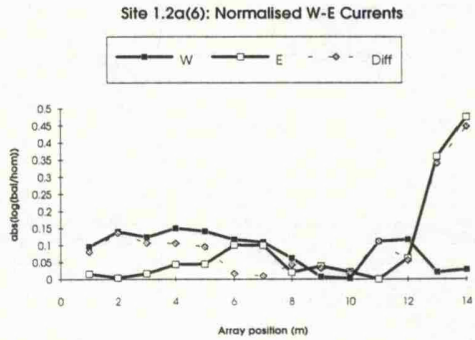
Site 1.2a(6): Normalised W-E Currents
W
E
Diff
abs(log(bal/hom))
0.5
0.45
0.4
0.35
0.3
0.25
0.2
0.15
0.1
0.05
0
0
2
4
6
8
10
12
14
Array position (m)

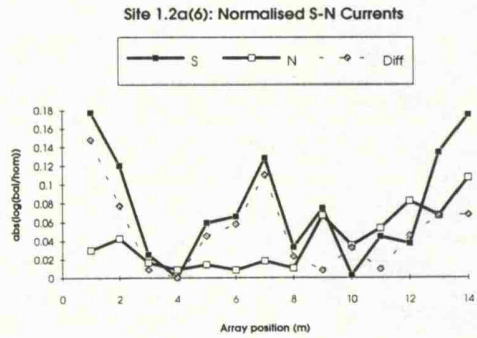
Site 1.2a(6): Normalised S-N Currents
S
N
Diff
abs(log(bal/hom))
0.18
0.16
0.14
0.12
0.1
0.08
0.06
0.04
0.02
0
0
2
4
6
8
10
12
14
Array position (m)

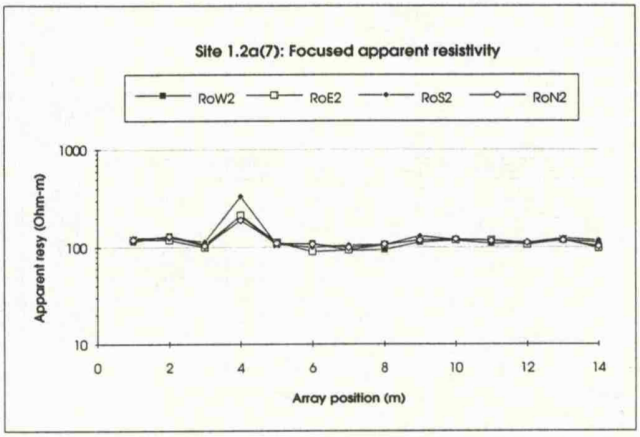
Site 1.2a(7): Focused apparent resistivity
RoW2
RoE2
RoS2
RoN2
Apparent resy (Ohm-m)
1000
100
10
0
2
4
6
8
10
12
14
Array position (m)

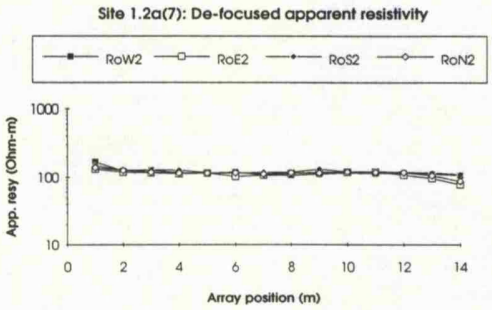
Site 1.2a(7): De-focused apparent resistivity
RoW2
RoE2
RoS2
RoN2
App. resy (Ohm-m)
1000
100
10
0
2
4
6
8
10
12
14
Array position (m)

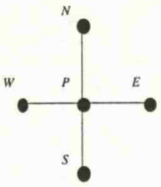
N
W
P
E
S

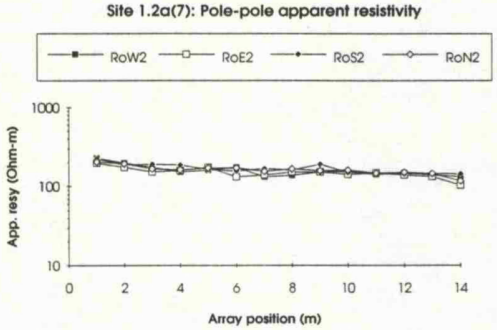
Site 1.2a(7): Pole-pole apparent resistivity
RoW2
RoE2
RoS2
RoN2
App. resy (Ohm-m)
1000
100
10
0
2
4
6
8
10
12
14
Array position (m)

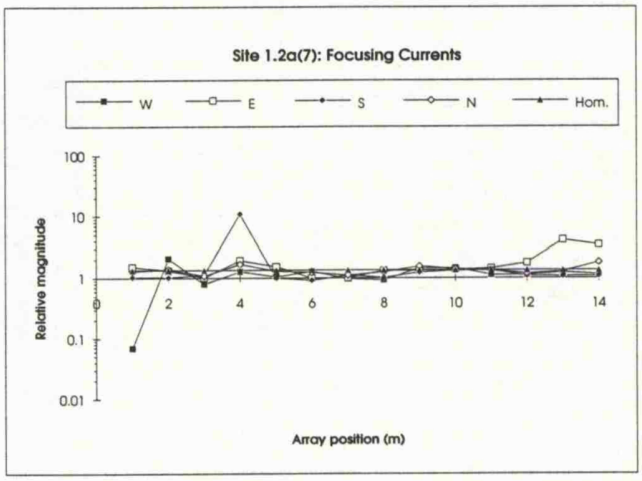
Site 1.2a(7): Focusing Currents
W
E
S
N
Hom.
Relative magnitude
100
10
1
0.1
0.01
0
2
4
6
8
10
12
14
Array position (m)

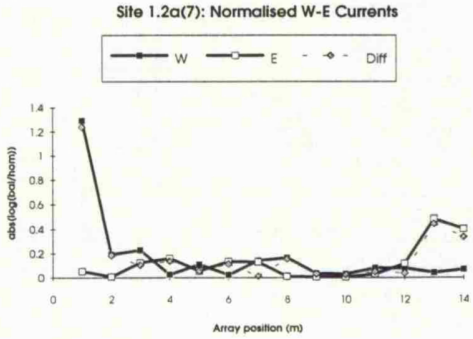
Site 1.2a(7): Normalised W-E Currents
W
E
Diff
abs(log(bal/hom))
1.4
1.2
1
0.8
0.6
0.4
0.2
0
0
2
4
6
8
10
12
14
Array position (m)

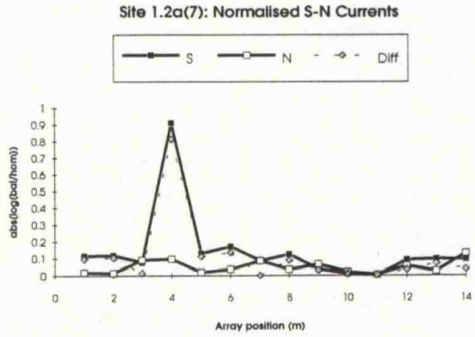
Site 1.2a(7): Normalised S-N Currents
S
N
Diff
abs(log(bal/hom))
1
0.9
0.8
0.7
0.6
0.5
0.4
0.3
0.2
0.1
0
0
2
4
6
8
10
12
14
Array position (m)

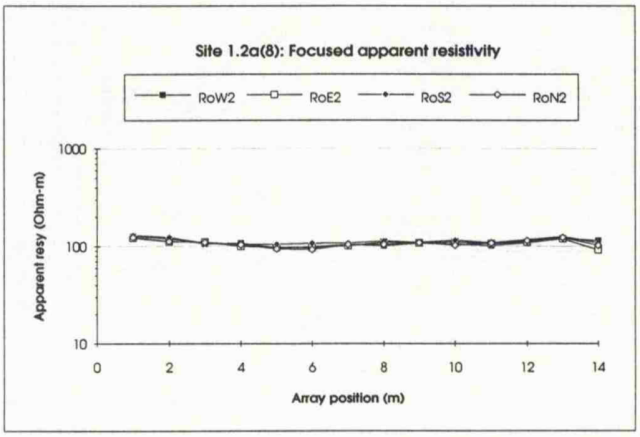
Site 1.2a(8): Focused apparent resistivity
RoW2
RoE2
RoS2
RoN2
Apparent resy (Ohm-m)
1000
100
10
0
2
4
6
8
10
12
14
Array position (m)

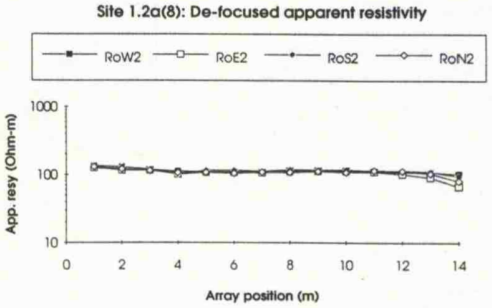
Site 1.2a(8): De-focused apparent resistivity
RoW2
RoE2
RoS2
RoN2
App. resy (Ohm-m)
1000
100
10
0
2
4
6
8
10
12
14
Array position (m)

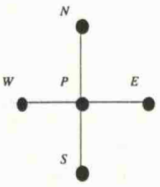
N
W
P
E
S

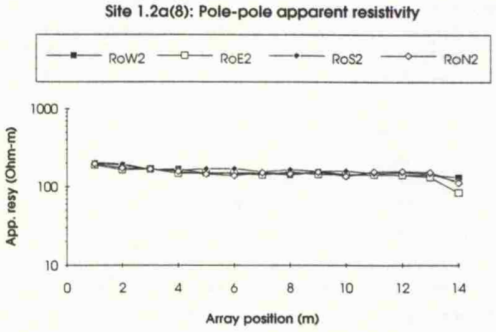
Site 1.2a(8): Pole-pole apparent resistivity
RoW2
RoE2
RoS2
RoN2
App. resy (Ohm-m)
1000
100
10
0
2
4
6
8
10
12
14
Array position (m)

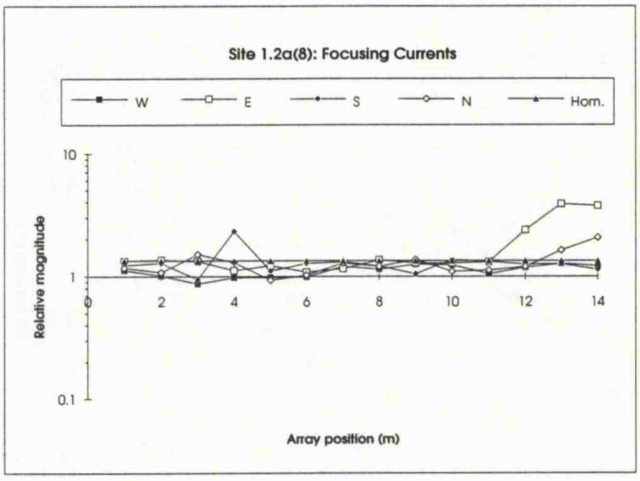
Site 1.2a(8): Focusing Currents
W
E
S
N
Hom.
Relative magnitude
10
1
0.1
0
2
4
6
8
10
12
14
Array position (m)

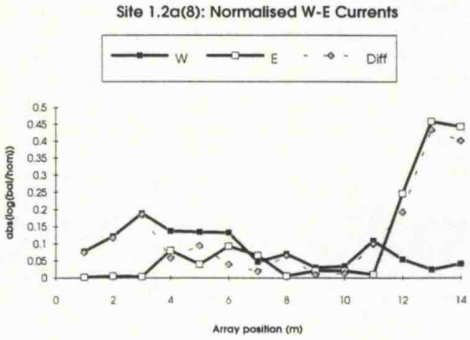
Site 1.2a(8): Normalised W-E Currents
W
E
Diff
abs(log(bal/hom))
0.5
0.45
0.4
0.35
0.3
0.25
0.2
0.15
0.1
0.05
0
0
2
4
6
8
10
12
14
Array position (m)

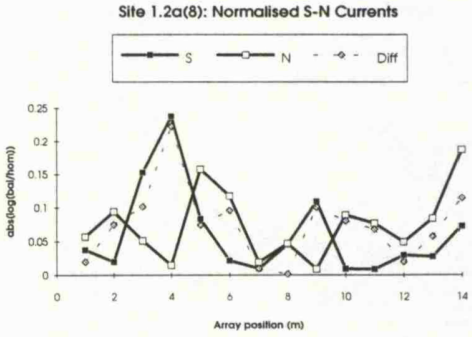
Site 1.2a(8): Normalised S-N Currents
S
N
Diff
abs(log(bal/hom))
0.25
0.2
0.15
0.1
0.05
0
0
2
4
6
8
10
12
14
Array position (m)

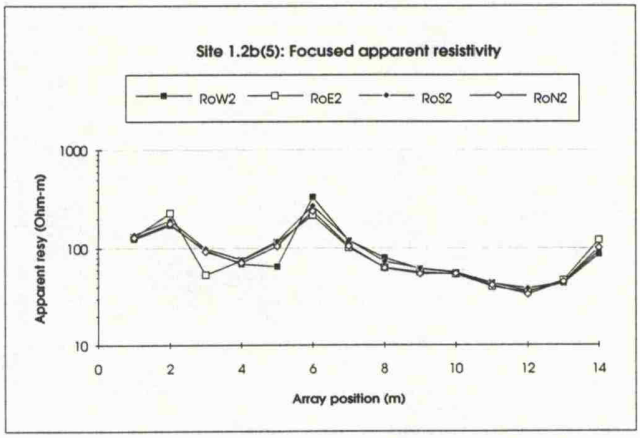
Site 1.2b(5): Focused apparent resistivity
RoW2
RoE2
RoS2
RoN2
Apparent resy (Ohm-m)
1000
100
10
0
2
4
6
8
10
12
14
Array position (m)

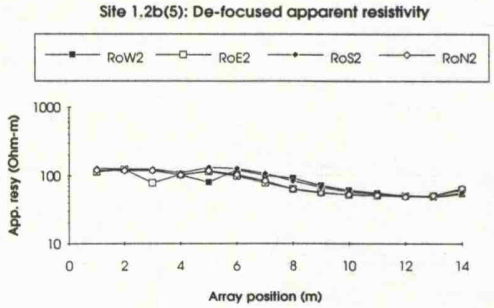
Site 1.2b(5): De-focused apparent resistivity
RoW2
RoE2
RoS2
RoN2
App. resy (Ohm-m)
1000
100
10
0
2
4
6
8
10
12
14
Array position (m)

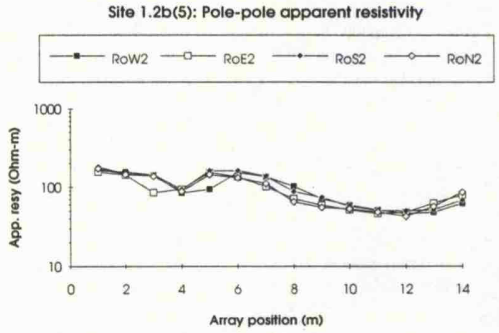
Site 1.2b(5): Pole-pole apparent resistivity
RoW2
RoE2
RoS2
RoN2
App. resy (Ohm-m)
1000
100
10
0
2
4
6
8
10
12
14
Array position (m)

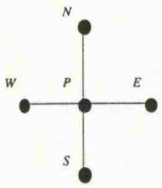
N
W
P
E
S

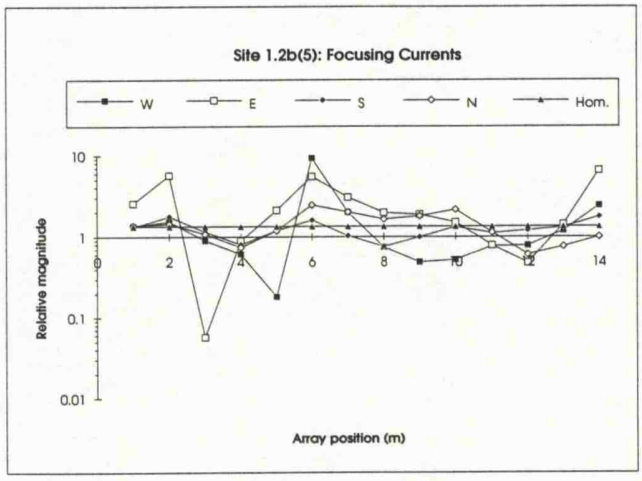
Site 1.2b(5): Focusing Currents
W
E
S
N
Hom.
Relative magnitude
10
1
0.1
0.01
0
2
4
6
8
10
12
14
Array position (m)

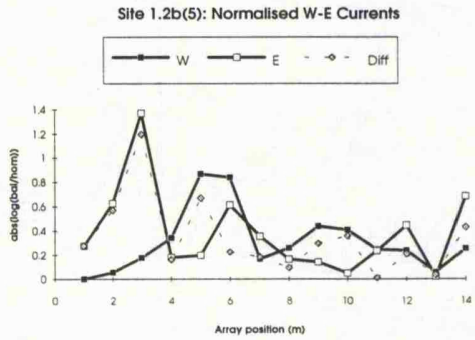
Site 1.2b(5): Normalised W-E Currents
W
E
Diff
abs(log(bal/hom))
1.4
1.2
1
0.8
0.6
0.4
0.2
0
0
2
4
6
8
10
12
14
Array position (m)

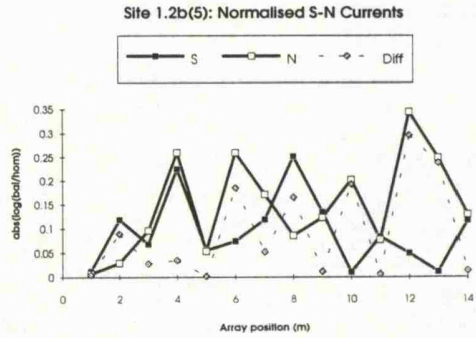
Site 1.2b(5): Normalised S-N Currents
S
N
Diff
abs(log(bal/hom))
0.35
0.3
0.25
0.2
0.15
0.1
0.05
0
0
2
4
6
8
10
12
14
Array position (m)

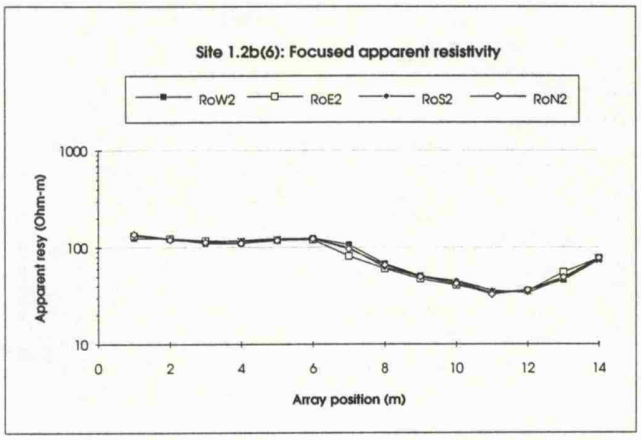
Site 1.2b(6): Focused apparent resistivity
RoW2
RoE2
RoS2
RoN2
Apparent resy (Ohm-m)
1000
100
10
0
2
4
6
8
10
12
14
Array position (m)

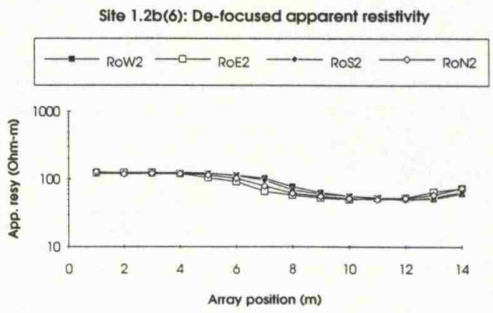
Site 1.2b(6): De-focused apparent resistivity
RoW2
RoE2
RoS2
RoN2
App. resy (Ohm-m)
1000
100
10
0
2
4
6
8
10
12
14
Array position (m)

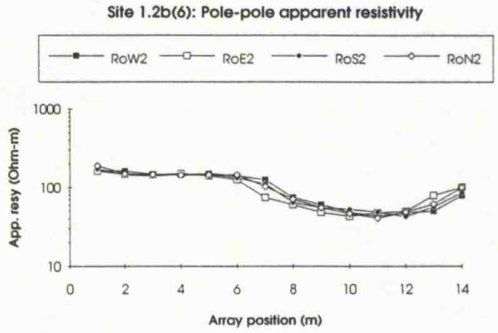
Site 1.2b(6): Pole-pole apparent resistivity
RoW2
RoE2
RoS2
RoN2
App. resy (Ohm-m)
1000
100
10
0
2
4
6
8
10
12
14
Array position (m)

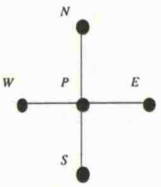
N
W
P
E
S

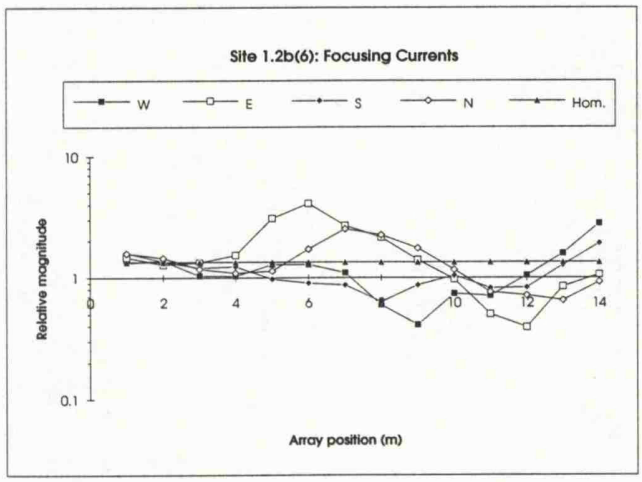
Site 1.2b(6): Focusing Currents
W
E
S
N
Hom.
Relative magnitude
10
1
0.1
0
2
4
6
10
12
14
Array position (m)

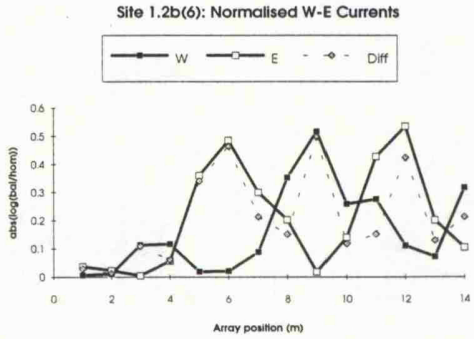
Site 1.2b(6): Normalised W-E Currents
W
E
Diff
abs(log(bal/hom))
0.6
0.5
0.4
0.3
0.2
0.1
0
0
2
4
6
8
10
12
14
Array position (m)

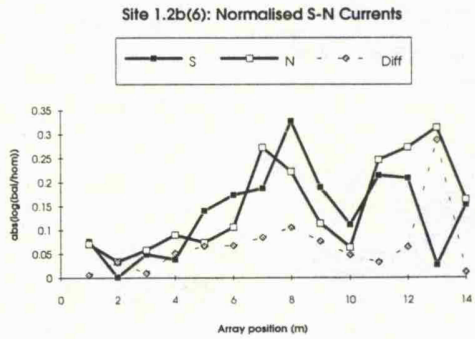
Site 1.2b(6): Normalised S-N Currents
S
N
Diff
abs(log(bal/hom))
0.35
0.3
0.25
0.2
0.15
0.1
0.05
0
0
2
4
6
8
10
12
14
Array position (m)

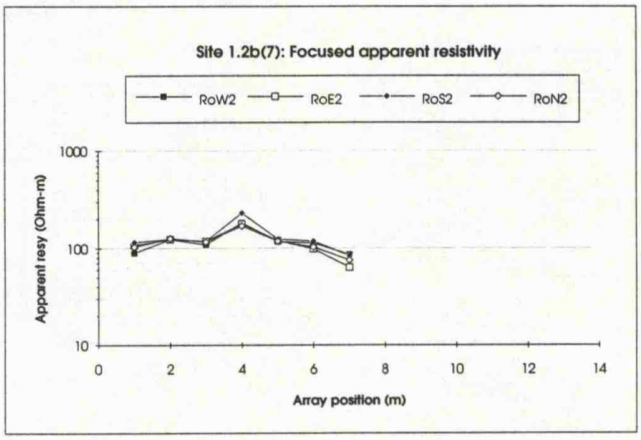
Site 1.2b(7): Focused apparent resistivity
RoW2
RoE2
RoS2
RoN2
Apparent resy (Ohm-m)
1000
100
10
0
2
4
6
8
10
12
14
Array position (m)

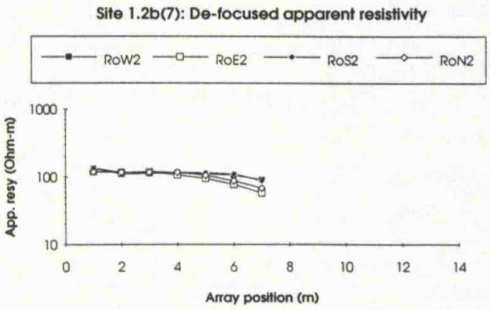
Site 1.2b(7): De-focused apparent resistivity
RoW2
RoE2
RoS2
RoN2
App. resy (Ohm-m)
1000
100
10
0
2
4
6
8
10
12
14
Array position (m)

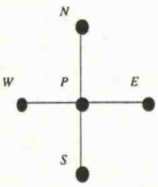
N
W
P
E
S

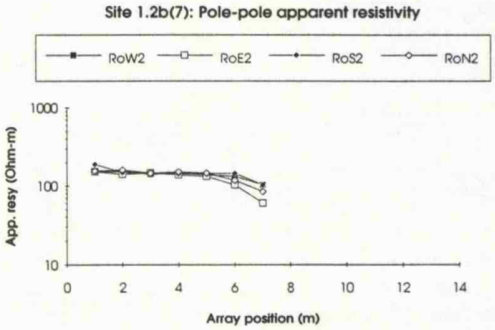
Site 1.2b(7): Pole-pole apparent resistivity
RoW2
RoE2
RoS2
RoN2
App. resy (Ohm-m)
1000
100
10
0
2
4
6
8
10
12
14
Array position (m)

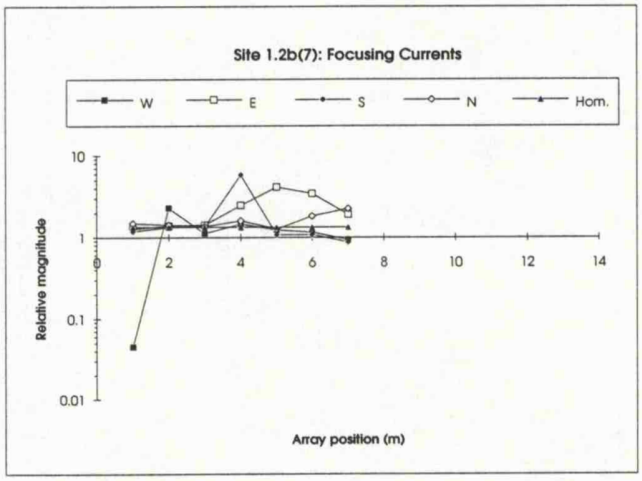
Site 1.2b(7): Focusing Currents
W
E
S
N
Hom.
Relative magnitude
10
1
0.1
0.01
0
2
4
6
8
10
12
14
Array position (m)

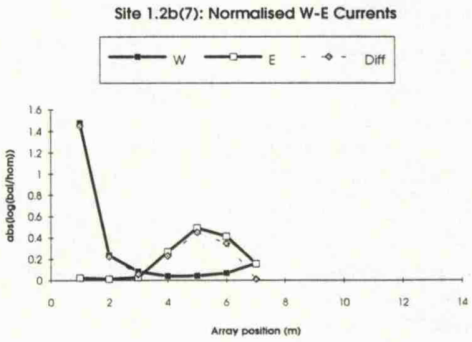
Site 1.2b(7): Normalised W-E Currents
W
E
Diff
abs(log(bal/hom))
1.6
1.4
1.2
1
0.8
0.6
0.4
0.2
0
0
2
4
6
8
10
12
14
Array position (m)

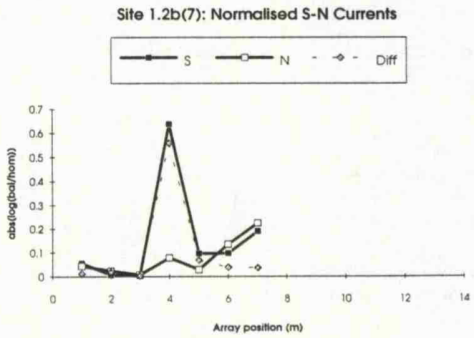
Site 1.2b(7): Normalised S-N Currents
S
N
Diff
abs(log(bal/hom))
0.7
0.6
0.5
0.4
0.3
0.2
0.1
0
0
2
4
6
8
10
12
14
Array position (m)

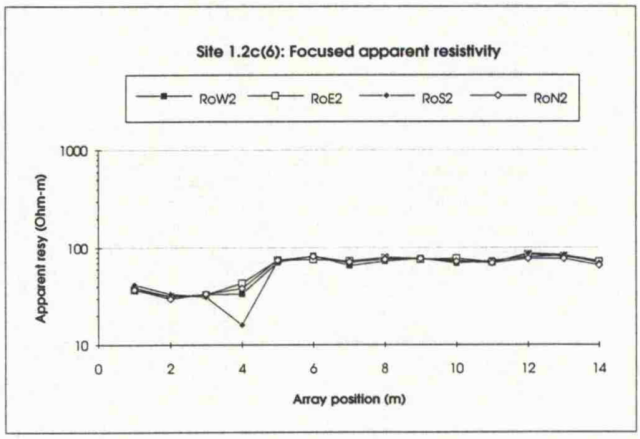
Site 1.2c(6): Focused apparent resistivity
RoW2
RoE2
RoS2
RoN2
Apparent resy (Ohm-m)
1000
100
10
0
2
4
6
8
10
12
14
Array position (m)

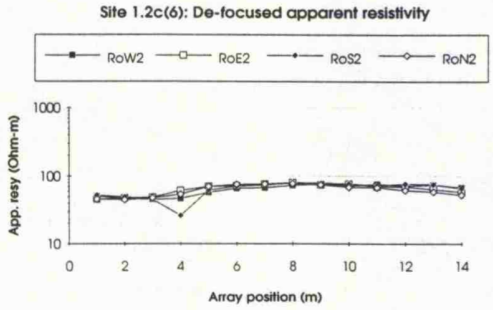
Site 1.2c(6): De-focused apparent resistivity
RoW2
RoE2
RoS2
RoN2
App. resy (Ohm-m)
1000
100
10
0
2
4
6
8
10
12
14
Array position (m)

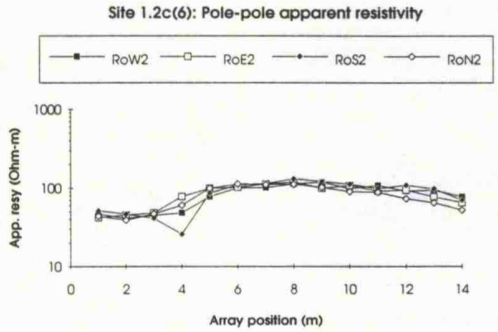
Site 1.2c(6): Pole-pole apparent resistivity
RoW2
RoE2
RoS2
RoN2
App. resy (Ohm-m)
1000
100
10
0
2
4
6
8
10
12
14
Array position (m)

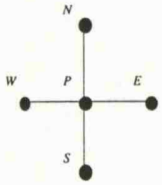
N
W
P
E
S

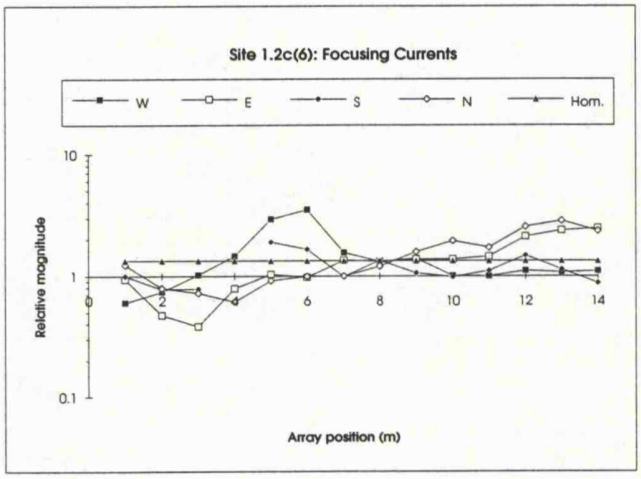
Site 1.2c(6): Focusing Currents
W
E
S
N
Hom.
Relative magnitude
10
1
0.1
0
2
4
6
8
10
12
14
Array position (m)

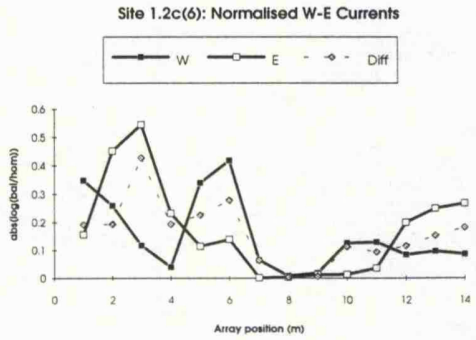
Site 1.2c(6): Normalised W-E Currents
W
E
Diff
abs(log(bal/hom))
0.6
0.5
0.4
0.3
0.2
0.1
0
0
2
4
6
8
10
12
14
Array position (m)

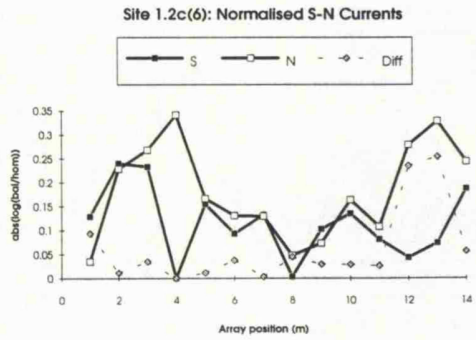
Site 1.2c(6): Normalised S-N Currents
S
N
Diff
abs(log(bal/hom))
0.35
0.3
0.25
0.2
0.15
0.1
0.05
0
0
2
4
6
8
10
12
14
Array position (m)

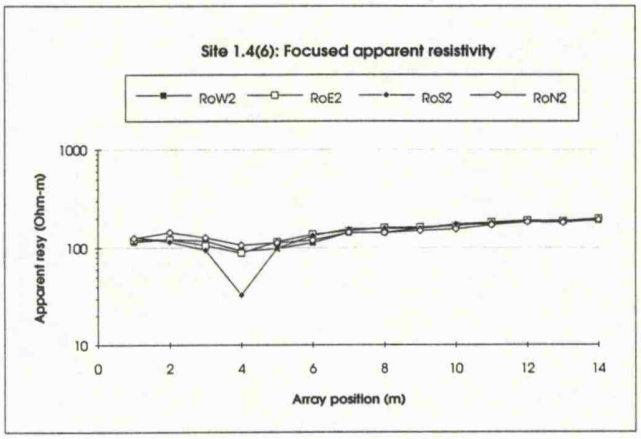
Site 1.4(6): Focused apparent resistivity
RoW2
RoE2
RoS2
RoN2
Apparent resy (Ohm-m)
1000
100
10
0
2
4
6
8
10
12
14
Array position (m)

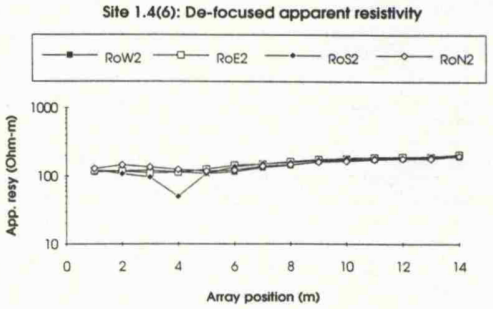
Site 1.4(6): De-focused apparent resistivity
RoW2
RoE2
RoS2
RoN2
App. resy (Ohm-m)
1000
100
10
0
2
4
6
8
10
12
14
Array position (m)

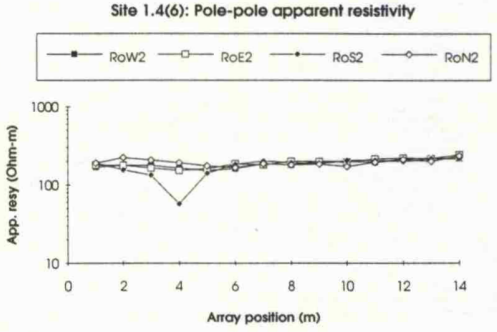
Site 1.4(6): Pole-pole apparent resistivity
RoW2
RoE2
RoS2
RoN2
App. resy (Ohm-m)
1000
100
10
0
2
4
6
8
10
12
14
Array position (m)

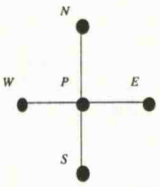
N
W
P
E
S

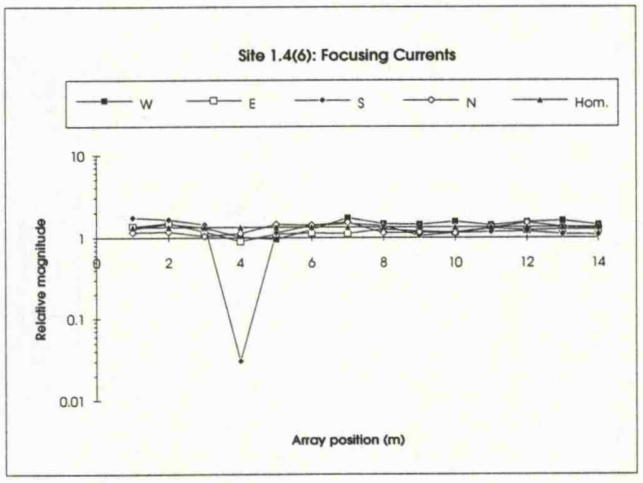
Site 1.4(6): Focusing Currents
W
E
S
N
Hom.
Relative magnitude
10
1
0.1
0.01
0
2
4
6
8
10
12
14
Array position (m)

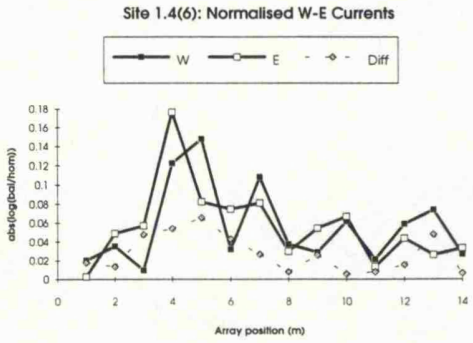
Site 1.4(6): Normalised W-E Currents
W
E
Diff
abs(log(bal/hom))
0.18
0.16
0.14
0.12
0.1
0.08
0.06
0.04
0.02
0
0
2
4
6
8
10
12
14
Array position (m)

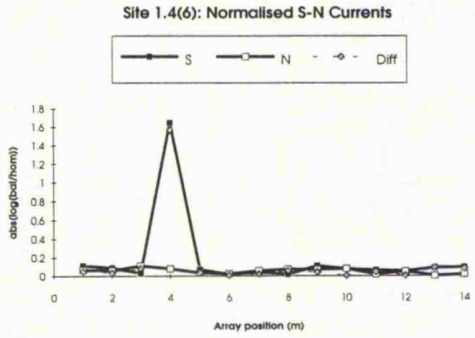
Site 1.4(6): Normalised S-N Currents
S
N
Diff
abs(log(bal/hom))
1.8
1.6
1.4
1.2
1
0.8
0.6
0.4
0.2
0
0
2
4
6
8
10
12
14
Array position (m)

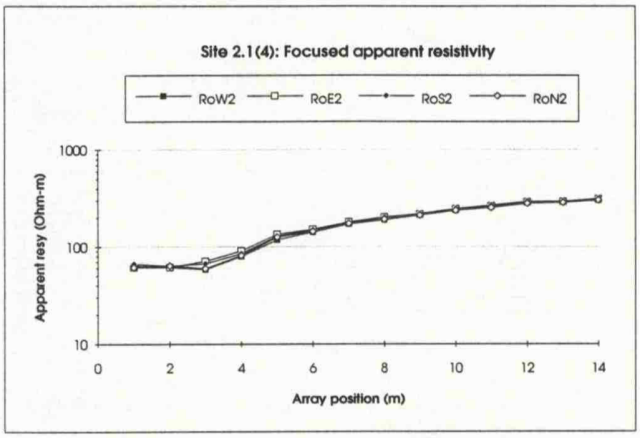
Site 2.1(4): Focused apparent resistivity
RoW2
RoE2
RoS2
RoN2
Apparent resy (Ohm-m)
1000
100
10
0
2
4
6
8
10
12
14
Array position (m)

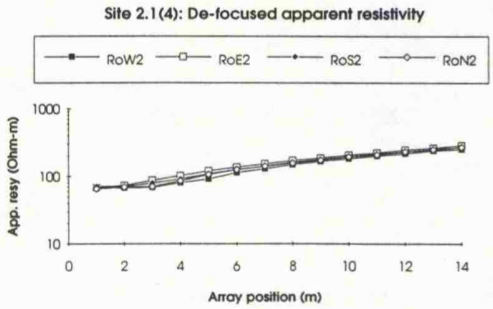
Site 2.1(4): De-focused apparent resistivity
RoW2
RoE2
RoS2
RoN2
App. resy (Ohm-m)
1000
100
10
0
2
4
6
8
10
12
14
Array position (m)

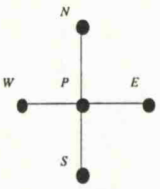
N
W
P
E
S

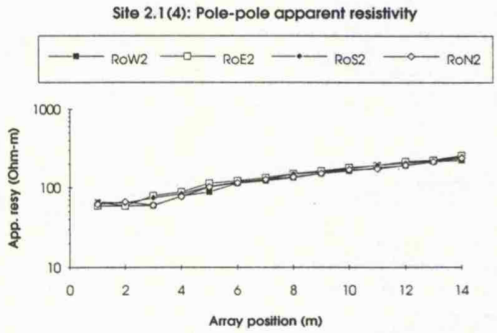
Site 2.1(4): Pole-pole apparent resistivity
RoW2
RoE2
RoS2
RoN2
App. resy (Ohm-m)
1000
100
10
0
2
4
6
8
10
12
14
Array position (m)

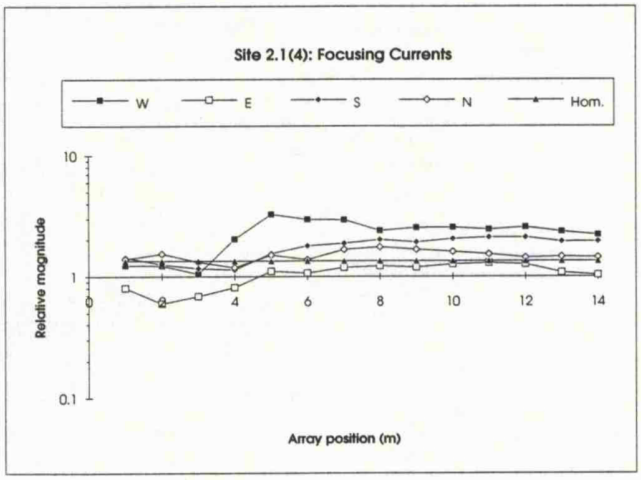
Site 2.1(4): Focusing Currents
W
E
S
N
Hom.
Relative magnitude
10
1
0.1
0
2
4
6
8
10
12
14
Array position (m)

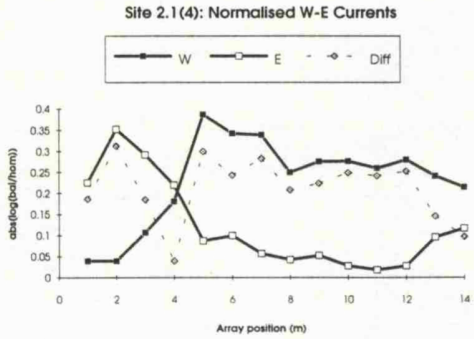
Site 2.1(4): Normalised W-E Currents
W
E
Diff
abs(log(bal/hom))
0.4
0.35
0.3
0.25
0.2
0.15
0.1
0.05
0
0
2
4
6
8
10
12
14
Array position (m)

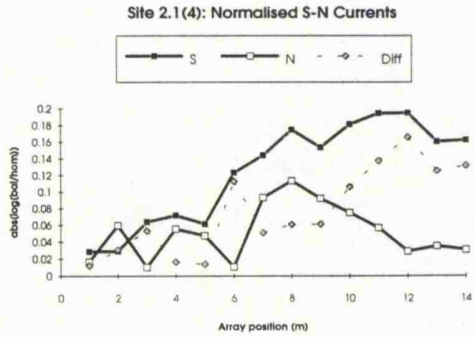
Site 2.1(4): Normalised S-N Currents
S
N
Diff
abs(log(bal/hom))
0.2
0.18
0.16
0.14
0.12
0.1
0.08
0.06
0.04
0.02
0
0
2
4
6
8
10
12
14
Array position (m)

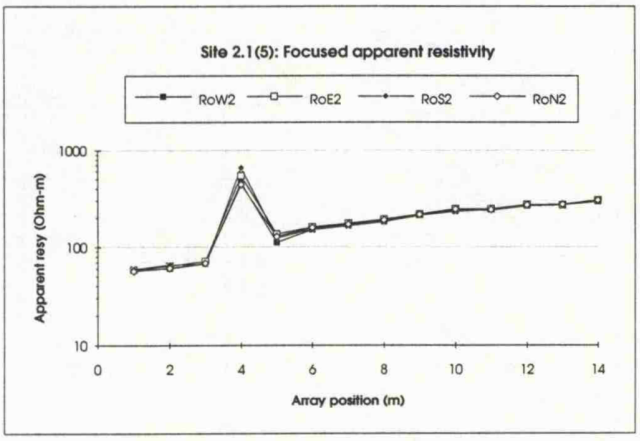
Site 2.1(5): Focused apparent resistivity
RoW2
RoE2
RoS2
RoN2
Apparent resy (Ohm-m)
1000
100
10
0
2
4
6
8
10
12
14
Array position (m)

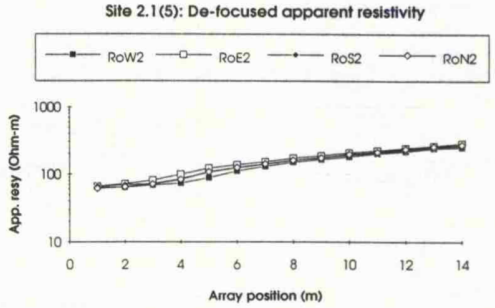
Site 2.1(5): De-focused apparent resistivity
RoW2
RoE2
RoS2
RoN2
App. resy (Ohm-m)
1000
100
10
0
2
4
6
8
10
12
14
Array position (m)

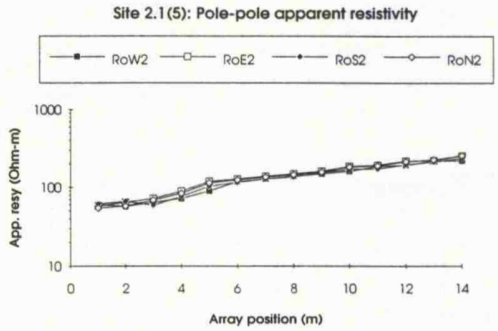
Site 2.1(5): Pole-pole apparent resistivity
RoW2
RoE2
RoS2
RoN2
App. resy (Ohm-m)
1000
100
10
0
2
4
6
8
10
12
14
Array position (m)

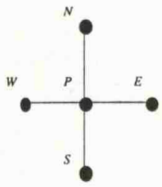
N
W
P
E
S

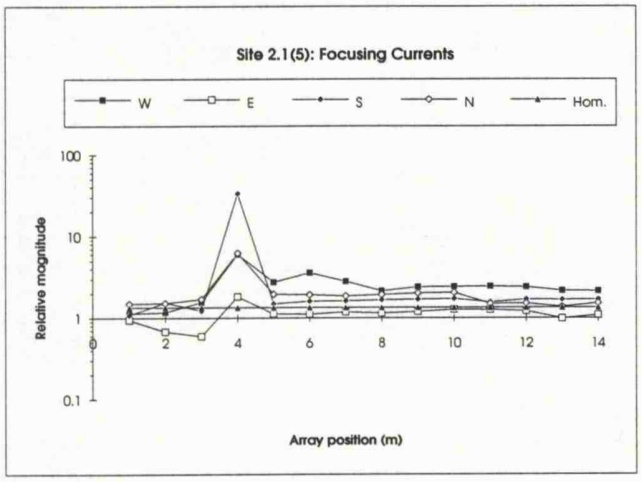
Site 2.1(5): Focusing Currents
W
E
S
N
Hom.
Relative magnitude
100
10
1
0.1
0
2
4
6
8
10
12
14
Array position (m)

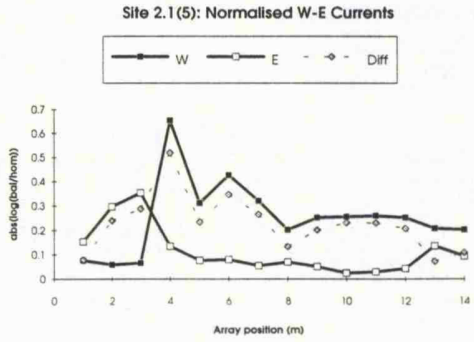
Site 2.1(5): Normalised W-E Currents
W
E
Diff
abs(log(bal/hom))
0.7
0.6
0.5
0.4
0.3
0.2
0.1
0
0
2
4
6
8
10
12
14
Array position (m)

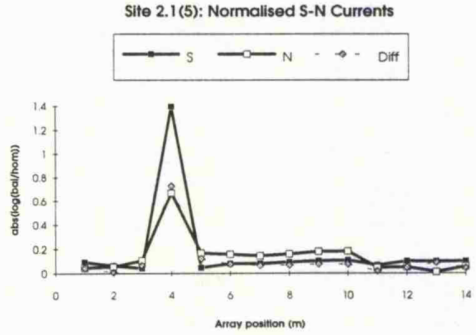
Site 2.1(5): Normalised S-N Currents
S
N
Diff
abs(log(bal/hom))
1.4
1.2
1
0.8
0.6
0.4
0.2
0
0
2
4
6
8
10
12
14
Array position (m)

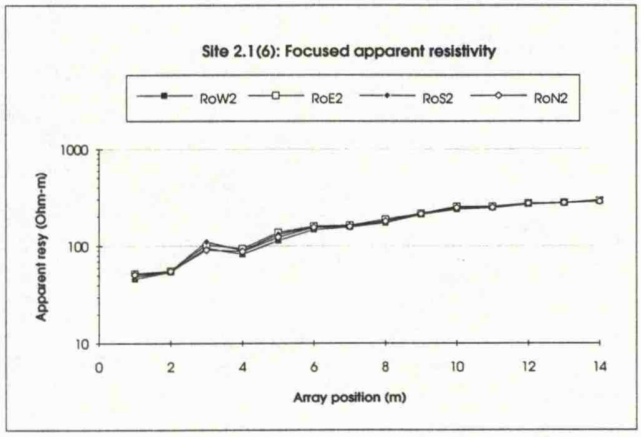
Site 2.1(6): Focused apparent resistivity
RoW2
RoE2
RoS2
RoN2
Apparent resy (Ohm-m)
1000
100
10
0
2
4
6
8
10
12
14
Array position (m)

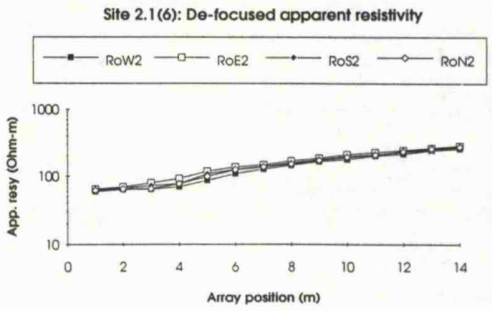
Site 2.1(6): De-focused apparent resistivity
RoW2
RoE2
RoS2
RoN2
App. resy (Ohm-m)
1000
100
10
0
2
4
6
8
10
12
14
Array position (m)

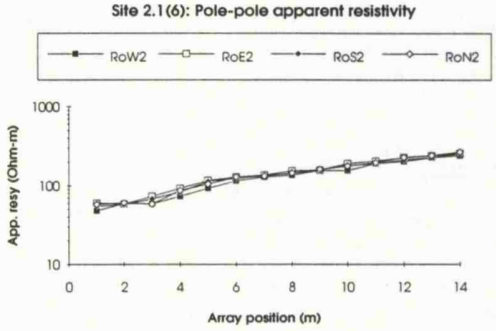
Site 2.1(6): Pole-pole apparent resistivity
RoW2
RoE2
RoS2
RoN2
App. resy (Ohm-m)
1000
100
10
0
2
4
6
8
10
12
14
Array position (m)

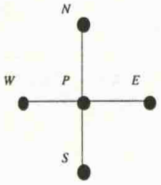
N
W
P
E
S

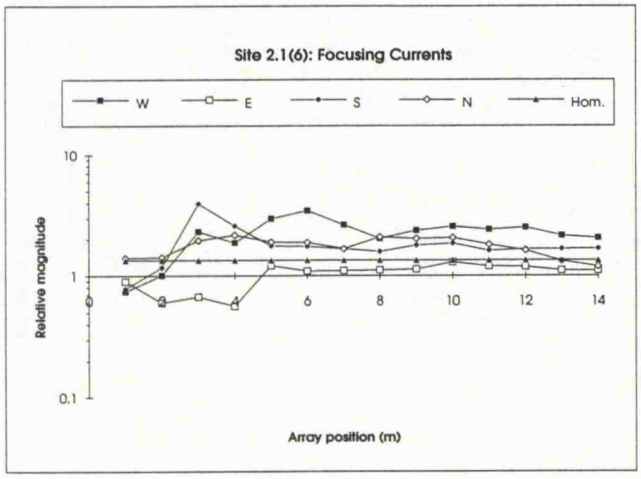
Site 2.1(6): Focusing Currents
W
E
S
N
Hom.
Relative magnitude
10
1
0.1
6
8
10
12
14
Array position (m)

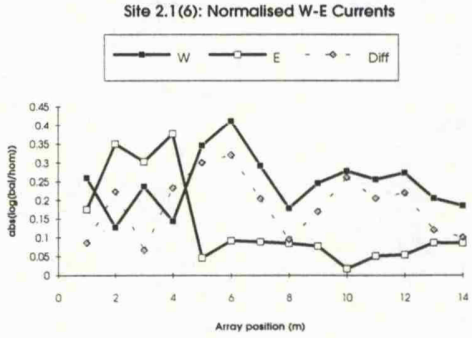
Site 2.1(6): Normalised W-E Currents
W
E
Diff
abs(log(bal/hom))
0.45
0.4
0.35
0.3
0.25
0.2
0.15
0.1
0.05
0
0
2
4
6
8
10
12
14
Array position (m)

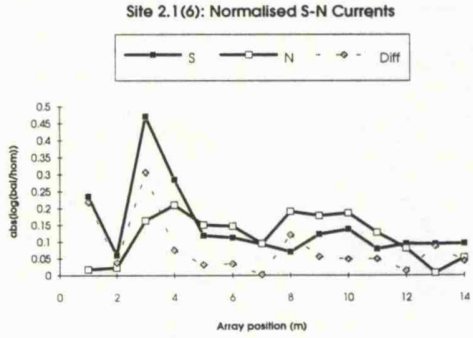
Site 2.1(6): Normalised S-N Currents
S
N
Diff
abs(log(bal/hom))
0.5
0.45
0.4
0.35
0.3
0.25
0.2
0.15
0.1
0.05
0
0
2
4
6
8
10
12
14
Array position (m)

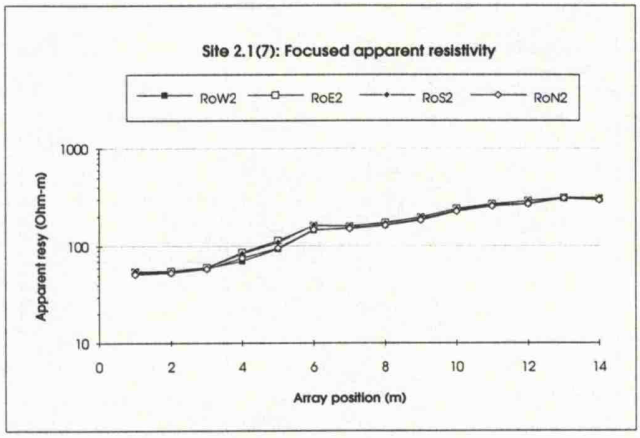
Site 2.1(7): Focused apparent resistivity
RoW2
RoE2
RoS2
RoN2
Apparent resy (Ohm-m)
1000
100
10
0
2
4
6
8
10
12
14
Array position (m)

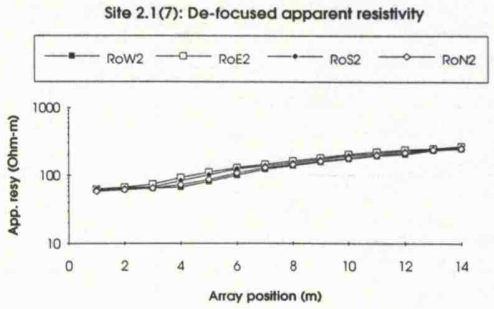
Site 2.1(7): De-focused apparent resistivity
RoW2
RoE2
RoS2
RoN2
App. resy (Ohm-m)
1000
100
10
0
2
4
6
8
10
12
14
Array position (m)

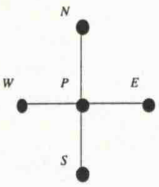
N
W
P
E
S

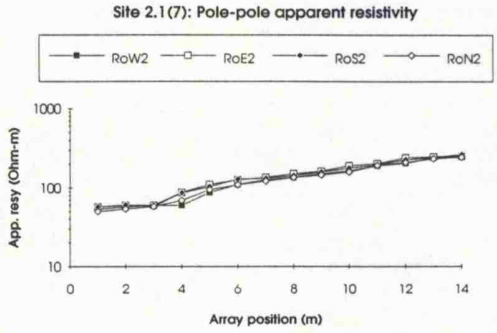
Site 2.1(7): Pole-pole apparent resistivity
RoW2
RoE2
RoS2
RoN2
App. resy (Ohm-m)
1000
100
10
0
2
4
6
8
10
12
14
Array position (m)

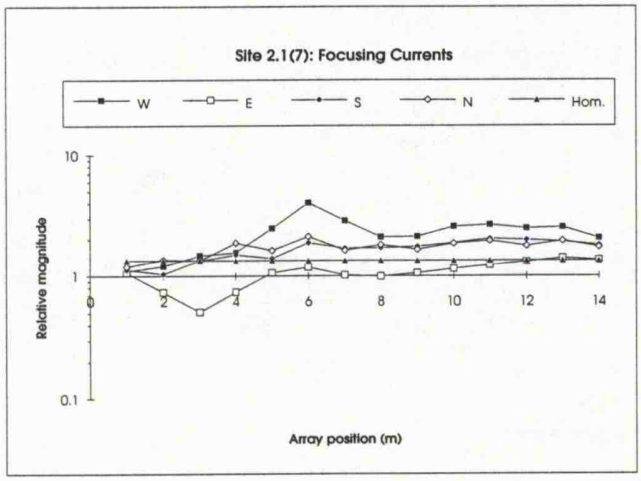
Site 2.1(7): Focusing Currents
W
E
S
N
Hom.
Relative magnitude
10
1
0.1
0
2
4
6
8
10
12
14
Array position (m)

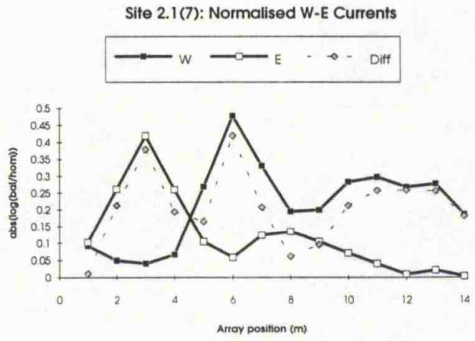
Site 2.1(7): Normalised W-E Currents
W
E
Diff
abs(log(bod/hom))
0.5
0.45
0.4
0.35
0.3
0.25
0.2
0.15
0.1
0.05
0
0
2
4
6
8
10
12
14
Array position (m)

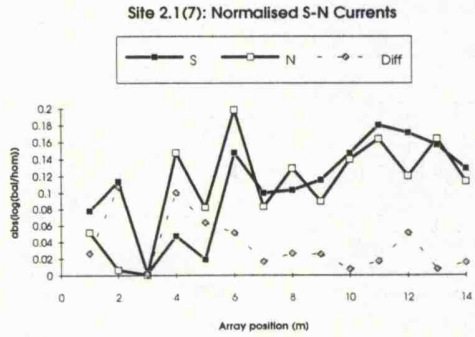
Site 2.1(7): Normalised S-N Currents
S
N
Diff
abs(log(bod/hom))
0.2
0.18
0.16
0.14
0.12
0.1
0.08
0.06
0.04
0.02
0
0
2
4
6
8
10
12
14
Array position (m)

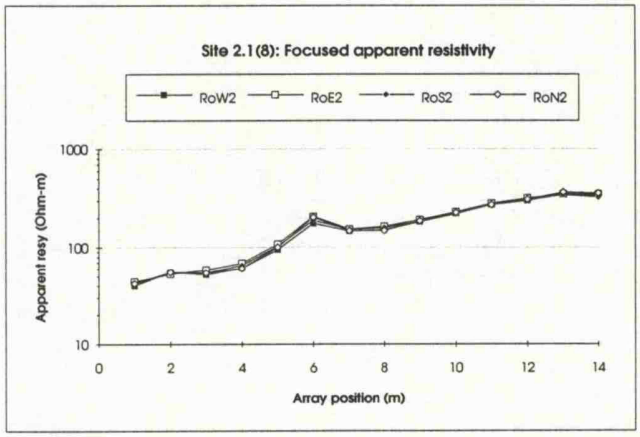
Site 2.1(8): Focused apparent resistivity
RoW2
RoE2
RoS2
RoN2
Apparent resy (Ohm-m)
1000
100
10
0
2
4
6
8
10
12
14
Array position (m)

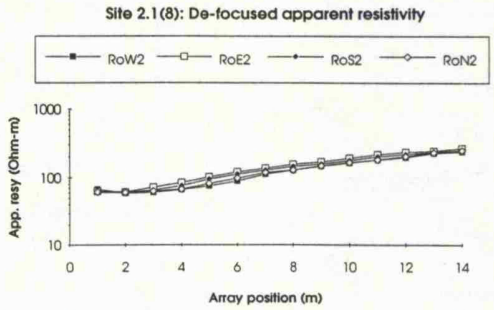
Site 2.1(8): De-focused apparent resistivity
RoW2
RoE2
RoS2
RoN2
App. resy (Ohm-m)
1000
100
10
0
2
4
6
8
10
12
14
Array position (m)

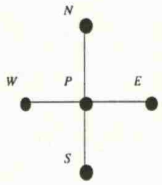
N
W
P
E
S

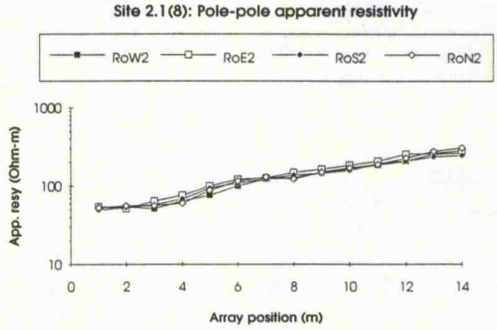
Site 2.1(8): Pole-pole apparent resistivity
RoW2
RoE2
RoS2
RoN2
App. resy (Ohm-m)
1000
100
10
0
2
4
6
8
10
12
14
Array position (m)

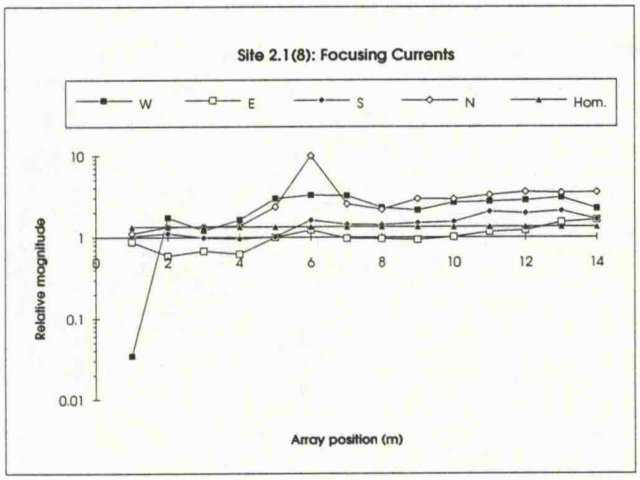
Site 2.1(8): Focusing Currents
W
E
S
N
Hom.
Relative magnitude
10
1
0.1
0.01
0
2
4
6
8
10
12
14
Array position (m)

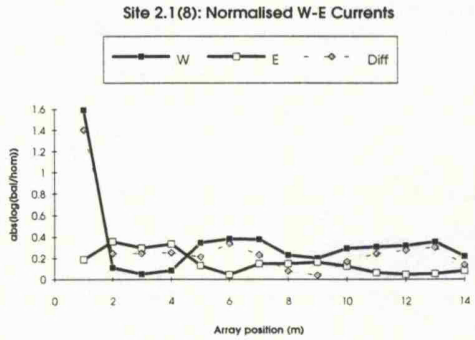
Site 2.1(8): Normalised W-E Currents
W
E
Diff
abs(log(bal/hom))
1.6
1.4
1.2
1
0.8
0.6
0.4
0.2
0
0
2
4
6
8
10
12
14
Array position (m)

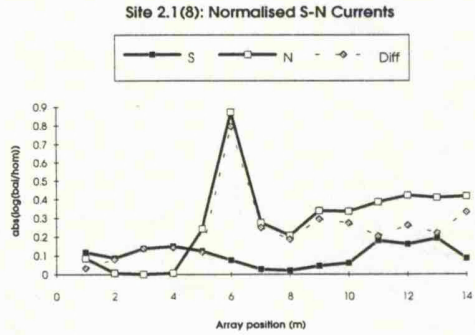
Site 2.1(8): Normalised S-N Currents
S
N
Diff
abs(log(bal/hom))
0.9
0.8
0.7
0.6
0.5
0.4
0.3
0.2
0.1
0
0
2
4
6
8
10
12
14
Array position (m)

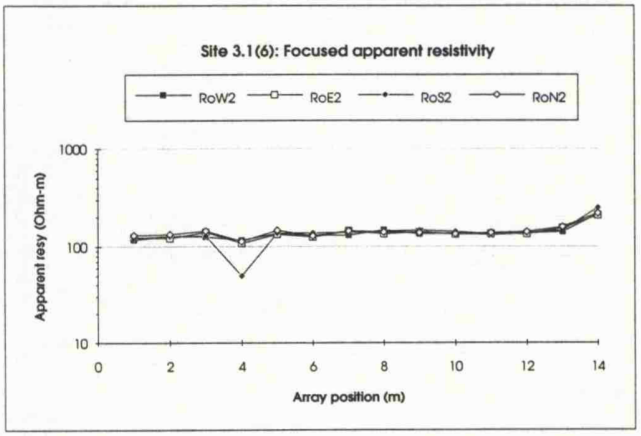
Site 3.1(6): Focused apparent resistivity
RoW2
RoE2
RoS2
RoN2
Apparent resy (Ohm-m)
1000
100
10
0
2
4
6
8
10
12
14
Array position (m)

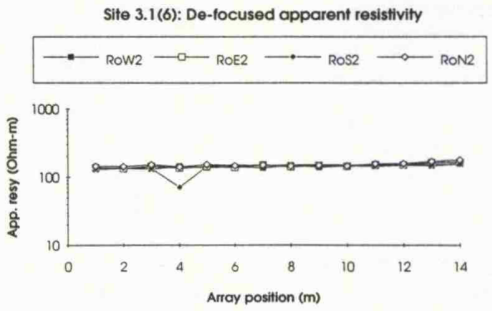
Site 3.1(6): De-focused apparent resistivity
RoW2
RoE2
RoS2
RoN2
App. resy (Ohm-m)
1000
100
10
0
2
4
6
8
10
12
14
Array position (m)

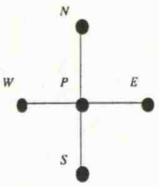
N
W
P
E
S

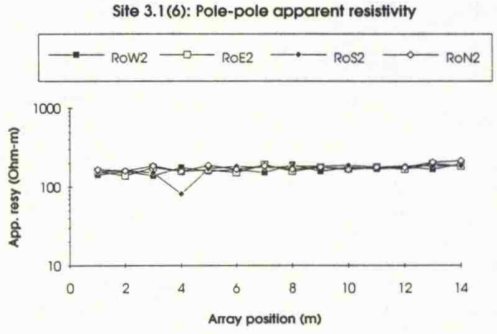
Site 3.1(6): Pole-pole apparent resistivity
RoW2
RoE2
RoS2
RoN2
App. resy (Ohm-m)
1000
100
10
0
2
4
6
8
10
12
14
Array position (m)

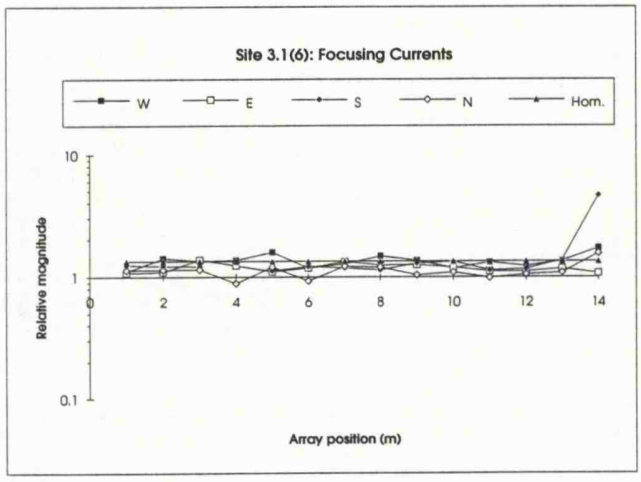
Site 3.1(6): Focusing Currents
W
E
S
N
Hom.
Relative magnitude
10
1
0.1
0
2
4
6
8
10
12
14
Array position (m)

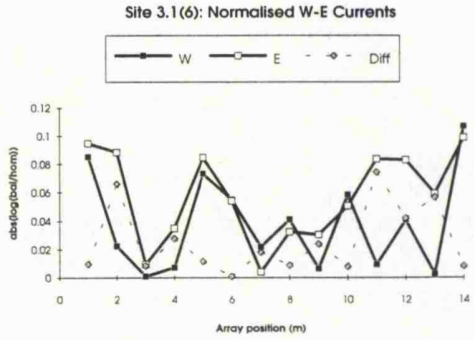
Site 3.1(6): Normalised W-E Currents
W
E
Diff
abs(log(bal/hom))
0.12
0.1
0.08
0.06
0.04
0.02
0
0
2
4
6
8
10
12
14
Array position (m)

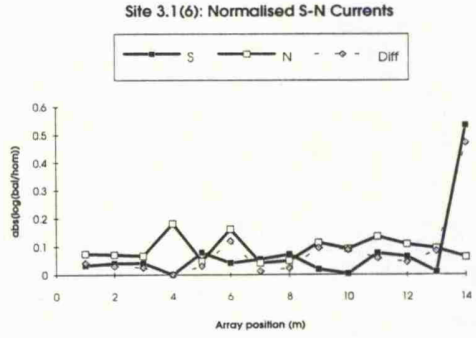
Site 3.1(6): Normalised S-N Currents
S
N
Diff
abs(log(bal/hom))
0.6
0.5
0.4
0.3
0.2
0.1
0
0
2
4
6
8
10
12
14
Array position (m)

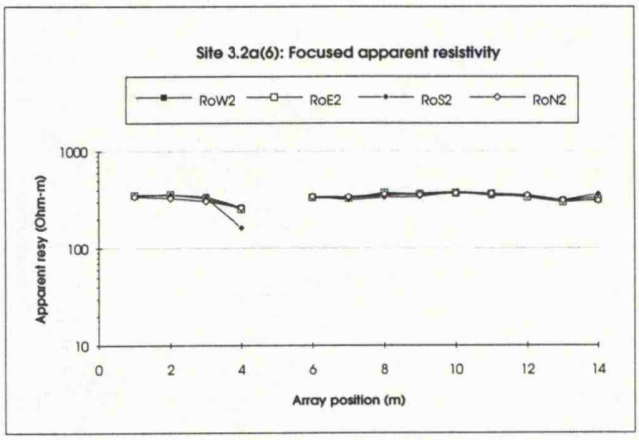
Site 3.2a(6): Focused apparent resistivity
RoW2
RoE2
RoS2
RoN2
Apparent resy (Ohm-m)
1000
100
10
0
2
4
6
8
10
12
14
Array position (m)

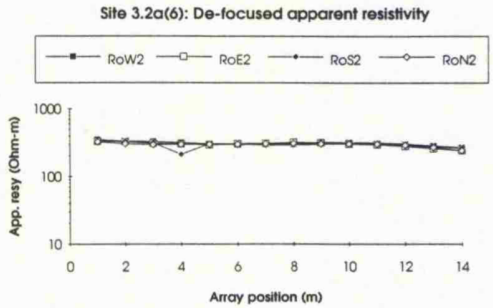
Site 3.2a(6): De-focused apparent resistivity
RoW2
RoE2
RoS2
RoN2
App. resy (Ohm-m)
1000
100
10
0
2
4
6
8
10
12
14
Array position (m)

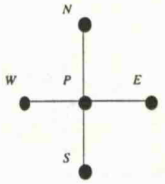
N
W
P
E
S

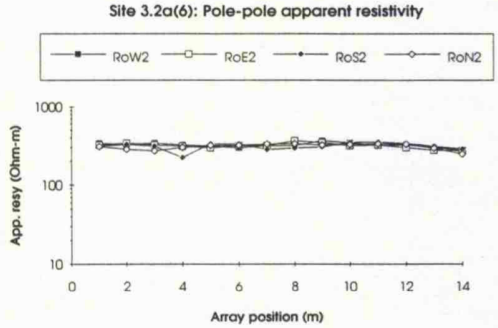
Site 3.2a(6): Pole-pole apparent resistivity
RoW2
RoE2
RoS2
RoN2
App. resy (Ohm-m)
1000
100
10
0
2
4
6
8
10
12
14
Array position (m)

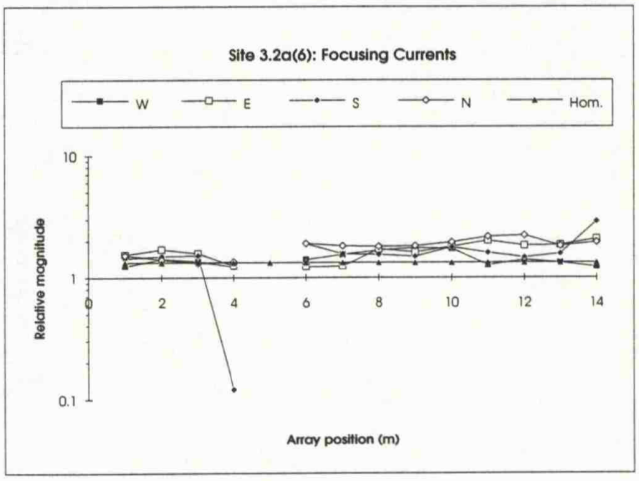
Site 3.2a(6): Focusing Currents
W
E
S
N
Hom.
Relative magnitude
10
1
0.1
0
2
4
6
8
10
12
14
Array position (m)

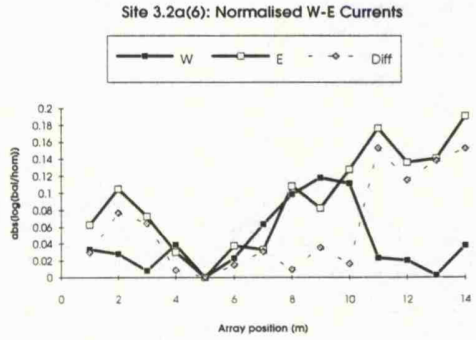
Site 3.2a(6): Normalised W-E Currents
W
E
Diff
abs(log(bal/hom))
0.2
0.18
0.16
0.14
0.12
0.1
0.08
0.06
0.04
0.02
0
0
2
4
6
8
10
12
14
Array position (m)

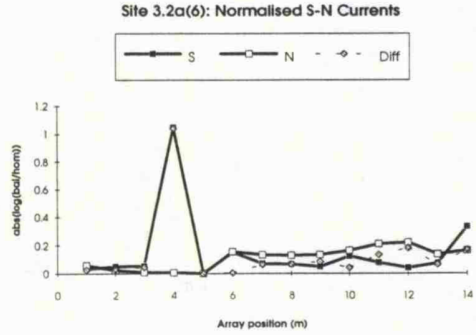
Site 3.2a(6): Normalised S-N Currents
S
N
Diff
abs(log(bal/hom))
1.2
1
0.8
0.6
0.4
0.2
0
0
2
4
6
8
10
12
14
Array position (m)

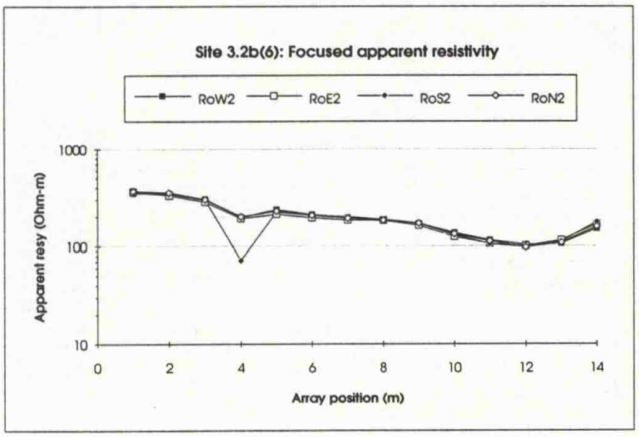
Site 3.2b(6): Focused apparent resistivity
RoW2
RoE2
RoS2
RoN2
Apparent resy (Ohm-m)
1000
100
10
0
2
4
6
8
10
12
14
Array position (m)

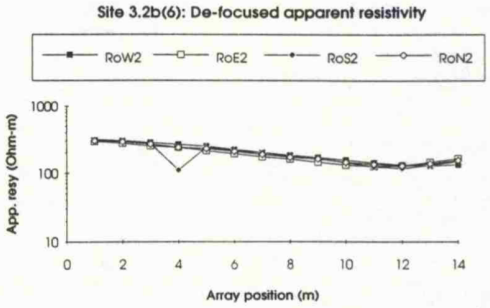
Site 3.2b(6): De-focused apparent resistivity
RoW2
RoE2
RoS2
RoN2
App. resy (Ohm-m)
1000
100
10
0
2
4
6
8
10
12
14
Array position (m)

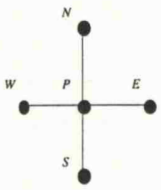
N
W
P
E
S

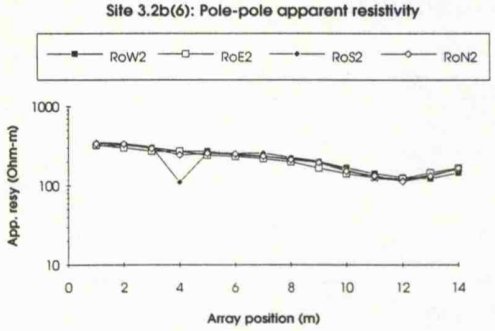
Site 3.2b(6): Pole-pole apparent resistivity
RoW2
RoE2
RoS2
RoN2
App. resy (Ohm-m)
1000
100
10
0
2
4
6
8
10
12
14
Array position (m)

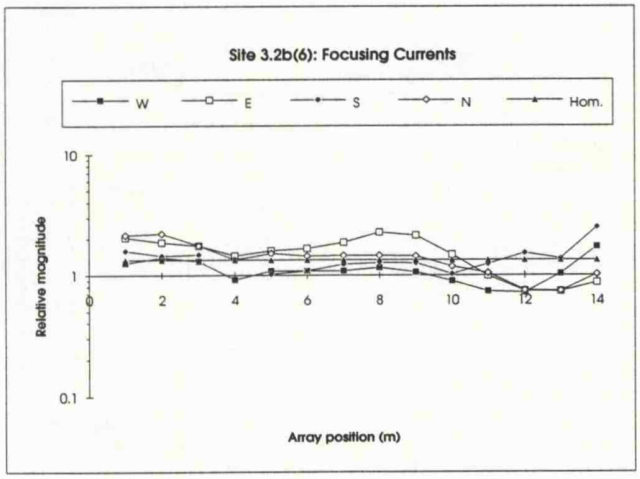
Site 3.2b(6): Focusing Currents
W
E
S
N
Hom.
Relative magnitude
10
1
0.1
0
2
4
6
8
10
12
14
Array position (m)

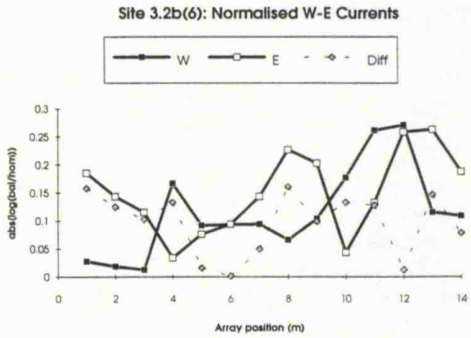
Site 3.2b(6): Normalised W-E Currents
W
E
Diff
abs(log(bal/hom))
0.3
0.25
0.2
0.15
0.1
0.05
0
0
2
4
6
8
10
12
14
Array position (m)

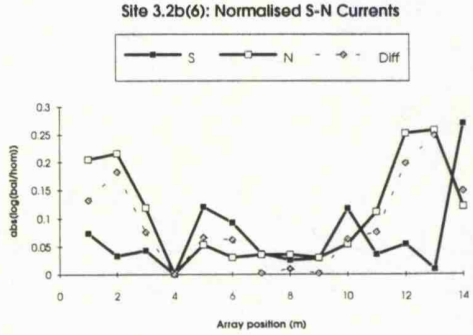
Site 3.2b(6): Normalised S-N Currents
S
N
Diff
abs(log(bal/hom))
0.3
0.25
0.2
0.15
0.1
0.05
0
0
2
4
6
8
10
12
14
Array position (m)

References

Allaud L. and Martin M. (1977) *Schlumberger, the History of a Technique*. John Wiley & Sons, Inc., New York.

Allaud L. A. and Ringot J. (1969) The high-resolution dipmeter tool. *The Log Analyst* **10**(3): 3–10.

Apparao A. and Roy A. (1971) Resistivity model experiments, 2. *Geoexploration* **9**(4), 195–205.

Apparao A., Roy A. and Mallick K. (1969) Resistivity model experiments. *Geoexploration* 7(1), 45–54.

Archie G. E. (1942) The electrical resistivity log as an aid in determining some reservoir characteristics. *Transactions of the American Institute of Mechanical Engineers* **146**: 54–62.

Aspinall A. and Walker A. R. (1975) The earth resistivity instrument and its application to shallow earth surveys. *Underground Services* **3**: 12–15.

Asten M. W. (1974) The influence of electrical anisotropy on mise à la masse surveys. *Geophysical Prospecting* **22**: 238–245.

Atkins E. R. and Smith G. H. (1961) The significance of particle shape in formation factor–porosity relationships. *Journal of Petroleum Technology* **13**(March): 285–291.

Beasley C. W. and Ward S. H. (1986) Three-dimensional mise-à-la-masse modeling applied to mapping fracture zones. *Geophysics* **51**(1): 98–113.

Beasley C. W. and Tripp A. C. (1991) Application of the cross-borehole direct-current resistivity technique for EOR process monitoring—a feasibility study. *Geoexploration* **28**: 313–328.

Bibby H. M. (1978) Direct current resistivity modeling for axially symmetric bodies using the finite element method. *Geophysics* **43**(3): 550–562.

Blohm E. K. and Flathe H. (1970) Geoelectrical deep sounding in the Rhinegraben. Report 27, Int. Upper Mantle Project. Sci., p239–242.

Bourke L. T. (1989) Recognizing artifact images of the Formation MicroScanner. In *Transactions of the Society of Professional Well Log Analysts 30th Annual Logging Symposium*, June 11–14, Denver, Colo., paper WW.

Bourke L. T. (1992) Sedimentological borehole image analysis in clastic rocks: a systematic approach to interpretation. In *Geological Applications of Wireline Logs II* (eds. A. Hurst, C. M. Griffiths and P. F. Worthington), pp. 31–42. Geological Society Special Publication No. 65.

Bourke L., Delfiner P., Fett T., Grace M., Luthi S., Serra O. and Standen E. (1989) Using Formation MicroScanner images. *The Technical Review* **37**(1), 16–40.

Bourne D. E. and Kendall P. C. (1977) *Vector Analysis and Cartesian Tensors*. Van Nostrand Reinhold (Int.), Wokingham.

Boyeldieu C. and Jeffreys P. (1988) Formation MicroScanner: new developments. In *Transactions of the Society of Professional Well Log Analysts 11th European Formation Evaluation Symposium*, Oslo, paper WW.

Brewer T., Lovell M., Harvey P. and Williamson G. (1995) Stratigraphy of the ocean crust in ODP Hole 896A from FMS images. *Scientific Drilling* **5**(2): 87–92.

Bugg S. F. and Lloyd J. W. (1976) A study of freshwater lens configuration in the Cayman Islands using resistivity methods. *Q. J. Eng. Geol.* **9**: 291–302.

Burden R. L. and Faires J. D. (1985) *Numerical Analysis*. Prindle, Weber & Schmidt, Boston.

Busby J. P. and Dabek Z. K. (1986) Resistivity and IP modeling of the three-array down-hole prospecting technique. *Geophysical Prospecting* **34**: 130–140.

Bussian A. E. (1983) Electrical conductance in a porous medium. *Geophysics* **48**(9): 1258–1268.

Carmichael R. S. (1989) *Practical Handbook of Physical Properties of Rocks and Minerals*. CRC Press, Boca Raton, FL.

Chang S.-K. and Anderson B. (1984) Simulation of induction logging by the finite-element method. *Geophysics* **49**(11): 1943–1958.

Chauvel Y., Seeburger D. and Orjuela A. (1984) Application of the SHDT Stratigraphic Dipmeter to the study of depositional environments. In *Transactions of the Society of Professional Well Log Analysts 25th Annual Logging Symposium*, June 10–13, New Orleans, LA, Paper G.

Chemali R., Gianzero S., Strickland R. and Tijani S. M. (1983) The shoulder bed effect on the dual laterolog and its variation with the resistivity of the borehole fluid. In *Transactions of the Society of Professional Well Log Analysts 24th Annual Logging Symposium*, UU1–25.

Choquette P. W. and Pray L. C. (1970) Geologic nomenclature and classification of porosity in sedimentary carbonates. *American Association of Petroleum Geologists Bulletin* **54**(2): 207–250.

Coggon J. H. (1971) Electromagnetic and electrical modeling by the finite element method. *Geophysics* **36**(1): 132–155.

Daily W. and Owen E. (1991) Cross-borehole resistivity tomography. *Geophysics* **56**: 1228–1235.

Daily W., Ramirez A., LaBrecque D. and Nitao J. (1992) Electrical resistivity tomography of vadose water movement. *Water resources research* **28**(5): 1429–1442.

Daniels J. J. (1977) Three-dimensional resistivity and induced-polarization modeling using buried electrodes. *Geophysics* **42**(5): 1006–1019.

Daniels J. J. and Dyck A. V. (1984) Borehole Resistivity and Electromagnetic Methods Applied to Mineral Exploration. *IEEE Transactions on geoscience and remote sensing* **GE-22**(1).

Davis J. and Annan A. (1989) Ground-penetrating radar for high-resolution mapping of soil and rock stratigraphy. *Geophysical Prospecting* **37**: 531–51.

Dennis B., Standen E., Georgi D. and Callow G. (1987) Fracture identification and productivity predictions in a carbonate reef complex. In *62nd SPE Annual Technical Conference*, September 27–30, Dallas, TX, paper SPE 16808.

deWitte L. and Gould R. W. (1959) Potential distribution due to a cylindrical electrode mounted on an insulating probe. *Geophysics* **24**(3): 566–579.

Dey A. and Morrison H. F. (1979) Resistivity modeling for arbitrarily shaped three-dimensional structures. *Geophysics* **44**(4): 753–780.

Doll H. G. (1951) The Laterolog: A new resistivity logging method with electrodes using an automatic focusing system. *Trans. Am. Inst. of Min., Metallurg., and Petr. Eng.* **192**, 305–316.

Doll H. G. (1953) The Microlaterolog. *Trans. Am. Inst. of Min., Metallurg., and Petr. Eng.* **198**, 17–32.

Doveton J. H. (1986) *Log Analysis of Subsurface Geology: Concepts and Computer Methods.* John Wiley & Sons, New York.

Edwards R. N., Nobes D. C. and Gómez-Treviño E. (1984) Offshore electrical exploration of sedimentary basins: The effects of anisotropy in horizontally isotropic, layered media. *Geophysics* **49**(5): 566–576.

Eisenstat S. C., Gursky M. C., Schultz M. H. and Sherman A. H. (1977) Yale sparse matrix package. Research report 112 and 114, Yale University.

Ekstrom M. P., Dahan C. A., Chen M. Y., Lloyd P. M. and Rossi D. J. (1987) Formation imaging with microelectrical scanning arrays. *The Log Analyst* **28**(3), 294–306.

Ellis D. V. (1987) *Well Logging for Earth Scientists*. Elsevier, New York.

Eskola L. (1992) *Geophysical Interpretation Using Integral Equations*. Chapman & Hall, London.

Focke J. W. and Munn D. (1987) Cementation exponents in Middle Eastern carbonate reservoirs. *SPE Form. Eval.* **2**: 155–167.

Ghosh D. P. (1971) The application of linear filter theory to the direct interpretation of geoelectric resistivity sounding measurements. *Geophysical Prospecting* **19**: 192–217.

Gianzero S. (1981) The mathematics of resistivity and induction logging. *The Technical Review* **29**(1): 4–32.

Gianzero S. C. and Anderson B. (1982) An integral transform solution to the fundamental problem in resistivity logging. *Geophysics* **47**(6): 946–956.

Grant F. S. and West G. F. (1965) *Interpretation Theory in Applied Geophysics*. McGraw-Hill Book Company, New York.

Grattoni C. A. and Dawe R. A. (1991) Electrical resistivity properties of porous media—model studies of some structural influences. In *Transaction of the Society of Professional Well Log Analysts 14th European Formation Evaluation Symposium ("THAMES")*, London.

Greenwood P. G., Jackson P. D., Meldrum P. I., Peart R. J. and Raines M. G. (1993) Methods for recognition of geological weakness and other surface discontinuities caused by underground mining in Carboniferous terrain. Technical Report WN/94/02, British Geological Survey, Engineering Geology and Geophysics Group, Keyworth, Nottingham.

Gunn J. E. (1964) The numerical solution of $\Delta \cdot a \Delta u = f$ by a semiexplicit alternating direction iterative method. *Numer. Math.* **6**: 181.

Guyod H. (1955) Electrical analogue of resistivity logging. *Geophysics* **20**(3): 615–629.

Halladay N. (1994) The development of a high temperature focussed resistivity tool. Report IR07/30, CSM Associates Ltd, Rosemanowes, Herniss, Penryn.

Harker S. D., McGann G. J., Bourke L. T. and Adams J. T. (1990) Methodology of Formation MicroScanner image interpretation in Claymore and Scapa Fields (North Sea). In *Geological Applications of Wireline Logs* (eds. A. Hurst, M. A. Lovell and A. C. Morton), pp. 11–25. Geological Society Special Publication No. 48.

Harrington R. (1968) *Field Computation by Moment Methods*. MacMillan, New York.

Hermance J. F. (1973) An electrical model for the sub-Icelandic crust. *Geophysics* **38**: 3–13.

Hermance J. F. (1983) DC telluric fields in three dimensions: a refined finite-difference simulation using local integral forms. *Geophysics* **48**(3): 331–340.

Hermance J. F. and Garland G. D. (1968) Deep electrical structure under Iceland. *Journal of Geophysical Research* **73**: 3797–3800.

Herrick D. C. and Kennedy W. D. (1994) Electrical efficiency—A pore geometric theory for interpreting the electrical properties of reservoir rocks. *Geophysics* **59**(6): 918–927.

Hiscott R. N., Colella A., Pezard P., Lovell M. A. and Malinverno A. (1993) Basin plain turbidite succession of the Oligocene Izu-Bonin intraoceanic forearc basin. *Marine and Petroleum Geology* **10**(October): 450–466.

Hohmann G. W. (1975) Three-dimensional induced polarization and electromagnetic modeling. *Geophysics* **40**(2): 309–324.

Hornby B. E., Luthi S. M. and Plumb R. A. (1992) Comparison of fracture apertures computed from electrical borehole scans and reflected Stoneley waves: an integrated interpretation. *The Log Analyst* **33**(1): 50–66.

Jackson P. D. (1976) Comments on "New results in resistivity well logging". *Geophysical Prospecting* **24**: 407–408.

Jackson P. D. (1981) Focused electrical resistivity arrays: some theoretical and practical experiments. *Geophysical Prospecting* **99**, 601–626.

Jackson P. D., Taylor-Smith D. and Stanford P. N. (1978) Resistivity-porosity-particle shape relationships for marine sediments. *Geophysics* **43**(6): 1250–1268.

Jackson P. D., Meldrum P. I. and Williams G. M. (1989) Principles of a computer controlled multi-electrode resistivity system for automatic data acquisition. Technical Report WE/89/32, British Geological Survey, Engineering Geology and Geophysics Group, Keyworth, Nottingham.

Jackson P. D., Jarrard R. D., Pigram C. J. and Pearce J. M. (1993) Resistivity/porosity/velocity relationships from downhole logs: an aid for evaluating pore morphology. In J. A. McKenzie, P. J. Davies, A. Palmer-Julson et al. *Proceedings of the Ocean Drilling Program, Scientific Results* **133**: National Science Foundation, College Station, TX (Ocean Drilling Program), 661–686.

James B. A. (1985) Efficient microcomputer-based finite-difference resistivity modeling via Polozhii decomposition. *Geophysics* **50**(3): 443–465.

Kaufman A. A. (1990) The electric field in a borehole with a casing. *Geophysics* **55**: 29–38.

Kearey P. and Brooks M. (1991) *An Introduction to Geophysical Exploration*. Blackwell Scientific Publications, Oxford.

Keller G. V. and Frischknecht F. C. (1966) *Electrical Methods in Geophysical Prospecting*. Pergammon Press Ltd., Oxford.

Kellogg O. D. (1967) *Foundations of Potential Theory*. Springer-Verlag, Berlin.

Kirkpatrick S. (1973) Percolation and Conduction. *Reviews of Modern Physics* **45**(4): 574–588.

Koefoed O. (1979) Geosounding Principles, 1. Resistivity Sounding Measurements. Elsevier, Amsterdam.

Korvin G. (1982) Axiomatic characterisation of the general mixture rule. *Geoexploration* **19**: 267–276.

Kunz K. S. and Moran J. H. (1958) Some effects of formation anisotropy on resistivity measurements in boreholes. *Geophysics* **23**(4): 770–794.

LaBreque D. J. and Ward S. H. (1990) Two-dimensional cross-borehole resistivity model fitting. In *Geotechnical and Environmental Geophysics*, **3** (ed. S. H. Ward), pp. 51–74. Society of Exploration Geophysicists, Tulsa, OK.

Lacour-Gayet P. (1981) The Groningen effect... causes and partial remedy. *The Technical Review* **29**(1): 37–47.

Le Masne D. and Poirmeur C. (1988) Three-dimensional model results for an electrical hole-to-surface method: Application to the interpretation of a field survey. *Geophysics* **53**: 85–103.

Lee K. H., Pridmore D. F. and Morrison H. F. (1981) A hybrid three-dimensional electromagnetic modeling scheme. *Geophysics* **46**(5): 796–805.

Lloyd P. M., Dahan C. and Hutin R. (1986) Formation imaging with micro electrical scanning arrays: a new generation of stratigraphic high resolution dipmeter tool. In *Transactions of the Society of Professional Well Log Analysts 10th European Formation Evaluation Symposium*, April 22–25, Aberdeen, Paper L.

Luthi S. M. (1990) Sedimentary structures of clastic rocks identified from electrical borehole images. In *Geological Application of Wireline Logs* (eds. A. Hurst, M. A. Lovell and A. C. Morton), pp. 3–10. Geological Society Special Publication No. 48.

Luthi S. M. and Souhaité P. (1990) Fracture apertures from electrical borehole scans. *Geophysics* **55**(7): 821–833.

MacLeod C. J., Parson L. M., Sager W. W. and Ocean Drilling Program Leg 135 Shipboard Scientific Party (1992) Identification of tectonic rotations in boreholes by the integration of core information with Formation MicroScanner and Borehole Televiewer images. In *Geological Applications of Wireline Logs II* (eds. A. Hurst, C. M. Griffiths and P. F. Worthington), pp. 235–246. Geological Society Special Publication No. 65.

Madden T. R. (1976) Random network and mixing laws. *Geophysics* **41**(6A): 1104–1124.

Maillet R. (1947) The fundamental equations of electrical prospecting. *Geophysics* **12**: 529–556.

Matias M. J. S. and Habberjam G. M. (1986) The effect of structure and anisotropy on resistivity measurements. *Geophysics* **51**(4): 964–971.

Mazac O., Kelly W. E. and Landa I. (1987) Surface geoelectrics for groundwater pollution and protection studies. *Journal of Hydrology* **93**: 277–294.

Meldrum P. I. and Williams C. G. (1995) Report on field work resistivity surveys, Saarland, Germany, September 15–24, 1994. Project note 95/19, British Geological Survey, Keyworth, Nottingham.

Meldrum P. I., Jackson P. D., Williams C. G., Gunn D. A. and Flint R. C. (1994) Automatic data acquisition for 3D resistivity surveys. Technical Report WN/94/19, British Geological Survey, Engineering Geology and Geophysics Group, Keyworth, Nottingham.

Mendelson K. S. and Cohen M. H. (1982) The effect of grain anisotropy on the electrical properties of sedimentary rocks. *Geophysics* **47**(2): 257–263.

Mitchell A. R. and Griffiths D. F. (1980) *The Finite Difference Method in Partial Difference Equations*. John Wiley & Sons Ltd, Chichester.

Moran J. H. and Gianzero S. (1979) Effects of formation anisotropy on resistivity-logging measurements. *Geophysics* **44**(7): 1266–1286.

Moran J. H. and Chemali R. (1985) Focused resistivity logs. In *Developments in Geophysical Exploration Methods* (ed. A. A. Fitch), pp. 225–260. Applied Science Publishers Ltd., London.

Mufti I. R. (1976) Finite-difference resistivity modeling for arbitrarily shaped two-dimensional structures. *Geophysics* **41**(1): 62–78.

Mufti I. R. (1978) A practical approach to finite-difference resistivity modeling. *Geophysics* **43**(5): 930–942.

Mufti I. R. (1980) Finite-difference evaluation of apparent resistivity curves. *Geophysical Prospecting* **28**: 146–166.

Oteri A. U. (1981) Geoelectric investigation of saline contamination of a Chalk aquifer by mine drainage water at Tilmanstone, England. *Geoexploration* **19**: 179–192.

Owen T. E. (1982) Detection and mapping of tunnels and caves. In *Developments in Geophysical Exploration Methods* (ed. A. A. Fitch), pp. Chapter 5. Applied Science Publishers Ltd., London.

Papamarinopoulos S., Jones R. E. and Williams H. (1988) Electric Resistance survey of the Southern Part of the Buried Ancient Town of Stymphalos. *Geoexploration* **25**: 255–261.

Parasnis D. H. (1986) *Principles of Applied Geophysics*. Chapman & Hall, London.

Parkhomenko E. I. (1967) *Electrical Properties of Rocks*. Plenum Press, New York.

Parra J. O. and Owen T. E. (1990) Synthetically focused resistivity for detecting deep targets. In *Geotechnical and Environmental Geophysics* (ed. S. H. Ward), pp. 37–50. Society of Exploration Geophysicists, Tulsa, OK.

Parson L., Hawkins J., Allen J. and ODP Leg 135 Shipboard Scientific Party (1992) *Proceedings of the Ocean Drilling Program, Initial Reports*, **135**. College Station, TX (Ocean Drilling Program).

Peart R. J., Jackson P. D., Greenwood P. G., Meldrum P. I., Williams C. G., Raines M. G., Beamish D. and Flint R. C. (1996) Methods for the recognition of geological weakness zones and other surface discontinuities caused by underground mining in Carboniferous terrain. Technical Report WN/95/37, British Geological Survey, Engineering Geology and Geophysics Group, Keyworth, Nottingham.

Petrick W. R., Sill W. R. and Ward S. H. (1981) Three-dimensional resistivity inversion using alpha-centers. *Geophysics* **46**: 1148–1162.

Pezard P. A. and Luthi S. M. (1988) Borehole electrical images in the basement of the Cajon Pass scientific drillhole, California; fracture identification and tectonic implications. *Geophysical Research Letters* **15**(9), 1017–1020.

Pezard P. A., Anderson R. N., Howard J. J. and Luthi S. M. (1988) Fracture distribution and basement structure from measurements of electrical resistivity in the basement of the Cajon Pass scientific drillhole, California. *Geophysical Research Letters* **15**(9): 1021–1024.

Pezard P. A., Lovell M. A. and Ocean Drilling Program Leg 126 Shipboard Scientific Party (1990) High resolution imaging of subsurface oceanic sediments. *EOS, Trans. American Geophysical Union* **71**: 709 & 718.

Plumb R. and Luthi S. (1986) Application of borehole images to geologic modeling of an eolian reservoir. In *61st SPE Annual Technical Conference*, October 5–8, New Orleans, paper SPE 15487.

Press W. H., Teukolsky S. A., Vetterling W. T. and Flannery B. P. (1992) *Numerical Recipes in FORTRAN: The Art of Scientific Computing*. Cambridge University Press, Cambridge.

Rauen A. and Lastovickova M. (1995) Investigation of electrical anisotropy in the deep borehole KTB. *Surveys in Geophysics* **16**(1): 37–46.

Reece G. (1986) *Microcomputer Modelling by Finite Differences*. Macmillan Education Ltd, Houndmills, Basingstoke, Hampshire.

Roach G. F. (1982) *Green's Functions*. Cambridge University Press, Cambridge.

Roy A. (1982) Focused resistivity logs. In *Developments in Geophysical Exploration Methods—3* (ed. A. A. Fitch), Chapter 3. Applied Science Publishers Ltd., London.

Roy K. K. and Rao K. P. (1977) Basement effect on line source d.c. apparent resistivity profiles. *Geoexploration* **15**: 163–172.

Sasaki Y. (1994) 3-D resistivity inversion using the finite-element method. *Geophysics* **59**(12): 1839–1848.

Schenkel C. J. and Morrison H. F. (1994) Electrical resistivity measurement through metal casing. *Geophysics* **59**(1): 1072–1082.

Schlumberger (1984) *Resistivity Measurement Tools*. Schlumberger Educational Services.

Schlumberger (1991) *Log Interpretation Principles/Applications*. Schlumberger Educational Services, New York, NY.

Schlumberger C. (1920) *Etude de la prospection electrique du sous-sol*. Gauthiers-Villars, Paris.

Schopper J. R. (1966) A theoretical investigation on the formation factor/permeability/porosity relationship using a network model. *Geophysical prospecting* **14**: 301–341.

Scriba H. (1981) Computation of the electric potential in three-dimensional structures. *Geophysical Prospecting* **29**: 790–802.

Seigel H. O. (1967) The induced polarization method. In *Economic Geology Report No. 26* (ed. L. W. Morley), pp. 123–137. Geological Survey of Canada.

Seiler D., King G. and Eubanks D. (1994) Field test results of a six-arm microresistivity borehole imaging tool. In *Transactions of the Society of Professional Well Log Analysts 35th Annual Logging Symposium*, June 19–22, Tulsa, OK, paper W.

Sen P. N., Scala C. and Cohen M. H. (1981) A self-similar model for sedimentary rocks with application to the dielectric constant of fused glass beads. *Geophysics* **46**(5): 781–795.

Serra O. (1989) *Formation MicroScanner Image Interpretation*. Schlumberger Educational Services, Houston.

Sinha A. K. and Bhattacharya P. K. (1967) Electric dipole over an anisotropic and inhomogeneous earth. *Geophysics* **32**: 652–667.

Snyder D. D. and Merkel R. M. (1973) Analytic models for the interpretation of electrical surveys using buried current electrodes. *Geophysics* **38**: 513–529.

Stefanescu S. and Stefanescu D. (1974) Mathematical models of conducting ore bodies for direct current electrical prospecting. *Geophysical Prospecting* **22**(2): 246–260.

Stefanescu S. S., Schlumberger C. and Schlumberger M. (1930) Sur la distribution électrique potentielle autour d'une prise de terre ponctuelle dans un terrain à couches horizontales, homogènes et isotropes. *Journal Physique et le Radium* **1**: 132–140.

Stoyer C. H. and Wait J. R. (1976) Resistivity probing of an "exponential" earth with a homogeneous overburden. *Geoexploration* **15**: 11–18.

Straley J. P. (1976) Critical phenomena in resistor networks. *Journal of Physics C: Solid State Physics* **9**: 783–795.

Stratton J. A. (1941) *Electromagnetic Theory*. McGraw-Hill, New York.

Straub A. (1995) General formulation of the electric stratified problem with a boundary integral equation. *Geophysics* **60**(6): 1656–1670.

Suau J., Grimaldi P., Poupon A. and Souhaité P. (1972) The Dual Laterolog–R_{xo} tool. In *47th Annual Technical Conference and Exhibition*, October 27–30, San Antonio, TX, paper SPE 4018.

Taylor B., Fjioka K. and ODP Leg 126 Shipboard Scientific Party (1990) *Proceedings of the Ocean Drilling Program, Initial Reports*, **126**. College Station, TX (Ocean Drilling Program).

Telford W. M., Geldart L. P. and Sheriff R. E. (1990) *Applied Geophysics*. Cambridge University Press, Cambridge.

Thanassoulas C. (1991) Geothermal exploration using electrical methods. *Geoexploration* **27**: 321–350.

Ting S. C. and Hohmann G. W. (1981) Integral equation modeling of three-dimensional magnetotelluric response. *Geophysics* **46**(2): 182–197.

Tripp A. C., Hohmann G. W. and Swift C. M., Jr. (1984) Two-dimensional resistivity inversion. *Geophysics* **49**(10): 1708–1717.

Trouiller J. C. (1988) Modeling of FMS tool response. In-house FMS Workshop, Schlumberger, Paris.

Varga R. S. (1962) *Matrix Iterative Analysis*. Prentice-Hall, Englewood Cliffs, NJ.

Wang T., Stodt J. A., Stierman D. J. and Murdoch L. C. (1991) Mapping hydraulic fractures using a borehole-to-surface electrical resistivity method. *Geoexploration* **28**: 349–369.

Wannamaker P. E., Hohmann G. W. and SanFilipo W. A. (1984) Electromagnetic modeling of three-dimensional bodies in layered earths using integral equations. *Geophysics* **49**(1): 60–74.

Waxman M. H. and Smits L. J. M. (1968) Electrical conduction in oil-bearing shaly sand. *Society of Petroleum Engineers Journal* **8**: 107–122.

Whelan P. M. and Hodgson M. J. (1978) *Essential Principles of Physics*. John Murray, London.

Winsauer W. O. and McCardell W. M. (1953) Ionic double-layer conductivity in reservoir rock. *Petroleum Transactions AIME* **198**.

Winsauer W. O., Shearin H. M., Jr., Masson P. H. and Williams M. (1952) Resistivity of brine-saturated sands in relation to pore geometry. *Bulletin of the American Association of Petroleum Geologists* **36**(2): 253–277.

Woodhouse R. (1978) The Laterolog Groningen phantom can cost you money. In *Transactions of the Society of Professional Well Log Analysts 19th Annual Logging Symposium*, R1–17.

Wyllie M. R. J. and Gregory G. R. (1953) Formation factors of unconsolidated porous media: Influence of particle shape and effects of cementation. *Petrol. Trans. AIME* **198**: 103–110.

Zemanian A. H. and Anderson B. (1987) Modeling of borehole resistivity measurements using infinite electrical grids. *Geophysics* **52**(11): 1525–1534.

Zienkiewicz O. C. (1971) *The Finite Element Method in Engineering Science*, 2nd edn. McGraw-Hill, London.